The Localisation of Reactive Oxygen Species in Human Hepatoma Cells Visualised by One and Two Photon Excitation Confocal Fluorescence Laser Scanning Microscopy

A diploma work submitted to the

Faculty of Natural Sciences of the University Witten / Herdecke

and the

Max-Planck-Institute for Molecular Physiology, Dortmund

for the degree of

Diplom-Biochemist

presented by

Verena Brand

accepted on the recommendation of:

Prof. Dr. H. Acker, examiner

Prof. Dr. H. J. Lipps, co-examiner

Witten, March 2001

Abstract

1 and 2 photon laser microscopy of dihydrorhodamine and dichloro-dihydrofluorescein for localising reactive oxygen species in HepG2 cells.

V.Brand, T.Porwol, H.Acker

Within a physiological range reactive oxygen species play a crucial role in signal transduction in the oxygen sensing pathway which is modulating genes like the erythropoetin gene or the one for vascular endothelium growth factor at least in the used human hepatoma cell line HepG2. These cells are a very suitable tool to investigate oxygen sensing mechanisms, as for example the inducible operation of the erythropoeitin 3' enhancer which was found later in multiple cell lines giving evidence that there is a widespread converging oxygen-mechanism on cellular and molecular level. (Maxwell et al. 1993)

Former experiments performed with conventional one photon excitation confocal laser scanning microscopy could not reveal if reactive oxygen species (ROS) were generated only inside of mitochondria or in the cytoplasm as well. Conflicting results have been obtained concerning the cellular localisation as well as response to hypoxia of reactive oxygen species (ROS) in human hepatoma HepG2 cells (Kietzmann 1998, 2000, Chandel et al. 1998, 2000). Chandel et al. working with mitochondria-depleted ρ^0 cells, concluded that ROS generation only can take place in mitochondria as cells lacking mitochondria does not produce ROS at all. Kietzmann et al. concluded from their experiments with HepG2cells and primary rat liver cells that reactive oxygen species are produced as well in the cytoplasm. Contradictory results could also be obtained, because of use of different fluorescent dyes to detect ROS. Therefore, we carried out a comparative study on dihydrorhodamine 123 (DHR) and 2´,7´dichlorodihydrofluorescin-diacetate (H_2DCFDA) stained HepG2 cells. H_2DCFDA after being cleaved by intracellular esterases to 2',7'-dichlorofluorescein (H_2DCF) and DHR are getting oxidised by ROS to fluorescent dyes excited with 488nm for 1 photon and with 798 nm for 2 photon laser scanning microscopy (CLSM). Oxidation resulted most likely from hydroxyl radicals ($OH^{\bullet}$) generated in a perinuclear (iron-dependent) Fenton reaction. For localisation of the Fenton reaction mitochondrial mass of HepG2 cells has been stained with MitoTracker RedCMX Ros(10µM)

excited with 543,5 nm for 1 photon CLSM and 798 nm in two photon excitation laser scan microscopy (TPE LSM). Furtherrmore cell nucleus was stained with DAPI (25µM). After about 20 minutes of staining cells have been washed and imaged by CLSM or TPE LSM. Laser light used in one photon excitation induced ROS generation in such a manner that the fluorescence of the applied dyes to detect ROS increased quickly just upon observation, demonstrating that one photon excitation fluorescence CLSM is highly destructive, and not suitable for measurement of those light-sensitive reactions. As the laser scans the specimen, the probe is selectively bleached in the X/Y plane and nonselectively bleached in the Z plane. Therefore we implemented a new method for performing the experiments: two photon excitation laser scanning microscopy. Because detailed knowledge of the two-photon excitation spectra of molecular fluorophores is required for determining if the fluorophores, used in conventional CLSM, are suitable for TPELSM, two photon excitation and emission spectroscopic measurement were performed. As optical characteristics of the new implemented microscope system, TPE laser scan microscopy were not known, experimental Point Spread functions (PSFs) in comparison to one photon excitation confocal PSFs were measured. PSFs control the image formation in all coherent (and incoherent) optical systems, therefore the obtained confocal data were deconvoluted with them for 3 dimensional reconstruction improving local resolution. Oxidised DHR, Rhodamine 123, and oxidised H_2DCF, DCF, could be colocalized with the mitochondrial mass as well with a perinuclear, non mitochondrial compartment. DCF could be visualised predominantly within the mitochondrial mass. About 30 minutes after staining oxidised DCF started to get localised and accumulated within the cell nucleus. Obviously DHR as well as DCF are getting oxidised at very distinct spots within the different cellular compartments. No difference in localisation could be detected between 1 and 2 photon laser microscopy. However 2 photon excitation resulted in a more pronounced emission intensity. We conclude that HepG2 cells give comparable results only after short term staining with DHR or DCF. Results obtained after 30 minutes or even longer give recordings which originate from different cellular compartments. The reported conflicting results in the literature might be partly explainable by our findings.

Max-Planck-Institut für molekulare Physiologie, Otto-Hahn-Strasse 11, D-44227 Dortmund

meinen Eltern

ACKNOWLEDGEMENTS

Hereby I wish to express my deep gratitude for the tremendous chance and the opportunity to complete my *Diplomarbeit* for the degree *Diplom-Biochemikerin* from the University *Witten/Herdecke* at the *Max-Planck Institut (MPI) für Molekulare Physiologie Dortmund*.

In particular I am grateful to:

Prof. Hans Joachim Lipps (University Witten/Herdecke),
my supervisor Prof. Dr. Helmut Acker (MPI Dortmund) for the interesting theme, his permanent scientific, humane support during this work, for discussions that we lead with him, for his patience and financial support,
Dr. Torsten Porwol for his assistance to realise my thesis, especially concering the two photon excitation laser scanning microscopy, the three dimensional reconstruction and visualisation,
Dr.Thomas Feurer, Gregor Stobrawa, Martin Hacker for co-operation to carry out the two photon excitation fluorescence spectroscopy in the Physical-Astronomical Faculty, in the Institute for Optic and Quantum Electronics of the Friedrich-Schiller-University in Jena,
Dr. Utta Berchner-Pfannschmidt for her collaboration and interesting discussions, Engineer Evelyne Merten for her never ending support in every aspect, Brigitte Bölling for her maintenance of cell culture, Dietmar Brümann for the technical assistance, Christoph Wotzlaw doing his diploma thesis as well, Felix Bestvater for both photos of two photon excitation fluorescence spectroscopy and laser scanning microscopy,
the services of the Max-Planck-Institute in Dortmund, especially the central documentation unit with Claudia Pieczka and Gesine Schulte,
Silicon Graphics, Nikon GmbH, Coherent GmbH, Newport, Scientific Volume Imaging b.v., Coord Automatisierung for co-operation, advice, and financial support in general for the project,
all my colleagues and friends,
as well as to my parents, my family and Siegfried Kruss.

Verena Brand, March 2001

TABLE OF CONTENTS

List of illustrations and tables

(without Figures of Results see chapter 8 –10)

List of (most often used) Abbreviations and Symbols

AVS	Advanced Visual Systems
a.u.	Arbitrary units (Intensity)
α	Aperture angle of the objective lens
1P	One Photon
2P	Two Photon
c	Concentration
C(F)LSM	Confocal (Fluorescence) Laser Scan Microscopy /Microscope
d	Distance
DAPI	4’,6-diamidino-2-phenylindole, dihydrochloride
DCF	2’,7’- Dichlorofluorescein
DHR	Dihydrorhodamine 123
DMSO	Dimethylsulfoxide
Em	Emission
Exc	Excitation
Exp	Experimental
FT	Fourier Transformation
FWHM	Full width (of) half maximum
$H(m,v)$	Modulation transfer function
H_2DCF	2’,7’- Dichlorodihydrofluorescein
H_2DCFDA	2’,7’- Dichlorodihydrofluorescein (= Dichlorofluroscin)-diacetate
IFT	Inverse Fourier Transformation
Max	Maximum
MT	MitoTracker®CMXRos
n	Number
n	Refractive index
NA	Numerical Aperture
NIR	Near-infrared light
LSM	Laser Scan Microscopy /Microscope
OPE	One Photon Excitation
PBS	Phosphate Buffered Saline
PMT	Photomultiplier Tube

PSF	Point Spread Function
r	Radius
RHO	Rhodamine 123
ROS	Reactive Oxygen Species
SHG	Second Harmony Generation (process of frequency doubling)
SPA	Single-Photon Absorption
Theo(ret.)	Theoretical
TOPAS	Travelling-wave Optical Parametric Amplifier of Superfluorescence
TPA	Two-Photon Absorption
TPE	Two Photon Excitation
UV	Ultraviolet light
VIS	Visible light
WF	Widefield mode (without Pinhole)

I INTRODUCTION

1. The Oxygen Sensing Cascade and the Role of Reactive Oxygen Species (ROS)

Aerobic life uses oxygen to oxidise carbon and hydrogen rich substrates to obtain the chemical energy and heat for life. Incomplete reduction of oxygen to water during normal aerobic metabolism generates in partially reduced reactive oxygen intermediates named reactive oxygen species (ROS), in particular singlet oxygen ($^1O_2$), superoxide anion radical ($O_2^{-\cdot}$), hydrogen peroxide (H_2O_2) as well as the hydroxal radical ($HO^\cdot$). By chemical reduction of oxygen, at the end of the mitochondrial electron transport chain, by cellular oxidases, peroxidases, and mono- and dioxygenases or in a non-enzymatic manner (e.g. by transition metals) ROS are generated that pose serious threat to all organisms, although oxygen as a final acceptor in the respiratory chain became an evolutionary advantage about 1 billion years ago. A part of the ROS are radicals and have the possibility to interact with various tissue components which may lead to functional disturbances. Consequently, development of cells in an oxygen-containing environment requires the presence of an oxygen sensing and of a defence system against ROS. The latter system includes enzymes and non-enzymatic antioxidants. Indeed, aerobic life is characterised by continuous formation of ROS, also called prooxidants, balanced by a similar rate of their consumption by antioxidants. (Böss 1997) There is a constant battle to remain redox homeostasis between the formation of ROS and its removal. A battle that becomes increasingly difficult to win when cells are exposed to environmental oxidants that increase ROS production, such as ultraviolett and ionising radiation, heavy metals, redox active chemicals, anoxia, hypoxia and hyperoxia (Dalton et al. 1999) If this homeostasis, the ratio of the prooxidant-antioxidant is disturbed, with prooxidants dominating, this is called oxidative stress. Subsequently proteins are oxidised, membranes are damaged and the DNA is mutated.

This classical view of oxygen toxicity, that oxidants are only destroying biological components, has undergone a paradigm shift in which their role in the regulation of physiological functions particularly signal transduction, is considered as well. This idea is supported by a number of observations that oxidants cause the stimulation and regulation of various signal transduction processes, referred to as redox signalling, which can be blocked by antioxidants.

To control the oxygen flux to the cells, mechanism were developed to measure the level of oxygen availability in tissue and to form reactions that avoid any mismatch between oxygen supply and oxygen demand that otherwise would result in hypoxia or hyperoxia with subsequent tissue damage. This measuring procedure is called cellular oxygen sensing.(Acker 1994)

1.1 Oxygen sensing

All aerobic organisms, bacteria, yeast, invertebrates or vertebrates, should have the capability to sense and respond to the availability of oxygen as cellular functions have to be adapted, in multicellular organisms to optimise specific organ functions. In general, the anoxic response (lack of oxygen) is cell survival or death, cells may adapt to hypoxia, but are optimising their cell function under normoxia. Adaptation to hypoxia for example requires a wide range at different organisational levels of the body. At the organism level, e.g., the increase in alveolar ventilation involves the interaction of chemoreceptors, the respiratory control centres in the medulla, the respiratory muscles, and lung/chest wall systems. At tissue level, e.g., pulmonary vascular smooth muscle cells constrict (hypoxic pulmonary vasoconstriction), increasing vascular resistance, thus diverting blood away from the lung during in utero development and optimising the matching of blood flow to alveolar ventilation after birth and during adulthood. Tissue-specific responses in dependence of $P(O_2)$ frequency distribution occur, for example, in Glomus-like cell types present in the carotid body, aortic bodies, neuroepithelial bodies, (known among others as peripheral chemoreceptors triggering ventilatory responses), in abdominal ganglia and pheochromocytoma (PC-12) cells. At the cellular level, e.g., the release of neurotransmitters by the glomus cells of the carotid body, secretion of the hormone erythropoetin by cells of the

kidney and liver, and the release of vascular growth factors by parenchymal cells in many tissues can be seen. The initiation of the response to hypoxia requires subsequently the existence of a fundamental cellular O_2-sensing mechanism that detects the fall in $P(O_2)$and initiates a signal transduction sequence that culminates in the activation of the particular functional response.

Originally, in mammals oxygen sensing was only attributed to the specialised chemoreceptor cells in the carotid and neuroepithelial bodies, but now it is assumed that all mammalian cells can sense changes in O_2 concentration within a measuring range and sensitivity of physiological tissue oxygen partial pressure $P_{(O2)}$ with a typical mean value between 20 and 40 Torr (mmHg, 0 °C), respectively ~ 0 to 90 mmHg at a constant arterial PO_2 of ~ 100 mmHg (= 13.3 kPa). (Acker 1994) Depending on their site at the arterial inflow or at the venous end, cells differ in metabolic properties and thus in their enzymatic equipment.

On molecular level, the universal response to reduced O_2 availability involves the expression of hypoxia-inducible factor 1 (HIF-1), *cis* element and trans-activating factor, i.e a transcriptional activator of genes encoding for example the hormone erythropoetin (EPO) (within the kidney and the liver),- EPO is a 34 kDa glycoprotein which stimulates erythropoiesis, i.e. red blood cell production-, and the vascular endothelial growth factor (VEGF) that induces angiogenesis, both serving to increase O_2 delivery; furthermore glucose transporters (GLUT1) and glycolytic enzymes, which facilitate ATP production in tissue with low $P(O_2)$. Glucokinase (GK) gene expression activated by insulin is upregulated, the one of Phosphoenolpyruvate carboxykinase (PCK), glucagon- dependent, is downregulated under hypoxic conditions. Furthermore hypoxia induces the expression of mammalian genes e.g. for Endothelin, Plateled derived growth factor β, Interleukin 1, Ornithine decarboxylase, Tyrosine hydroxylase (TH), and more glycolytic enzymes like Phosphofructokinase, Aldolase A (ALDA), Glyceraldehyde-3-phosphate dehydrogenase, Phosphoglycerate kinase, Enolase, Pyruvate kinase, Lactate dehydrogenase. (Fandrey 1995). Among others Hemoxygenase 1, and inducible NO-synthase gene expression is also modulated by the oxygen tension.

HIF-1 is a basic-loop-helix-loop-PAS heterodimer consisting of two subunits HIF-1α and HIF-1β or ARNT (the vertebrate aryl hydrocarbon receptor nuclear translocator), member of the PAS (Per, ARNT, Sim)domain superfamily. PAS domains can transduce signals by means of the protein-protein interactions that they mediate. (Pellequer 1999) The PAS do-

main is extensively utilised for O_2 and redox sensing in *Archea, Bacteria* (e.g., FixL), and *Eucarya.*

There are several hypothesis for oxygen sensing in discussion, in which oxygen interact with an 0_2- sensor activating signalling cascades. The regulator for this signal transmission system should possess DNA- or RNA-binding ability to modulate gene activity. Oxygen or its metabolites, the ROS, as second messenger might be involved along this signalling cascade, which may include beside oxidation reactions and hydroxylation, phosphorylation or other chemical modifications

Putative oxygen sensors involved in oxygen sensing are heme-proteins, the mitochondrial respiratory chain, membrane ion channels, extracellular and or perhaps intracellular acidity or the NAD(P)H oxidase. There is an integrative model for oxygen sensing for the carotid body, but how oxygen is sensed primarily is not known. In every case, an O_2- sensing system has to control the short term reactions, within seconds or minutes, by modification of channel or enzyme activities and the long-term adaptation of cellular functions via regulation of gene expression. (Chandel and Schumacker 2000, Kietzmann et al. 2000, Lahiri 2000)

1.2 Models for Oxygen sensing

At least, four diverse models of primary oxygen sensors to mediate the transcriptional response to hypoxia have been proposed so far with partially conflicting hypotheses.

In the first two models, an iron-containing unit in the form of either a heme group or an iron/sulfur cluster is involved, that undergoes a change in activity during hypoxia that triggers the transcriptional response. The other two models involves the generation of ROS by mitochondria (complex III and IV of the respiratory chain) or by a haem- and flavoprotein-containing NAD(P)H-oxidase as a putative sensor involving a complicated signal cascade including protein kinases. Figure 1_1 illustrates these four models.

***FIG 1_1* Models of O_2-sensing (next page)**

(Acker, Xue 1995; Chandel, Schumacker 2000; Porwol, Ehleben, Brand, Acker 2001, Semenza 1999)

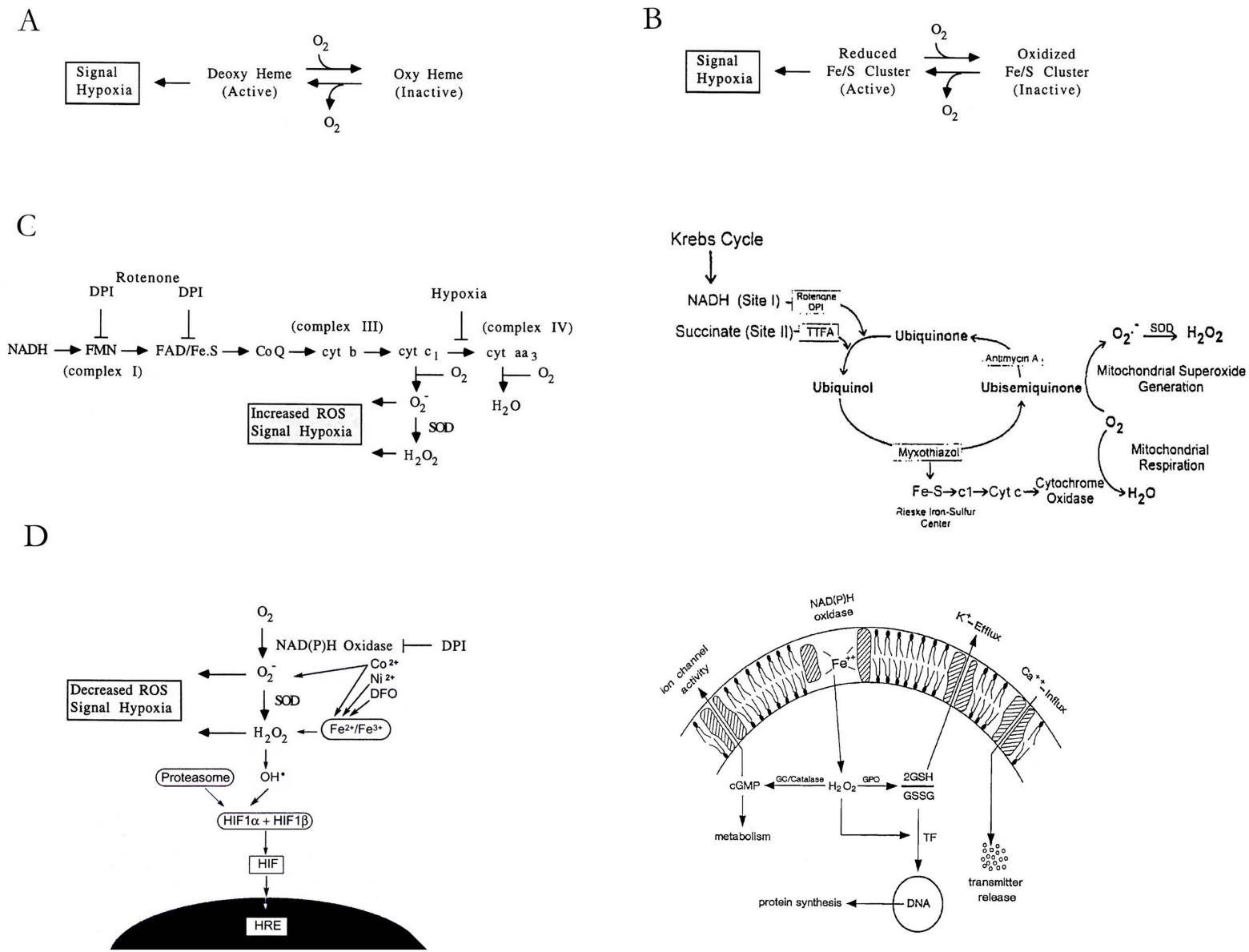

Figure 1_1 Models of O_2-sensing

(A) The activity of a hemoprotein sensor is determined by the presence or the absence of bound O_2.
(B) The activity of a sensor protein containing an iron/sulfur cluster is detemined by its oxidation state.
(C)Proposed model of mitochondrial oxidant signal generation involved in O_2 sensing. Mitochondrial respiration involves transport of reducing equivalents generated in the electron transport chain (ETC), through the ETC to cytochromoxidase (cyt aa_3), which transfers 4 electrons to O_2.
(left) Hypoxia inhibits the activity of cyt aa_3 leading to an increased mitochondrial ROS generation.
DPI is an inhibitor of flavoproteins, including NAD(P)H oxidases and ETC complex I, whereas rotenone is a specific of the latter.
(right) Ubisemiquinone, a free radical intermediate in the electron transport chain, can potentially generate superoxide via univalent electron transfer to O_2. Boxes show sites of inhibition. SOD, superoxide dismutase; cyc c, cytochrome c.
(D) Scheme of an oxygen sensor (NAD(P)H-oxidase) localised in the cell membrane generating H_2O_2 as second messenger, depending on P_{O_2}.
(left) Decreased cytosolic ROS generation signals hypoxia. Gene expression is mediated by hydroxyl radical dependent HIF stabilisation.
(right) Scavenging H_2O_2through gluthathione peroxidase (GPO), the quotient of reduced vs. oxidised gluthathione, (2 GSH/GSSG) determines either open probability of potassium and therefore calcium influx or genetic expression and synthesis of erythropoetin by interaction with transcription factors (TF). H_2O_2 might also influence 3',5'-cyclic monophosphate (cGMP) level, with consequences consequences for ion channel activity and metabolism, by being scavenged through catalase, which interacts with guanylate cyclase (GC).

In each of these models, O_2 or ROS could either dircetly with effector proteins (such as a Potassium channel or HIF1α) or instead activate a signal transduction pathway (such as a kinase cascade) leading to effector activation.

(Acker, Xue 1995; Chandel, Schumacker 2000; Porwol, Ehleben, Brand, Acker- in pres, Semenza 1999)

1.2.1 The Heme-Protein Hypothesis

In the first, the simplest model, the sensor which is a heme protein binds O_2 directly. When the O_2 concentration decreases, the fraction of sensor molecules containing bound ligand declines. In absence of bound ligand kinase activity is permitted ("on" state), in its presence the heme domain turns off kinase activity ("off" state) (Gong 1998) (Figure 1_1A) Such a two-component signalling system is found in the bacterium *Rhizobium meliloti*. FixL, a hemoprotein histidinkinase is active in the deoxy state, catalysing its own autophosphorylation and the transphosphorylation of FixJ, a transcription factor. In *Vitreoscilla* a dimeric hemoprotein composed of two single heme domain polypeptides (VGB) was found in the cytosol, when overexpressed also in the periplasmatic space. In mammalian cells a simple ligand model has not be proven experimentally, but it is possible that O_2 sensing involves molecular interactions with one or more hemoproteins. (see below)

1.2.2 The Non Heme Iron binding Protein Hypothesis

Iron-sulfur clusters represent another intracellular target for O_2 (Figure 1_1B). Iron regulatory protein 1 is degraded via iron-sulfur cluster formation in the presence of O_2. It was suggested that HIF-1 contained non-heme iron, but results supporting this hypothesis could not be reproduced. The second messenger mechanism could be de/phosphorylation.

1.2.3 Mitochondrial Hypothesis of O_2-sensing with mitochondria derived ROS changing gene expression

In an alternative model, the mitochondrial electron transport chain (ETC) complex III or IV plays an important role in oxygen sensing.

The mitochondrial electron transport chain of all aerobic organisms reduces oxygen to water by a 4-electron transfer by cytochrome *c* oxidase. The electrons are received from NADH or from flavoprotein-linked dehydrogenases and reduction takes place after a series

of site-specific electron transfers through inner mitochondrial membrane components of the electron transport chain that have sequentially more positive reduction potentials. An estimated 1-4% of the total oxygen consumed during electron transport, however, is reduced not to water by cytochrome c oxidase but rather to superoxide by the iron-sulfur proteins and by the coenzyme Q semiquinone in the proton-motive Q-cycle. (Figure 1_1C left). Playing a dual role, reduced coenzyme Q prefers to scavenge reactive oxygen, whereas a high rate of oxygen utilisation, coupled with a more-oxidised coenzyme Q state, will promote higher rates of mitochondrial superoxide formation, like does energy uncoupling of mitochondria by Ca^{2+} (if the cytosolic level of Ca^{2+} is high) and by opening of the mitochondrial permeability transition pore(MPTP) affected by the redox state of thiols and pyridine nucleotides.(Dalton et al. 1999)

The model proposes that under hypoxic conditions the reduction of O_2 is inhibited, resulting in the release of electrons upstream at complex III and generation of O_2^- (Figure 1_1C) This model is supported by the fact that inhibition of complex I by Diphenyliodonium (DPI), which is also an NADPH oxidase inhibitor, or rotenone attenuates the superoxide anion formation, thus inhibiting the induction of HIF-1 and downstream genes in response to hypoxia. This is contradictory to the last model (see below), but it could be that the regulation is more complex. In ρ^0 cells, which lack mitochondrial DNA and ETC activity, generated by incubating wild-type cells (e.g. HepB3) in medium containing ethidium bromide(25 ng/ml), sodium pyruvate (1mM), and uridine (50 µg/ml), hypoxia does not induce ROS production or the expression of HIF-1 or downstream genes. Chandel et al. (2000) conclude therefore that mitochondria-derived ROS are both required and sufficient to initiate HIF-1α stabilisation during hypoxia. At least respiring mitochondria are required for the trancriptional response to hypoxia.. Additionally they found that wild-type Hep3B cells increase ROS generation during hypoxia (1.5 % O_2) or $CoCl_2$ incubation, which seems to mimick hypoxic conditions via a nonmitochondrial mechanism, m-RNA of erythropoetine gene could not be found in ρ^0 cells during hypoxia, however under $CoCl_2$ treatment HIF-1 and m-RNA of erythropoetine gene was also found. HIF-1 can be stabilised under hypoxia by a proteasome inhibitor, lactacystin, EPO mRNA expression is not activated. Experiments in which different H_2O_2 concentrations were added to wild-type cells showed indeed an stabilisation of HIF-1α at a concentration not too high. It is possible, that an ROS concentration dependent scavenging system exists as higher concentrations of H_2O_2 failed to stabilise HIF-1α; and the regulation is influenced by mitochondrial-nuclear-cross-talk and

downregulation of cytochrome oxidase genes, as the V_{max} of cytochrome oxidase decreases by ≈ 50% during hypoxia in hepatocytes.

1.2.4 The NAD(P)H Oxidase Hypothesis

Already on the level of bacteria, in *E. coli*, a NAD(P)H oxidase, a monomeric flavohemoprotein with a single heme binding domain and a single flavin binding domain was found and had been proposed as oxygen sensor (HMP). It is located primarly in the cytosol, when overexpressed also in the periplasmatic space. In HMP the function of the flavin is to transfer electrons from NAD(P)H to the heme moiety, maintaining it in the Fe^{2+} state required for oxygen binding. Bound molecular oxygen will either be reduced to water (by protonation) or to superoxide anion O_2^-. (Bunn 1996)

Contradictory to the latter model C, Fandrey et al. (1994) found that extracellular oxygen is directly related to the production of ROS triggering Epo production in HepG2 cells, which can be induced 50-100 fold in hypoxic human hepatoma cells. In HeLa and Hep3B cells for the Epo gene, and in endothelial cells for the VEGF gene, it was shown that the alpha-subunit of HIF-1 is constitutively degraded by hydoxyl radicals ($^{\bullet}OH$) , whereas stimulation of the cells by hypoxia leads to lower intracellular ROS concentrations and subsequently to the formation of an active heterodimeric complex of the alpha- and beta-subunit responsible for upregulation of the Epo gene, indicating a more general mechanism. (Cool et al. 1998 and references therein, Shweiki et al. 1992, Huang et al. 1996).

The proposed model represented in Figure 1_1 D is that in oxygenated cells a flavo-heme protein, consisting of two subunits: gp91 containing FAD, and p22 including a heme protein, in the plasma membrane functions as a cytochrome *b*-like NAD(P)H oxidase (dehydrogenase). O_2 is bound by a heme-binding component of cytochrome b_{558}, that transfers electrons to molecular oxygen, generating superoxide anions (O_2^-). The electrons are delivered by a membran-bound flavin dehydrogenase complex. O_2^- is dismutated to hydrogen peroxide (H_2O_2) as a second messenger catalysed by superoxide dismutase (SOD). H_2O_2, being a non-charged molecule which can cross membranes and participating in one-electron transfer reactions, is an ideal candidate as a second messenger for O_2. Further reduction of hydrogen peroxide requires a reductive cleavage of the bond between the oxygen atoms, a reaction catalysed by transition metals, e.g. iron in a Fenton type reaction, a

one-electron process. A Fenton reaction involves several steps with well characterised kinetics. One important intermediate is the hydroxyl radical $^{\bullet}OH$, which has been detected by several spectroscopic methods (Walling 1975) and the hydroxyl anion arises as well.

$Fe(II) + H_2O_2 \rightarrow Fe(III) + {}^{\bullet}OH + OH^-$ (Fenton reaction)

The reduction of a transition metal (M) by hydrogen peroxide will lead to the hydroperoxyl radical $HO_2^{\bullet}$

$M(III) + H_2O_2 \rightarrow M(II) + {}^{\bullet}OOH + H^+$

Since H_2O_2 itself is a relatively inert reaction partner, its degradation products are of great importance. $^{\bullet}OH$ reacts with practically every organic molecule in its immediate environment very fast, by abstracting hydrogen or adding double bonds, initiating (autooxidation) chain reactions that its radius of diffusion in cells is expected to be only a few angstroms. Although it might do considerable local damage, $^{\bullet}OH$ is ill-equipped to be selective, target-specific ROS, whereas hydrogen peroxide qualifies well as an ROS and a potential signalling molecule.

As desferrioxamine (DFO), an iron chelator, antagonises H_2O_2 mediated effects, the Fenton reaction is probably involved in the signal transduction pathway.

There are at least two targets of these ROS as second messengers. On the one hand as a result at high oxygen tension HIF-1α is oxidatively modified, ubiquitinated, recognised by the proteasome, and rapidly degraded, on the other hand (left) the conductance of " O_2-sensitive K+ channels" may be changed (right).

HIF-1α is only stable at low oxygen tension and can thus form a heterodimer with constitutively expressed HIF1-β. This activated heterodimer HIF-1 translocates to the nucleus and binds to response elements in hypoxia inducible genes. H_2O_2 is scavenged through catalase or by gluthathione peroxidase. The first scavenging mechanism leads to the formation of a heme- containing catalase compound I with guanylate cyclase by interaction of two heme groups, enhancing the guanosine3',5'-cyclic monophosphate (cGMP) level. This results in an $P(O_2)$-dependent cell cGMP level activating different cytosolic activator proteins. In carotid body the cGMP level decreases under hypoxia, influencing the ion channel activity, increasing carotid body chemoreceptor discharge, when arterial $P(O_2)$ falls from 100 to ~ 30 Torr (mmHg, 0 °C) (13.332 to ~ 4.000 kPa), corresponding to a decrease of the microvascular $P(O_2)$ from 50 to ~ 10 Torr. (6.666 to ~ 1.333 kPa).

Direct spectral analysis of cells in which oxygen sensing plays a critical role (Acker 1995), gave support to a central role of a NAD(P)H oxidase as an oxygen sensor in mammalian cells. Deconvoluted difference spectra in the visible range in the presence and absence of inhibitors of respiratory cytochromes in both type I carotid body (Cross et al. 1990) and HepG2 cells (Görlach et al.1993, Ehleben et al. 1998, Porwol et al. 2001) revealed among others, absorbance maximum at 558 nm, hinting the presence of a *b*-like cytochrome, which represented estimated about 6 % of the total cytochrome *b* in the cell, appears to bind oxygen with a relative low affinity and also CO. This non-respiratory cytochrome b_{558}, is very similar to the cytochrome b_{558} found in the NADPH-oxidase complex of phagocytes such as neutrophiles and macrophages shown in Figure 1_2 which include a low (mid-point) potential flavocytochrome b_{558}, consisting of a heme-containing 22kDa α-subunit ($p22_{phox}$) (phox for phagocyte oxidase factor), and a 91 kDa β-subunit ($gp91_{phox}$), residing in the plasma membrane of neutrophils and in membranes of neutrophil-specific granules, and two additional cytosolic cofactors $p47_{phox}$, $p67_{phox}$ shown in Figure 1_2. Cytochrome b_{558} functions probably as the final electron transporter from NADPH to molecular oxygen. Superoxide production is activated by $p21^{rac}$, a small GTP triphosphatase protein of the Ras/Rho family of proteins (Goldschmidt-Clermont et al. 1999), which involves the dissociation of $p21^{rac}$ from its inhibitory GDP/GTP exchange protein (rhoGDI) followed by its transition to the plasma membrane (Abo 1994). These four subunits could also be detected probably as non-phagocytic isoforms by immunohistochemistry, molecular biology, (Western blot analysis - Görlach et al. 1993) in oxygen-sensing cells, e.g. HepG2 cells, neuroepithelial bodies of the lung, smooth muscle cells of the pulmonary vasculature and type I cells of the carotid body. Therefore Kietzmann, Fandrey and Acker (2000) suggest that an oxygen sensor could be an NADPH-oxidase isoenzyme, a “low-output oxidase” that is closely related, but clearly distinct from the “high-output oxidase” in neutrophils, thus a metabolite of O_2 may be sensed, although an oxidase – mitochondrial or cytocolic- has not yet been identified (Ushio-Fukai 1996. Acker, Xue 1995) However, in B- cell lines deficient in $gp91_{phox}$ and $p22_{phox}$ the VEGF and aldolase mRNA response to hypoxia or CoCl2 were preserved. This could be due to polymorphism or different regulatory mechanisms or expression levels or even isoforms of the other components may cause deviating activities of the oxidase complexes of phagocytic and non-phagocytic origin. (Cool et al. 1998). In HepG2 cells this NADPH - oxidase reacts very sensitive to low concentrations of NAD(P)H and reaches about 60 nM O_2/ 10^6 cells, only 5% of the maximal

output of oxygen of neutrophils during respiratory burst by extracellular application of NAD(P)H. (Ehleben et al.1998, Acker 1994)

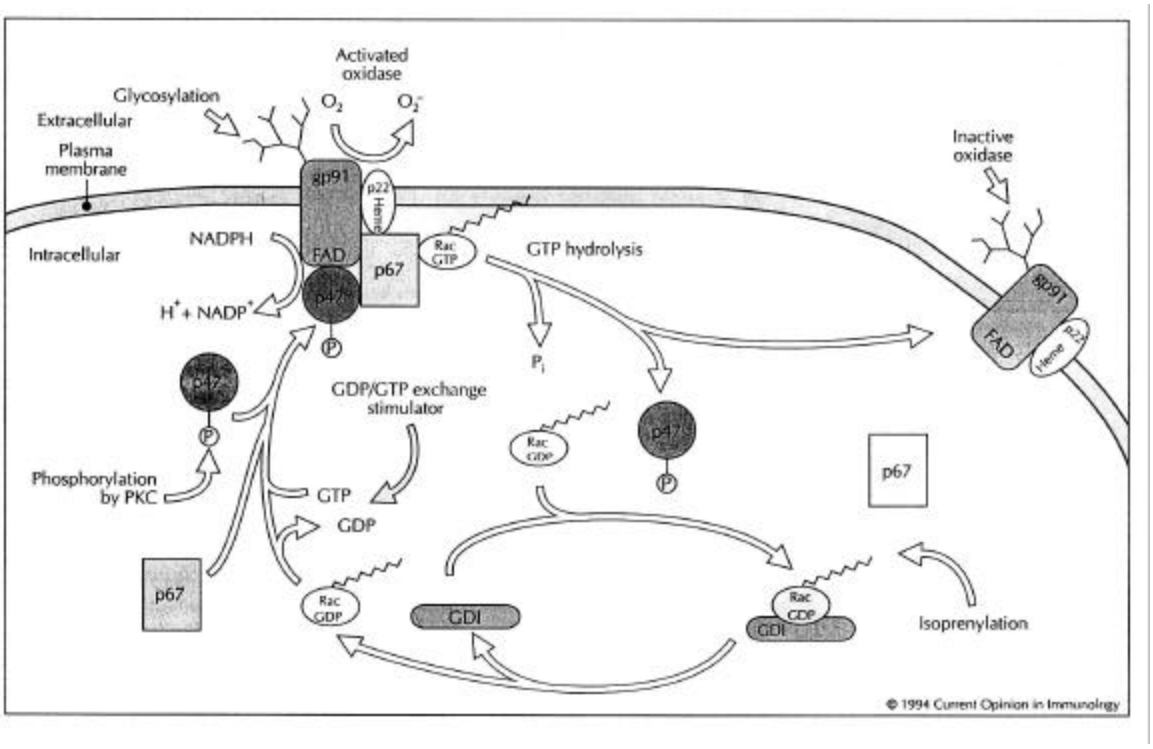

FIG 1_2 Schematic representation of structural features of the activation of NADPH oxidase. The cytochrome b_{558} is an integral membrane protein with two subunits, $gp91_{phox}$ (gp91) and p21 respectively $p22_{phox}$ (p21). The glycosylation site of the cytochrome is on the exterior, and the FAD and NADPH binding sites are on the interior of the plasma membrane. On activation, cytosolic constituents $p47_{phox}$ (p47), $p67_{phox}$ and Rac2 ($p21^{rac}$) are translocated to the plasma membrane where they bind to the cytochrome and initiate O_2^-synthesis. Activation requires dissociation of a GTP dissociation inhibitor (GDI) from Rac2 (for HepG2 Rac1) followed by exchange of GDP for GTP. This exchange may be protein stimulated. Oxidase acitvation also involves phosphorylation of at least one of the cytoplasmatic subunits, $p47_{phox}$. Isoprenylation of the Rac protein (represented in this figure by a zigzag) is necessary for oxidase activity and may function as a membrane anchor that helps stabilise the assembled oxidase complex. Hydrolysis of GTP bound to Rac leads to inactivation and dissociation of the oxidase complex. Regulation of GTPase activity of Rac may be a key factor in the regulation of NADPH oxidase assembly. (Bastian and Hibbs1994)

Treatment with cyanide, a ETC poisoner, demonstrated that this non-mitochondrial cytochrome b_{558}, but also mitochondrial cytochrome b_{563} were cyanide-insensitive and hypoxia-affected. Cytochrome *c* unresponsive to hypoxia was reduced by cyanide. Different reduction characteristics by cyanide and oxygen deprivation did not give a clear result for cytochrom aa_3 as oxygen sensor. Cobalt treatment of HepG2 cells, however, abolished only the response of *b*-like cytochromes to hypoxia, whereas the redox state of mitocho n-

drial cytochromes *c* and aa_3 were unaffected. As both *b*-type cytochromes (mitochondrial and non-mitochonrial) correlate with enhanced gene expression under hypoxia, there are both candidates for an oxygen sensing protein.

Another evidence which is taken for that the mechanism of oxygen sensing most probably involves the operation of a flavoprotein oxidoreductase is that the known NADPH (flavin) oxidase inhibitor diphenyle iodonium (DPI) inhibited the hypoxia-dependent expression of VEGF, lactate dehydrogenase A (LDHA), glucose transporter 1 (GLUT1), and the normoxia-dependent placental growth factor (PLGF) gene. However these results are problematic concerning the production of ROS. However, coincubation with cobalt or desferrioxamine still activated the hypoxic signalling pathway probably at a site downstream from action of Diphenylene iodonium (Ph_2I^+) In carotid and neuroepithelial bodies DPI stimulated depolarisation. supporting the NAD(P)H model, (this could either be due to an influence on the channel activity by DPI). (Gleadle et al. 1995) Studies of oxygen-regulated erythropoetin gene expression in the human hepatoma cell lines HepG2 and Hep3B showed that EPO gene expression is stimulated by particular transition metals such as cobaltous ion (CoCl2)or nickel ion (NiCl2) as does hypoxia. (Porwol et al. 1998). Cobalt chloride ($CoCl_2$) even could antagonise by coincubation with NADPH, NADH and pyrogallol, their O_2^-liberating effects. (Fandrey et al 1997) $CoCl_2$ causes changes in the spectra of HepG2 spheroids at a wavelength around 558 nm (the region of the *b*-cytochrome), probably interacting with the NADPH-oxidase. Cobalt chloride oxidises nonrespiratory as well as respiratory heme proteins, and increases oxygen consumption whereas the nickel ion does the contrary, reducing respiratory hemeproteins and decreasing the oxygen consumption. $CoCl_2$ appears to effect the cellular redox state at multiple sites, especially it interacts with the P_{450} system, another member of the cytochrome *b* family. The activity of gluthation peroxidase (GPO), which is an important intracellular scavenger of H_2O_2, is also stimulated by cobalt chloride. Figure 1_1 D (left) illustrates this change in the quotient of reduced versus oxidised glutathione (2 GSH/GSSG). Glutathione peroxidase by scavenging H_2O_2 is lowering the ratio 2GSH/GSSG. Higher level of GSH due to lower H_2O_2 under hypoxia could lead to closing of GSH-sensitive potassium channels. Type I cells of the carotid body show reduced K^+-channel activity when the pressure of O_2 in the surrounding medium is decreased. The lower the quotient because of peroxidase activity the higher the K^+-efflux, (Model of redox dependent inactivation of potassium channel as effector of the

vasoconstriction response: and transcription factors like HIF for hypoxia-inducible gene expression, like GK (insulin-dependent) or EPO, will bind (with reduced thiol groups) to Hypoxia Responsible Elements (HRE). Under high oxygen tension, produced hydroxyl radicals can oxidise the SH groups of the certain cytosolic transcription factors, thus shifting the balance between reduced and oxidised forms to a more oxidised state. TF then bind to Normoxia Response Element, like for PCK gene (glucagon-dependent). Under high H_2O_2-levels, H_2O_2 is scavenged by catalase and a hem containing catalase-compound I complex may be formed which activates the hem containing guanylate cyclase, the 3',5'-cyclic guanosin monophosphate (cGMP) level becomes enhanced, which modulates the membrane ion channel activity/conductivity and/or leads to an activation of different cytosolic activator proteins for the NAD(P)H oxidase. The NAD(P)H oxidase with cytochrome b_{558} then generates ROS. (Acker 1994, Acker and Xue 1995, Chandel et al 1998 and 2000, Dagsgaard et al. 2001, Ehleben et al. 1997 and 1998, Fandrey et. al 1997, Görlach et al. 1993 and 1994, Kietzmann et al. 1998 and 2000, Porwol et al. 1998, Semenza 1999, Zhu 1999 and references therein)

1.3 Reactive oxygen species as cellular messengers in signal transduction

ROS are any species (in a broader sense also compounds with hydrogen, chlorine and nitrogen) in different states of oxido-reduction and electronic excitation more reactive than the ground state oxygen molecule which is in a relatively inert triplet state $^3O_2$, as the two unpaired of its twelve electrons have parallel spins, and occupy spaces in the highest unfilled orbital at opposite ends of the molecule, creating two free radical centers. Therefore Oxygen is a diradical, and paramagnetic. $^3O_2$ is the most stable configuration of the molecule, because only spin-allowed reactions with other paramagnetic ions or molecules easily take place, i.e. binding of oxygen to ferrous ion of hemoglobin or reaction with free radicals in lipid peroxidation.

All ROS interconvert freely, therefore the detection of one single species is difficult, although the species have very different properties and reactivities. To have an effect, an ROS must have both a high reactivity towards a specific target and a chance to reach it. This often requires a compromise between reactivity and diffusion distance, influencing

the biological function. Partially reduction in one-electron steps, by addition of one, two, and four electrons to O_2 'activates' oxygen and it reacts readily with a variety of substances. The scheme of these reduction steps is

$$\begin{array}{ccccccccc} O_2 & \xrightarrow{e^-} & O_2^{\bullet -} & \xrightarrow{e^-} & O_2^{2-} & \xrightarrow{e^-} & O^- & \rightarrow & O^{2-} \\ \downarrow & & \downarrow H^+ & & \downarrow 2H^+ & & \downarrow H^+ & & \downarrow 2H^+ \\ {}^1O_2 & & HO_2^{\bullet} & & H_2O_2 & & {}^{\bullet}OH & & H_2O \end{array}$$

Possible species are: singlet oxygen $^1O_2$, the the superoxide anion radical $O_2^{\bullet -}$, (or used as a synonym the superoxide anion O_2^-), hydroperoxyl radical $HO_2^{\bullet}$, peroxide ion HO_2^- (the basic form of hydrogen peroxide), hydrogen peroxide H_2O_2, and the hydroxyl radical $^{\bullet}OH$.

Under physiologic conditions reactive oxygen species (ROS) generate delicate, transient changes in the cellular redox state. Thus they can serve as physiological second messengers for receptor-mediated cell signalling, in the course of which ligand-receptor interactions produce reactive oxygen species, which in turn, elicit signalling by targeting some signal transduction component molecules. Often Ca^{2+} -signalling is stimulated. As mitochondria represent a quantitatively important pool for internal Ca^{2+}, they could be a mediator of signal transduction mimicry by oxidants. (Suzuki et al.1997), but the increase in intracellular calcium in carotid body type I cells under hypoxia is obviously mediated by a calcium influx through voltage-dependent calcium channels. (Acker, Xue 1995)

The majority of reactive oxygen species action can be divided among five overlapping categories: 1) cytokine, growth factor, and hormone action and secretion; 2) ion transport; 3) transcription; 4) neuromodulation (only demonstrated for reactive nitrogen species (RNS) so far; and 5) apoptosis. A fully understood signal transduction pathway requires identification of the proteins involved in the generation of signalling molecules, the proteins activated or inhibited, the molecular basis of the triggering event, and the downstream physiological response. Often some parts are missing, e.g. the source or immediate target of these species. Therefore, many of the studies are somewhat descriptive. In general, the regulation of these pathways is achieved at three levels: 1) generation of the reactive species; 2) target susceptibility; and 3) scavenger activity. (Lander 1997)

ROS formed in the mitochondria and in the cytosol are important determinants of the redox state of protein cysteinyl residues. Therefore, they constitute a common regulatory mecha-

nism of protein conformation and function. ROS-dependent redox cycling of cysteinyl thiols is critical for the establishment of the protein-protein and protein-DNA interactions that determine many aspects of a signal transduction pathway. Gluthatione (GSH) is the key regulator of the redox state of protein cysteinyl thiols. These thiols react with GSSG if their pK_a value is low enough to generate a reduction potential greater than that of glutathione thiolate anion. Reactivity will tend to increase if electron withdrawing substituents, such as those in basic amino acids, are in close vicinity to a cysteinyl residue, because they will tend to decrease its pK_a. The intracellular levels of GSSG increase from metabolism of H_2O_2 by gluthathione peroxidase and decline from export of GSSG from the cell and from gluthathione reductase – and NADPH-mediated reconversion of GSSG to GSH. (Dalton et al. 1999 and references therein) It was even suggested that ROS, that are toxic in high doses being beneficial or even indispensable at low concentration, contribute to a continuous 'life-signal' which may be necessary to keep cells alive and released superoxide, O_2^-, and hydrogen peroxide, H_2O_2, may participate. Already in 1989 it was hypothesised that superoxide could act as a biological 'messenger' rather than a mediator of cellular damage. In biological milieu superoxide has an estimated half-life of 400-10^{-6} ns and a diffusion pathway of 55 nm -3 µm. (Burdon 1995)

1.4 Detection of ROS

The last two conflicting models for oxygen sensing makes clear that measuring ROS levels as a function of O_2 concentration is not sufficient. Direct measurement of ROS, however, are technically difficult to perform. Experiments with different probes becoming fluorescent upon oxidation by ROS (dihydrorhodamine 123, dichlorofluorescin diacetate) have yielded to data supporting one or the other of the latter two models. Perhaps different probes are detecting different oxidants generated in response to hypoxia and are not precise enough for specific ROS. Another possibility is that different O_2 – sensing mechanisms in different cell types or even within a single cell exist as conflicting results have been obtained using the same cell line. (Chandel et al 1998, 2000, Dagsgaard et al. 2001, Ehleben et al. 1998, Semenza 1999)

2. Confocal Fluorescence Laser Scanning Microscopy (CF LSM)

Webb (1999) remarked that a confocal microscope is most valuable in seeing clear images inside thick samples more than can do a conventional wide-field epifluorescence microscope. This chapter will line out the principles of confocol fluorescence laser scan microscopy with one and the next chapter with two photon excitation, point out its possibilities and limitations. In biology, fluorescence imaging in general has become increasingly important because biological activity can be traced by the fluorescence of markers associated with particular atomic or molecular species as they move through the cell. If fluorescence markers have different emission spectra, they can be detected separately with the choice of appropriate emission filters.

In 1957, Minsky invented the first confocal scanning microscope. The image quality in Minskys microscope was not very impressive because of the quality of the oscilloscope display and not because of lack of resolution achieved by the microscope itself. Minsky named the 'confocal' configuration the 'double-focusing stage-scanning microscope' as a point illumination and a point detector are used together. (Minsky 1988) He was aware of its unique optical sectioning capability as light originating from out-of-focus points is effectively suppressed.

The basis of a confocal laser scan microscope is a conventional microscope with optimised mechanics. Two techniques are combined with conventional light microscopy (lateral optical resolution about 300 nm, vertical does not exist, only 2-D imaging), which lead to a better resolution (lateral about 200 nm, vertical (axial) about 500 nm, 3-D imaging). One is the confocal principle, the other the application of laser light as light source.

2.1 The confocal principle

In summary, the basic requirements for a CLSM are point illumination, point detection, a scanned image, and a confocal lens system.

The conventional microscope is characterised by the parallel imaging of all image points. Therefore the collected light of the in-focus image of one plane within the thick sample

and all of the out-focus images of other planes will be recorded, whereas optical scanning microscopes image the object points as pixels one after another. Hence the sample or illumination beam need to be raster scanned, thereby light originating from out-of-focus points is effectively suppressed, and a very thin slice of the object can be imaged. Like this thick objects can be imaged in three dimensions. The sectioning capability, which means, that defocusing objects does not create blurring, but gradually cuts out parts of the object as they move away from the focal plane, is achieved by using a small pinhole detector. The parts become darker, as the light intensity is highest in the focal plane, and eventually disappear in practical consequence. Figure 2_1 illustrates the basic principle of confocal laser scan microscope. A collimated beam from a laser is focused onto a pinhole. Laser light, passing through the pinhole with a wavelength (between 400 and 1100 nm) is turned via a x-y deflection mechanism into a scanning beam, focused by a microscope objective lens and forms a diffraction-limited spot (< 1 µm in diameter) on the specimen. A beamsplitter then deflects the reflected/emitted beam to a separate detector pinhole, thereby deviating the reflected light. The use of two pinholes eliminates the reflected light from the diaphragm surrounding the illumination pinhole.

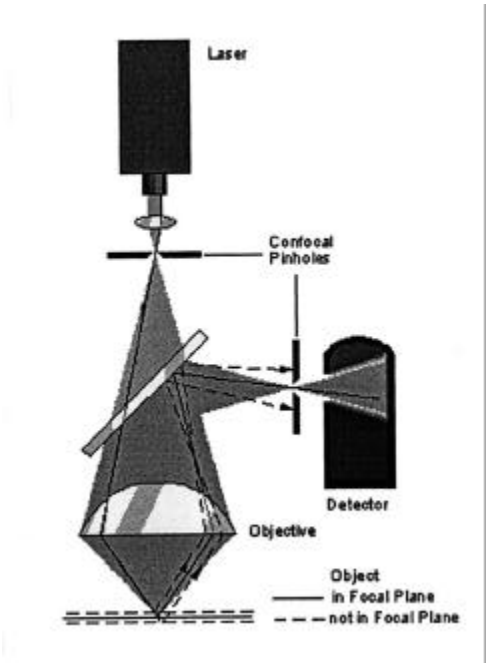

Fig 2_1 The basic principle of a confocal microscope (www.confocal-systems.de/confocal_basics/content.html)

Since only one point is illuminated at a time, speckle is eliminated. Speckle appears in coherently illuminated imaging system because of sidelobes that add in or out of phase at the

detector due to reflection from different points of an optically rough surface [rough on the scale of the light wavelength].

All structures out of focus are suppressed at image formation by an arrangements of diaphragms which, at optically conjugated points of the path of rays, act as a point source and as a point detector respectively. Therefore the microscope is 'confocal' as the objective lens is used twice, both to illuminate and to image the sample. The focal point for the illumination and the detection beam are the same. If the sample moves out of the focus of the lens, the light reaching the detector pinhole is defocused at the pinhole and hence does not pass through it to a detector located behind. Consequently, the light intensity received by a detector behind the pinhole decreases rapidly with the defocus distance, and the image disappears. The small dimension of the illuminating light spot in the focal plane minimises stray light. Out-of-focus rays do not reach the detector because of the detection pinhole. The smaller the detection pinhole is, the better is the optical sectioning of the object. Thus without cutting the object, images of cellular structures in various depths can be collected in their natural state. Scanning the object in x/y – direction and in z-direction (along the optical axis) allows viewing the object from all sides. By image processing, many slices can be superimposed, giving an extended focus image. This can only be achieved in conventional microscopy by reduction of the numerical aperture of the objective, sacrificing resolution. The numerical aperture of the objective used, beside the wavelength of light and the diameter of the diaphragm, determines the depth of the focal plane. The confocal effect can be reduced at a wider detection pinhole. For a full image, the image point is moved across the specimen by mirror scanners. The emitted light passing through the detector pinhole is transformed into electrical signals by photomultiplier tubes (PMTs) and displayed on a computer monitor screen. A PMT is a secondary electrons multiplier. During absorption in a photocathode emitted electrons ('photoelectrons') will generate secondary electrons in an anode. Several of these complementary electrode pairs are put together to amplify the signal of photonic current.

2.2 Information flow in a Confocal Laser Scanning Microscope

Figure 2_2 shows the information flow in a generic CLSM.

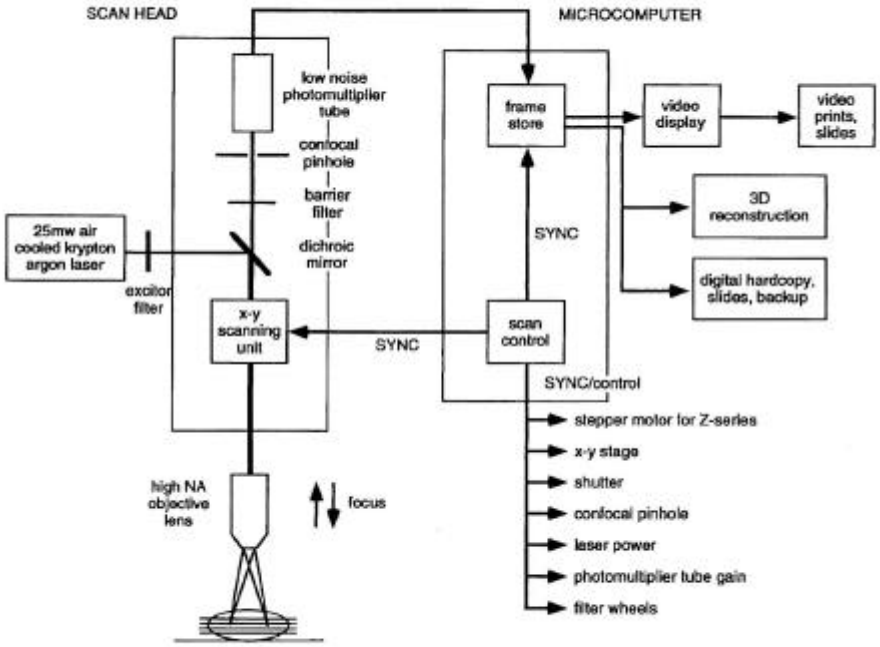

FIG 2_2 Information flow in a generic CLSM (Paddock 1999)

The focal point of the laser will be line scanned in a plane (x, y) perpendicular to the optical (z-) axis. Optical cuts through transparent biological objects can be performed by moving the specimen, the objective or the laser beam in direction of the z-axis. The analog signals (A) are converted into a digital number (D) by an Analog to Digital converter (A/D) (frame grabber/store) and passed to the computer system. The obtained volume data files represent the micromorphology of the objects in the three directions of space.

In confocal fluorescence microscopy the choice of appropriate emission (barrier) filters for detection of the electromagnetic radiation of fluorescence markers for different cell compartments with different emission spectra leads to a spatial separation of different cellular structures.

In our case the photo multiplier tubes was a separated unit from the scan head connected by glass fibres to the scan head on the one side and to the nearby computer (primary electronics) on the other side. Thus the electronic noise is reduced (accumulating when the

signal is transmitted over a long wire) and the weight and size of the scan head as well. However, the light efficiency is lower compared to an on-board photomultiplier tubes (PMT´s) due to light losses when coupling into and out of the second set of fibres. (Corle 1999)

This procedure of generation optical slices through biological objects is involved with some problems and limitations.

2.3 Limitations of one photon excitation fluorescence CLSM

Beside the exact focal intensity distribution, the confocal imaging process may also be very strongly influenced by the object itself, e.g. absorption and scattering of both the excitation and the fluorescence light may cause points deep within in the object to appear relatively dark. (Visser 1992) That drop-off of visibility limits the sample thickness to about 50 µm in many cases, although there are many instances of looking 0.5 mm into tissue. (Webb 1999)

As the time for obtaining all volume data files is high – in the range of 1 min to 6 min – the influence of the measuring system has an great impact on the observed data. A good signal to noise ratio is only obtained with high laser output power, but the light induces photo-bleaching of the fluorophores, in relation to the detected photons more than in conventional fluorescence microscopy as the whole object is illuminated within the double cone, however, only the emission of the focus plane is detected. The pinhole aperture may cause chromatic aberrations. These problems can be solved by two photon excitation microscopy.

(www.confocal-systems.de/confocal_basics, Corle 1996, Paddock 1999, Visser 1992, Webb 1999)

3. Two-photon excitation fluorescence spectroscopy and LSM

In two-photon excitation spectroscopy or fluorescence laser scan microscopy two photons are absorbed by one atom or molecule. Although the excitation efficiency is much lower than that of a single photon with about half the wavelength, this has several advantages for microscopy, e.g. because of the longer wavelength the excitation signal can penetrate the object deeper while at the same time it causes less bleaching damage. The images show the distribution of fluorescent material which is sensitive to half the wavelength of the illumination. Therefore two-photon excitation, unlike conventional or one-photon excitation, allows us to achieve fluorescence at a wavelength shorter than the excitation wavelength by a large anti-Stokes´ shift.

In 1931 Maria Göppert-Mayer first predicted in her dissertation that a chromophore may be excited with two photons simultaneously by absorbing them in the very same quantum event. (Göppert-Mayer 1931) At the beginning of the 90´s, Denk et al. first succeeded in applying this phenomenon to fluorescence laser scanning microscopy exploiting its intrinsic confocal properties (Denk, Strickler, Webb 1990) The terminology of two-photon excitation (TPE) is used, in particular in those applications related to fluorescence microscopy and spectroscopy. (see references in Diaspro 1999)

3.1 Two photon absorption/excitation and emission fluorescence spectroscopy

Two-photon absorption is allowed dependent on both the properties of the molecule, the laser polarisation, energy and transverse mode structure used to generate a ‘simultaneous’ two-photon transition in the molecule. (Birge 1986) The condition to obtain this effect is that the summation of energies of the two photons is close to the transition energy. (Delysse et al. 1997) That the electron has reached the higher electronically excited state is detected by the consequential and spontaneous emission of another photon, the induced fluorescence. In fluorescence a basic parameter is the fluorescence excitation cross section. Although for a one-photon absorption (OPA) a wide range of molecule spectra are well

documented little is known of two- or three-photon absorption (TPA/ThPA) spectra of biological useful fluorophores. Furthermore, because of differences in selection rules for one-photon excitation (OPE) and two photon excitation (TPE) and the effects of vibronic coupling, it is difficult to predict from one-photon data multiphoton, especially two- photon excitation spectra. Three photon excitation spectra parallel the corresponding one-photon excitation spectra because the same initial excited states can be reached without violating any selection rules. (Xu et al.1996) In OPA only 'dipole-allowed' transitions can be excited, whereas 'dipole-forbidden' transitions usually do not appear. (Dick 1981)

For an allowed transition , the excitation must be both symmetry and spin allowed. (Drake 1994) One and two photon selection rules are not only determined by spatial symmetry ('gerade' <-> 'ungerade' transitions are one-photon allowed and two-photon forbidden, both 'gerade' <-> 'gerade' and 'ungerade' <-> 'ungerade' transitions are one-photon forbidden and two-photon allowed), but by alternancy symmetry ('minus' <-> 'plus' transitions are one-photon allowed and two-photon forbidden, both 'minus' <-> 'minus' and 'plus' <-> 'plus' transitions are one-photon forbidden and two-photon allowed) as well. (Masthay 1988: 11; Schmidt 2000) In alternant and 'quasi-alternant' hydrocarbons with π-systems, e.g in porphyrins, the effects of alternancy symmetry on the excited singlet state wavefunctions were discussed by Masthay. The fluorescent dyes Rhodamine 123 and Dichlorofluorescein may also be counted to the 'quasi-alternant' π– systems, with structural similarities to the examined molecule. In his dissertation 'molecular orbital and two-photon spectroscopic studies of conjugated π-systems' Masthay demonstrated the characteristics of plus and minus states, which are well-established at the valence bond level of approximation, in which electrons are localised on individual atomic centres: The 'plus' wavefunctions are 'uncorrelated' (i.e., more than one electron allowed to occupy a given region of space) and consist primarly of 'ionic' (more than one electron per atomic center) valence bond (VB) structures and are one-photon allowed. The 'minus' wavefunctions are 'correlated' (i.e. only one single electron allowed to occupy a given region of space) and consist primarily of 'covalent' (one single electron per atomic centre) VB structures and are one photon forbidden. (Masthay 1988: 7 and Chapter 4) Mastay remarks that the utility of two-photon spectroscopy is rooted in the effects of alternancy symmetry as 'covalent' two-photon allowed stated tend to be preferentially lowered in energy with respect to 'ionic' one-photon allowed states. He suggests when two photon spectroscopy is used in

conjunction with one-photon absorption spectroscopy, may determine the electronic level ordering of low-lying singlet states in π-conjugated systems (Mastay 1988:3)

3.2 Principle of two photon excitation

In one-photon fluorescence excitation, a single photon has sufficient energy to excite the fluorescence molecule from the ground state to an excited state in our case and often for n (non-binding, singulett character), to π* (anti-binding),or for π to π*- transitions of molecule orbitals (Barrow 1982, Schmidt 2000)) The excited molecule then relaxes to a state from which it decays back to the ground state with the emission of a longer wavelength photon. This is called the Stokes´ shift ranging from 50 to 200 nm nanometers for typical fluorescent probes in use in fluorescence cytometry.

In multi-photon fluorescence excitation, two or more photons, which individually have insufficient energy to excite the fluorescence molecule, interact co-operatively to achieve excitation. The excitation process depends on 2 or more photons arriving in a very short space of time, i.e. 'simultaneous', combining their energy to reach the excited state. The simplified Jablonski Diagram in Figure 3_1 illustrates a co-operative absorption of two photons via a 'virtual intermediate state' K within 0.1 fs (in 10^{-16} – 10^{-18} seconds), i.e. in a single quantum event. For a similar number of absorption events as in one-photon excitation the photon density has to be 10^6 times higher, this is achieved by focusing the laser beam, such as the photons become crowded spatially, but also by concentrating the photons in time (by using the pulses from a mode-locked laser, see section 7.6.4) The required high photon fluxes are delivered in TPE LSM by pulsed lasers, with an optimum pulse repetition rate of ≈ 100 MHz, resulting in a 10 ns (10^{-9}s) temporal separation of pulses. Because fluorescence lifetimes are about ≤ 10 ns, an excited molecule can relax to the ground state before the next pulse arrives. The used lasers have a moderate average power, but the output power of the periodically arriving pulses is very high. Since the energy of a photon is inversely proportional to its wavelength, the two photons should be about twice the wavelength required for single-photon excitation. A fluorophore usually absorbing ultraviolet light (~ 350 nm) can be excited by two red photons (~ 700 nm). The different excitation processes will show different absorption spectra (as the absorption cross sections

differ), as these two excitation pathways populate different energy (vibrational) levels. (Vroom 1998) Emission spectra, however should not differ, as the vibrational energy level from which fluorescence takes place is the always the same for the low energy two-photon (or multi-photon) and the more energetic one-photon excitation and relaxation process of the chromophor. Molecules in condensed phases, with a few rare exceptions, always rapidly relax without visible radiation to the lowest vibrational level of the singlet state S_1. This process is called internal conversion and generally occurs in 10^{-12} s or less. Since fluorescence lifetimes are typically near 10^{-8} s, internal conversion is generally complete prior to emission. Hence, fluorescence emission generally results from a thermally equilibrated excited state, that is, the lowest-energy vibrational state of S_1. (Jablonski 1999)

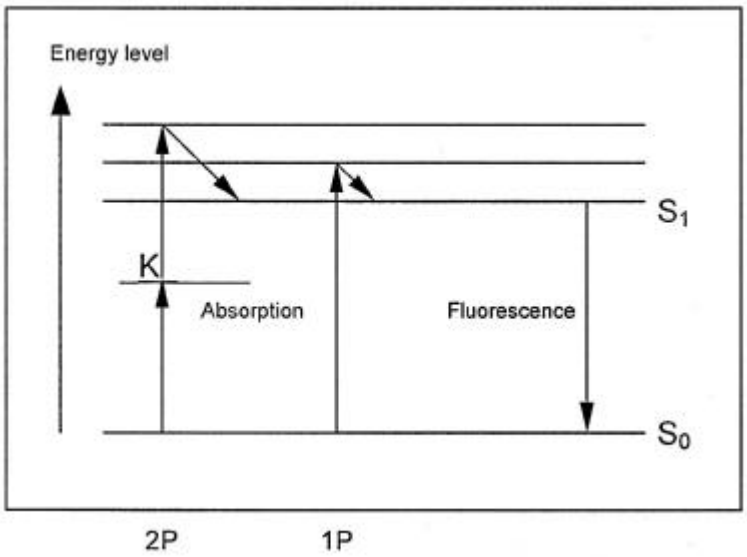

FIG 3_1: Principles of Fluorescence Excitation (simplified Jablonski-Diagram)

There are some investigations about two-photon excited fluorescence measurements with theoretical considerations about the power dependence in TPE and modified two-photon excitation cross section (Fischer et al. 1998), and excitation and action TPE cross section of several fluorophores. (Xu and Webb 1996), which demonstrate that the number of photons absorbed per molecule by means of TPE is proportional to the two-photon absorption cross section δ and to the square of the incident intensity I as TPE is a second order process. The attempts to determine the two photon power dependence rely on the Heisenberg uncertainty principle to estimate the lifetime of the virtual level accessed upon interaction of a molecule with the first photon, therefore instantaneous power in these models is used.

Another approach is a rate expression of two-photon excitation by modelling the response as a single-step, intermolecular reaction to demonstrating a quadratic relationship with instantaneous power.

3.3 Principle of non-linear imaging in two-photon NIR laser scan microscope

There are two main differences between multiphoton and confocal microscopy:

- The source is an ultrafast laser (usually Ti:Sapphire) with very high peak power, but low average power.
- The confocal aperture is unnecessary, because all of the fluorescent light originates from the laser focus spot

Because the two-photon excitation depends on simultaneous absorption of two photons, the resulting fluorescence emission depends on the square of the excitation intensity. This quadratic (nonlinear) dependence gives rise to many of significant advantages associated with two-photon excitation microscopy (Piston 1999) The demonstration of a quadratic relationship between collected fluorescence intensity and the laser illumination intensity can be used as check of the two-photon excitation. (Diaspro 1999)

With a point source producing a stream of pulses at a duration of about 100 fs, a typical laser pulse duration, with a repetition rate of 80 MHz, the probability that a certain fluorophore absorbs two photons during a single pulse is given by:

$$\mathbf{n_a \approx d \times (P)^2 \times f_p^{-1} \times x \times (NA^2/ hc\, l)^2}$$

n_a	probability, that a certain fluorophore absorbs two photons during a single pulse
δ	the two-photon cross section, e.g typical about (10^{-48} -)10^{-58} [m^4s] per photon
P	the average power of the laser, e.g 50 mW
f_p	the repetition rate e.g. 80 MHz
ξ	the so-called two photon advantage given by $\xi \approx 0.664 \cdot (f_p \cdot \tau_p)^{-1}$.
τ_p	duration of pulse in sec, e.g 100 fs (10^{-15} s)
NA	the lens numerical aperture, e.g 1.4
h	Planck´s constant ~ 6.626 x 10^{-34} Js
c	the velocity of light ~ 300 m/s and
τ_p	duration of pulse in sec, e.g 100 fs (10^{-15} s)

For a two-photon cross section δ of approximately 10^{-58} [m^4s] per photon, focusing through a high quality objective, the average incident laser power of ~ 50 mW would saturate the fluorescence output at the limit of one photon pair per pulse per fluorophore. (Denk, Piston, Webb 1995) The average power of the used laser was 40 mW, the pulse duration 120 fs, the repetition rate 76 MHz and the NA =1.2 (water immersion) respectively 1.3 (oil immersion).

Beyond the focal region as it is demonstrated in Figure 3_2 the photon density is low and the probability of two-photon excitation within 'the absorption cross section' of a chromophore very low. The excitation volume corresponds to the detection volume, therefore biological tissue is less damaged and the photobleaching of dyes is minimised.

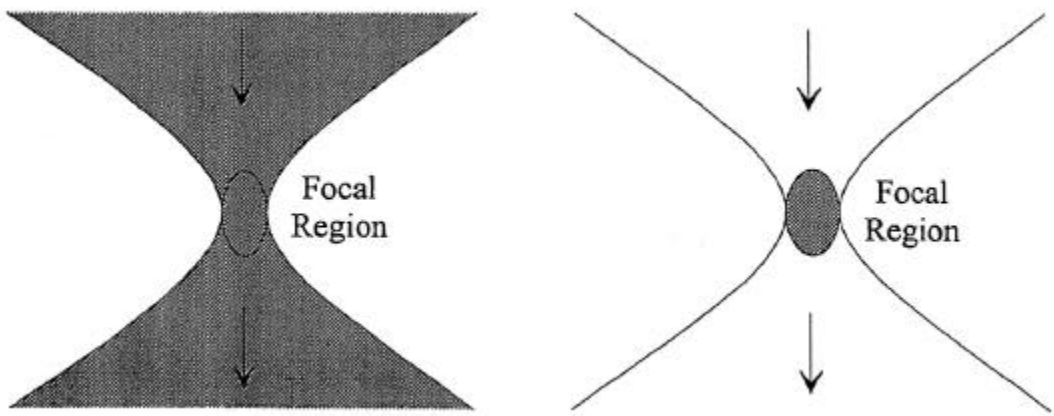

FIG 3_2 Principle of conventional confocal fluorescence imaging (left) and non-linear imaging in two-photon NIR microscopes (right)

In conventional confocal microscopy, the application of pinholes in the image plane results in spatial supression of 'out-of-focus' fluorescence. Because the excitation volume is larger than the detection volume, photostress and photobleaching occur through the entire depth of the cell. In contrast, the small sub-femtoliter (~0.1 fL) excitation volume during two-photon excitation and the absence of efficient NIR-absorbers reduces photobleaching and stress to the focal plane. (König, Simon, Halbhuber 1996)

3.3.1 Advantages of Multiphoton-Excitation

Multiphoton microscopy allows high-resolution imaging and efficient detection of fluorescence signal, solving problems of LSCM: improving the signal-to-noise ratio by eliminating fluorescence except at the focal point of the laser, and reducing or eliminating photobleaching and phototoxity by *using low average power*. Especially in highly scattering environments TPE LSM is advantageous because of using a longer wavelength as the quantity of straylight, which depends on the probability for elastic scattering, caused by smallest particles, is inverse proportional to the inverse fourth power of wavelength. (Rayleigh-Criterion). This and because more laser light is arriving at the focal region as it is not absorbed beforehand causes a triple penetration depth of NIR radiation compared to conventional CLSM, therefore deeper optical sectioning of biological specimen is possible up to ~ 300 µm (usually ~ 100 µm). In contrast to the high frequent laser light used in CLSM the low frequent laser light, poor in energy, of TPE LSM hardly has a negative influence on the cell vitality.

3.3.2 Used Lasers for TPE

Lasers with a pulse duration of about 20 –100 femtosecond have to be used because they provide a near optimal combination of pulse duration, peak power and pulse rate. Mode-locked lasers delivering 100 fs pulses at a repetition rate of 100 Mhz and delivering a peak power up to 100 kW (10^5 –10^6 higher than one-photon-excitation), i.e. hundreds mW in terms of average power are generally used as TPE instruments. Picosecond laser sources have been also successfully used. The laser source also needs a broad tunability in the near IR, long-term stability and low amplitude noise. In the 80`s a CW modelocked Nd:YAG laser synchronously pumping a dye and colliding pulse mode-locked (CPM) dye laser was used for TPE. (Denk et al. 1990)
Since the 90´s mode-locked Ti:Sapphire lasers pumped by solid state lasers (nowadays 5 W diode-pumped lasers with green output) is state of the art.

4. Data restoration by determining the optical characteristics of the microscope system

The data processing of the obtained confocal images includes their restoration. This will remove disturbances within the image, which are appearing during the imaging process, because of the imaging characteristics of the image acquisition system, the movement of the objects,... In general, it should be possible to measure or at least to estimate the disturbance function, which will superimpose the image. A correction function can be derived from it to calculate the original object or image function. This calculation is important, as it corrects a systematic error during data acquisition.

With a simple signal model shown in Figure 4_1, the process of image degradation can be represented. as

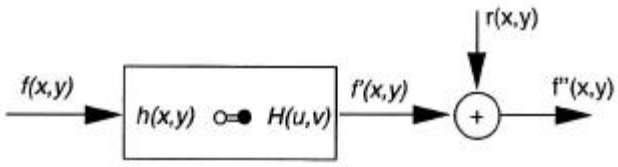

FIG 4_1 Signal model of the image degradation.(Ehricke 1997)

The original image signal *f(x,y)* will be changed by the disturbing signal *h(x,y)*. As the location is invariant the disturbed image signal *f'(x,y)* can be described - shown in the formula 1 in short form, in integral form in formula 2 - as a convolution of the original signal with the disturbance signal *h(x,y)*, which is the impulse response of the acquisition system.

$$f'(x,y) = h(x,y) \otimes f(x,y) \qquad (1)$$

$$f'(x,y) = \iint f(m,n)h(x-m, y-n)dmdn \qquad (2)$$

Digitised images are discrete, because each pixel or voxel (for volume data files) is described by a integer number of the color or gray scale and a position. In the pixilated image each point has a discrete value, i.e. an integer number (on colored or gray scale) and a position, therefore a discrete Fourier transformation can be performed: Each point is presented as a sum of smaller distances. Thus an image can be reconstructed out of points even if they are superimposed. Therefore a convolution of the original signal with the disturbing signal is possible in the discrete region.

The phase, not the amplitude contains the most important information of the original image in periodic structures.

The disturbed image signal is further more superimposed by a noise function in an additive way, in the simplest case it is signal independent, i.e. the noise function does not correlate with the image signal. The resulting image function *f'' (x,y)* is represented in the next formula 3:

$$f'(x,y) = \sum_{m=0}^{M-1}\sum_{n=0}^{N-1} f(m,n)h(x-m, y-n) + r(x,y) \qquad (3)$$

(Ehricke 1997)

The added noise is the variation in the detected and digitized signal that is not associated with a feature in the specimen. Sources of noise are the background of the sample (electromagnetic and thermal radiation in the surroundings of the sample), the Poisson distribution of light (intrinsic noise, shot noise, *photon noise*), the *detector noise* of the photomultiplier tubes and the *electronic noise* of amplification and processing of signals and data after the photomultiplier tubes. There are several causes for detector noise: *Schottky*-noise (*Johnson* / *Nyquist* noise) occurs when current in the form of moving charge loaded material is passing a transition zone like there is in photo cells. *Schrot* noise is due to the discrete nature of emitted photoelectrons. *Recombination* noise originate in photo conductor because of recombination processes after charge separation. *1/f* noise is determined by a declining energy reciprocal to the signal frequency. *Thermal* noise appears because of the thermal excitation of electrons and other charge carrier in resistors, condenser, radiation detectors if there is a resistor incorporated. This noise is proportional to the temperature and the quantity of the resistance. An air-conditioning system can reduce this kind of noise. (Schmidt 2000)

The discrete nature of voxels lead to following expression for a volume data file:

$$f'(x,y,z) = \sum_{m=0}^{M-1}\sum_{n=0}^{N-1}\sum_{w=0}^{O-1} f(m,n,v)h(x-m, y-n, z-w) + r(x,y,z) \quad (4)$$

The original data file consisting of pixels, described by a place and an amplitude in the local space can represented by a superposition of sinus functions with different frequency, phase and amplitude in the frequency space. The mostly applied mapping rule is the Fourier Transformation (FT). Also non periodic functions can be shown as a superposition of sinus-like components (for further explanation see Uszczapowski 1985 or Arsac 1961) The

transformation of a function out of the frequency space in the local space is called inverse Fourier transformation (IFT).

In the Fourier region the signal functions can be represented as it is described in the following formula 5:

$$F''(m,n) = F(m,n)H(m,n) + R(m,n) \qquad (5)$$

$H(m,v)$ is the modulation transfer function

$R(m,n)$ is the noise function

$F(m,n)$ is the measured image

$F''(m,v)$ is the restored image

The aim of the image restoration is to calculate from the disturbed image signal *f''(x,y,z)* a signal *f*(x,y,z)* that the original image signal *f(x.y,z)* is optimally approached. The disturbances, i.e. aberrations which occur during the image acquisition of biological objects by laser scanning microscopy are due to the optical imaging characteristics of the used microscope system represented by the point spread function. Literally, a PSF is the image of a single point object. The degree of spreading (blurring) is a measure for the quality of an optical system.

4.1 Imaging Characteristics of the Confocal Microscope: The Point Spread Function (PSF)

The PSF, defined by linear system theory, can completely describe the imaging in a conventional fluorescent microscope and in a confocal microscope can completely described because in both imaging systems the image formation is *linear*. When two objects A and B are imaged simultaneously, the result is equal to the sum of the independently imaged objects and vice versa. For a linear spatially invariant imaging system, the image can be calculated by convoluting a function characterizing the transmission *t(x,y)*, (*t(x,y,z)*) or reflectivity *r(x,y,)*, (*r(x,y,z)*) or the fluorescence *f(x,y)*, *f(x,y,z)* of the sample with the PSF of the system. Analogue in electrical circuit theory an arbitrary signal is convoluted with the response of a circuit. The PSF is the two-dimensional for a standard microscope or three-dimensional for a confocal microscope optical analog of the electrical impulse response of a circuit to a delta function input of infinitesimally narrow pulse.

Three dimensionally an ideal point is represented as growing disk proportional to the distance from the focal plane. The whole intensity of one disc, homogeneously distributed over the area of the disc, corresponds to the intensity of the point. As the diameter of the disc increases linearly with the distance to the focus, the intensity decreases with the square of the distance. The ideal point spread function is a double cone, rotation symmetric to the optical axis, the tips of the two cones meet at the origin of the point. The aperture angle of the cones is equal to the aperture angle of the lens. Outside of the double cone the value of the point spread function is zero. The point-spread functions are due to the lens and the pinhole. The smaller the lens and the bigger pinhole aperture, the wider the pattern (and the lower the resolution). A lens with a small aperture has a large point-spread function and a low resolution. A lens with a large aperture has a smaller point-spread function, subsequently can resolve much smaller structures. The term numerical aperture (NA) refers to a measure of the lens aperture in angle and takes into account the smaller wavelengths in a refractive medium. (NA = $n \sin \alpha$, and $\lambda = \lambda_0 / n$. $\lambda_0 = \lambda$ in vacuum) (Webb 1999)

Following the laws of linear system theory the single point spread functions can be overlaid and added, thus being valid for the whole volume. This is illustrated in Figure 4_2.

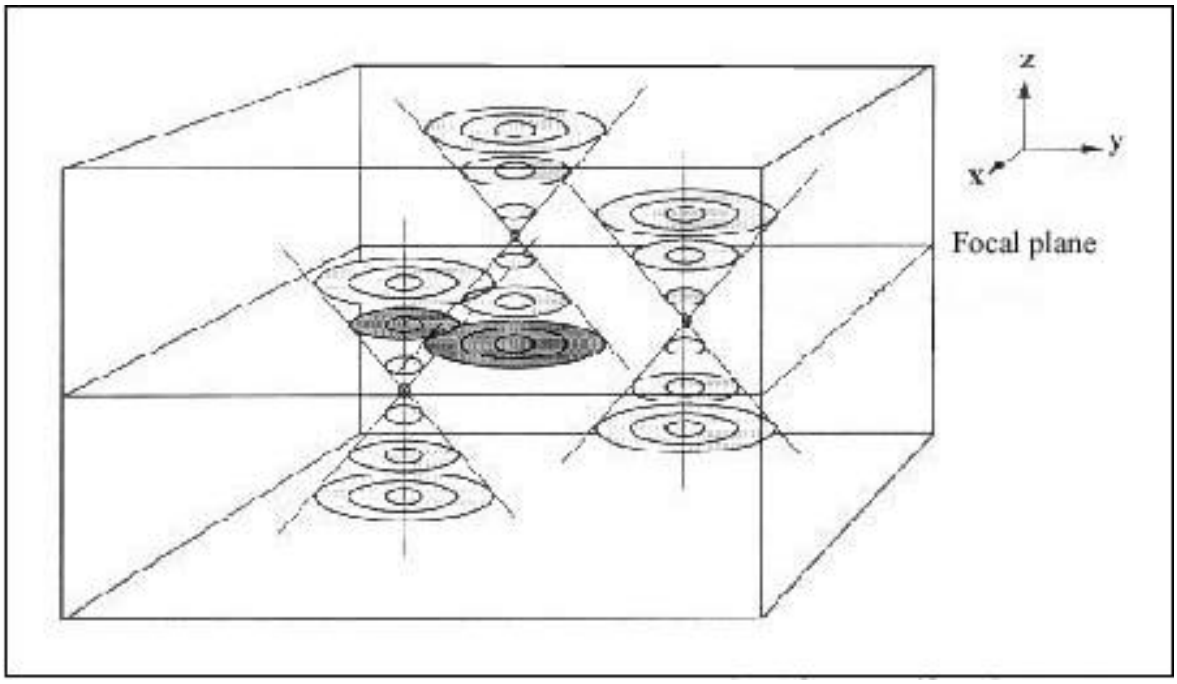

FIG 4_ 2 Superposition of Point Spread Functions in the Three-Dimensional Space

Thus the performance of an imaging system can be quantified by calculating its point spread function (PSF). The images for determination of the PSF had to be sampled at the

Nyquist frequency (criterion), because the sampling density (see Materials and Methods, section 7.4.5) of the (3Dpixel) voxels has not to be too high (oversampling), not too low (undersampling). If specimen are undersampled, information of the sample will be lost as the voxels are too elongated from each other.

4.1.1 Resolution limits of a Fluorescence Confocal Microscopy - FWHM

The CSLM intensity image of simple objects such as edges and points, is the square of their intensity image produced by a standard microscope. The intensity distribution and subsequently the resolution limit in fluorescence microscopy is defined as the full width at the half-power points of the image of the point-like fluorescence object fully in focus (FWHM = Full Width of Half-Maximum). Therefore the resolution capacity of a confocal fluoescence laser scanning microscope is better than for a conventional fluorescence wide-field microscope, because the width is smaller.

The lateral FWHM of the light intensity as a function of the lateral coordinates, *x* or *y*, of a standard fluorescence (fl) widefield (x,y) microscope is about:

$$\mathbf{FWHM_{(fl\ x,\ y)}} = \frac{0.61\,l}{NA(objective)} \qquad (5)$$

(This corresponds to the radius of the airy disc, a diffraction pattern)

In opposite, for a confocal (conf) fluorescence (fl) microscope the lateral FWHM is about:

$$\mathbf{FWHM_{(fl\ conf\ x,\ y)}} = \frac{0.46\,l}{NA(objective)} \qquad (6)$$

The full-width-half-maximum of the light intensity as a function of the axial coordinate, *z*, for a confocal (conf) fluorescence (fl)LSM is about:

$$\mathbf{FWHM_{(fl\ conf\ z)}} = \frac{8.4\,l}{8p\sin^2(\frac{a}{2})} \qquad \text{(Kriete 1992)} \qquad (7) \qquad \text{or}$$

$$\mathbf{FWHM_{(fl\ conf\ z)}} = \frac{0.45\,l}{n(1-\cos a)} \qquad \text{(Robenek 1995)} \qquad (8)$$

FWHM	Full width half maximum in nm
λ	Excitation wavelength in nm
$NA_{(Objective)}$	Numerical aperture of the objective lens = $n \sin\alpha$
n	Refractive index of the immersion medium
α	Aperture angle of the light cone of the objective lens

The lateral FWHM of a confocal microscope, i.e the single-point resolution is about 75 % of a conventional fluorescence microscope. That means an improvement of 32 % in single-point resolution. The two-point resolution or Rayleigh-Criterion, given, if there is a difference of amplitude of 26.5 % between the intensity maximum and minimum of two points with overlapping energy or intensity distribution curves, - is only 8 % better for a CSLM than for a standard microscope. (Corle 1996) The Rayleigh Criterion is the double of the single-point resolution or the FWHM.

Equation 7 slightly underestimates the section thickness (Kriete 1992), as does for high numerical apertures equation 8, for NA = 0.95 around 6 %, for NA = 0.9 around 2 %. For more precise definitions, the non-paraxial scalar theory has to be applied, which will not give closed formula (Robenek 1995)

4.1.2 Aberrations in confocal microscopy

The role of aberrations in confocal microscopy is very important. The axial resolution, needed for optional sectioning, is strongly influenced by (even weak) aberrations, this was pointed out by Sheppard 1988. By measuring the axial response of the CLSM affected by spherical aberrations with a scanning mirror, Wilson and Carlini found that the axial intensity distribution is not symmetric with respect to the image plane, illustrated in Figure 4_3.

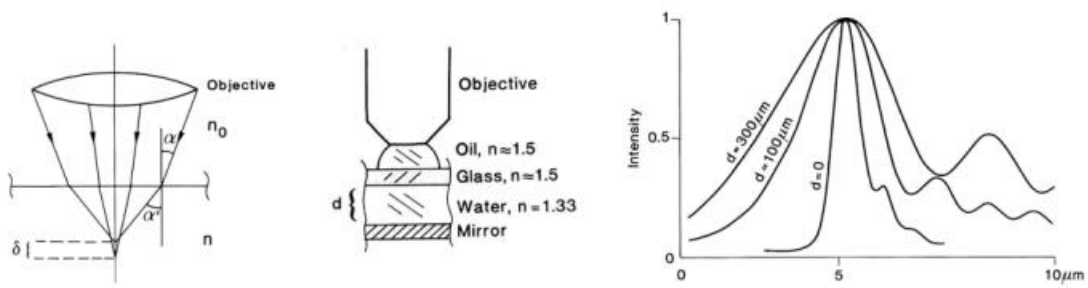

FIG 4_3 a *b* *c*

(a) Aberration (δ) introduced when light propagates from one medium with the refractive index n_0 into a medium having a lower refractive index n, because refraction will take place at the boundary between the two media, i.e. $\alpha' \neq \alpha$., (b) The experimental set-up for measuring the influence of refractive mismatch on depth discrimination, the specimen volume consisted of water (n_{water} = 1.33), an 40 x/1.0 NA oil-immersion objective (n_{oil} = 1.5) was used (c) Influence of focusing depth, d, on depth discrimination. (Carlsson 1990, Kriete 1992)

According to Snell´s law, when considering a converging light cone travelling in a medium with refractive medium n_1 with marginal rays making an angle α_1 which is focused by a lens into a second medium with refractive index n_2, the light is refracted: $n_1 \sin \alpha_1 = n_2 \sin \alpha_2$.In the second medium the marginal rays are making an angle α_2. Because of refractive indices mismatching, ray paths do not converge to a single focus when an oil-immersion objective is focused deep into the aqueous specimen, because of refraction at the cover glass-specimen interface, which is more extreme for the off-axis rays. A refractive index mismatch will cause a magnification error in the axial direction and will result in spherical aberration as it is shown in Figure 4_2c. Especially when one is imaging deep within the specimen, the effects of spherical aberration due to refractive index errors become important in the image formation, the PSF will deteriorate. As a result restoration become less effective and less reliable with increasing depth.

As the refractive index of biological sample in general does not match that of immersion oil, the water objective with a high numerical aperture was invented. With an ideal water-immersion objective, spherical aberration is not experienced when focusing deep into an aqueous specimen. (Only small zig-zag refraction is occurring as the rays pass through the cover glass with a different refractive index, from the immersion water to the aqueous specimen.)

If the refractive index of the mounting media and the lens media differ too much total reflection can occur, this can only happen if the light beam passes from a optical thicker medium (refractive index higher) to a optical thinner medium, i.e. $n_2 < n1$. But the light beam in the confocal microscope comes from one direction and is reflected from the sample, so that in every case, this can happen when the difference between the refractive indices is high. The angle of total reflection is $\alpha g = \alpha \sin (n_2 / n_1)$. It depends from the Numerical Aperture from the Objective lens if total reflection plays a role in image formation.

$NA_{real} = n$ (lens medium) $\cdot \sin \alpha g$ with $\alpha g = \alpha \sin (n_2 / n_1)$

If NA_{real} is smaller than the NA of the objective total reflection really happens. For the immersion oil objective NA is 1.3, $n_1 = 1.508$, $n_2 = 1.334$ of the embedding (mounting) medium, which is PBS. $\alpha g = 59.55°$, NA_{real} is 1.3, which corresponds to the given value.

For the water objective the NA is 1.2, $n_1 = 1{,}452$ (Vectashield), $n_2 = 1.334$ (water as lens medium) $\Rightarrow \alpha g = 66{,}74° \Rightarrow NA_{real}$ is 1.2255. For Mowiol $n_1 = 1{,}4025$ as mounting medium, $\alpha g = 72° \Rightarrow NA_{real}$ is 1.2687. The real NAs are even higher than the given value.

These calculations demonstrate that total reflection could never occur for the applied objectives.

4.1.3 The relationship of the original image function, PSF and noise function: Data reconstruction

The convolution of a 3D- object *f(x,y,z)* with the PSF *h(x,y,z)* corresponds if Fourier transformed to a multiplication of the both functions according to the Fourier Theories. The Fourier transformed PSF in incoherent (fluorescence) imaging is called the optical transfer function (OTF). Fourier transformation is performed by integration of the convoluted functions. Therefore the measured image function *f''(x,y,z)* is the convolution integral of the true (original) image function *f(x,y,z)* and the PSF *h(x,y,z)* and the addition of the noise function.

The convolution is one of the most important operations in imaging processing. 2D-and 3D convolution follow the same laws, only the shape of the PSF (OTF) is different. The PSF demonstrates the distortions which are generated during image recording of biological objects with the CLSM due to the optical characteristics of the microscope.

4.2 Deconvolution – Optical transfer function

To determine the original image *f(x,y,z)* from the measured image *f'(x,y,z)* is referred to as deconvolution according to Fourier Theories:

Fourier Transforms of f, f ', h => F, F', H are simply related by:

$$\mathbf{F' = F * H \;\hat{U}\; Tf' = Tf\,H \;\hat{U}\; f = T^{-1}\,(H^{-1}\,T\,f') \;\hat{U}\; f = (T^{-1}\,H^{-1}) * f'}$$

h is the measured PSF,

H is called the optical transfer function (OTF) and is the Fourier transform of the Point Spread Function,

T is the Fourier transform operator.

i.e. the convolution of the object function f(x,y,z) with the PSF in the locate room corresponds to a multiplication of the attached Fourier transforms. The measured Fourier transformed image is multiplicated with the inverse OTF (H^{-1}) and the result of this operation is

subsequently transformed back with the inverse Fourier transform operator (T^{-1}). The reconstruction can also be carried through directly in the locate space convoluting the focus series with the Fourier transformed OTF^{-1} (T^{-1} H^{-1}).(Jähne, 1989)
Therefore the advantage of the Fourier transforms for the calculation of the original image is a less amount of necessary calculations. For deconvolution the Fourier transform of the measured image will be multiplied with the inverse OTF and the result of this operation2D, 3D (de)convolution follow the same principles, only in 3D imaging functions have three variables to describe completely the location of a point.

Therefore the relationship of the Fourier transform can be also expressed in the frequency domain:
F'(f) = F(f) H (f),
where f represents the 2D or 3D spatial frequency variable, depending upon application. The bandlimit for a 2D OTF is f_c = NA/ λ_1 (NA Numerical Aperture, λ_1 wavelength of the emission light). The OTF has the shape of a dunce cap. The 3D optical transfer function as it is shown for the confocal fluorescence microscopy in Figure 4_4 has a missing cone region , therefore is degrading the image in two regions, thus in two ways.

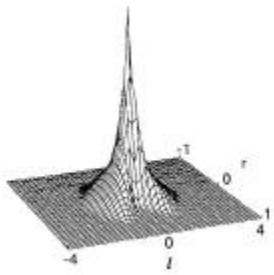

FIG 4_4 The 3-D OTF for a confocal fluorescent scanning microscope with a finite-sized detector (with a pinhole radius r_n =10) (Kriete 1992)

First, where the OTF is nonzero, it functions as a low-pass filter by suppressing high frequency components in the image. Secondly, where the OTF is zero, it totally removes the Fourier components.
To recover these missing Fourier components is the challenge of the image reconstruction techniques for fluorescence microscopy, and for optical imagery in general. (Kriete 1992)

5. Purpose of the project

Because of the conflicting hypothesis reported in oxygen sensing models concerning the cellular localisation as well as response to hypoxia of reactive oxygen species (ROS) in human hepatoma HepG2 cells a new, more sensitive approach to reveal ROS generation especially the housing of the Fenton reaction should be realised. It was expected that TPE LSM would be more suitable to localise hot spots of ROS generation. Former experiments performed with conventional one photon excitation confocal laser scanning microscopy (OPE CLSM) could not reveal if ROS were generated inside of mitochondria or in the cytoplasm as well.. As conflicting results could also be due to different use of fluorescent molecules, we carried out a comparative study on dihydrorhodamine 123 (DHR) and 2´,7´dichlorodihydrofluorescein-diacetate (H_2DCFDA) stained HepG2 cells with one photon excitation (conventional) confocal and two photon excitation laser scan microscopy (TPE LSM). It is known that CLSM is highly destructive, and not very suitable for measurement of those light-sensitive reactions. As the laser scans the specimen, the probe is selectively bleached in the X/Y plane and nonselectively bleached in the Z plane. Therefore we implemented a (new) method for performing the experiments: TPE CLSM. It is known that TPE needs about the double excitation wavelength, but it cannot be predicted precisely from one photon data. Therefore several methodical questions had to be answered beforehand.

(1) Own measurements of UVVIS absorption spectrophotometrie and fluorescence spectroscopy of the oxidised fluorophores Rhodamine 123 and 2’,7’-Dichlorofluoroescein and of the mitochondrion specific fluorescent dye MitoTracker Red CMX Ros in PBS should serve as a basis, because available fluorescence spectra are usually done in an organic solvent and not in PBS, which was used for mounting the cell specimens, for answering the following two questions:

(2) Are the fluorophores, used and established in conventional CLSM, suitable for TPE LSM, i.e. where are the TPE excitation maximums (in PBS)?

This was also performed for the DNA-label DAPI, and

(3) How do they differ from theoretical extrapolated comparable one photon excitation spectra and excitation maximums?

(4) Is there a difference between one photon and two photon emission maximums?

It should be expected that there is no one, as emission should always take place from the same, the lowest vibrational level of the excited singulett S_1 level.

(5) What are the optical characterics of the TPE LSMicroscope

(6) in comparison to OPE CLSM

(7) and in comparison to conventional widefield fluorescence microscopy?

(8) Where are the resolution limits of the new implemented microscopical system?

As PSFs control the image formation in all coherent (and incoherent) optical systems, the optical characteristics were determined by measuring the point spread function

It was expected that these PSFs used for confocal data restoration should improve local resolution. All this was undertaken to have the optimum performance quality of the microscope system, including data restoration and visualisation, to solve the following question:

(9) Are hot spots of ROS generation only colocalised within mitochondria or can other perinuclear cytosolic compartements be found which are generating ROS most probably by the Fenton reaction ?

Because of these questions

1. UV/VIS Absorption Spectrophotometry of the dyes used and the optical barrier filter which should be appropriate to the emission maximums of the dye,
2. One Photon and Two Photon Excitation Fluorescence Spectroscopy of the dyes to determine the excitation and emission maximums and
3. Different Point Spread Function in PBS and the mounting media Mowiol and Vectashield were measured and

finally used to localise ROS generation in human HepG2 cells by CLSM and TPE LSM.

II MATERIALS AND METHODS

6. Materials

6.1 Cell Culture, Media

Basalmedium Supplement (BMS) (S5175)	Biochrom KG (Berlin*)
Dulbecco`s Phosphate Buffered Salts = Phosphate Buffered Saline (PBS) Tablets (2810305) Without calcium and magnesium (1Tablet = 100 ml)	Biochrom (Berlin) ICN Biomedicals, (Eschwege)
Glutamin stable (N-acetyl-L-alanyl-L-glutamine) (200 mM)	Biochrom KG (Berlin)
HepG2 cells (HB 8065)	ATCC (USA)
Four Well Pod	Nunc (Denmark)
Incubator (5 % CO2 in humidified air) Stericult 200	Labotect (Göttingen)
RPMI 1640 without Glutamin, Phenol Red 5 mg/l With 2.0 g/l NaHCO3 Without L-Glutamine (F-1295)	Biochrom (Berlin)
Penicillin/Streptomycin (10000 IU, 10000 µg/ml)	Biochrom (Berlin)
Streptomycin sulfate (research grade)	Serva -Boehringer Ingelheim Bioproducts Partnership (Heidelberg)
Tissue Culture Flasks (25 cm², 75 ml; 75 cm², 250 ml) (0,2 µm Vented Blue Physical Cap)	Becton Dickinson Labware Europe (Le Pont De Claix, France)
Trypsin-EDTA in HBSS w/o Ca^{++} & Mg^{++} w/EDTA-4 Na^{+}	Gibco BRL Life Technologies GmbH, (Karlsruhe)

* If not specified, the country of origin is the Federal Republic of Germany (FRG)

6.2 Dyes

4´,´6- Diamidino-2-phenylindole dihydrochloride (DAPI)(A1001)	AppliChem (Darmstadt)
2´,7´- Dichlorofluorescein (ACS Reagent:D-9053)	Sigma-Aldrich (Deisenhofen)
2´,7´- Dichlorofluorescin – Diacetate (D-399)	Mobitec (Göttingen)
Dihydrorhodamine 123 (D-632)	Mobitec (Göttingen)
MitoTracker ®Red CMX Ros (M-7512)	Mobitec (Göttingen)
Rhodamine 123 (R-302)	Mobitec (Göttingen)
PS- Speck™ Microscope Point Source Kit (P-7220)	Molecular Probes, Mobitec (Göttingen)

6.3 Chemicals

DMSO	Serva -Boehringer Ingelheim Bioproducts Partnership (Heidelberg)
Acetic acid	Carl Roth GmbH (Karlsruhe)
Ethanol	
HCl	
Isopropanol	
Mowiol 4-88 (475904)	Calbiochem (Bad Soden)
Aqua bidest.	Millipore
Mucasol	Band GmbH (Wertheim)
Poly-D-Lysin	Serva Electrophoresis GmbH (Heidelberg)
Vectashield (H –1000)	Vector Laboratories, Inc. (Burlingame, CA)

6.4 Instruments

Autoklav 23	Melag
Finnpipettes Digital 0.5–10µl, 5-40 µl, 40-200µl, 200-1000 µl	Labsystems (Helsinki, Finland)
pH- mV Meter	Knick
pH- mV Meter	Schott Geräte
Precision balance 0.00001- 20 g	E.Mettler (Zürich, CH)
Refractometer	Carl Zeiss (Oberkochem)
Precision Cuvettes made out of Quarzglas SUPRASIL (10mm) for Absorption and Fluorescence Spectrophotometrie/copy	Hellma
Safe Locks (reaction tubes) 0,5 ml; 1 ml; 2 ml	Eppendorf (Hamburg)
Varipette 0.5-10 µl	Eppendorf (Hamburg)

6.5 Spectrophoto- and Fluorometer

Double Beam UV-Vis Spectrophotometer Uvikon 933	Kontron Instruments
LS 50 B Luminescence Spectrometer	Perkin Elmer (Überlingen)

6.6 Microscopes and Utilities

Cover glasses, round, ∅ 17 mm; ∅: 12 mm,	Oehmen Labortechnik
selected thickness:∅ 0,17 mm ± 0,01 mm	Quadrolab (Essen)
Immersion oil	Nikon (Düsseldorf)
Kimwipes	Kimberly-Clark
Fluorescence Filter Set B-2A Ex: 450 –490 nm	Nikon (Düsseldorf)
(Dichroic Mirror) DM: 505 nm	
(Barrier (Emission) Filter) BA: 520 nm	
Long Pass Filter, Medium	

Fluorescence Filter Set G-2A Ex: 510 –560 nm	Nikon (Düsseldorf)
(Dichroic Mirror) DM: 575 nm	
(Barrier Filter) BA: 590 nm	
Long Pass Filter, Medium	
Fluorescence Filter Set D-F-R	Nikon (Düsseldorf)
Simultaneous representation	
of DAPI + FITC + Rhodamine	
Inverted Microscope Eclipse TE300	Nikon (Düsseldorf)
Microscope Eclipse E1000M/E1000	Nikon (Düsseldorf/FRG)
Micro slides	Oehmen Labortechnik Quadrolab (Essen)
PCM(Personal Confocal Microscope System)2000	Nikon (Düsseldorf)
Power Supply V-PS100DU-1/V-PS100E	Nikon (Düsseldorf)
V-IBS Beam Splitter Module	Nikon (Düsseldorf)
EZ 2000 for PCM (Personal Confocal Microscope System) 2000 Version 2.1.0/2.1.3 (Software and Hardware: PC extension boards: SGRB framegrabber and PCM serial interface board, PCM scan head and Cables, RFA z-drive, Transmitted Light Detector (PCM 2000 Controller: Photomultiplier Tubes 1- 3) EZ 2000 Viewer Version 2.1.0 and 2.1.3	Nikon Europe B. V. (Bad Hoevedorp), Coord Automatisierung (Apeldoorn, NL)
Physik Instruments Objective Scanner: Low Voltage Piezoelectric Translator E-662 (LVPZT) Amplifier / Position Servo Controller Model P-723.17 Measurement range: 200 µm, 0 – 10 V, Step Size: 0,5 V	Physik Instrumente (Waldbronn)
Mercury short arc lamp HBO 100 W/2	Osram
Micro slides	Oehmen Labortechnik Quadrolab (Essen)
Objectives:	
Plan Fluor 40x/1.3 Oil DIC H ∞/0.17 WD 0.2	Nikon (Düsseldorf)
Plan Apo 60x/1.2 Water DIC H ∞ /With cover glass correction WD 0.22	Nikon (Düsseldorf)

6.7 Optical Barrier Filters

All in Diaphot filter ring for a PCM2000- Filter holder, 2P optical filter blocked with OD 6, bandpass until 1100 nm, A/R coating, ∅ 18 mm, thickness max. 4.5 mm

1P- and 2P barrier filter D 470/30	AF Analysentechnik
1P- and 2P barrier filter HQ 515/30	(Tübingen)
1P- and 2P barrier filter HQ 515/30	
2P- Barrier Filter HQ 535/30	
1P- and 2P barrier filter HQ 590/60	
2P barrier filter HQ 620/60	

6.8 Laser and Utilities

Air-cooled Argon Ion Laser Model 263C Wavelength 488 nm	Spectra Physics (Mountain View, CA, U.S.A)
Digital Shutter System Model 845	Newport Cooperation (Irvine, California)
Helium – Neon Laser Model 1600 Series Wavelength (nm) 543,5 nm	Uniphase Lasers & Fibre Optics Ltd. (Eching, Muenchen,FRG)
High Speed Photodiode Module PDM-400 (200 ps puls rise time, 400 ps FWHM)	Becker & Hickl GmbH
Low Voltage Piezoelectric Translator E-662 (LVPZT) Amplifier / Position Servo Controller	Physik Instrumente (Waldbronn)
Miniature Autocorrelator	MIRCO$COR, New Technologies and Consulting (FRG)
Mira Model 900 modelocked Titanium: Sapphire laser 8 Watt	Coherent Laser Group (Santa Clara, CA)
Mira - Grating Dispersion Compensator (GDC)	Coherent (Santa Clara, CA)
Optical Power Meter Model 840	Newport (Irvine, California, U.S.A.)
PCM 2000 Scan Head	Nikon GmbH (Düsseldorf)
Post Fiber Compressor	Coherent Laser Group (Dieburg)

RTE Series Refrigerated Bath/Circulator	Neslab (Frankfurt)
Verdi^{TM} V-5 Diode-Pumped Laser	Coherent (Santa Clara, CA)
Vibration Control System - Stabilizer	Newport (Irvine, California, U.S.A.)
High Performance Laminar Flow Isolator I – 2000 Series	
Super High Pressure Mercure Lamp	Nikon GmbH (Düsseldorf)
Power Supply Model: HB 10103/4 AF	
Two Channel Digital-Real Time Oscilloscope TDS 200	Tektronix, Inc. (Wilsonville, OR, US)
Optical Power Meter (Model840-C)	Newport (Irvine, California)
Wave Scan Laserspectrometer	Angewandte Physik and Elektronik GmbH APE (Berlin)

6.9 Hardware and Software

APE Las Scan 2.2	APE Instrumentation Control
AVS/ Express	Advanced Visual Systems Inc. (Waltham, Mass. U.S.A)
EZ 2000 for PCM 2000 (Version 2.1.0, 2.1.3)	Nikon Europe B.V. (Badhoevedorp), Coord Automatisering (Appeldorn, NL)
FL WinLab (Software Package)	Perkin Elmer (Überlingen)
Huygens System 2.20	Scientific Volume Imaging b.v. (Hilversum,NL)
Silicon Graphics Octane Workstation	Silicon Graphics (Mountain View, CA, USA)
TechPlot(Technisch-wissenschaftliche Software)	Software für Forschung und Technik, Dr. Ralf Dittrich (Braunschweig)

7. Methods

7.1 UV and Visible Spectroscopy of the Used Filter and Dyes

7.1.1 Principle of Operation of a Typical Double-beam Recording Visible (VIS)-near-ultraviolet (UV) Spectrophotometer

For near-ultraviolet operation a mirror is rotated in order to change from the tungsten to the deuterium lamp. The absorbance in the sample beam relative to that in the reference beam is obtained by inserting an optical attenuator into the reference beam. The latter is attenuated until the two detected signals are equal. When the sample is absorbing strongly this optical null method has the disadvantage of reducing drastically the intensity in the reference beam.

7.1.2 UV/VIS Absorption Spectrophotometrie of the Applied Barrier Filters

The transmission range of the applied filters and the absorption maximums of the (oxidised) dyes were measured by the UVIKON 933 Double Beam UV-Vis Spectrophotometer. Before measuring a baseline correction was carried out. The filter were measured against air. The barrier filter was put in front of the cuvette holder for measuring the sample and a wavelength scan over the range of 900 to 200 nm was performed with air 'as blind sample'. Each filter together with the filter-ring was put in a filter holder and fixed with a piece of double sided tape at the bottom of the filter holder, to be able to close the cover of the spectrophotometer.
The measured optical barrier filter are listed in Table 7_1 and 7_2.

Wavelength (nm)	488	515	590
Bandwidth (nm)	10	30	60

Table 7_1 Filter for one photon excitation

The given wavelength is at the middle of the optical filter. The first filter (488 nm +- 5 nm) is an excitation filter, the other are emission filters.

Wavelength (nm)	470	515	535	590	620
Bandwidth (nm)	15	30	30	60	60

Table 7_2 Filter for two photon excitation

7.1.3 UV/VIS Absorption Spectrophotometrie of the Used (Oxidised) Dyes

PBS was taken as blind sample for the dyes, because they were solved in PBS to have physiologic conditions for Hep G2 cells. A wavelength scan from 900 nm to 200 nm was performed.

Stock Solutions in DMSO	Stock Solutions in DMSO c (µM)	Solutions for Use in PBS (µM)	Measured con-centrations (µM)
2',7'-Dichlorofluorescein (DCF) (Mr = 401.2 g/mol)	11	20 µM	3, 5, 9, 12, 15
MitoTracker RedCMX Ros (MT) (Mr = 495 /mol)	1	10 µM	2.5, 5, 10
Rhodamine 123 (RHO) (Mr = 380.83 g/mol)	25	25 µM	1, 4.5, 6.7, 10

Table 7_3 Stock solutions, Solutions for use, and measured concentration of the (oxdised) dyes in UV-VIS Spectrocopy

(for structural details of the dyes is referred to paragraph 7.2)

Several dilutions in PBS were measured, in order to have some which absorb within the linear range of 0.1 to 1.5 Absorption Units. The listed measured concentrations were within the linear range of UV-VIS spectroscopy.

7.2 One Photon Fluorescence Spectroscopy

One Photon Fluorescence Spectroscopy was performed on Perkin Elmer LS 50B Luminescence Spectrometer.

7.2.1 System Description of the Used Luminescence Spectrometer

7.2.1.1 The Optical System

With the help of the Luminescence Spectrometer the excitation and emission scans of fluorescence of five different dyes were performed in a continuous scan over the wavelength range of the instrument (200 nm to 800 nm for excitation, 200 to 900 nm for emission). The excitation source which is a special xenon flash tube is triggered at line frequency (50 or 60 Hz) by a small festoon lamp close by to produce an intense, short duration excitation pulse of radiation over the spectral range of the instrument. The optical system consists of two reflection grating monochromators, a series of mirrors and the reference and sample photomultiplier detectors. The path of the radiation is shown in Figure 7_1.

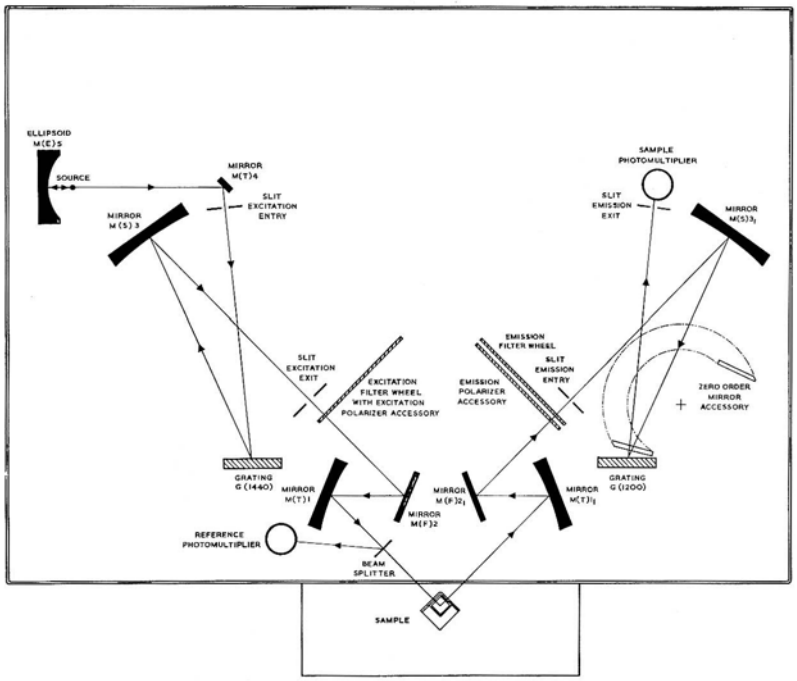

FIG 7_1 *The LS50B Optical Diagram (Perkin Elmer LS50B User´s Manual)*

Energy from the source is focused by the ellipsoidal mirror M(E)5 and reflected by the toroidal mirror onto the entrance slit of the excitation monochromator. It consists of the entrance slit, a 1440 lines per millimeter grating, a spherical mirror and an exit slit. A narrow wavelength band emerges from the exit slit, with the centre wavelength being determined by the setting of the grating, the angle of which is controlled by a step motor. Via the focusing toroidal mirror M(T)1 the majority of the excitation beam is transmitted to the sample area, a small proportion is reflected by the beamsplitter onto the reference photomultiplier.

The toroidal mirror M(T)11 focuses the energy emitted by the sample onto the entrance slit of the emission monochromator. This monochromator consists of the entrance slit, a spherical mirror M(S)31, a 1200 lines per mm grating and the exit slit. A narrow wavelength band emerges from the exit slit, with the centre wavelength being determined by the setting of the grating, the angle of which is controlled by a step motor. The excitation and emission monochromators were scanned over their ranges independently. The signals from the detectors are processed by the instruments electronics and displayed on the PC screen.

7.2.1.2 The Electronics System and Signal Handling

The instrument when operating in the fluorescence mode performs four integration for every data collection cycle. From the emission channel two integration are taken and two from the excitation channel. With respect to the last source flash these integration are performed at fixed times.

Of both the excitation and emission main signals an integration is taken. The emission from the source has a width at half peak height of less than 10 microseconds. The integrators are opened for 80 microseconds to collect all the signal. By gating open both channels a second time just before the next flash and integrating the signal the effect of dark current is eliminated. The dark current signals (signals produced when no light is falling on the photomultiplier) are then subtracted from the main fluorescence signals to give a dark current corrected signal.

7.2.1.3 Signal Conversion

After integration the photomultiplier signals are multiplexed, fed into the auto-ranging amplifier and then into the auto-ranging amplifier and then into the 12-bit successive approximation Analogue to Digital (A-D) converter. To optimise the A-D conversion the auto-ranging amplifier increases the gain of the signal The conversion is obtained by using a 12 bit digital to analogue (DAC) converter and a comparator, where a 12 bit word is successively approximated to the analogue signal, with the control loop being supervised by the on-board microprocessor. From the reference signal and likewise from the sample signal the dark current is digitally subtracted, to give a true zero.

7.2.2 Used Dyes

7.2.2.1 2´, 7´-Dichlorofluorescein (DCF)

Molecular Formula: $C_{20}H_{10}Cl_2O_5$
Molecular Weight: 350.25 g/mol
CAS Number /Name: 76-54-0
(D-9053) Sigma
Stock solution: 11 mM in DMSO
Structure for DCF

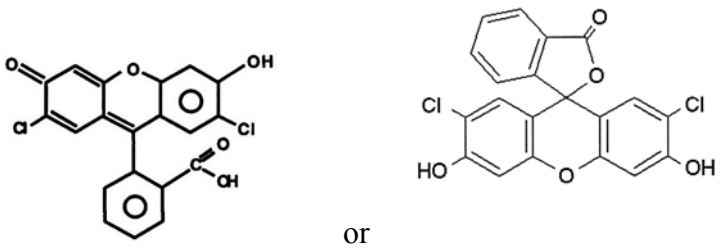

or

FIG 7_2 *Chemical Structure of 2´, 7´-Dichlorofluorescein (DCF)*

7.2.2.2 MitoTracker® Red CMXRos

Molecular Formula: $C_{32}H_{32}Cl_2N_2O$

Molecular Weight: 531.52 g/mol

CAS Number/Name: Not determined

(M-7512) Mobitec (Göttingen)

Structure for MitoTracker® Red CMXRos

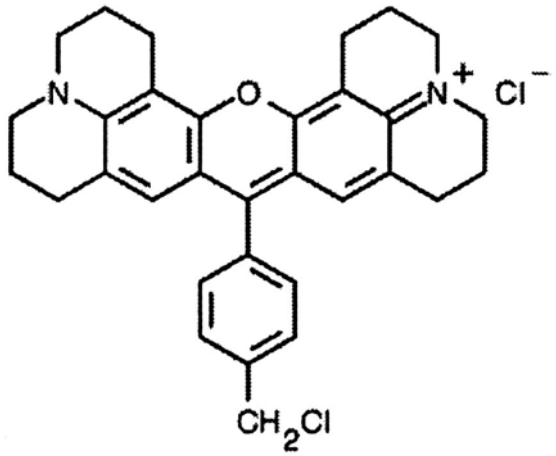

FIG 7_3 *Chemical Structure of MitoTracker® Red CMXRos*

7.2.2.3 Rhodamine 123 (RHO)

Molecular Formula: $C_{21}H_{17}ClN_2O_3$

Molecular Weight: 380.83 g/mol

CAS Number/Name: 62669-70-9 /

Xanthylium, 3,6-diamino-9-(2-(methoxycarbonyl) phenyl, chloride

(R-302) Mobitec (Göttingen)

Structure for Rhodamine 123

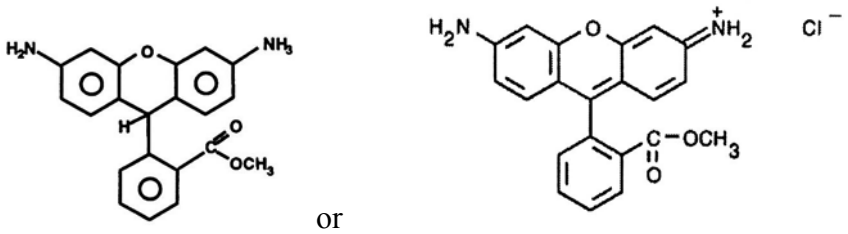

FIG 7_4 *Chemical Structure of Rhodamine 123*

7.2.3 Spectroscopic Measurement of the Dyes

From 2',7'-Dichlorofluorescein Acs Reagent (D-9053-14) (Sigma) $C_{20}H_{10}Cl_2O_5$, Mr = 401.1 g/mol a 11 mM stock solution with DMSO was made.(5.5125 mg in 1161.28 µl DMSO) A dilution 1:220 with PBS was produced and then solutions of 25 nM, 50 nM, 100 nM and 200 nM DCF.

From Rhodamine 123 (R-302) (Mobitec GmbH) Mr = 380.83 g/mol a 1 mM stock solution was made with DMSO. A dilution with PBS, final concentration of 10 µM was prepared which was used to have the following solutions for performing excitation and emission like described above: 20, 40, 50, 60, 80, 100 nM. The last solution was too concentrated to be measured.

From MitoTracker CMXRos (M-7512) (Mobitec GmbH) (Mr = 531,52 g/mol) 50 µg was put in 94 µl DMSO to get a 1mM stock solution. Concentrations of 0.45, 0.67, 0.83,1, 1, 1.25, 2.5, 5.0 and 10 µM were prepared.(Results: The last dilution was out of the linear range)

To determine the excitation and fluorescence emission maximum, the prepared dilutions were measured immediately with LS 50 B Luminescence Spectrometer. Usually an excitation and emission scan were performed immediately each after the other with the highest excitation and emission rate. For the excitation scan the wavelength of the emission maximum was taken as fixed wavelength, for the emission scan the fixed wavelength was the wavelength of excitation maximum.

7.3. Two Photon Fluorescence Spectroscopy of the Used Dyes

The process of single-photon absorption (SPA) is in principle different from two-photon absorption (TPA). As different absorption spectra (absorption cross sections) for one and two photon excitation are very complicated to calculate, the two photon excitation and emission spectra for the used dyes were determined .

7.3.1. Experimental Setup of Two Photon Fluorescence Microscopy

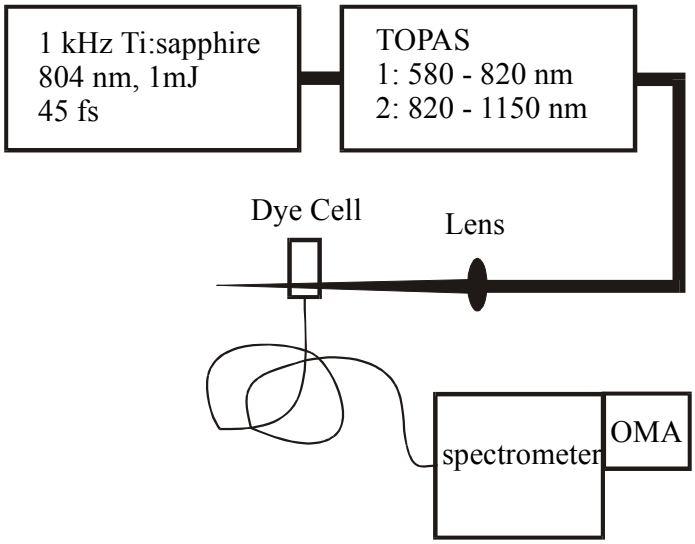

FIG 7_5 Experimental setup of the two photon fluorescence spectroscopy. The laser pulses (TOPAS) were focused into a dye cell and the excited fluorescence was picked up by a multimode fiber. The fiber was connected to a grating spectrometer equipped with an optical multichannel analyzer (OMA).

The experimental setup is shown in figure 7_5 and consists of three units. First, a Ti:sapphire laser delivering 45 fs long pulses at 804 nm with a pulse energy of 1 mJ and a repetition rate of 1 kHz. The spectrum and the pulse width were constantly monitored using a spectrometer and a second order intensity autocorrelator.

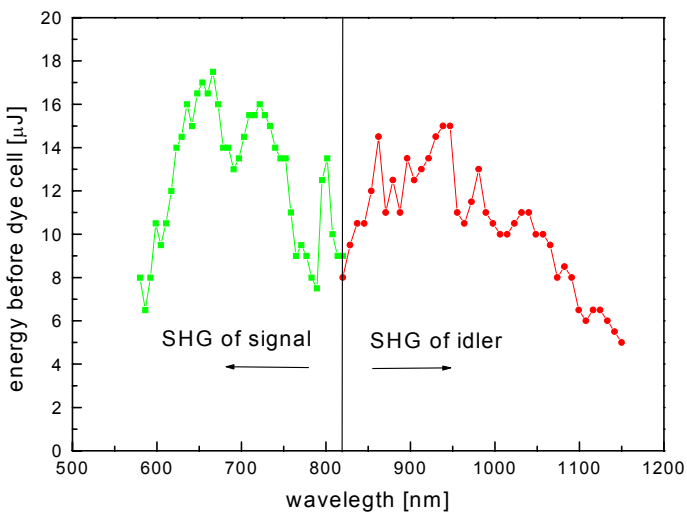

FIG 7_6 Pulse energy as a function of wavelength for both scan ranges.

Second, an optical parametric amplifier (TOPAS) which was used to tune the wavelength continuously between 580 nm and 1150 nm. Figure 7_6 shows the energy per pulse as a function of the wavelength for the two wavelength ranges used.

Third for measuring the two photon excitation and emission spectra, the output of the parametric amplifier was focused by a fused silica lens with a focal length of 400 mm. The distance of the dye cell to the lens was adjusted so that at no excitation wavelength white light generation in the cell was observed. The excited fluorescence was collected by a multimode fibre which was connected to a grating spectrometer. The spectrum ranging from 400 to 720 nm was recorded simultaneously by an optical multichannel analyser with 1024 pixel. The measuring procedure was as follows. The excitation wavelength was changed in equidistant steps and for each step two hundred single fluorescence spectra were averaged. In order to extract the absorption as a function of the excitation wavelength the fluorescence curve was integrated and the result was divided by the square of the excitation intensity assuming a two photon absorption process.

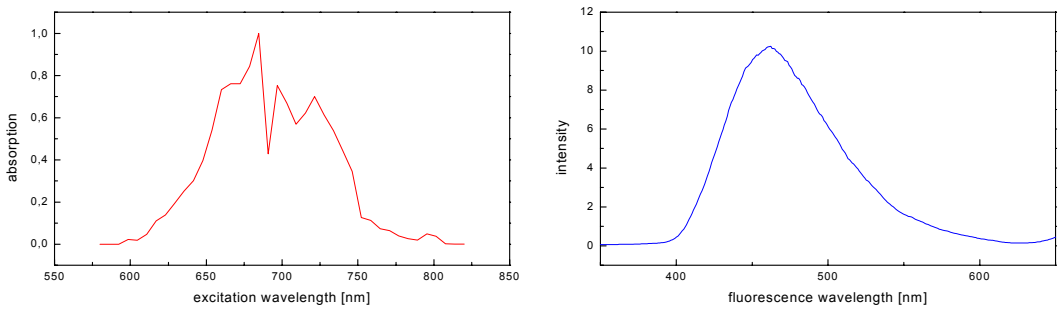

FIG 7_7 Left: Two-photon absorption spectrum of DAPI. Right: Fluorescence spectrum of DAPI at an excitation wavelength of 690 nm.

In Figure 7_4 an example is shown. The maximum of the two-photon excitation of DAPI occurs at (690 +/- 10) nm and the maximum of the fluorescence band is at (460 +/- 5) nm. In comparison, for one photon excitation the maxima are 358 nm and 461 nm, respectively. Clearly, the two photon excitation peak occurs at around twice the one photon peak and the fluorescence maximums are identical. For a few dyes the fluorescence yield was measured as

a function of the excitation intensity and a quadratic dependency was found again supporting the two-photon excitation process.

7.3.1.1 Design and Principle of operation of TOPAS (Travelling-wave Optical Parametric Amplifier of Superfluorescence)

TOPAS operation, based on a second order nonlinear optic process, is a three photon parametric interaction in noncentrosymmetric crystals. It consists of an independently pumped superfluorescence generator with two preamplifiers, and power amplifier, and employs a four amplifier stage configuration, geometrically arranged, using a single nonlinear crystal (BBO or LBO). The first stage, a low-energy preamplifier, produce a seed signal, emitting broadbanded superfluorescence. Placed in the far field of the seeder are preamplifiers (second and fourth passes) which shape the beam, acting as a small amplifying aperture. All those low-energy preamplifiers are optimised for the best spectral and spatial filtering properties. The amplification in third pass through nonlinear crystal usually is negligible. The last amplification stage (fifth pass through nonlinear crystal), usually pumped by the bulk of the available pump, boosts the energy of the parametric pulse. The power amplifier uses <90% of the pump energy and is adjusted for high conversion effiency (Energy conversion into parametric radiation up to 25 %) along with the beam quality and duration of the converted pulses. “TOPAS” emits beam with divergence close to the diffraction limit with a highly coherent pump beam and carefully adjusted pump beam diameter in the preamplification stages. The configuration has the advantage that dielectric mirrors, relatively narrow-bandwidth, are used to direct the pump beams. All the amplification stages are driven to saturation to achieve high reproducibility of generated pulses. The pump energies and intensities are adjusted for the particular pump pulsewidth and power used at each stage. Metal coated mirrors are used in the beam path of signal pulse. In this way, full tuning range can be covered without replacing the optics.

The Design of Topas is shown in Figure 7_8.

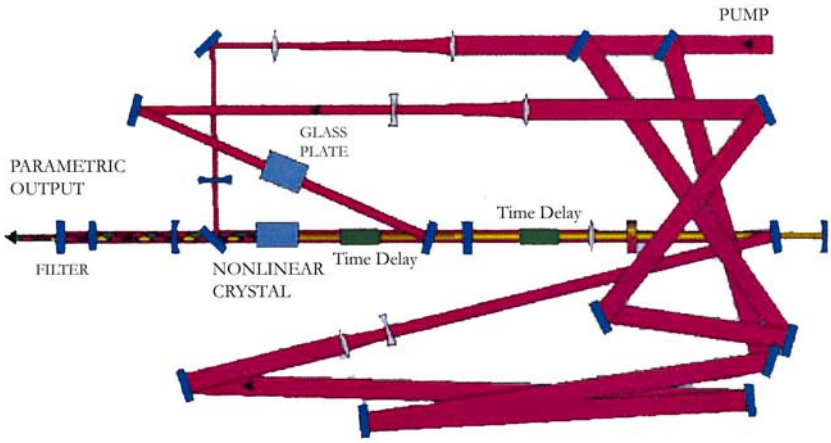

FIG 7_8 Design of TOPAS

7.3.1.2 Wavelength tuning

As high pump power is used, tuning results from changing the crystal setting angle, which is much faster than temperature tuning in non-critical phase matching crystals, but rises problems related to beam/pulse displacement which are partly solved by a quartz compensation plate. The pump wavelength and IR-absorption edge of the particular nonlinear crystal (BBO or LBO = Lithiumtriborat) restrict the tuning range of TOPAS, which is notably extended by the frequency up- and down conversion of the TOPAS output, and tuning can be done continuously across the whole accessible wavelength range and for generation of several synchronous pulses at different wavelengths by different frequency mixing schemes.

The next photo shows the two photon fluorescence spectroscopy system.

FIG 7_9 Two Photon Excitation Fluorescence Spectroscopy performed at the Institute for Optic and Quantum Electronics of the Friedrich-Schiller-University in Jena (next page)

Two Photon Excitation Fluorescence Spectroscopy

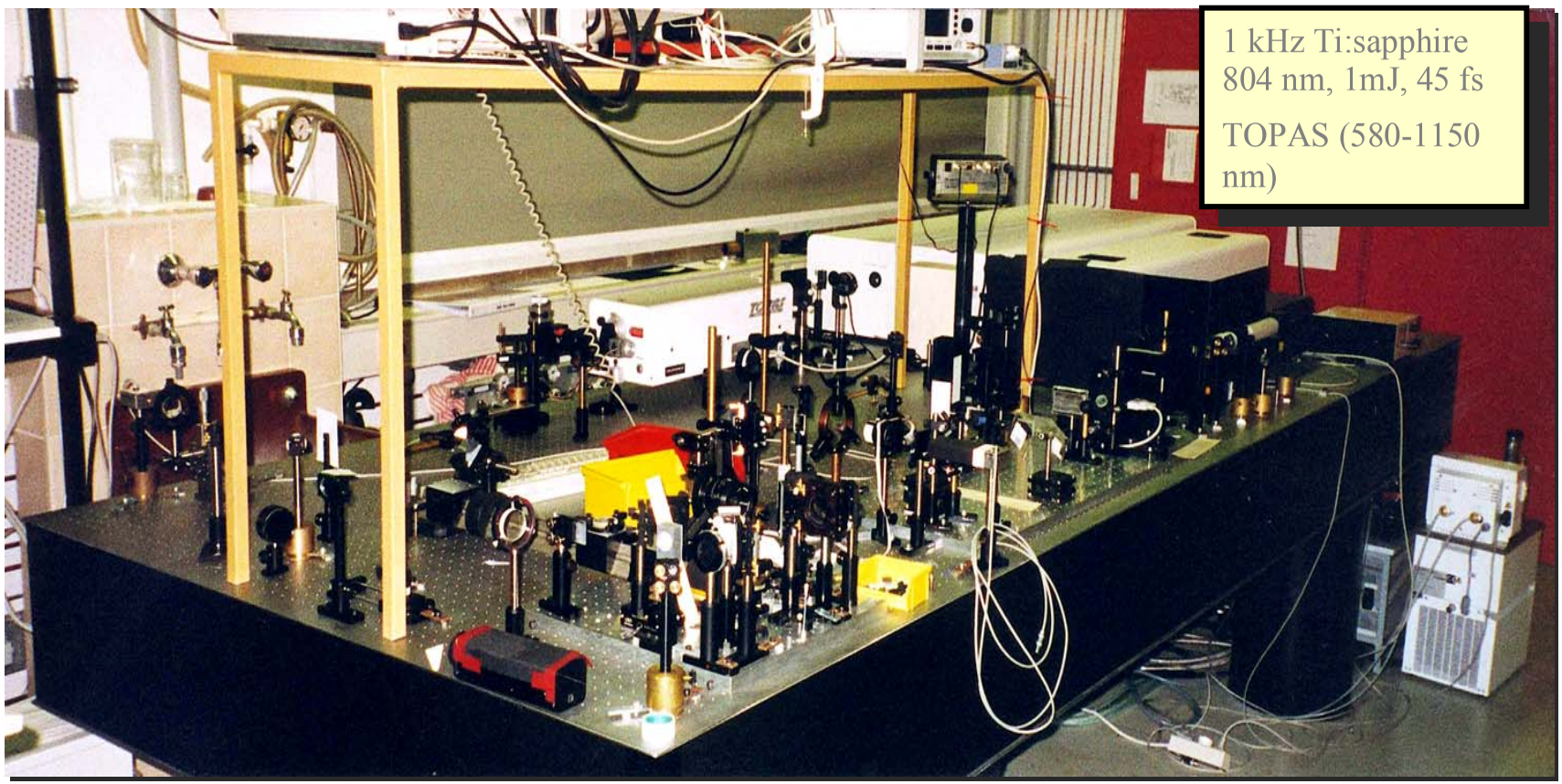

7.3.2 Used Dyes

2´, 7´-Dichlorofluorescein (DCF)
MitoTracker® Red CMXRos (MT)
Rhodamine 123 (Rho)
For details is referred to the chapter 'One Photon Spectroscopy'

DAPI (4´, 6- diamidino-2-phenylindole, dihydrochloride)
Molecular Formula: $C_{16}H_{17}Cl_2N_5$
Molecular Weight: 350.25 g/mol
CAS Number /Name: 28718-90-3 /
1H-Indole-6-carboximidamide, 2-[4-(aminoiminomethyl)phenyl]- , dihydrochloride
(A 1001) AppliChem (Darmstadt),
Stock solution: 25 mM in bidest (Storage-20°C/4°C)
Structure for DAPI

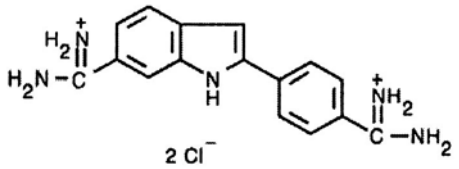

FIG 7_10 Chemical Structure for DAPI

7.3.3. Preparation for Measurements

DAPI (4´, 6- diamidino-2-phenylindole, dihydrochloride) was measured at a concentration of 25 mM diluted in water (stock solution), 2',7'- Dichlorofluorescein at a concentration of 11 µM in PBS (Dilution 1:1000 from the stock solution 11 mM in DMSO, Rhodamine 123 at a concentration of 1 µM in PBS (diluted 1:1000 from a stock solution 1mM in DMSO), Mito-Tracker CMXRos at a concentration of 1 µM in PBS (diluted 1:1000 from a stock solution 1 mM) in DMSO.
For measuring around 200 µl of the dilution were put in the dye cell (cuvette) with a width of 0,196 cm.

7.4 The point spread function

7.4.1 Coating of the object slides

Object slides were cleaned with 1% v/v HCl (35,5%), 70 % v/v Ethanol (96 %).
After being dried object slides were covered for 5 min with Poly-D-Lysine solution (0,1 mg/ml Aqua bidest, filtered before using – wear gloves!)
Object slides are let dripped off over night.

7.4.2 Coating of the cover glasses

Cover glasses selected thickness:0,17 mm ± 0,01 mm were incubated over night with 20 % v/v Ethanol / 3 % v/v Acetic acid, washed with 70 % v/v Ethanol 10 min, air dried, coated with Poly D-Lysin 30 min at 37°C, air dried dust free.

7.4.3 Preparation of the mounting media

Phosphate buffered saline: One tablet had to be put in a bit more than 100 ml of bidestilled water and autoclaved 1h at 121°C at 1 bar overpressure for 50 min in MELAG Autoklav 23. The pH of autoclaved PBS was 7,4 ± 0,1.
Mowiol: 10 g Mowiol was stirred for 24 h in 40 ml PBS, 20 ml glycerine was added and the mixture was again stirred for 24 h. Aliquots of 1 ml in Eppendorf tubes were frozen at – 20°C. (16,6% w/v Mowiol)
Vectashield was bought ready to use as a thick liquid.

7.4.4 Mounting of the fluorescent latex beads

Molecular Probes`PS-SpeckTM Microscope Point Source Kit (P-7220) was used. It contains four different colours of fluorescent microspheres, properties listed in Table 7_3:

Colour	Excitation Maximum (bead) nm	1 Photon Excitation Wavelength nm	Emmission Maximum (bead) nm	Used Optical Barrier Filter nm
Blue	360	Non appropriate	440	none
Green	505	488	515	515 ± 15
Orange	540	543,5	560	590 ± 30
Deep red	633	Non appropriate	660	620 ± 30 (2P)

Table 7_3 Excitation and Emission Maximums of the fluorescent beads and used excitation wavelength (for 2P excitation it was always 798 nm) and optical barrier filter

Neither when applying one photon excitation nor two photon excitation laser scanning confocal microscopy, the blue fluorescent microspheres could be measured with a 470 ± 15 nm optical filter for the emission radiation.

The diameter of one microsphere is 175 ± 5 nm. McNally (1999) proposes for conventional fluorescence microscopy that it should be a third of the Rayleigh Criterion, i.e. of the two-point resolution limit. The minimum distance which can be resolved for conventional microscopy it is 1.22 λ / NA, for confocal microscopy 0.92 λ / NA with λ, the emission wavelength and NA, the numerical aperture of the objective. (NA(oil immersion objective, 40 x) = 1.3, NA(water objective, 60 x) =1.2. The beads were mainly used for confocal OPEor TPE LSM. The used emission filters had wavelengths between 515 nm and 620 nm. Hence the beads should have a diameter of 140 ± 18.5 nm. The Huygens System 2 Owner´s Guide recommends beads below 250 nm diameter.

Each aqueous suspension of the fluorescent microspheres has a density of 3 x 10^9 beads/mL. Before dilution the solution was shaken by a Vortex.

When the mounting medium was Phosphate buffered saline (PBS) the suspension was diluted 1:6 fold with PBS and a drop of this dilution (2,5 µl) was put on a coated microscope slide, covered with a coated coverglass with corrected thickness of 0,17 ± 0,1 mm, en-

closed with nail enamel. When the nail enamel was air-dried the sample was imaged with the confocal microscope with the appropriate sampling distance.
For Mowiol and Vectashield the aqueous suspension of the fluorescent microspheres were diluted 1:300 in Aqua bidest. 10 µl were put on the cover glass and air-dried. Then 2 µl of the Mounting medium was put onto the microslide and covered by the cover glass. When using Vectashield the cover glass was immediately surrounded by nail enamel. Specimen in Mowiol had to dry overnight before surrounded by nail enamel.

7.4.5 Requirements for recording bead images: Nyquist Theorem

A scanned and digitally recorded specimen is represented by a sampled function, i.e. light intensity is known only at positions where samples have been recorded. A small inter-sample distance is needed to obtain images with high resolution and with all information present in the signal is represented in the samples. The Nyquist *rate* is the minimal sampling density at which an image or signal must be recorded (sampled). However, because of the limited optical resolution, the (inter)sampling density has neither to be below a certain limit. If for confocal data aquisition, the Nyquist criterion is taken into consideration the analogue image information should be completely transferred to the digitised image. Between the highest spatial frequency of interest in the data and the minimum rate at which samples must be taken if they are to record all the possible significant variations in that signal accurately, there is a fixed relationship: The sampling frequency for nonperiodic data should be at least twice or 2.3 times higher than the highest frequency present in the signal that is to be sampled.
Undersampling, i.e. a sampling rate lower than the Nyquist rate brings about a serious problem as spatial frequencies get ‘aliased’, i.e. fine details in the object get represented by structures at a different scale. Aliasing artifacts emerge in different ways, e.g. undersampling a regular pattern creates low frequency waves, sampling geometrical objects (having an infinite Nyquist rate) nearly always results in ‘jagged’, for instance lines in a digitised image.
Using the spatial frequency bandwidth for a (perfect) confocal microscope, the Nyquist rate can be expressed as it is described in Porwol et al. in Methods Enzymol. 307 (1999) with one correction.

The lateral sampling distance for the confocal microscope perpendicular to the optical axis is:

$$\Delta_x = \frac{l}{8n\sin\alpha} \qquad (1)$$

for incoherent imaging.

In the depth dimension the corresponding distance, i.e. the distance between the recorded sections along the optical axis can be expressed as

$$\Delta_z = \frac{l}{4n(1-\cos\alpha)} \qquad (2) \qquad \text{or}$$

$$\Delta_z = \frac{l}{8n\sin^2\left(\frac{\alpha}{2}\right)} \qquad (3) \qquad \text{(Kriete 1992)}$$

with $\alpha = \arcsin(NA/n)$ as the numerical aperture is $NA = n\sin\alpha$,

with n the refractive index of the mounting medium,

λ the used wavelength , Porwol et al. propose of the emission light (that means the middle of the used optical filter).

Perpendicular to the optical axis the Nyquist rate is only dependent on the N.A. and the emission wavelength.:

$$\Delta_x = \frac{l}{8n\sin\alpha} \quad \text{and} \quad \alpha = \arcsin\left(\frac{NA}{n}\right) \qquad (4)$$

$$\Rightarrow \Delta_x = \frac{l}{8n\left(\arcsin\left[\frac{NA}{n}\right]\right)} = \frac{l}{8n\, NA/n} \qquad (5)$$

$$\Rightarrow \Delta_x = \frac{l}{8NA} \qquad (6)$$

The refractive indices n were determined with a refractometer at room temperature 23°C and represented in Table 7_4.

Medium	Mowiol	PBS	Vectashield	Aqua bidest	Immersion oil
n	1.4025	1.334	1.452	1.508	1.334

Table 7_4 The refractive indices of the used mounting and immersion media

The mounting media are Mowiol, PBS, and Vectashield. The objective lens (immersion media) are Aqua bidest. and Immersion oil.

E.g. the sampling distance Δ_x for the green fluorescent microspheres, TPECLSM was:

Emission maximum and middle of the emission filter: 515 nm

Mounting medium: PBS, refractive index $n_{(PBS)}$1.334

using 2 Photon Excitation wide field and

the water objective, Magnification: 60x,

Δ_x = 1/8 * 515 nm : 1.2 = 53.646 nm, the sampling distance

Δ_z = 515 nm : (4 * 1.334 * (1 – cos (arcsin(1.2 / 1.334)) = 171.373 nm.

The digitisation with the confocal LSM took place with a bit shorter sampling distance, i.e. slightly oversampled to be sure not to undersample the probe.

⇒ The applied sampling distances were Δ_x = 53.516 nm, Δ_z = 150 nm.

As we used a Piezo instead of the z-drive along the z-axis multiples of 50 nm could be taken as sampling distance Δ_z, therefore in this case Δ_z was 150 nm.

For one photon excitation, the Huygens System User´s Guide recommends to take for λ the excitation wavelength to be on the safe side as the local resolution in the confocal microscope depends 50% on the excitation light (first pinhole) and 50 % on the emission light (second pinhole). As the set up of the confocal microscope has its limits of precision a compromise was taken. The used sampling densities, and the performed optical sections for the measured and theoretical Point Spread Functions are listed in the following Tables 7_5 and 7_6:

Exc (nm)	**Objective (x)**	**r (Pinhole) (µm)**	**Medium**	**EmFilter (nm)**	**Axis**	**Sampling distance (nm)**	**Pixel exp (the)**
798	60	WF	Vectash.	515 ± 15	x, y z	55.469 200	96 80 (78)
798	60	WF	Mowiol	590 ± 30	x, y z	60.937 200	90 80
798	60	WF	PBS	515 ± 15	x, y z	53.516 150	98 96
798	60	WF	PBS	590 ± 30	x, y z	58.203 150	90 96
798	60	WF	PBS	620 ± 30	x, y z	64.453 200	84 70

Table 7_5 Sampling distances for PSFs for TPE LSM

Exc (nm)	**Objective (x)**	**r (Pinhole) (µm)**	**Medium**	**EmFilter (nm)**	**Axis**	**Sampling distance (nm)**	**Pixel exp (the)**
488	40	10	Vectash.	515 ± 15	x, y z	49.219 150	80 (76) 60
543.5	40	10	Mowiol	590 ± 30	x, y z	56.250 150	80 (76) 64
488	60	10	Vectash.	515 ± 15	x, y z	53.516 200	70 50
543.5	60	10	Mowiol	590 ± 30	x, y z	58.203 200	72 56
488	60	10	PBS	515 ± 15	x, y z	48.828 150	80 (78) 64
543.5	60	10	PBS	590 ± 30	x, y z	61.328 150	70 70
543.5	60	25	PBS	590 ± 30	x, y z	61.328 150	80 72
543.5	60	WF	PBS	590 ± 30	x, y z	121.875 350	384 60

Table 7_6 Applied sampling distances for one photon excitation CLSM

The sampling densities given by Equations 2 and 6 represent what is needed to exactly reconstruct the original, non-sampled, image function. In practise, the spatial frequencies close to bandwidth limit only contribute little to the image signal and the highest spatial frequencies are attenuated due to abberations and other factors in a real imaging system. Therefore in many practical situations larger sampling distances than those given by the equations can safely be used, which was done during cell imaging. A benefit of using larger inter-sampling distances is that light from a larger specimen area can be collected for each pixel value, thereby giving an improved signal-to-noise (S/N) ratio. However a trade-

off between quality and image size cannot be made. (Kriete 1992, Pawley 1995, Porwol et al. 1999, Scientific Volume Imaging 1997)

7.4.6 The microscopic Point Spread Function

The prepared specimen were measured after having adjusted the beam of laser light by the micrometer screws for x, y direction for optimal illumination of the specimen. The micrometer screw of the z direction had been adjusted once and should not be changed during the daily operation. A slide of a fluorescent stained cut of a pine tree.... was used for optimisation.

The field z was chosen for 64 optical slices, i.e. 64 pixel.

The region (field) of interest (zoom) was chosen for 512 x 512 pixel.

The focal plane of the microscope had been adjusted with the middle (zero) of the z motor, so that the middle of the beads, when focused by the inverse microscope in the epi illumination fluorescence mode were almost in the middle of the z series when switching to the confocal mode.

Two different objective of the inverted microscope ECLIPSE TE 300 from Nikon were used to image the point spread functions:

Objective lens system	Magnification	NA	Immersion medium	Working Distance (mm)	Cover glass thickness (mm)
Plan Fluorite	40 x	1.3	Oil	0.2	0.17
Plan Apochromat	60 x	1.2	Water	0.22	With cover glass correction

Table 7_7 Used Objectives for measuring the psf

Both objectives are ‘infinity corrected’ (∞), i.e. the intermediate image could be located at infinity, as the *rays of the light beam* leaving the objective are *parallel*. They can be used for differential interference contrast microscopy (DIC - H) with a module H for the condensor. They are corrected for field curvatur, giving a flat, i. e. planar, image of the sample (Plan). Both objectives are *chromatic aberration free*, the Fluorite (Fluor) objective is corrected for two wavelength (green and red), bringing the focus points of rays with various colours increasingly low, the Apochomate (Apo) objective is even corrected for three

wavelength (Fraunhofer lines: green, red, blue) have a magnification power of from 40 x a 60 x. The oil objective had to be used for the observation of the samples with a cover glass 0.17 mm thick to reduce spherical aberration. Therefore we used corrected cover glasses of 0.17 mm ± 0.1 mm thickness and then 0.17 mm was chosen as cover glass correction for the water objective. The *lens aperture* of both objectives are *very narrow* to have best performing quality, the highest possible NA until now is 1.4, because of the needed working distance. (Castano et al. 1998)

7.4.6.1 Dynamic Range & PMT Gain and Offset: Signal optimisation

The image dynamic range is the ratio between the brightest structure of interest and the dimmest. The dynamic range of the confocal microscope is limited by the 256 levels of the 8-bit analogue to digital converter (A2D, the video frame grabber), which takes the optical signal from the PMT and converts it into a number (0 to 255). (The dark adapted eye has a dynamic range in excess of 1 to 10000.)

Because of the limited dynamic range of the A2D converter it is crucial to set the minimum and maximum levels of the image to match the fixed range closely. Good matching was achieved by carefully setting the offset and gain of the PMT, so that it output used the fixed range of the A2D fully. The maximal pixel value could be determined by a histogram.

If the signal was too weak, there were several possibilities to increase it. As increasing the PMT gain roughly linear increase the photonic current, but exponential increase electronic noise, it was preferred to increase the pixel dwell time for measuring the PSF (Minimum: 3.0 µs, Maximum: 20 µs, for the PSF about 6 µs were recommended, but cell imaging is also very sensitive to increased pixel time because of photobleaching). The signal will be integrated over a longer time period, resulting in a better output. In certain limits, the laser power could be increased (e.g. from 5 to 5,5 Watt), which gives less noise, but increases the rate of photo-bleaching (and the risk of bleed through, cross talk if scanning with two channels - only in cell imaging).

On the other hand, if the laser power was too high, a neutral density filter could attenuate the laser signal. Often the laser power had to be dimmed and the pixel dwell prolonged in order to have a good signal output.

In general signal to noise ratio depends on the dye concentration and its quantum yield, the laser power, the pinhole size, the PMT voltage, the signal averaging and integration.

The imaged confocal data were transferred by FTP (File Transfer Protocol) to the workstation Silicone Graphics Octane (SGI)

7.4.6.2 Averaging the bead image

For typical confocal conditions beads should be smaller than 50 nm diameter in order to be used directly as PSF, but because of Signal to Noise problems sufficiently bright objects of this size does not exist, because of limited dynamic range of the A2D converter and bleaching effects which limit the averaging count between 32 and 64.
This situation is remedied by averaging over a number of carefully aligned bead images. This is only possible with beads of sufficient strength, limiting the minimum bead size. Large beads, however, induce more uncertainty in the PSF reconstruction procedure. The used beads are a good compromise between those contradictory demands. If development in fluorescent dyes, anti bleaching agents and microscope data acquisition systems progress, recording of smaller beads with a sufficient S/N ratio could become possible.
Signal averaging or integration is done by adding scans of the same object together and dividing the result for each pixel by the number of scans. In principle, noise being random, will approach zero with increasing number of scans averaged, while the signal being a finite value will approach the finite value. Signal to noise ratio will increase in proportion to the square root of the number of scans performed, e.g. averaging four scans will yield an image with half the noise compared to a single scan image. Therefore, several images from different positions in the specimen were taken in order to have enough beads to get at least a certain level of signal to noise ratio. For the sake of simplicity it is assumed that the PSFs of the coherent optical system are fairly constant over the whole confocal image, even they may vary from place to place in the specimen.
Some of the beads which were averaged to determine the experimental PSF, as they are presented in the Huygens System 2 are shown in Figure 7_11a in MIP and in Figure 7_11b as a x,y slice in the middle of the z- extension. In this example four beads are imaged, but only three are accepted, because the biggest one is overdone. Huygens2 count also the background as one object, so the program will accept 3 out of 5. For these beads both the

distance to each other and to the border of the image stack of z-slices is far enough that there is no disturbance or cut-off of the signal.

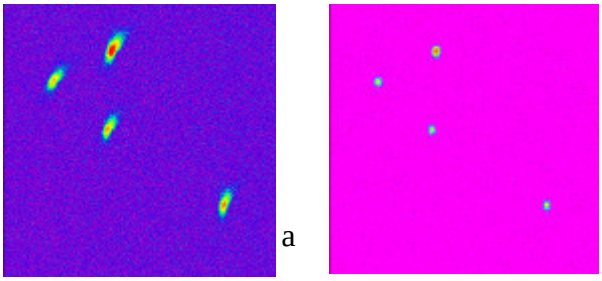

FIG 7_11 Green fluorescent microspheres (Latex beads) of 175 nm imaged with the 2P Laser Scan Confocal Microscope viewed in the Huygens2 System

a) Overview of the volume image along the z-axis (MIP)

b) The section in the middle of the z-axis (orthogonal slice)

Maximum Intensity Projection (MIP): For each vertical column of voxels a ray is traced and corresponds to a pixel in a in the 2D Projection Image: The largest value is selected and assigned to the screen image.

7.4.6.3 Reconstructing the PSF from an averaged bead image

As mentioned images of the beads cannot be directly used as PSF because the size of the bead will broaden the bead image with respect to the PSF. Only with extremely small beads this broadening could be neglected, which is not the case, therefore the PSF had either to be reconstructed from the averaged bead image.

This deconvolution is possible as the bead image is the result of a convolution of the *unknown* PSF with the *known* object model, because more *a priory* information is available. The type of microscope (confocal, conventional) and other important microscopic parameters like the finite-sized detector pinhole, high numerical aperture which were to be specified in Huygens System 2 (see below) imposes constrictions on the shape of the PSF. The axial resolution of a confocal microscope is roughly proportional to the square of half-aperture angle. ‘The key to obtain a theoretical PSF of a confocal microscope is the calculation of the intensity distribution at some point in the focal region of the objective.’ (Van der Voort, Strasters 1995, page 170) This involves evaluation of an integral over all amplitudes on the reference sphere on the basis of electromagnetic diffraction theory. The theoretical PSF is the product of the (1)computed excitation distribution near the focus of a

perfect lens and the (2) computed detection distribution for an (i) infinitely small pinhole at the effective emission wavelength convoluted with the (ii) pinhole geometry, i.e. i ⊗ ii is second element of the multiplication. (Van der Voort, Strasters 1995)

A bead model with a theoretical PSF is computed automatically when starting the tool 'Reconstruct PSF'. The Point Spread Function (PSF) was reconstructed from bead images by following the User´s Guide of the Huygens System 2 for `How to get a microscopic PSF´. First a number of images at the used microscope settings were recorded, then the "average spheres tool" (Average spheres with final baseline correction for the last image) was used to align and average the individual bead images from the files. The parameters to be specified for this step were: the bead *radius*, and the estimated signal-to-noise ratio. Then more parameters had to be specified. The bead image above were taken under the following conditions:

Geometry (nm)	
x, y sample size:	48.828 nm
z sample size:	150.00 nm
Optical parameters	
Microscope type:	Wide field
Numerical aperture:	1.2
Pinhole radius (backprojected):	-
Refractive indexes:	
Lens (Water):	1.334
Medium:	1.334
Parameter for channel:	
Excitation wavelength:	798 nm
Emission wavelength:	515 nm
Excitation photons:	2

For each measurement the parameters were specified, in particular

the x,y,z sampling distance; the microscope type (confocal for 1P, wide field for 2P), the Numerical Aperture NA (1,2 for the water , 1,3 for oil immersion objective),

the backprojected pinhole radius of the circular detector aperture $r_b = r_{phys} / (m_{obj} \cdot m_{system})$

with r_{phys}, the physical pinhole radius: 10 µm in general or 25 µm for the big pinhole,

m_{obj}, the magnification of the objective = 40 x or 60 x,

m_{system}, the magnification of the system = 1

($r_{b(40x)}$ = 250 nm for the small, 625 nm for the big pinhole,

$r_{b(60x)}$ = 167 nm for the small, 417 nm for the big pinhole),

for refractive indexes see Table 7_4

the excitation wavelength 798 nm for 2P, 488 nm or 543 nm for 1P,

the emission wavelength, i.e. the middle wavelength of the used optical filter, 470 nm, 515 nm, 535 nm, 590 nm or 620 nm, and

the excitation photons 1 or 2.

The mean background, i.e. the average background in a non-object area in the image, including the baseline and the average background noise was estimated by the analysis tool "Estimating background", and the maximal voxel value determined by the analysis tool "Compute histogram" or by the view tool "Image statistics"

The signal to noise ratio was calculated with the following formula

$$\frac{S}{N} = \sqrt{\frac{\max voxelval}{background}} \qquad (7)$$

This S/N ratio should be beyond 20 for good results. The usual range is 30 (averaged set of poor confocal bead images) to 60 for a single bead image recorded with a high quality WF microscope.

Then the PSF was reconstructed and stored in ICS image format. With the parameters specified for the experimental point spread function (PSF) the theoretical PSF was computed.

As the reconstructed experimental PSF should completely determine how images are formed from fluorescent objects in the used microscope, a control was done. Beads used for reconstructing the 2P PSF from green fluorescent bead images in PBS were deconvoluted with the reconstructed PSF itself in order to see if the obtained image corresponds to reality.

Those generated experimentally measured PSF were used to deconvolve the images of the human hepatoma HepG2 cells.

7.5 Tissue culture and Staining of the human hepatoma Hep G2cells

7.5.1 Cultivation of HepG2 cell line

The human hepatoma carcinoma cell line HepG2 (ATCC HB 8065) was delivered frozen at the 107th passage. The cells were defrozen and maintained in RPMI1640 medium, without Glutamine, Phenol red 5 mg/l, supplemented with 10 % of BMS and 1% of Penicillin /Streptomycin (10000 IU/10000 µg/ml). Alternatively of serum, 2 mM stable Glutamin (N-acetyl-L-alanyl-L-glutamine was added. Cells were routinely cultured in tissue culture flasks at 37 °C in an incubator containing 5 % CO_2 in humidified air. Cells were passaged once a week to 25 cm² culture flasks with an initial number of 1 x 10^5 cells in 5 ml RPMI the medium was renewed (5-7 ml) every two to three days. After 3 to 11 passages, cells were used for experiments (sample preparation).

7.5.2 Preparation of the cell specimen

Cover glasses with a diameter of 12 mm were coated with 300 µl of Poly-D-Lysin (0.1 µg/µl in bidest, steril filtered), incubated 30 min at 37°C, washed two times with sterile PBS

The cells after being washed two times with PBS or medium were detached with Trypsin-EDTA (3 ml per 250 ml tissue culture flask). To speed up the detachment the flask was put for about 10 min in the incubator and as soon as the adhesion had gone the process was stopped with medium containing BMS. The cells were sown in the four-well dishes with a density of 0,2 to 0,3 x 10^5/ml. Medium was added and the cells were grown 24 – 72 h, approaching confluence, before being used for staining.

7.5.3 Dyes

The stock solutions of the dyes and the handling solutions were prepared as it is described in the following paragraphes.

7.5.3.1 DAPI, (4´,6-diamidino-2-phenylindole dihydrochloride)

Detailed structure is shown in paragraph 'Two photon fluorescence spectroscopy'
Stock solution: 25 mM in Aqua bidest (storage -20°C/4°C),
1:5 diluted in DMSO (5 mM), 1:200 diluted in PBS, final concentration: 25 µM
DAPI is an organelle specific dye for nuclear DNA.

7.5.3.2 2',7'-dichlorodihydrofluorescein diacetate (2',7'-dichlorofluorescin di-acetate;) H_2DCFDA (cell permanente)

Molecular Formula: $C_{24}H_{16}Cl_2O_7$
Molecular Weight: 487.29 g/mol
(D-399) Mobitec (Göttingen)
CAS Number/ Name: 4091-99-0 /
Benzoic acid, 2-[3,6-bis(acetyloxy)-2,7-dichloro-9H-xanthen-9-yl]-
11 mM Stock solution in DMSO, final concentration in PBS: 11 µM
Structure for H_2DCFDA

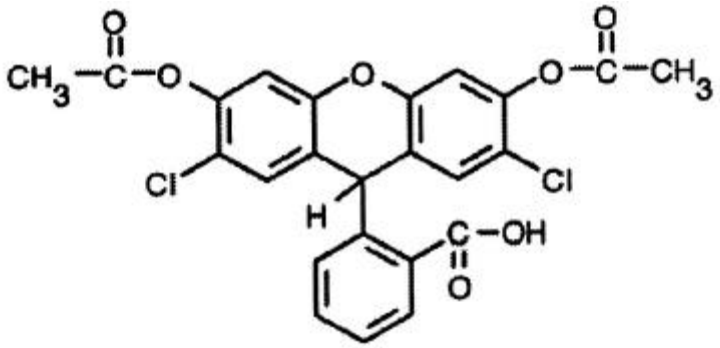

FIG 12 Chemical Structure for H_2DCFDA

2´,7´-Dichlorodihydrofluorescein-diacetate, also known as dichlorofluores*cin*, is the di-acetate derivative of 2´, 7´-dichlorodihydrofluorescein and is quite stable. Intracellular the acetates are cleaved by endogenous esterases, releasing the corresponding dichlorodihydro-fluorescein derivative, the chemically reduced form of 2´,7´-dichlorofluorescein, a color-less, nonfluorescent leuco dye. It has been reported that H_2DCF is not directly oxidised by either superoxide or free hydroxyl radical in aqueous solution.

The hypothesised reaction mechanism for the oxidation of H_2DCF to DCF is the same as it is explained in the next paragraph for Dihydrorhodamine 123. The reaction takes place at the equivalent bonds. Fluorescein belongs to the Xanthen (Phtalein) (Dibenzo-γ-pyran) pigments.

7.5.3.3 Dihydrorhodamine 123 (DHR)

Molecular Formula: $C_{21}H_{18}N_2O_3$

Molecular Weight: 346.38 g/mol

CAS Number/Name: 109244-58-8 /

Benzoic acid, 2-(3,6-diamino-9H-xanthene- 9-yl)-, methyl ester

(D-632) Mobitec (Göttingen)

25 mM Stock solution in DMSO, handling concentration in PBS: 25 µM,

final concentration: 10 µM (150 µl PBS and 100 µl handling solution of DHR)

Structure for DHR

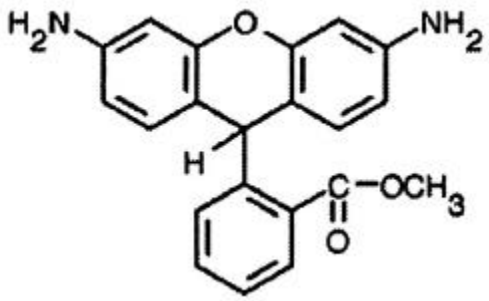

FIG 7_13 Chemical Structure for DHR

Dihydrorhodamine 123 is the uncharged and nonfluorescent reduction product of the mitochondrion-selective dye rhodamine 123. This leuco dye diffuses passively across most cell membranes and is oxidised to cationic rhodamine 123, which localises in mitochondria. The selective uptake is dependent on the mitochondrial membrane potential. The fluorescence is quenched by a high reduction potential and increases with mitochondrial depolarisation. (Ehleben et al. 1997) Like H_2DCF, dihydrorhodamine 123 (DHR) does not directly detect superoxide, but rather reacts with hydrogen peroxide in the presence of peroxidase, cytochrome *c* or Fe^{2+}. The proposed chemical conversion of the colorless DHR to Rhodamine 123 is shown in Figure7_14. Rhodamine is a Dialkylaminoxanthen and can be obtained by condensation of 1 mole Phthalacid anhydride with 2 mole of a 3-Aminophenol.

7.5.3.4 MitoTracker â RedCMXRos (MT)

For details see paragraph ‘One Photon Fluorescence Spectroscopy’
Stock Solution: 1 mM in DMSO (50 µg powder were solved in 94 µl DMSO)
Solution for handling in PBS: 10 µM
Final concentration: 400 nM

MitoTracker RedCMXRos, a rosamine, is a cell-permanent mitochondrion-selective fluorescent stain that contains a mildly thiol-reactive chloromethyl moiety. During labeling MitoTracker passively diffuses across the plasma membrane and accumulates in active mitochondria.(of living cells) There it can react with accessible thiol groups on peptides and protein to form an aldehyd-fixable conjugate. The dye is retained after passing the membrane, therefore double-labelling is possible. The uptake is dependent on the mitochondrial membrane potential.

7.5.4 Staining procedure of the human hepatoma (HepG2) cells

The cells were grown in tissue culture up to 72 h on a coverslip (corrected thickness of 0,17 mm). The staining procedure always started by staining the mitochondria by Mito-

Tracker RedCMXRos. 240 µl of the RPMI medium in which the cells were grown were kept back, 10 µl handling solution of MitoTracker RedCMXRos was added to obtain a final concentration of 400 nM. The cells were stained 30 min at 37°C in an (dark) incubator containing 5 % CO_2 in humidified air. The cells were washed three times with preheated (37 °C) PBS. Then either the cells were stained with 10 µM Dihydrorhodamine (250 µl) 25-30 min at 37 °C in an incubator containing 5 % CO_2 in humidified air or the cells were stained with 11 µM H_2DCFDA (250 µl) 45 min at 37°C under the same conditions. Again the cells were washed three times with preheated PBS.
If the nucleus was stained, cells covered with 199 µl PBS and 1µl of 5 mM DAPI were put in the well of a four-well plate. Staining took place for 5-10 min at room temperature in the darkness. The cells were washed three times with preheated PBS (20 °C).
After the cells being stained with two or three dyes and being washed, the cover glass with the cells was put inversely on an object slide. The cover glass was immediately surrounded by nail enamel. The microscope slide with the specimen was put in the dark until the nail enamel became solid, the surrounding with the nail enamel was repeated once to be sure that the sample will not run dry during confocal microscopy and to have optimal conditions for the cells to be examined. As soon as the nail enamel became solid, the cells were imaged, the confocal microscope being optimal adjusted in advance.

7.5.5 Ideal properties for dyes

Properties for an ideal agent for localising endogenous ROS and to detect changes in concentration and production rate of specific reactive oxygen species would be: (a) cell membrane permeability such that significant intracellular concentrations are achieved, (b) minimal cellular toxicity, (c) conversion from the nonfluorescent to fluorescent form of the probe, (d) intracellular sequestration of the fluorescent, oxidised form of the probe. a and b are required for all (intra)cellular dyes which are used for visualisation of living cells.
The esterified form of dichlorofluorescin, dichlorofluorescin diacetate, crosses cell membranes and then is deacetylated by intracellular esterases. The resulting compound, dichlorofluorescin, should be trapped within the cell and is susceptible to reactive oxygen species-mediated oxidation to the fluorescent compound, dichlorofluorescein. Already used for detecting H_2O_2 revealed that the oxidation rate with H_2O_2 alone was slow. H_2O_2 medi-

ated oxidation is markedly increased in the presence of iron. (Royall, Ischiropoulos 1993 and references therein)

7.5.6 Oxidation Mechanism of H_2DCF and DHR by ROS to DCF and RHO

H_2DCF and DHR have a great homology in chemical structure shown in Figure7_14a. Therefore the same chemical conversion of colourless dihydrorhodamine 123 and colourless 2',7-dichlorodihydrofluorescein can be proposed.

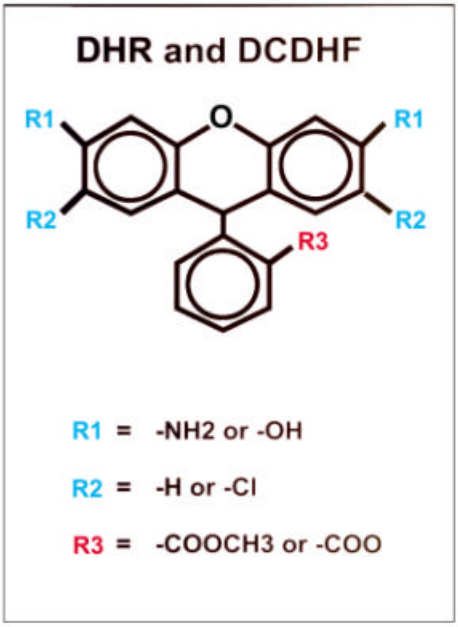

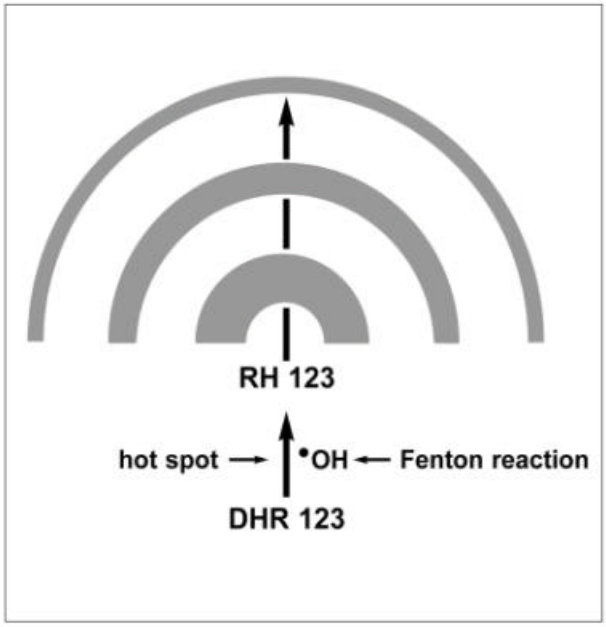

FIG 7_14a: Chemical structure of DHR and DCF *FIG 7_14b*: Diffusion within the tissue of oxidised dye (Porwol et al. in press 2001)

DHR 123 and 2',7'-DCF are getting oxidised by ROS. DHR 123 in particular scavenges $^{\bullet}$OH generated from H_2O_2 in an iron-dependent perinuclear Fenton reaction (see below). Thereby it is converted into fluorescent rhodamine 123 (H_2DCF in DCF). The oxidation of both dyes is chemical irreversible and is mediated by a Fenton reaction generating hot spots of fluorescent rhodamine (RH) 123 (or 2',7'-Dichlorofluorescein) which diffuses into the tissue. (Figure7_14b)

The reaction with H_2O_2 is rather slow under ambient conditions. The addition of iron compounds either free or bound (cytochrome c) yields in a fast oxidation to the fluorescent indicator.

Therefore the following reaction mechanism is proposed for the conversion of nonfluorescent dihydrorhodamine 123 to rhodamine 123 (and equivalent for the conversion of nonfluorescent 2',7'-dichlorodihydrofluorescein to 2',7'-dichlorofluorescein): The reaction of $^{\bullet}OH$ with dihydorhodamine 123 under production of water yields a tertiary free radical. This is known to be rather stable. The radical is able to rearrange the π-electron system (outlined by arrows on the bottom right hand side of Figure 7_15) The electron in excess can either be abstracted by another $^{\bullet}OH$ resulting in an hydroxyl anion OH^- or by hydrogen peroxide generating additionally an hydroxyl radical. The latter reaction can be the starting point for a new cascade. (Ehleben 1997)

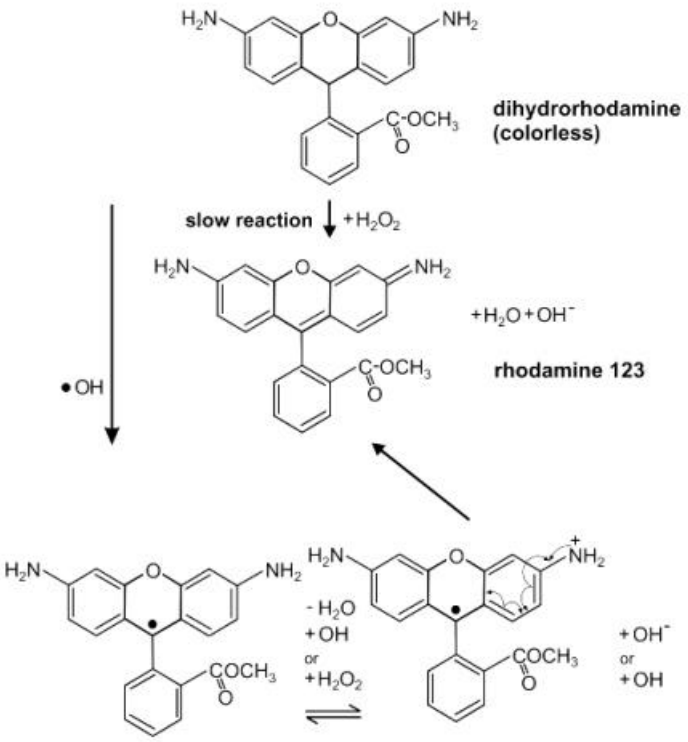

FIG 7_15: Proposed chemical conversion of colorless dihydrorhodamine 123 to fluorescent rhodamine 123 in reaction with H_2O_2 mediated by $^{\cdot}OH$. (Ehleben et al. 1997)

7.6 The Laser Scan Microscope System

For one and two-photon fluorescence imaging the compact confocal microscope system of Nikon (Personal confocal microscope (PCM) 2000) was used.

7.6.1. The one and two photon excitation units

The one photon excitation (OPE) continuous wave laser light from the Helium Neon laser and / or Argon Ion laser goes directly through a glass fiber to the Scan head with one excitation and two emission channels connected to an inverted microscope.
The two photon excitation (TPE) pulsed laser unit consists of three components: The Diode-Pumped Laser (Verdi^{TM}V-5), the Titanium-Sapphir laser (The Coherent Mira Model 900-F Laser) and the MIRA-GDC (Grating Dispersion Compensator). The laser beam is divided in two parts in the GDC by a dichroic mirror. One part is used for beam diagnostics, eg. for determination of the puls width by an autocorrelator and to monitor spectroscopic parameters like wavelength spectrum of the pulsed laser by the laserspectrometer APE, Wavescan VIS. (see beam diagnostics below), the other part of the laser light will pass through a glass fibre from the GDC to the Post Fibre Compressor (PFC) which is pegged to the Scan head when using two photon excitation.

The following pages are illustrating the used laser microscope system for one and two photon excitation fluorescence imaging. First a photo of the two photon excitation LSM is shown in Figure 7_16, then an schematic drawing of the TPE confocal laser scanning microscope using the PCM2000 scanning head coupled to conventional (1P) or pulsed (2P) sources using the same optical path within scanhead and microscope is demonstrated in Figure 7_17.

FIG 7_16 Two Photon Excitation Laser Scan Microscopy (see next page)

Two Photon Excitation Laser Scan Microscopy

Argon
Pump Laser
Verdi

Group
Velocity
Control
(GVC)
Mira GDC

Output
Coupler

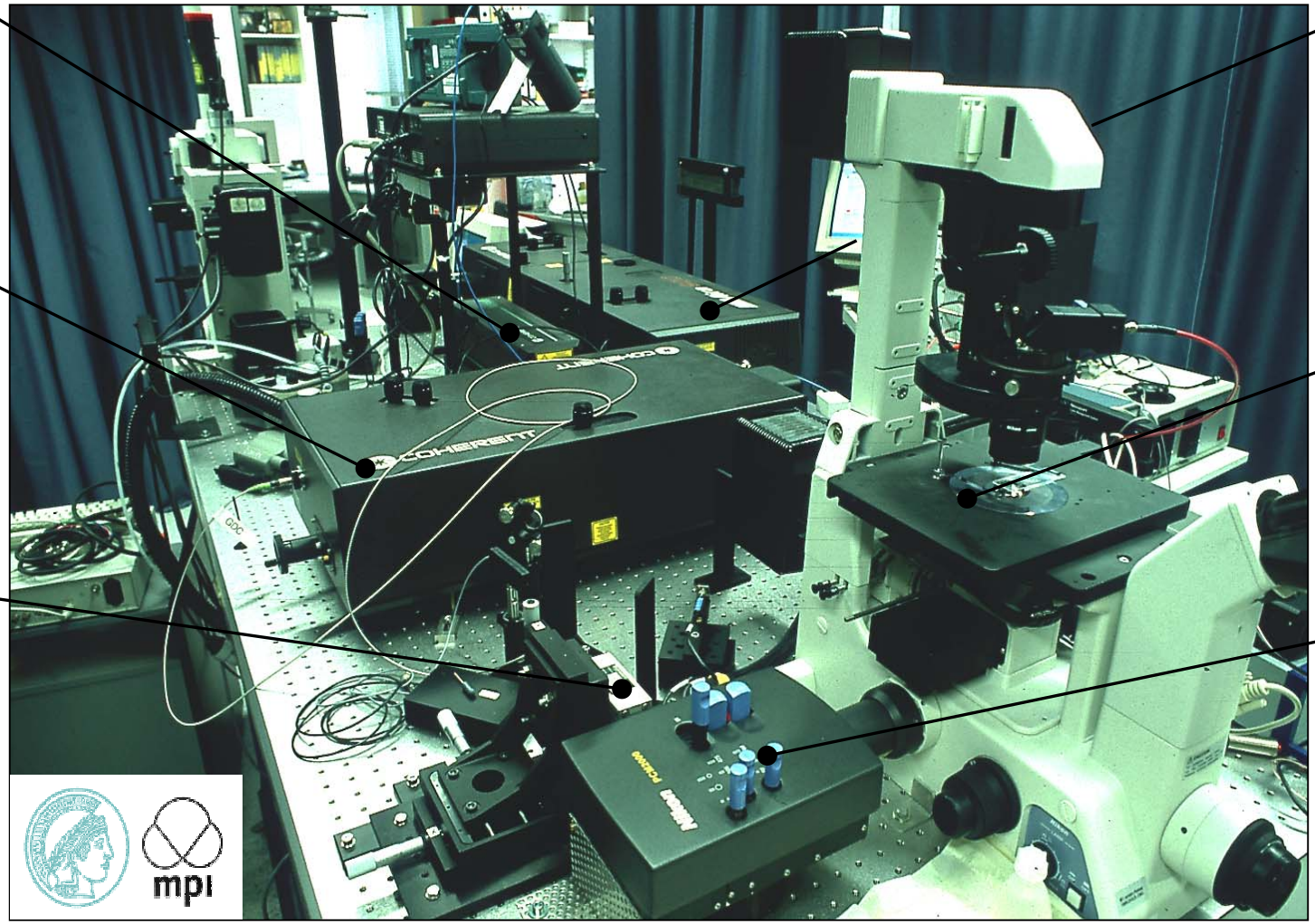

Modelocked
Ti:Sa Laser
Coherent
Mira 900

Inverted LSM
Nikon
PCM2000

Scan Head

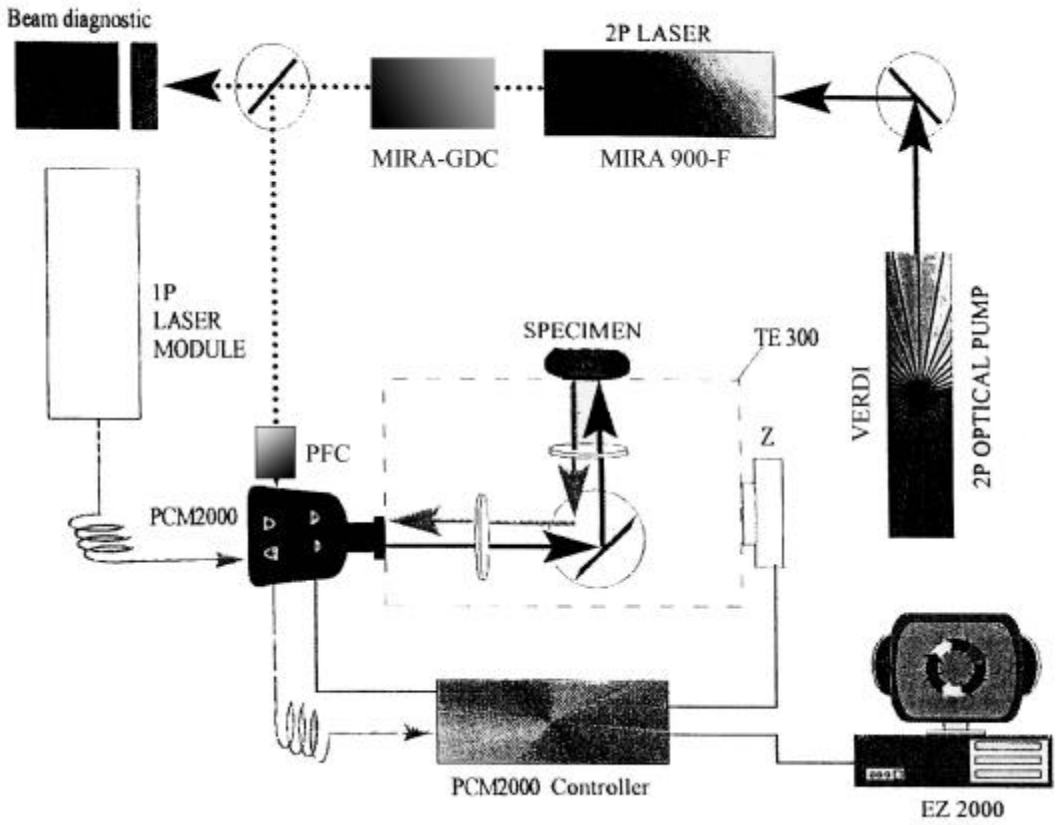

FIG 7_17 Schematic drawing of the TPE confocal laser scanning microscope using the PCM2000 scanning head coupled to conventional (1P) or pulsed (2P) sources using the same optical path within scanhead and microscope. The excitation at PCM2000 input can be easily switched to single photon excitation using single-mode fibre delivery. Dichroics, pinholes, and filters can be inserted or removed using manual sliders. PCM2000 electronics, governing scanning and acquisition, is completely computer controlled. Beam diagnostics is performed using the laser spectrometer APE, wavescan VIS, an optical power meter from Newport, and an autocorrelator. (Diaspro et al. 1999)

7.6.2 One photon excitation

7.6.2.1 The Argon-Ion Laser

A ring discharge takes place in a rectangular tube with two different diameters. The laser path has a smaller diameter than the excitation path. The laser path is situated in a resonator, consisting of a spheric mirror and a prisma, resulting in a continuous beam output with only transverse mode. (Tradowsky 1979) The power of the used Ar^+ Laser (488 nm) output is high about 15- 30 mW, 5.5 Ampère. At the end of the fibre entering the scan head through a neutral density filter, the output was between 6.5 mW and 7.4 mW. In front of the objective used for visualising cells an average power of about 1.5 mW – 2.9 mW was measured. As the discharge in ionised gas (plasma) is connected with high electric currentthe laser has to be cooled..

7.6.2.2 The Helium-Neon Laser

In this gas laser Helium has a filling pressure of 1 Torr, Neon only 0.1 Torr. This mixture is necessary for the excitation in the gas discharge of ionised atoms. Helium is necessary to get the inversion, the transition of Neon is the output of the laser. Energy resonance occuring at the 2^1s energy level of Helium is corresponding with the 3s level of Neon and the 2^3s level of Helium corresponds to the 2s-level. A lot of atoms are lifted to the high energetic levels of Helium as there are ten times more atoms in the gas. These levels are metastabile as transition to the ground state is forbidden. The energy is given to the Neon atoms. They will reach the 1p level over the 2p level which is lower than 3s or 2s levels. The 1p level is depleted by inelastic shocks. From the 2p level a high spontaneous emission exist.

As the excitation takes place in a tube of Quartz the laser beam has to be linear polarised to be able to pass through the final window of the tube within the resonator without losses. (Tradowsky 1979)

The power output of the HeNe Laser (543.5 nm) at the end of the fibre was 0.5 mW (maximal 0.78 mW)

7.6.3 Two photon excitation pulsed laser

7.6.3.1 Pulsed laser parameters

The excitation wavelength of the laser light of the two photon excitation confocal laser scanning microscopy was 798 nm, the Full Width Half Maximum of the modelocked Ti:Sapphir laser was 13.02 nm. The laser had an average power of 40 mW before entering the scanning head, operating at a pulse (repetition) rate of a 76 MHz pulse with a pulse width of about 120 fs (10^{-15} s) (, that means light was just covering 36 µm in this time).
Further the Ti:S laser had the following parameters:
Energy per pulse = average power/pulse = 40 mW / 76 MHz = 0.526 nJ
Peak power = energy per pulse/pulse width = 4386 W
Duty cycle = pulse width * pulse rate = 0.000912 %
Period (time between the pulses) = 131.58 µs
(Coherent 2000)
In front of the Nikon 60x/1.4 NA water immersion IR objective used for visualising cells an average power of about 2 mW was measured. NIR fs pulses were fed into the scanning head by a light fiber after being compensated for the positive dispersion of the fibre (in the Grating Dispersion Compensator, Post Fiber Compressor).

7.6.3.2 The Verdi V-5 Diode Pumped Laser

Each laser requires a pumping source, a high reflector, the gain medium and an output coupler/partial reflector. The resonator consist at least of two mirrors enclosing the gain medium. Within the resonator standing waves are formed, called modes. The beam profile and subsequently the beam divergence is depending on the mode profile. The slightest divergence is achieved when the laser is oscillating in the fundamental TEM_{00}-mode. Diode pumped laser use laser diodes for exciting the gain (laser) medium, which is mostly a solid crystal.
The compact solid-state Verdi V-5 diode-pumped Laser frequency-doubled Neodymium Vanadate ($Nd:YVO_4$) laser that provides single-frequency continuous-wave green (532

nm) output with low noise at power levels greater than 5 Watts is required as pump laser to excite Titanium in the Ti:S laser. It is a good pumping source as its whole pump power (about 90 % within 10 nm) emits exactly at the absorption wavelength of its own gain medium, resulting in an efficiency of over 50 %, having a very good electric-optical efficiency.

The laser head utilises a Neodymium *Vanadate* ($Nd:YVO_4$) crystal (Neodymium ions are doped into a yttrium orthovanadate) as the gain medium (which is held fixed at a nominal setting of 30°C) with the pump power provided by fiber delivery. The characteristic lasing wavelength of neodymium-doped vanadate is nominally 1064 nm (near-infrared region of the optical spectrum). This infrared light is in fact the oscillating or "fundamental" wavelength of the Verdi V-5 resonator. Advantages of $ND:YVO_4$ are the high absorption of the pump radiation and the high amplification, the uniaxial birefringent of the crystal associated with a natural polarisation. Therefore no further optical elements in the resonator like a Brewster plate for polarisation is needed for the following frequency doubling process thus the efficiency is increased. The nonlinear medium (frequency *doubling crystal* / second harmonic generation) is a Type I, non-critically phase matched Lithiumtriborat (*LBO*) birefringent crystal held at approximately 148 °C. The laser head optics are schematically represented in Figure7_18.

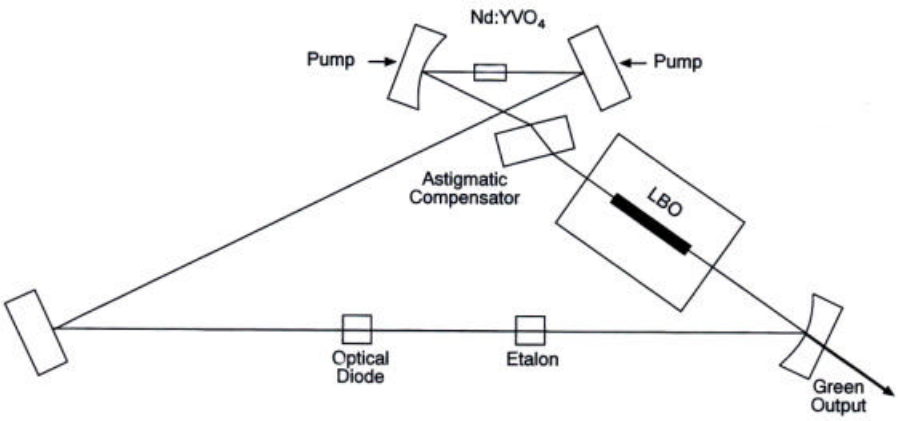

FIG 7_18 The Verdi Diode Pumped Laser Head Optical Schematic (Coherent Laser Group 1998)

The design is a ring cavity, employing intracavity second harmonic generation, single direction lasing is accomplished with an intracavity *optical diode* that induces lower losses for light travelling around the ring in the preferred direction in comparison to the counter-propagating direction. Single-frequency selectivity associated with unidirectional oscillation is further enhanced with a temperature-stabilised intracavity *etalon as the single-*

frequency optic (Temperature range: 25 °C to 75 °C). The resonator also incorporates a Brewster-plate *compensator to eliminate the astigmatism,* associated with the use of spherically curved mirror surfaces at non-normal incidence angles; and can be categorised as an "end-pumped" design with *two pump mirrors,* in which the pump light from the diode bars propagates collinear to the optical axis within the gain medium. Careful control of the spatial overlap between the mode volume defined by the resonator geometry with *two end mirrors* and the actively pumped volume of the gain medium constrains laser oscillation to the lowest-order transverse mode (TEM_{00} mode operation, which is oscillating in direction of the axis). This can be achieved by adjusting the mirrors without "hard" apertures that can introduce beam distortions through diffraction effects. Output optics are a collimating lens and *a pair of high-reflectance beam-steering mirrors* (external of the laser resonator but still within the sealed resonator enclosure) that allow adjustment of the output beam position.

7.6.4 Mira Model 900-F Laser

The Model 900 Mira is a modelocked ultrafast laser, consisting of the laser head and controller, tunable from 710 to 1000 nm. A Titanium:sapphire (Ti:S) crystal is used as gain medium. The technique used to modelock the Mira laser is referred to as Kerr Lens Modelocking (KLM), an all-solid-state technique. The schematic diagram of the optical cavity of the Coherent Model 900-F is shown in Figure 7_19.

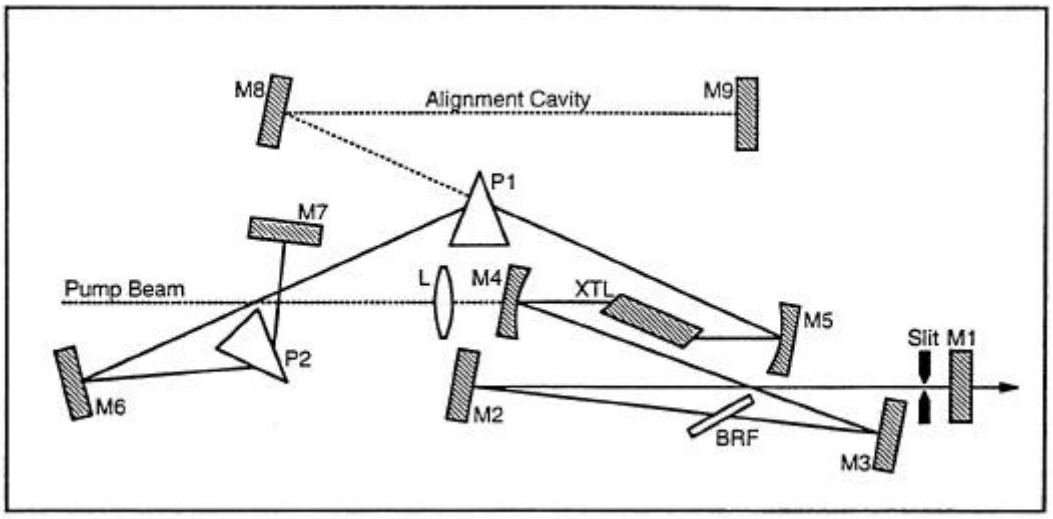

FIG 7_19 Optical schematic of the Coherent Model 900-F Ti:sapphire laser. **M1**, output coupler; **M2**, **M3**, **M6** and **M7**, high reflecting mirrors; **M4**, focussing mirror coated to pass the pump beam and reflect the intracavity beam; **M5**, focusing, high-reflector mirror; **XTL**, Titanium:sapphire (Ti:AlO_3) crystal; **P1** and **P2**, prism pair for introducing negative GVD; **L** lens. (Fisher et al 1997)

Features included in this system are an auxiliary cavity which produces an alignment beam, built in alignment apertures, an internal power meter, and an internal fast photodiode. They aid to align and to optimise the output.

7.6.4.1 Single Pulse Properties

If the laser is modelocked, a single short light of pulse bounces back and forth between the mirrors within the cavity. A small portion of the pulse escapes from the output coupler at each bounce to form the output of the laser. The time between the pulses is equal to the time it takes for light to make one round trip from the output coupler to high reflector at the other end of the cavity back to the output coupler, in the case of Mira Model 900-F laser approximately 13,2 ns, the inverse of the time is the repetition (rep) rate (pulses per second) or “frequency”: 76 Megahertz.

As atoms excited by the passage through the gain medium return to the ground state, emitting light, insufficient atoms are in the exited state for a period of time after passage to

form and amplify another pulse. Consequently only a single pulse is formed at a time, the output consists of a sample of this one pulse periodically arriving at the output coupler.

7.6.4.2 Kerr lens formation

The laser is passively self-modelocked using the optical *Kerr Lens Effect*, i.e. a nonlinear process of self-focusing which changes the spatial profile of the beam produced, as an optical medium placed in a strong electrical field changes its index of refraction (Light is an electromagnetic wave). Like the two photon absorption the Kerr effect occurs via the third-order susceptibility, χ, i.e. the Kerr lens is only formed when the intensity of light is extremely high, which is the case for the focused Gaussian laser beam. Because of the non-linear light-induced change in the index of refraction inside the Ti:sapphire crystal, illustrated in Figure 7_21, the crystal acts as lens, focusing the higher-peak power (mode-locked) mode of operation to a greater extent than the lower-peak-power continuous wave (cw) mode, resulting in higher round trip gain in the modelocked (differential gain) versus cw (differential loss) operation. As self-focusing concentrates the high-peak-power part of the intracavity beam in the centre of the Ti:sapphire crystal , where gain is the highest, differential gain occurs due to an increased overlap between the pumped gain profile and the circulating cavity mode. In addition, an aperture is placed at a position within the cavity enhance the loss (differential loss) in the CW operation, represented in Figure 7_20.

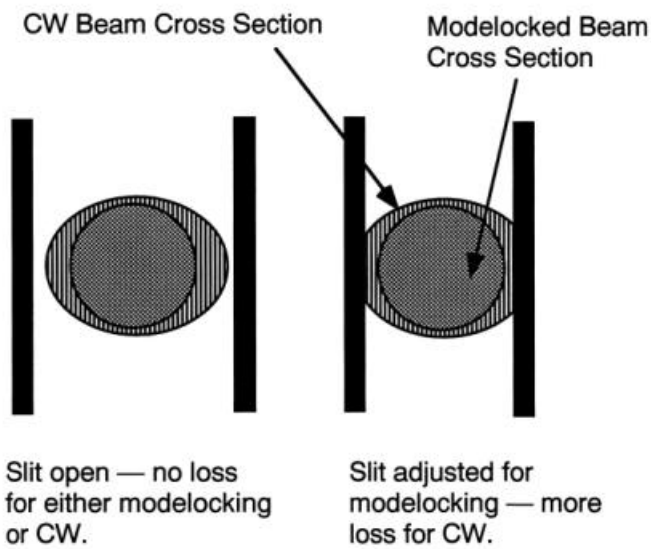

FIG 7_20 Beam cross section of the Mira Saturable Absorber System (Coherent Laser Group 1997)

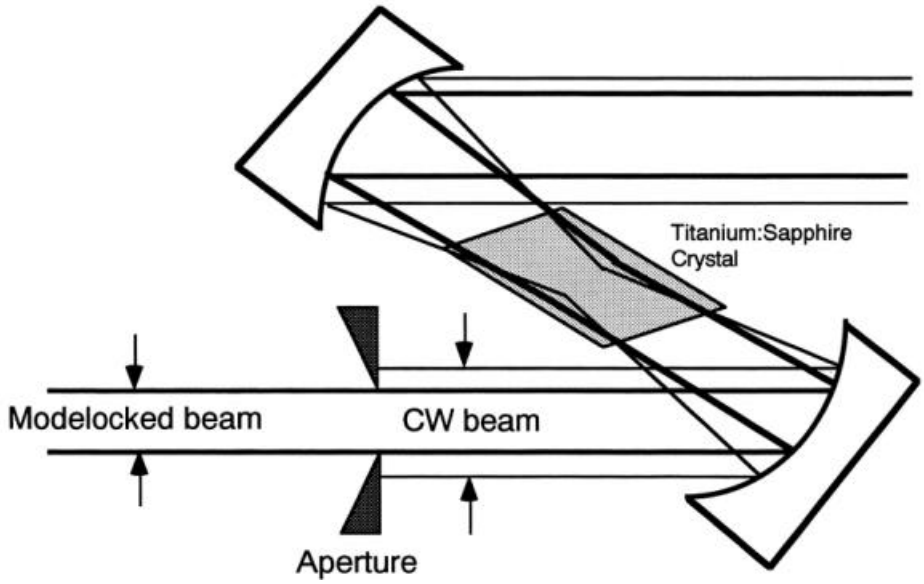

FIG 7_21 Beam geometry of the Mira Saturable Absorber System (Coherent Laser Group 1997)

7.6.4.3 Modelocking

A laser can operate at a number of wavelengths which satisfy the condition that an integral number of half wavelength will ”fit” between the high reflector and the output coupler (laser cavity). Each of these wavelengths is called longitudinal mode. Several modes, lasing simultaneously, add to each other, but only when the phase between each mode is adjusted

non-randomly and held constant, the peak power become much larger and the random spiking between these pulses diminishes. This is referred to as locking the modes together, hence the term modelocking. The larger the number of modes locked together, the higher the pulse intensity and the narrower the pulse. The frequency of the pulses is precisely equal to the frequency separation of adjacent longitudinal modes. The resulting pulsewidth depends upon the gain bandwidth of the laser medium, the accuracy of the frequency setting, and the stability of the laser cavity. The Mira Ti:Sapphire laser generates modelocked pulses with output pulsewidth in the 50 fs to 150 fs regime.

7.6.4.4 Advantages of Kerr lens mode-locking

The Kerr lens mode-locking is not wavelength dependent, because no molecular resonance is required for saturable absorber action and the cavity length need not to be tuned to sub-micrometer resolution, as in synchronously pumped systems, to maintain modelocking.
Group velocity dispersion compensation is used to produce near transformed pulses of 200 femtoseconds.

7.6.4.5 Pulsewidth

The product of the pulsewidth and the spectral bandwidth of a laser pulse have a lower bound (i.e. $\Delta\lambda \times \Delta\tau \geq$ Constant) due to the uncertainty principle. Thus as the pulsewidth decreases, the spectral bandwidth inceases and a 70 fsec pulse is spread over 13 nm. (Denk et al 1995)
Further group velocity dispersion (GVD) and self-phase modulation (SPM) broaden the short pulsewidth in the Ti:sapphire laser. GVD results from the wavelength dependance of the index of refraction of various cavity optics, therefore individual frequency components in the pulse passing dispersive materials like a glass (silicon) fibre (SiO_2) have different velocities. Intracavity elements like the Ti:S crystal, the dielectric mirror coatings (**M1-M7** in Figure 7_19), and the birefringent filter (BRF) cause positive GVD (wherein red spectral components with a longer wavelength travel faster than blue ones with a shorter wavelength) The smaller the pulse width, the larger the corresponding optical bandwidth, the

higher the introduced positive GVD. The gain of the Ti:S crystal determines the passive bandwidth, the bandwidth of the mirror coatings and the BRF have to be added. Dispersion experienced inside the cavity is balanced with a prism pair (components **P1** and **P2** in Figure 7_19) to introduce negative GVD.

Self-phase modulation is a second intensity dependent nonlinear Kerr effect appearing during KLM as the local index of refraction is dependent on the light field intensity. SPM affects the spectrum of the pulse and is responsible for spectral narrowing in consequence of energy transfer from blue to red end of the spectrum and vice versa, resulting in longer pulse length. The leading and trailing edges of the pulse will cause less change in the index than the centre, therefore parts of the pulse move faster, thus altering the pulse shape, generating new optical frequencies or eliminating others and introducing a time-dependent phase shift. The frequencies are inherently chirped and broaden the pulse unless the chirp, which is either positive, is compensated.

7.6.5 The Grating Dispersion Compensator (GDC)

The fempto-Mira-GDC consists of the grating dispersion compensator (Pulse Strechter), the fibre (3 m), and the post fibre compensator unit (PFC) (Final Dispersive Unit). In order to compensate for the wavelength-dependent speeds introduced by the glass fibre, the GDC-Unit stretches the pulse dependent on its wavelength bandwidth (about 10 nm at 800 nm) on about 6 ps by putting high frequent parts of the light in front of low frequent parts, introducing a negative chirp. The glass polarisation-preserving single-mode fibre will reduce this pulsewidth to about 3 ps because of its properties and the length of 3 m, until the pulse is entering the post fibre compressor. There the pulse will be corrected and recompressed to obtain the original length of 120 fs, before it will enter the scanhead of the CLSM (PCM 2000, nikon).

The following Figure 7_22 exemplifies the grating dispersion and its compensation of a pulse on its way to the scanhead.

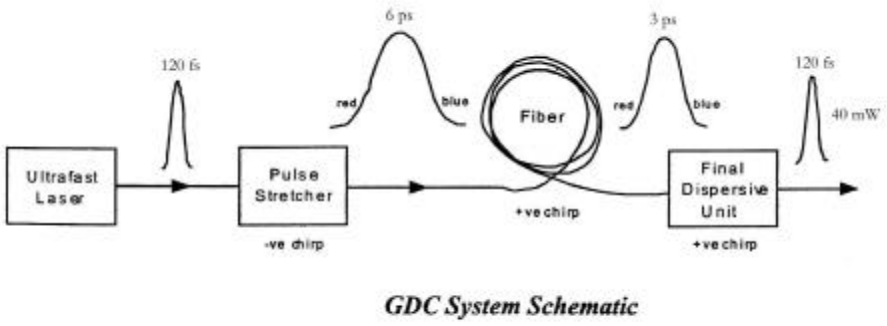

FIG 7_22 GDC System Schematic (Coherent Laser Group 1999)

7.6.5.1 The Pulse Stretcher

The GDC (Pulse Stretcher) uses a single, gold-coated holographic grating in a four-pass configuration. A lens and mirror combination image the pulse from the front of the grating back on itself. This compact, highly dispersive design allows both the second and third-order dispersive terms to be corrected independently (up to 1.3 x 10^6 fs^2). By adjusting the amount of stretching with the GDC, it is possible to exactly compensate the positive dispersion of the fibre and PFC units.

Figure 7_23 represents a simplified diagram of the single, goldcoated holographic grating in a four- pass configuration.

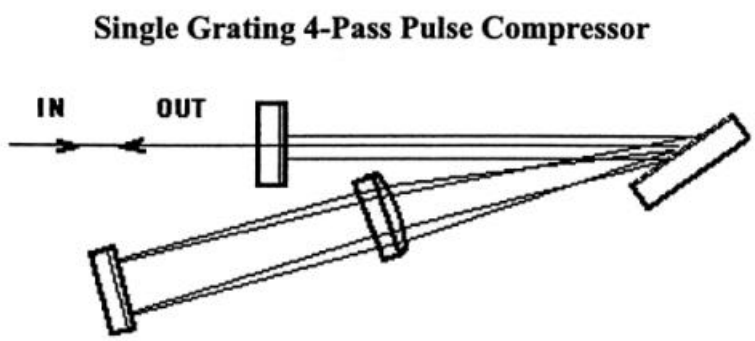

FIG 7_23 Pulse Expander Simplified Diagram (Coherent Laser Group 1999)

The single-mode quality of the fibre is responsible for the low average power of short pulses being transmitted through the system. The fibre is polarising-preserving, i.e. outer circumstances (motion, pressure, temperature) does not effect polarisation and does not disturb data. The small core size (about 5.5 µm) implies high power densities (i.e., 50 mw average power, 100 fs at 76 MHz gives a power density in the fibre of 28 x 10^9 W/cm²) which is responsible for self-phase modulation. Due to SPM in the fibre the amount of power that can be transmitted through the system is limited to 50 mW average power.

7.6.5.2 The final dispersive unit

The PFC is also required for high average power (> 50 mW) to be delivered to the system. The average power is improved by a longer pulsewidth maintained throughout the entire length of the single-mode fibre. To accomplish this and deliver short pulses, a post fibre compressor (PFC) is used at the fibre output. It is a single block of highly dispersive material which is used to reduce the effects of self-phase modulation. Figure 7_24 shows that the beam is passed through the material 7 times, given a total dispersion of 105 fs².

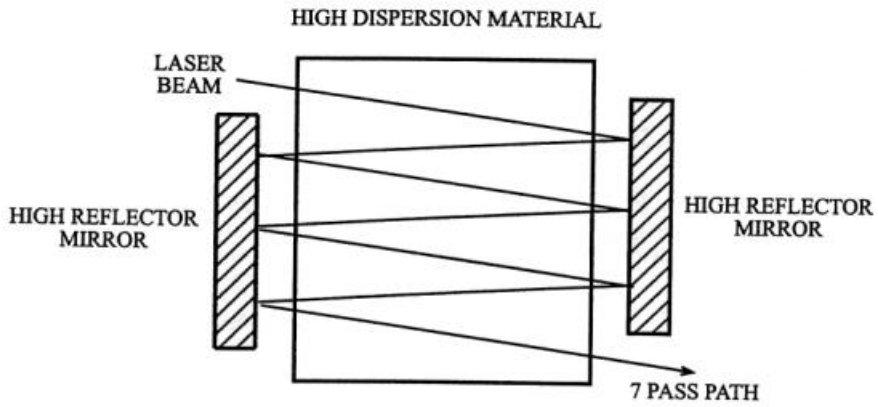

FIG 7_24 Post Fiber Compensator (Coherent Laser Group 1999)

The PFC unit is connected with micrometer screws with which the coupling of light from the PFC into the scan head can be optimised in a three-dimensional manner (x, y, z –axis). The z-axis (the distance of the PFC to the scan head) is optimised once. In x, y direction the light beam is adjusted for daily operation with the help of fluorescent slices on object slides put on the inverted microscope and imaged confocally.

7.6.6 Beam Diagnostic Instrumentation

The key optical parameters in an ultrafast laser system are wavelength, average power, peak power, pulsewidth, and pulse repetition rate. In addition, it is important to know that the laser is fully modelocked, and to be alerted to cw (continuous wave) breakthrough. All measurements were done at the reference beam leaving the GDC.

7.6.6.1 Measuring Wavelength

The wavelength and the full width half maximum of the pulse (shape) was measured by a Wave Scan Laserspectrometer and presented by the software APE Las Scan 2.2.: Las Scan- Spectrometer Control- Real Time Mode, Wavescan VIS.

7.6.6.2 Measuring Pulsewidth

The width of an ultrafast laser pulse cannot be measured directly. Instead the pulsewidth must be inferred from secondary measurements. The preferred method for determining pulsewidths is to use an *autocorrelator*. An autocorrelator determines the pulsewidth by separating the beam into two parts and focusing them to the same point in angle-matched nonlinear crystal; then observing the second-harmonic output while varying the path-length difference between the two beams. By making assumptions about the shape of the pulse (e.g., Gaussian, Lorentzian), the output is de-convoluted and the pulsewidth obtained. The optical schematic diagram is shown in Figure 7_25.

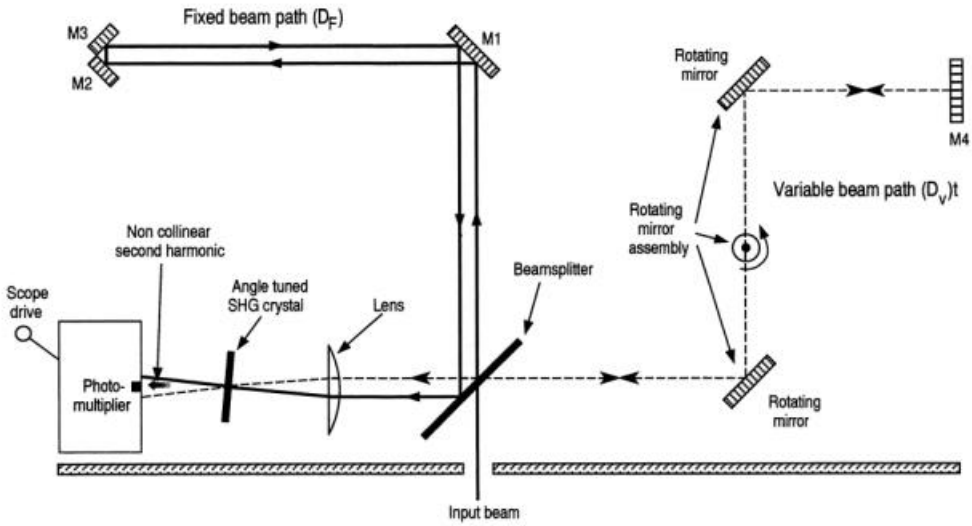

FIG 7_25 Autocorrelator Optical Schematic Diagram (Coherent Laser Group 1997)

7.6.6.3 Measuring Average Power

The average power was measured with an optical power meter from Newport.

7.6.6.4 Measuring Peak Power

The peak power cannot be measured directly, because the pulse repetition rate and the pulsewidth are beyond bandwidth and resolution limits of conventional power and energy meters. The peak power has to be calculated by the formula:

$P_{peak} = P_{avg} / (f \times \tau)$

where f is the pulse repetition rate and τ is the pulsewidth. The pulse repetition rate is fixed by the laser geometry to be found in the laser specification table, in this case 76 MHz. P_{avg} = 40 mW, τ = 120 fs => P_{peak} = 4386 W, which has be calculated above as well. (Coherent Laser Group 1997)

7.6.7 Personal Confocal Microscope (PCM) 2000

7.6.7.1 The Scan Head

The Optical Schematic of the Scanhead of the Technical Instruments Brite*i scanning optical microscope shown in Figure 7_26 corresponds to the one used in One-Photon-Excitation and Two-Photon-Excitation CLSM. For TPE the pinhole was opened to its maximum.

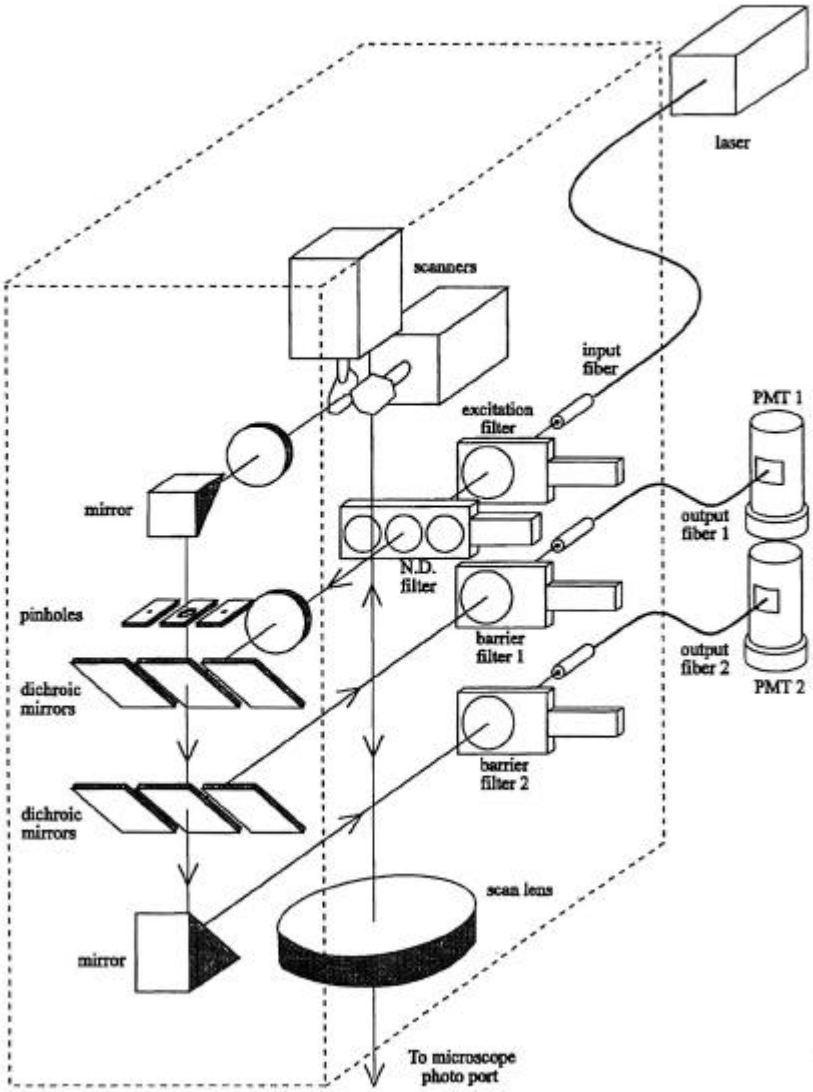

FIG 7_26 Diagram of the Technical Instruments Brite*i scanning optical microscope [Courtesy: V. Cejna and G. Q. Xiao, Technical Instruments Corporation, San Jose, California, USA] (Corle 1996)

The used lasers as already mentioned were an Air-cooled Argon-Ion laser with an output wavelength of 488 nm, and a Helium-Neon Laser with an output wavelength of 543,5 nm. A single-mode, non-polarisation-preserving fiber brings the light into the scanning head assembly. This fiber also acts as a spatial filter for the optical system. The fiber coupling optics use an achromatic lens with a spectral range of 450-650 nm. An adjustment screw has been added to control the centering of the fiber at its input end, thus it is possible to adjust the illumination intensity. In addition with the help of a neutral density filter the illumination intensity can be adjusted in coarser increments. A 488 nm Argon laser line (excitation) filter in the illumination path isolate the system from light caused by secondary lines and fluorescent emission from the laser tube.

After having passed through the laser line and neutral density filter, a relay lens focuses the end of the fibre onto the pinholes. Two different pinhole sizes are provided, 20 µm and 50 µm, and a through beam path not containing a pinhole. The same pinhole is used for both illumination and imaging. After the light has passed through the pinhole, a second lens collimates the light, before the scanners reflect the light.

Galvanometer mirrors are used both for *x* and *y* scans. The scan rate of these mirrors is more than 1 frame/second for a 512 pixel x 512 pixel scan. The scan rate can be slowed down by the user changing the pixel dwell time from 3 ps per pixel up to 20 ps per pixel to allow longer integration on the detectors if desired. The maximal volume (x, y,z) which can be scanned is 200 µm x 200 µm x 200 µm with 512 pixel x 512 pixel x 96 optical sections, limited by the hardware of the used system.

After passing through the scanners, the light is relayed to the microscope by the scan lens. There it is focused onto the sample by the objective lens. The reflected or fluorescent light from the sample retraces its path through the optical system, is descanned by the galvanometer mirrors, and focused onto the pinhole plane. From the pinholes the light is transmitted by a set of dichroic mirrors to the output fibers and then to the PMT detectors.

7.6.7.2 Scanner Stability

In a CSOM either the sample or the illuminating beam has to be scanned in order to build up the image point by point. Sample, objective, and beam scanning techniques all have been developed. In our case the objective was moved (either by the z-motor or) by a

Piezo(translator) for precise position in the nanometer range in order to have a stable scanner without drift or lateral jumpes, when going from one x-y plane to the next.
The scanner stability is a function of temperature and mechanical vibrations, which can be reduced by the setup, and other electronic or mechanical design-dependent features. Movement along the optical axis influences the resolution of the optical sectioning capabilities. (Porwol, Strohmaier, Spiess 1999) For precise, reproducible optical sectioning a piezoelectrically driven movement of the objective was necessary. The Piezo regulates the position of the objective very precisely with a 50 nm resolution. It encloses the used objective and works nearly without hysteresis (less than 0.2 %) . The Piezo itself is controlled by voltage changes of a potentiometer in a digitised way in the range of the zero to the maximal nominal value of 200 µm with a resolution of 12 Bit by a LVPZT (Low Voltage Piezo)-amplifier/Servo-controller with a RS-232-interface and a 12-Bit-Digital-Analog-Converter for low voltage piezos. (200 µm maximal nominal displacement divided by 2^{12} = 4096 (for 12 bit) ≈ 4000 = 50 nm resolution)
The nominal movement either for the Piezo and the z-motor does not always correspond to the actual movement of the focal plane in the specimen as the ratio of both is dependent of the refractive indices of the immersion medium and the mounting medium. If both are the same as for as immersion medium water and PBS as mounting medium, the nominal and actual movement should be the same.
Furthermore, mechanical vibrations were suppressed by a vibration control system (Newport), a vibration free working platform whereupon the 2P Laser and the CLSM was installed. The table surface was isolated during scanning from floor motion by the Stabilizer™ pneumatic suspension system.

7.6.7.3 Data acquisition

For data acquisition a modificated inverted light microscope (Nikon, TE 300) with either a 60 fold magnifying water objective (Plan Apochromat) with a numerical aperture of 1.2 and coverglass correction or an oil immersion objective (Plan Fluor) with a numerical aperture of 1.3 which had to be used with coverglasses of a controlled thickness of 0.17 ± 0.1 mm.

When the specimen receives the laser pulses, absorbing their electromagnetic radiation, getting excited, it will emit light in all directions, also in the direction of the water objective. This part will pass through the water objective to the galvonometric scan mirrors to the pinhole that will shut off stray light of out-of-focus planes. Afterwards the emitted light is parted in 1:1 ratio on the two emission channels, passing through an emission filter in each channel. Filters were chosen appropriate to the used dyes. A glass fibre brings the signals to the photomultiplier tubes within the light detection module, in which the module for controlling the mirror scanners is incorporated and which is communicating with a serial interface with the PC. The PC working on the basis of Windows 95 contains the frame grabber (A2D) which will convert the analog signals of the light detection module in digitised image data. The software EZ 2000 Version 2.1.3 was used for data aquisition, representation and processing of data.

7.6.7.4 Optimisation of the System Performance

In order to obtain most realistic images of the biological structures by optical sectioning of the object, several conditions listed in the following paragraphs were necessary.

7.6.7.4.1 Adaptation of the refractive indices

The used cover glasses, the immersion and the mounting media for the cells should have the minimal differences in refractive indices as emitted rays not parallel to the optical axis are refracted at the interfaces mounting medium/ coverglass/ immersion medium according to Snell´s law. (see Introduction) Refractive mismatches result in spherical aberrations and a loss of light intensity. This is reduced by using thin coverglasses and the water objective. Thus the system with the immersion medium water and the watery mounting medium reduce losses in resolution in deep layers of the cells.

7.6.7.4.2 Calibration of the magnification

The applied programs EZ 2000, Huygens2 and AVS-Express 5.0 need specifications about the ratio of the pixel number respectively the number of optical sections and the reel scanned distances of an object. The calibration in the x, y plane was performed by a calibration glass. For the optical axis z a coverglass with known thickness was line-scanned along the optical axis. Two Gaussian curves were obtained, the distance between the two maximums is equivalent to the nominal thickness. The data were saved in the program EZ 2000.

7.6.7.4.3 Reduction of cell movement

For correct results it is very important that during a scan there will be no movement of the cells along the three axis. Therefore cell specimen were grown on special coated coverglasses with Poly-D-Lysin, fixing the cells as the surface resistance is augmented, but they are still able to change their shape. These movements were reduced by lowering the temperature on about 20 °C without vitality losses of the cells.

7.6.7.4.4 Determination of the Experimental Point Spread Function

As described in section 7 the experimental point spread functions were detemined to deconvolve with them the scanned confocal images to obtain the most realistic images. Deconvolution is a computational method used to reduce out-of-focus fluorescence in three-dimensional microscope images. Using experimental point spread functions instead of theoretical ones makes that fluorescence intensity will appear more homogeneously distributed which corresponds more to the reality.

7.7 Three Dimensional Reconstruction and Visualisation

7.7.1 General protocol for acquisition of the volume data

This paragraph describes the conditions which were kept constant during confocal imaging.

The room in which the CLSM was installed was darkened with a room temperature regulated to 23 °C. For cross talk reduction emission filters were applied. As for two photon excitation shortpass filters, reflecting laser light longer than 700 nm.. Before starting scans the sensitivity of the photomultiplier tubes were adjusted by the image acquisition software to optimise the influence of the fluorescent dyes on the measuring channel and to reduce it on the second channel, thus the cross talk was below 10 % per channel. This was a compromise between the signal of the dye to be detected in the measuring channel and the suppression of other fluorescent dyes localised in the cell respectively the autofluorescence of the cells.

For 3-D reconstruction series from 30 up to 64 optical z-sections (average section distance 400 nm) were recorded with an x-y resolution of 512 x 512 pixel at a scanning speed of about 2 sec per image (pixel dwell time 3 µs to 10 µs for cells, up to 20 µs for PSF). The number of optical sections was limited by the present computer hardware.

7.7.7.2 Specifications for the image data

The next table gives specifications about the PMT gain and the dimensions of the whole imaged cell volumes (sampling densities in x, y, z- direction and the imaged field in these directions) and the optical cuts performed in z direction. For the x, y –plane one or a few HepG2 cells, along the optical axis of the cells, were imaged according to their dimensions.

Figure	Staining	PMT gain	Pixel	Axis	Sampling	Pixel	Field

			time (µs)		density (nm)		(µm)
10_1	1P		3.0	x	195.313	512	100.0
	DHR	2.9		y	195.313	512	100.0
	MT	2.4		z	400	50	20.0
10_2	1P		3.0	x	73.047	512	37.4
	DCF	3.2		y	73.047	512	37.4
	MT	3.0		z	400	30	12.0
10_3	1P		3.0	x	109.766	512	56.2
	DCF	2.7		y	109.766	512	56.2
	MT	2.9		z	400	30	12.0
10_4	2P		3.0	x	341.797	512	175.0
	DHR	3.8		y	231.641	512	118.0
	MT	2.4		z	400	40	16.0
10_5	2P		3.0	x	165.430	512	84.7
	DCF	2.8		y	165.430	512	84.7
	MT	2.7		z	400	40	16.0
10_6	2P		10.0	x	280.469	512	143.6
	DCF	3.4		y	195.312	512	100.0
	MT	2.9		z	700	34	23.8
10_7	2P DAPI	3.7	3.0	x	133.984	512	68.6
	DHR	3.7		y	133.984	512	68.6
	MT	3.4		z	400	50	20
10_8	2P DAPI	3.3	3.0	x	85.156	512	43.6
	DCF	3.6		y	85.156	512	43.6
	MT	3.6		z	300	64	19.2
10_9	2P DAPI	3.6	3.0	x	85.156	512	43.6
	DCF	4.4		y	85.156	512	43.6
	MT	4.0		z	300	64	19.2

Table 7_8 specifies the conditions under which the images of the HepG2cells were recorded: The photomultiplier (PMT) gain, pixel dwell time, the sampling density, the number of pixels and the volume dimensions

For one photon excitation usually the small pinhole was applied (physical radius r_{phys} = 10 µm) backprojected pinhole radius r_b for one photon excitation:

$r_b = r_{phys}$ / (magnification of the system * magnification of the objective)

with magnification of the system = 1

magnification of the objective lens = 40 x or 60 x

r_b = 250 nm for 40 fold magnification and small pinhole of 20 µm diameter; respectively 167 nm (for 20 µm pinhole), the pinhole of 50 µm has a backprojected pinhole radius of 417 nm for 60 fold magnification. No pinhole was used for 2 photon CLSM.

The acquired image stacks were preprocessed by deconvolution to improve image quality prior to 3-D visualisation. The mathematical algorithm implemented in Huygens2 software removes noise and artifacts, sharpens the images and correct for problems with contrast and brightness.

7.7.2 Reconstruction per Deconvolution

For deconvolution of data sets 3-D point spread functions of the CLSM was measured as described using subresolution fluorescent microspheres with emission of 515, 590, 620 nm. Subsequently, the noisy original confocal images and the appropriate PSF were fed together into an iterative Maximum Likelihood Estimation (MLE) restoration alghorithm optimised for treatment of high noise images. The MLE algorithm is performed for restoring low light level images with a the signal to noise ratio between 3 and 30. An example of deconvolution is shown in the Figures 7.7_1 and 7.7_2. Maximum Intensity Projections of cells stained with DAPI, Dihydrorhodamine (DHR) and MitoTrackerRedCMXRos (MT) are shown before in Figure 27 a, b, c and after deconvolution in Figure 28 a, b, c. The three dimensional visualisation can be seen in Figure 10_7

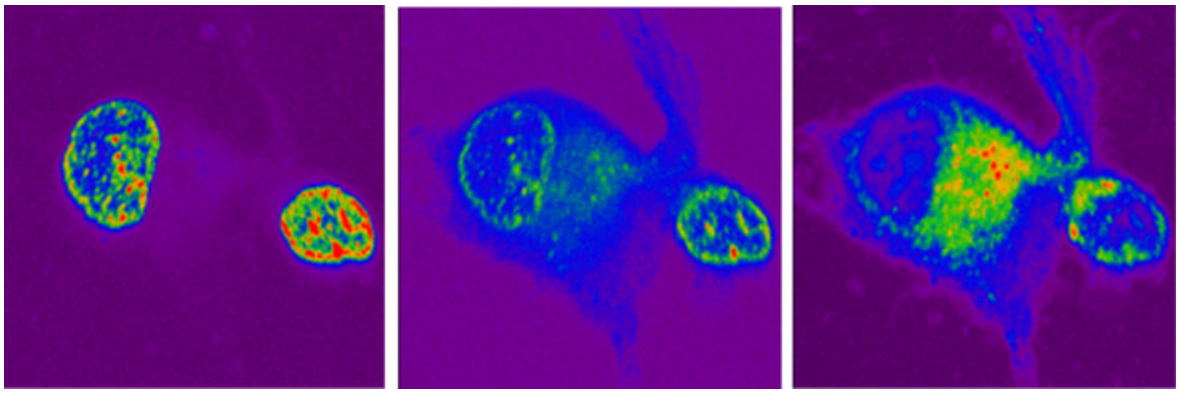

FIG 7_27 HepG2 Cells in MIP-Projection before deconvolution in Huygens2 stained with
a DAPI b DHR c MT imaged with
470 ± 15 nm 515 ± 15 nm 620 ± 30 nm emission filter.

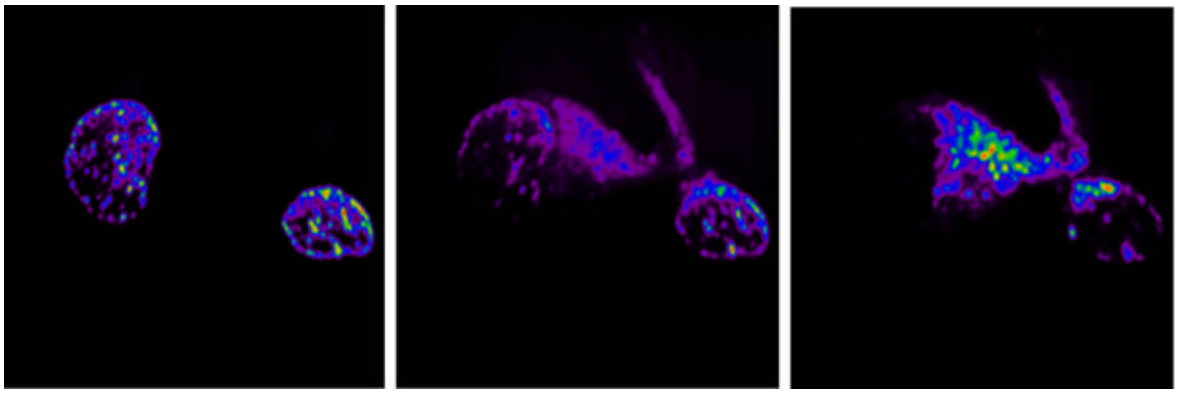

FIG 7_28 HepG2 Cells in MIP-Projection after deconvolution in Huygens2 stained with
a DAPI b DHR c MT imaged with
470 ± 15 nm 515 ± 15 nm 620 ± 30 nm emission filter.

With MLE algorithm of the Huygens System noise can effectively removed and lost details recovered. Maximum likelihood estimation (MLE) is a mathematical/computational optimisation strategy generally used for producing estimates of quantities corrupted by some form of random noise, in our case due to the statistical nature of the quantum photon emissions (Poisson point process of image noise) and the effects of diffraction in typical low light level situations. The strategy is to produce the estimate of the fluorescence dye concentration, $\lambda()$, which has the highest likelihood of having given rise to the specific data collected. The estimate of the real object is obtained by iterations, that means that the algorithmus converges to a result with increasing steps. The MLE-algorithmus estimates the real object and convolutes it with the known optical characteristics (PSF) of the micro-

scope. If the difference measured by *I-divergence* or *cross-entropy* between the representation of the imaged object and the simulation of the representation by convolving the estimate with the measured PSF is higher than a fixed value, the algorithmus continues with a new iteration with a modified estimate of the real object. The principle of I-divergence difference measure is the only choice for objects which are restricted to zero or positive values. The progress in the minimising process between the current estimate and the measured image, is expressed in the form of an (increasing) *quality factor*. The quality factor displayed by the MLE algorithm in the Huygens System reports the quality relative to the first estimate. In this way the quality factor is always a number greater or equal to 1.
The iterations were performed by "Fast Mode" which is more effective at the cost of a marginal increase of computing time per iteration and the addition of one extra (hidden) temporarily image. The algorithmus was stopped if several subsequent estimates differ less than a certain value (< 0,1 %), which was specified as the threshold for quality factor increase.

7.7.2.1 Simplified Data Collection Model

The modelling of data collection process for wide field fluorescence and confocal fluorescence microscopes is summarised by the following equations:
$\mu_n(x,y,z) = \mu_r(x,y,z) + N(x,y,z)$ and $\mu_r(x,y,z) = \mu(x,y,z) + b(x,y,z)$
and $\mu(x,y,z) = \lambda(x,y,z) \otimes h(x,y,z)$
where x and y are the in-plane (transverse) spatial variables, z is the axial spatial variable, b(x,y,z) is a background level primarily due to dark current, N() is the random noise, primarily due to quantum photons, $\lambda()$ is the fluorescence dye concentration and h() the PSF.
The convolution (denoted by $\otimes$) with h() represents the blur in the image. The aim of the deblurring algorithm is to produce an estimate, or reconstruction, of $\lambda()$. The background level b(x,y,z) is measured in a calibration protocol "estimating mean background", that measures the average background in a non-object area in the image, and which includes the *baseline* (for the electronics-induced offset) and the average background (Poisson) noise. The background level is accounted for in the image reconstruction algorithm by incorporating it within each algorithm iteration.

7.7.2.2 Maximum Likelihood General Principles

In a heuristic interpretation of MLE, one might think of the collected image data as a random host of other possible random quantities.
In mathematical terms classically interpreted, we are formulating a *log-likelihood function* that represents a measure of the likelihood that one would collect the noisy data that were actually collected. This function is actually a functional (i.e. a function of a function) of $\lambda()$, h() and $\mu_{n()}$, based on the random Poisson nature of the quantum photon noise. In principal, this derivation is solved for its maximum value. As μ_n is known and h() (the experimental PSF) has been measured the deblurring algorithm is only solved for $\lambda()$, the fluorescence dye concentration. (Pawley 1995).

7.7.2.3 Deconvoluted image stacks

Colours are added by false colour representation, segmenting the image of the object. Since each pixel in a 8-bit greyscale confocal image (with values 0 [black] to 255 [white] in PCM 2000) corresponds to fluorescence intensity at a point within the specimen, the pixels with lower values represent areas with lower fluorescence while the pixels with higher values represent brighter regions. Assigning colour to the intensity images is done by thresholding. In Huygens 2, the lowest intensity is represented in dark, then violett, green, blue, green, yellow, orange, red for highest intensities.
The significant bits size (layout) for the datasets is changed from an integer representation format, 8 bit (grey scale values) to a real representation format of 32 bit. The size for 3-D visualisation is a float representation format of 64 bit.

7.7.3 Volume Visualisation

After the image stack was processed by 2-D image processing techniques, it was reconstructed into a 3-D volumetric dataset. This can achieved by either volume or surface rendering techniques as computer graphics technique. We applied surface rendering, whereby

the volumetric data are converted into geometric primitives, by an isosurfacing process. These primitives (such as polygon meshes or contours) are then rendered for display using conventional geometric rendering techniques. Because the 3-D data set is reduced to a set of geometric primitives, this results in a significant reduction in the amount of data to be stored, provides fast display and manipulation of the 3-D reconstruction produced by this method, but internal structures and details may be lost in contrast to volume rendering, which can be performed without knowledge about the geometries of the data sets (www.cs.ubc.ca/spider/ladic/overview.html)

Calculation of the isosurface was performed on a IRIX-based Silicon Graphics Octane workstation on the basis of the advanced visual system (AVS/Express, Version 5.0). This program consists of modules and is applied universally in scientific graphical data processing. By individual logical linkage of single modules, the programmer generates an applicable program. Thus the following requirements were achieved:

1. Representation of cell compartments and labelled structures in different colours.
2. Different regions were represented in an opaque manner, such as the spatial order of the interwoven objects became clear.
3. An system of axis was integrated.
4. The generated images could be saved.

The connection of modules for the visualisation of the three dimensional properties of the imaged objects are illustrated in Figure 7_29.
The module *read field* is reading the volume data set as an *ics (image cytometric structure)* image (default image format), which is stored in two files. (One file (extension *ics*) is written in ASCII to include information about the format of the image data, and optionally, information about the sample, experiment, etc. The image data is written separately into a binary file with the extension *ids*.) Attached is the module *axis*, responsible for the representation of the co-ordination system. The module *bounds* is posing a square around the dimension of the volume data files. The module *isosurface* illustrates regions of the data file with equal fluorescence intensities graphically. The colour can be varied. The understanding of the extensions of the cell compartments is indeed supported. The module *uviewer3D* is visualising the initially read and then belaboured data files. With *output file*

those can be saved in the AVS proper format *x*. All obtained images were saved in a 1024 x 1024 pixel format and then converted in a TIF (Adobe Tagged Image File) format (versatile format that can handle all bitmapped images) for the IRIX- operating system by the program *Mediaconvert*, the files were transferred by FTP from the workstation to a personal computer on the basis of the operating system Windows NT 4.0, and in the picture editing program Adobe Photoshop 5.0 the function *Auto-Tonwertkorrektur* was applied. The images were printed on the laser printer Adobe PS Tektronix Phaser 750 DP.

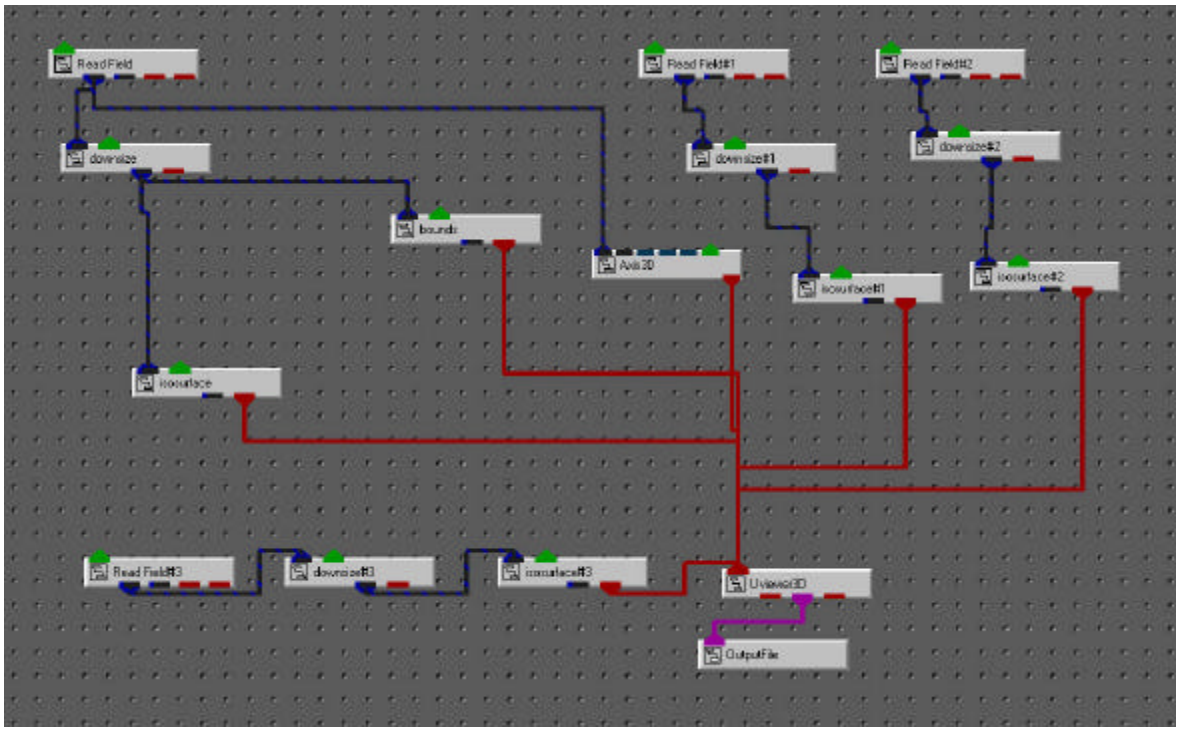

FIG 7_29 Module of AVS/Express for cell visualisation

The calculation of the isosurface was repeated for individual data set and a specific colour was chosen for the geometries, in particular red for DNA stained 5 –10 min (20 °C) with 25 µM 4´, 6´-diamidino-2-phenylindole dihydrochloride (DAPI) and violet for mitochondrial mass stained 30 min (37 °C) with 10 µM MitoTracker RedCMXRos (MT). Yellow, white, blue, green was chosen from high to low Rhodamine 123 (RHO) or 2´,7´dichlorofluorescein (DCF) fluorescence intensity levels after incubating cells for 25 min(37°C) with 10 µM dihydrorhodamine 123 or for 45 min (37°C) with 11 µM 2´,7´dichlorofluorescin-diacetate.

The values of the Iso levels (green for DCF or RHO, violet for MT) as a threshold, beyond which all pixels do not contribute significantly to the object of interest and hence can be

eliminated, were determined by using the values indicated in Huygens2 for the transition from violet (lowest intensities) to dark(background), which was between 200 and 300. To have comparable values the threshold was set on 300 for the cells, if this value was found within the violet region and not in the blue one, which represents the next higher fluorescence intensities, to be sure that no image information about the outer borders of the distinct compartments will be lost. For the hot spots, the regions containing the intensities of interest could be preserved, and non-consecutive, lower ranges of intensities were eliminated, by choosing an Iso level nearer to the maximal value of the Isosurface.

III RESULTS

8. Spectral Analysis of DAPI, 2'7'-Dichlorofluorescein, MitoTrackerCMXRos, Rhodamine 123 and the used Optical Barrier Filters

8.1.UV/ VIS Spectroscopy (One Photon Excitation)

8.1.1 Absorption Maximums and Molar Extinction Coefficient of applied (oxidised) dyes in one photon excitation CLSM

The molar extinction coefficient $\varepsilon(\lambda)$ was determined by UV-VIS spectroscopy with the Uvikon 933 Double Beam Spectrophotometer in PBS pH = 7.3 - 7.5 as solvent, applying the law of Lambert-Beer.

$$\log (I_0/I) = A(\lambda) = \varepsilon(\lambda)\, dc$$

with the layer thickness of d = 1cm and c = concentration of the dye
I_0: Light Intensity before, I = after passing through the cuvette,
A: Absorbance (Absorption) units, $\varepsilon(\lambda)$ = Molar extinction coefficient

$$\Rightarrow \varepsilon(\lambda) = A(\lambda)/(cd)$$

Therefore the absorption of the dyes at various concentration was measured and the molar extinction coefficient $\varepsilon(\lambda)$ was calculated for the Absorption Maximums. The data are listed out in the last column of the tables.

8.1.1.1 2´,7´-Dichlorofluorescein

Concentration (µM = 10^{-6} M)	3	5	9	12	15	
Maximal Absorbance Units	0.3032	0.4874	0.9264	1.1719	1.4741	
Absorption Maximum (nm)	503	503	503	503	502	∅ 503
ε (cm^{-1} M^{-1})	101 066	97 480	102 933	97 658	98 273	∅ 99 482

Table 8_1: Absorption Maximums and Molar Extinction Coefficient ε(λ) of 2',7'-Dichloroflourescein

8.1.1.2 MitoTracker RedCMXRos

Concentration (µM= 10^{-6} M)	2.5	5	10	
Maximal Absorbance Units	0.1474	0.2796	0.6278	
Absorption Maximum (nm)	578	578 / 579	578	∅ 578
ε (cm^{-1} M^{-1})	58 960	55 920	62 780	∅ 59 220

Table 8_2: Absorption Maximums and molar extinction coefficient ε(λ) of MitoTracker RedCMXRos

8.1.1.3 Rhodamine 123

Concentration (µM= 10^{-6} M)	1	4.5	6.7	10	
Maximal Absorbance Units	0.0604	0.2987	0.4597	0.7565	
Absorption Maximum (nm)	500	500	500	500	∅ 500
ε (cm^{-1} M^{-1})	60 400	66 378	68 612	75 650	∅ 67 760

Table 8_3: Absorption Maximums and molar extinction coefficient ε(λ) of Rhodamine 123

The Absorption Maximums of the dyes are 503 nm for 2', 7'-Dichlorofluorescein, $\varepsilon_{(DCF)}$ = 99 482 cm^{-1} M^{-1}; 500 nm for Rhodamine 123, $\varepsilon_{(RHO)}$ = 67 760 cm^{-1} M^{-1}; 578 nm for MitoTrackerRedCMXRos, $\varepsilon_{(MT)}$ = 59 220 cm^{-1} M^{-1}.

8.2 One and TPE Fluorescence Excitation and Emission Spectra of the applied (oxidised) dyes in one photon excitation confocal and TPE LSM

The Nucleic Acid stain DAPI was only analysed by two photon spectroscopy and only used by TPE CLSM. The excitation scan is shown in Figure 8_1, the series of emission scans three dimensionally in Figure 8_2. Over an excitation wavelength from 580 nm to 820 nm, every 6- 7 nm a whole emission wavelength scan was performed over a range from 254 nm to 709 nm emission wavelength. In Figure 8_3, the emission is shown for excitation with the wavelength of the excitation maximum, and the used wavelength in TPE CLSM. Due to instrumental restrictions, the latter excitation wavelength was 795 nm, not 798 nm, which was applied in microscopy.

The oxidised dyes 2'7'-Dichlorofluorescein, MitoTrackerCMXRos, and Rhodamine 123 were analysed by one and two photon excitation (TPE) fluorescence spectroscopy. In this alphabetic order the excitation and emission scans are first shown for one photon excitation (OPE) (Figures 8_4, 8_9, 8_14). The small boxes within the graph illustrate the linear dependency of fluorescence excitation and emission intensities for the measured range. Higher concentrations will not give linearly higher intensities, because of the inner filter effect, a quenching effect, which appears, if the concentration of the fluorescent molecule is high.

Then theoretical doubled OPE excitation scan and the measured TPE excitation scan are contrasted, neglecting the original intensities (Figures 8_5, 8_10, 8_15), in order to compare more easily the effects of the two excitation modes on absorption, followed by OPE and TPE emission scans (Figures 8_6, 8_11, 8_16). The measured TPE Emission scans are represented three dimensionally in Figures 8_7, 8_12, 8_17. The procedure was as follows: Over an excitation wavelength from 820 nm to 1100 for Rhodamine 123, respectively to 1150 nm for 2',7'- Dichlorofluorescein and MitoTrackerCMXRos, every 6- 7 nm a whole emission wavelength scan was performed over a range from 254 nm to 709 nm of emission wavelength. Finally the emission is shown for excitation with the wavelength of the excitation maximum, and the used wavelength in TPE CLSM. Because of instrumental restrictions, the latter excitation wavelength was 820 nm, not 798 nm, which was applied in microscopy. (Figures 8_8, 8_13, 8_18). The results of OPE and TPE spectroscopy are summarised in Table 8_4.

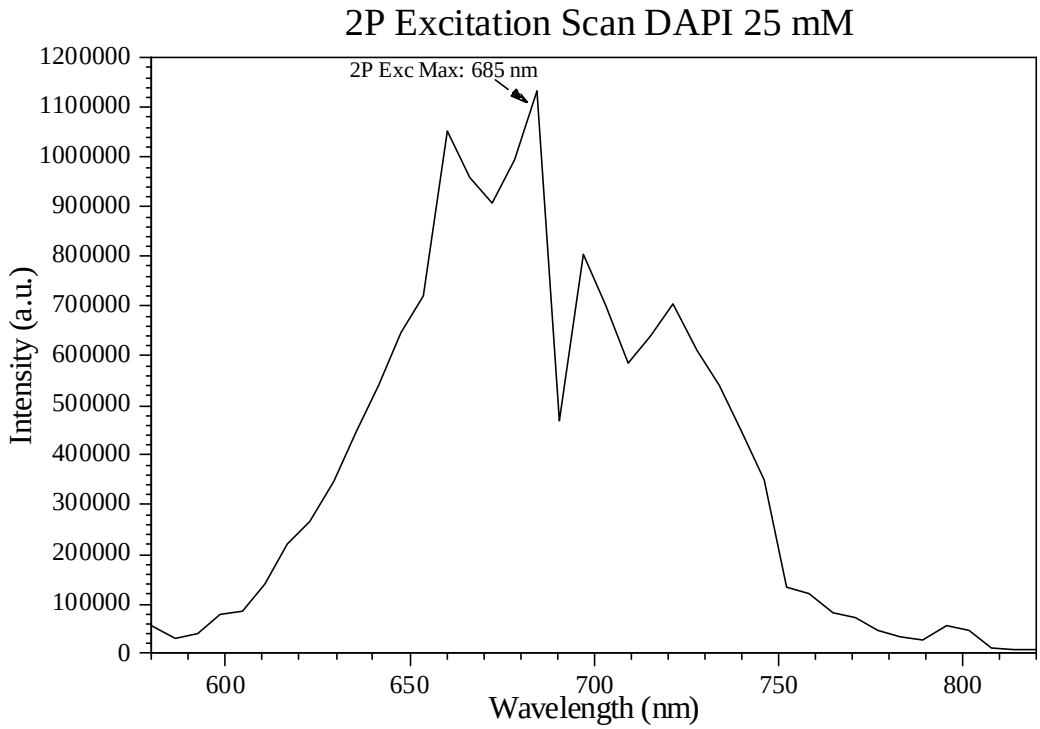

FIG 8_1: TPE Excitation Wavelength Scan of DAPI 25 mM in PBS. Excitation Maximum: 685 nm

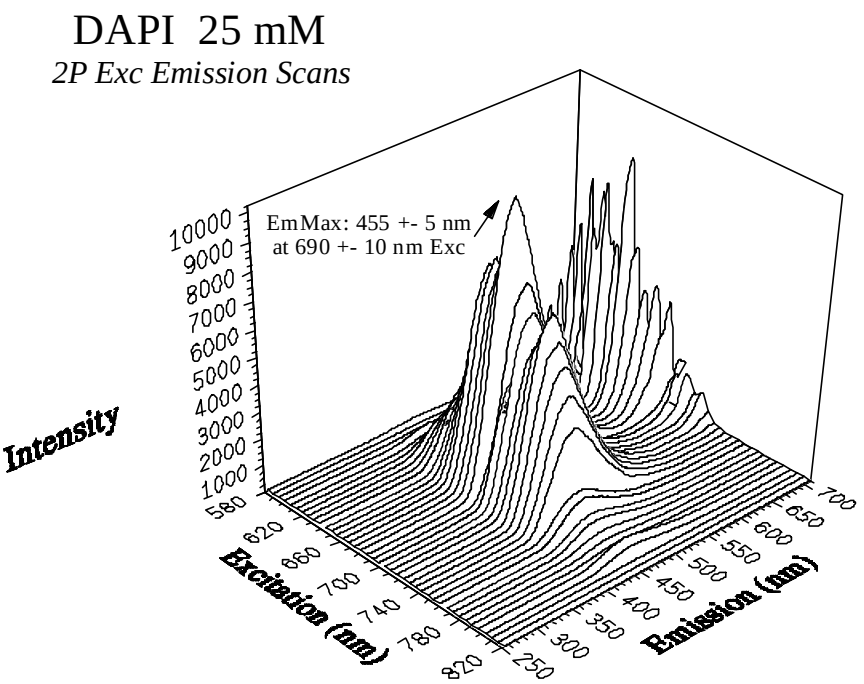

FIG 8_2: TPE Emission scans of DAPI 25 mM in PBS, from 580 to 820 nm excitation, every 6 -7 nm an emission wavelength scan was performed over a range of 254 to 710 nm.

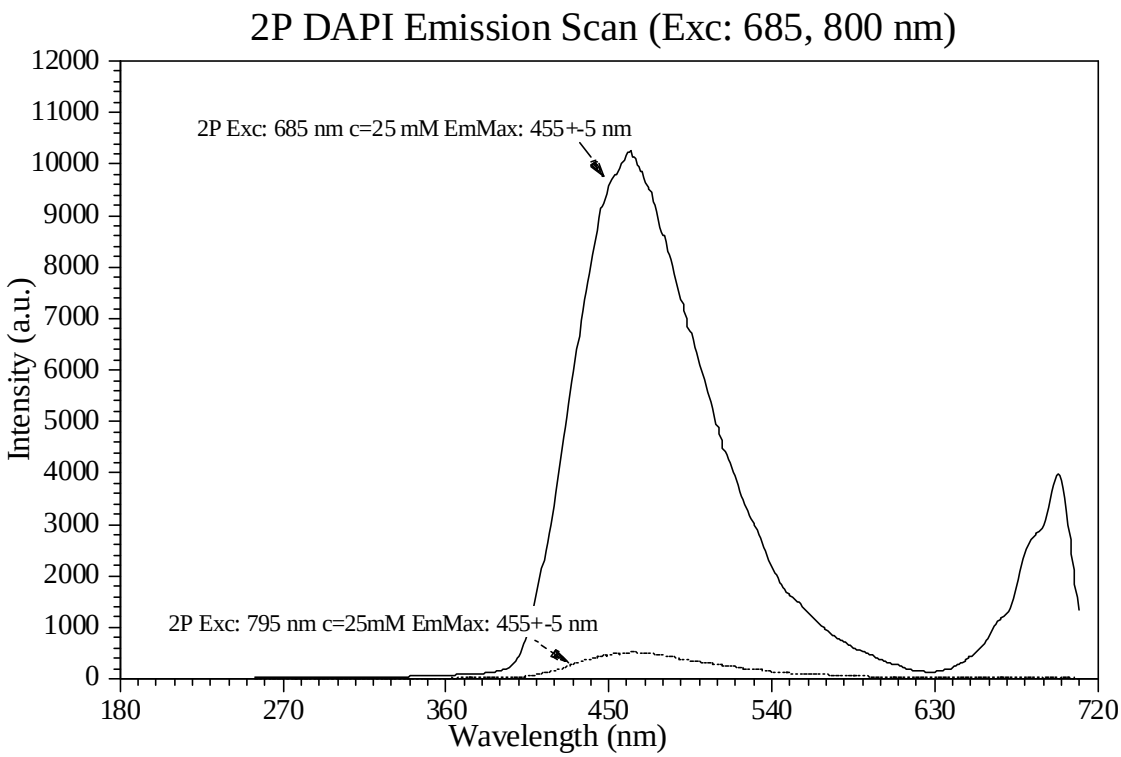

FIG 8_3:Two TPE Emission scans of DAPI 25 mM in PBS. One at the excitation maximum of 685 nm, the other near the used excitation wavelength of 798 nm for TPE laser scan microscopy (LSM)

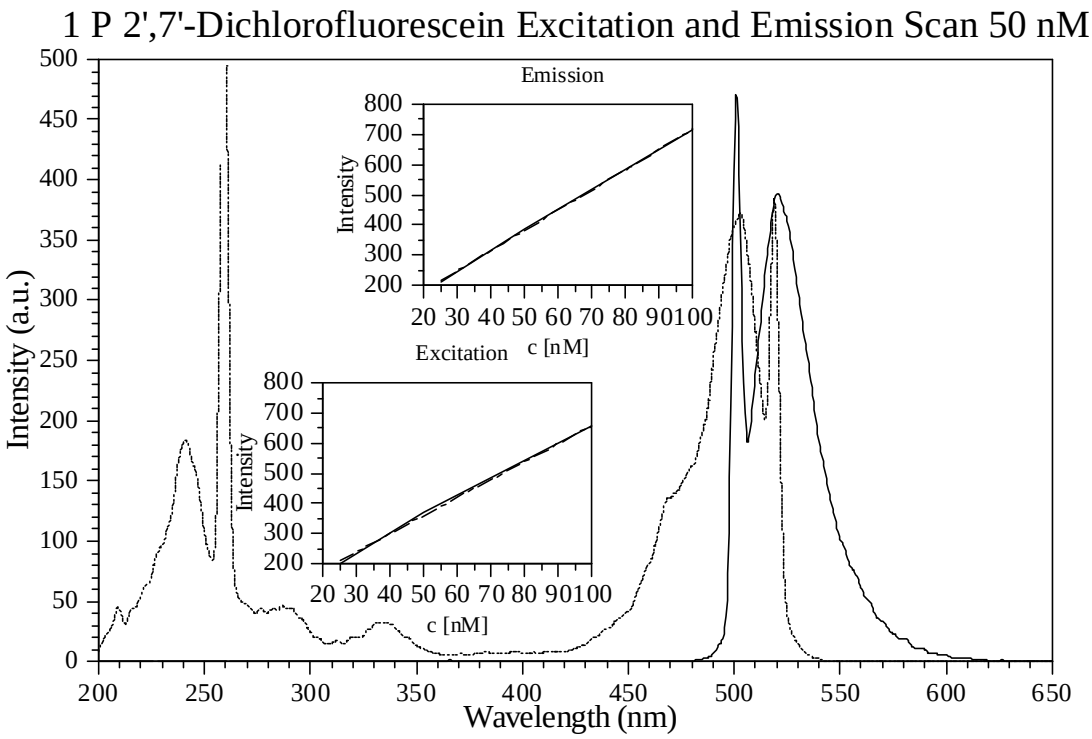

FIG 8_4: One Photon Fluorescence Spectroscopy of 2', 7'-Dichlorofluorescein ····Excitation, — Emission The small boxes illustrate the linear dependency of fluorescence intensity on the concentration for the measured range for Excitation Max: 501 ± 1 nm and Emission Max: 522.5 ± 1.5 nm --- Regression line

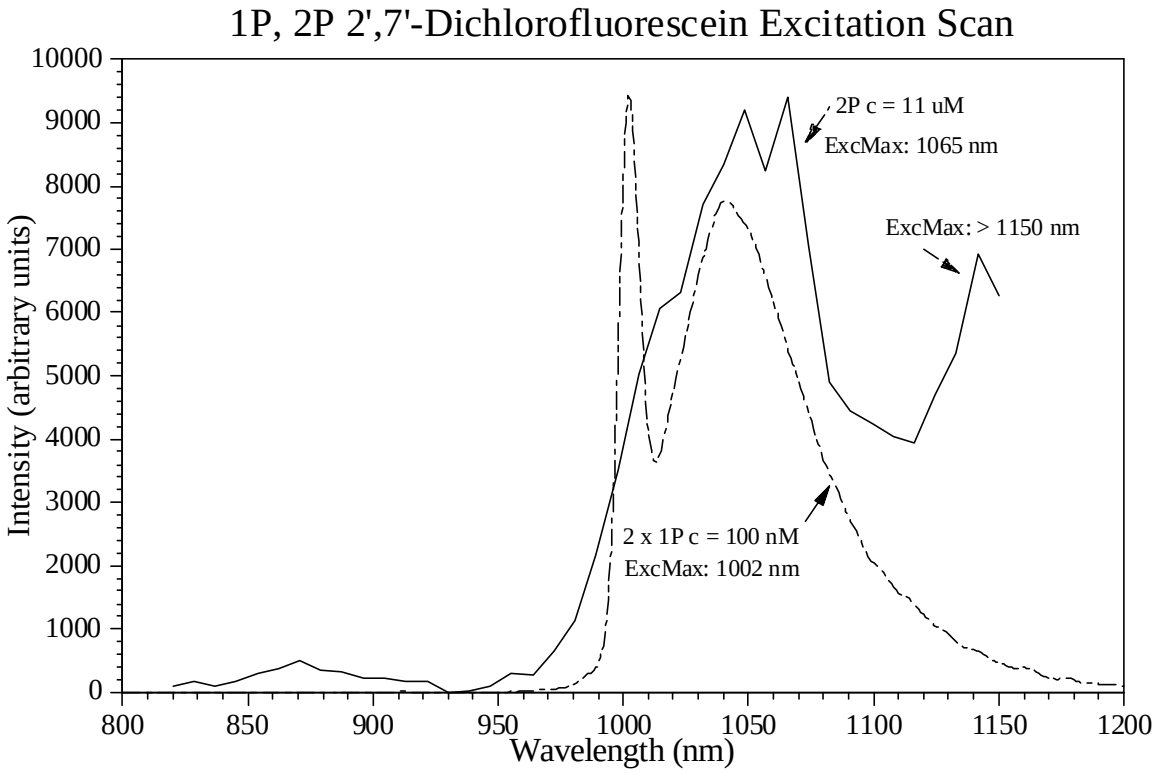

FIG 8_5 : -·-· Theoretical doubled one photon excitation scan (c = 100 nm) ExMax: 1002 nm and —TPE excitation wavelength scan (c = 11 µM) ExMax: 1065 nm and > 1150 of 2', 7'-Dichlorofluorescein

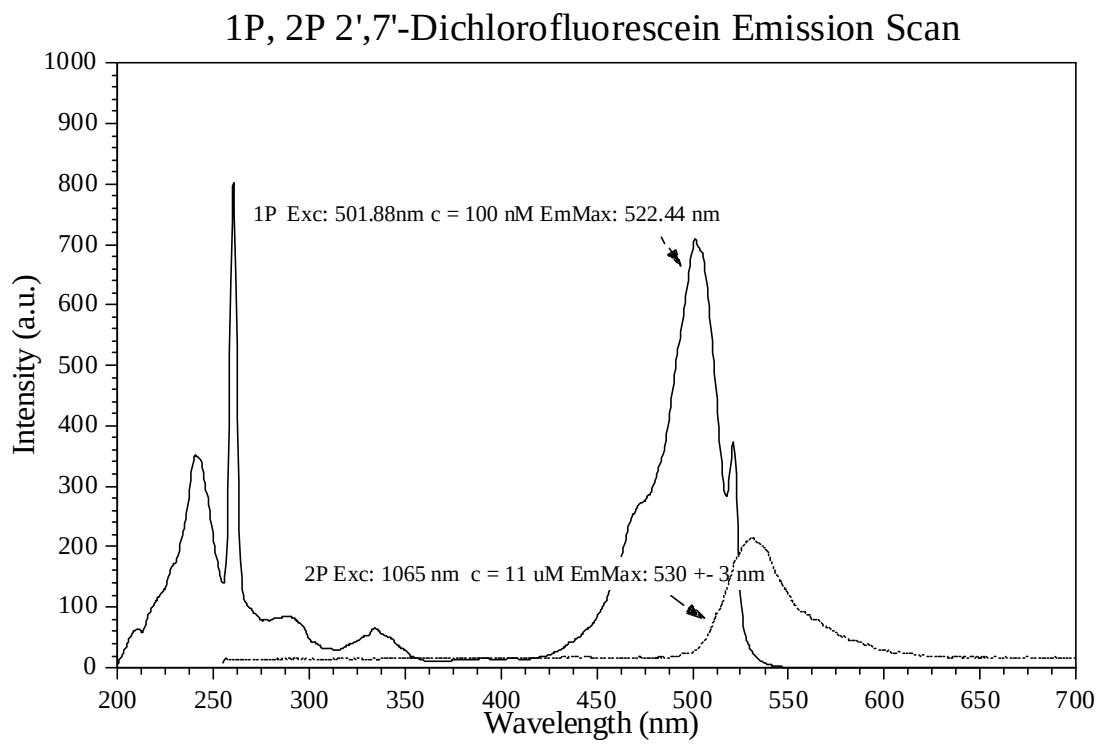

FIG 8_6: One and TPE Emission wavelength scan for 2', 7'-Dichlorofluorescein, excited at the absorption maximums: 501.88 nm for 1P, concentration c = 100 nM, 1065 nm for 2P, c = 11 µM

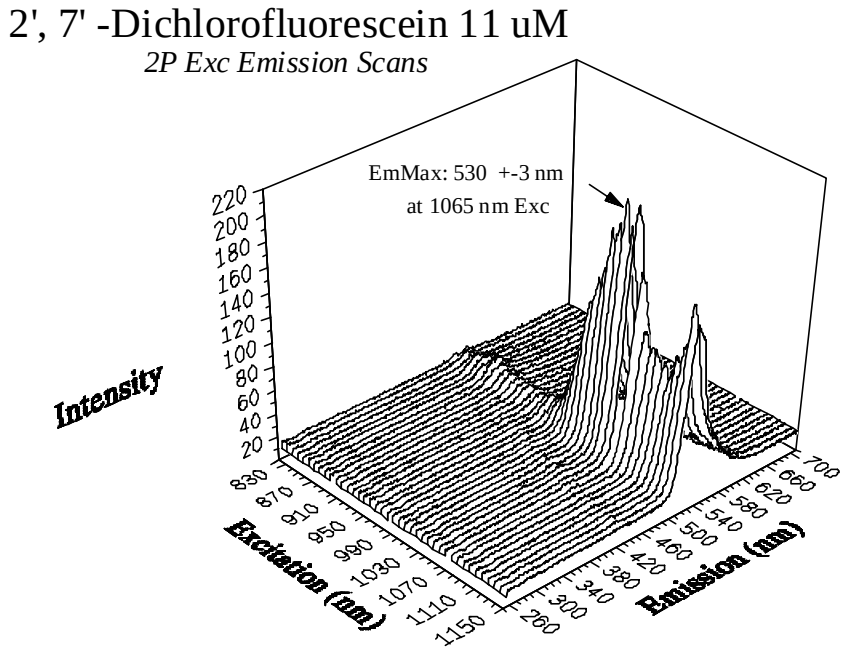

FIG 8_7: TPE Emission scans of 2’,7’-Dichlorofluorescein 11 µM in PBS, from 820 to 1150 nm excitation, every 6 -7 nm, an emission wavelength scan was performed over a range of 254 to 710 nm.

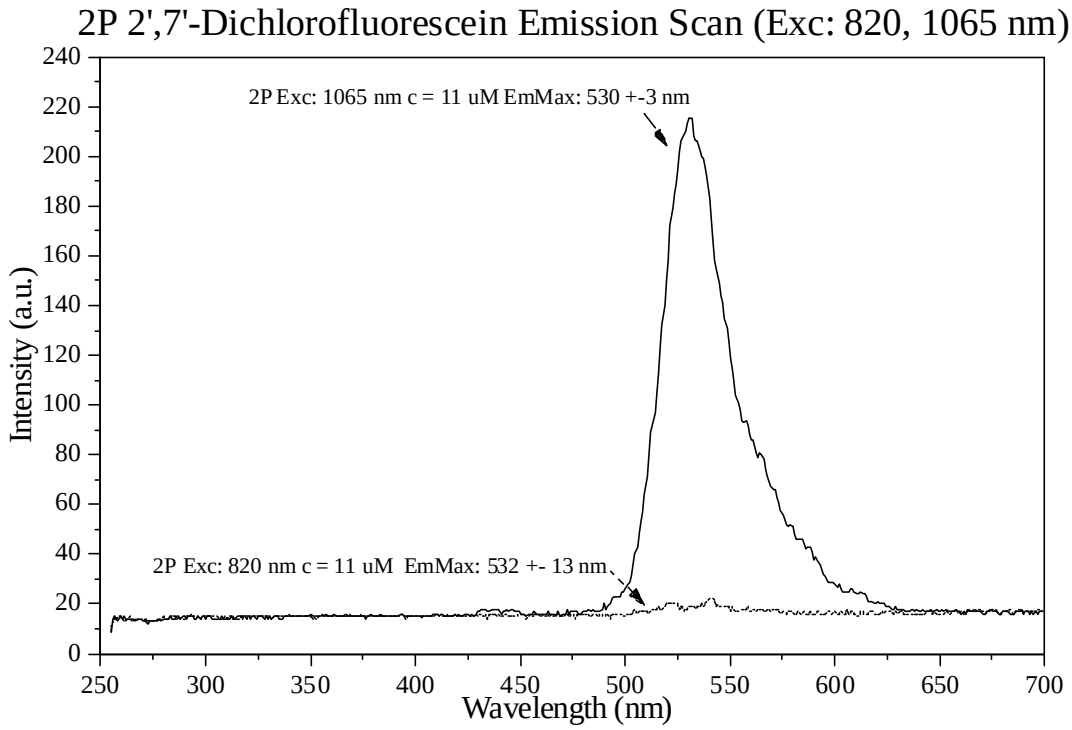

FIG 8_8: Two TPE Emission scans of 2’,7’-Dichlorofluorescein 11 µM in PBS. One at the excitation maximum of 1065 nm, the other near the used excitation wavelength of 798 nm for TPE laser scan microscopy (LSM)

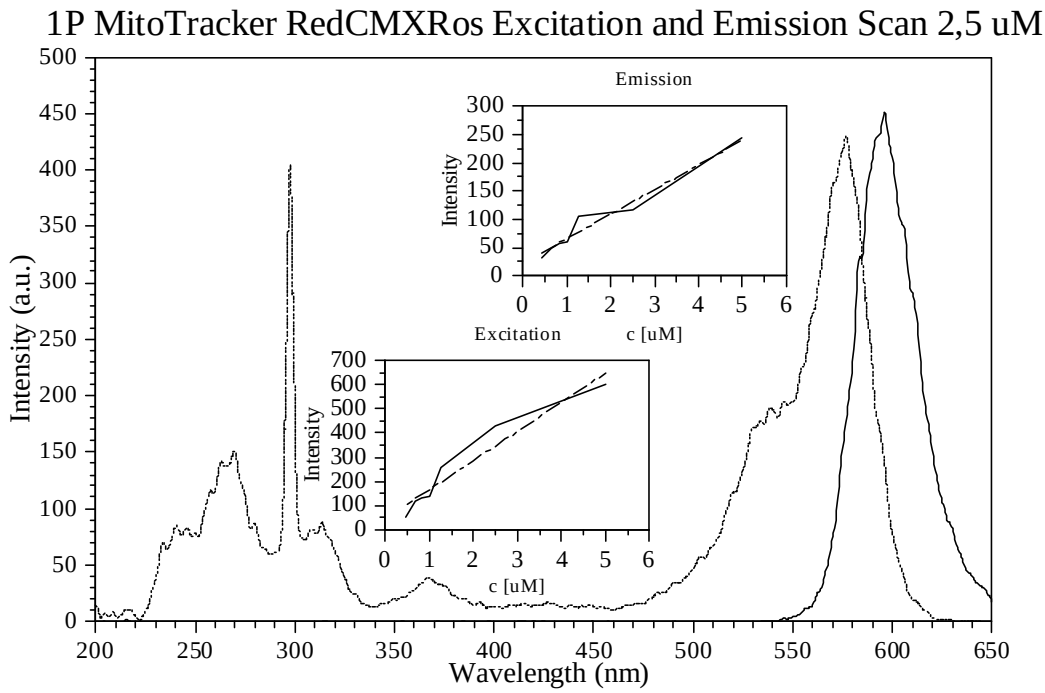

FIG 8_9: One Photon Fluorescence Spectroscopy of MitoTracker RedCMXRos, c = 2.5 µM ¨Excitation (Exc), ¯ Emission. The small boxes illustrate the linear dependency of fluorescence intensity on the concentration for the measured range for Exc Max: 575 ± 2 nm and Emission Max: 594.5 ± 3.5 nm --- Regression line

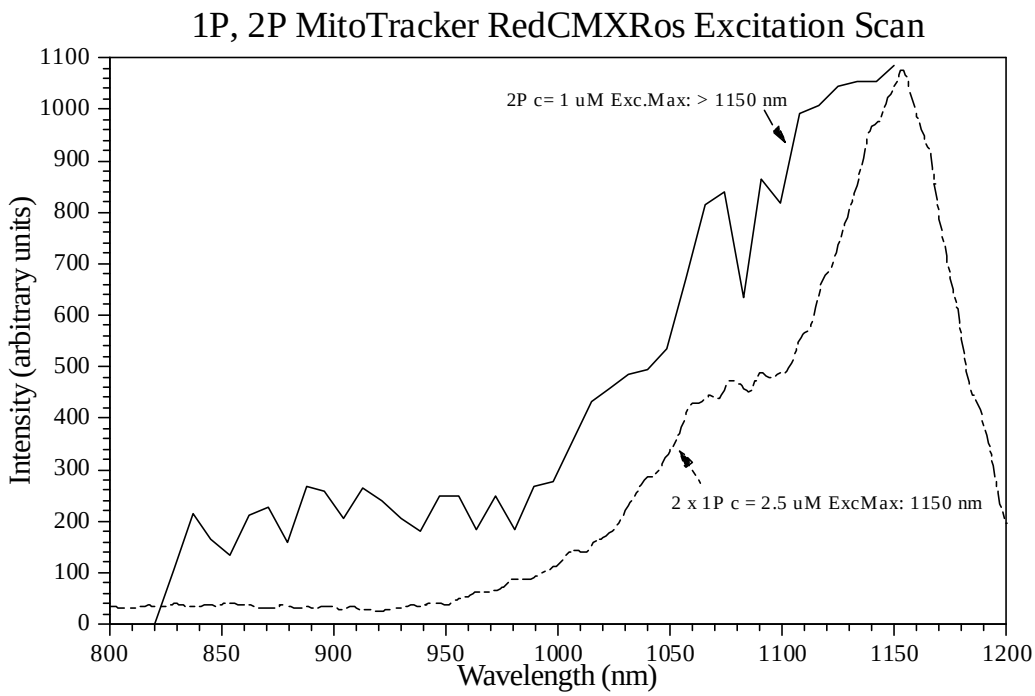

FIG 8_10: **-.-.** Theoretical doubled one photon excitation scan (c = 2.5 µm) ExcMax: 1150 nm and ¯TPE excitation wavelength scan (c = 1 µM) ExcMax: > 1150 nm of MitoTrackerCMXRos

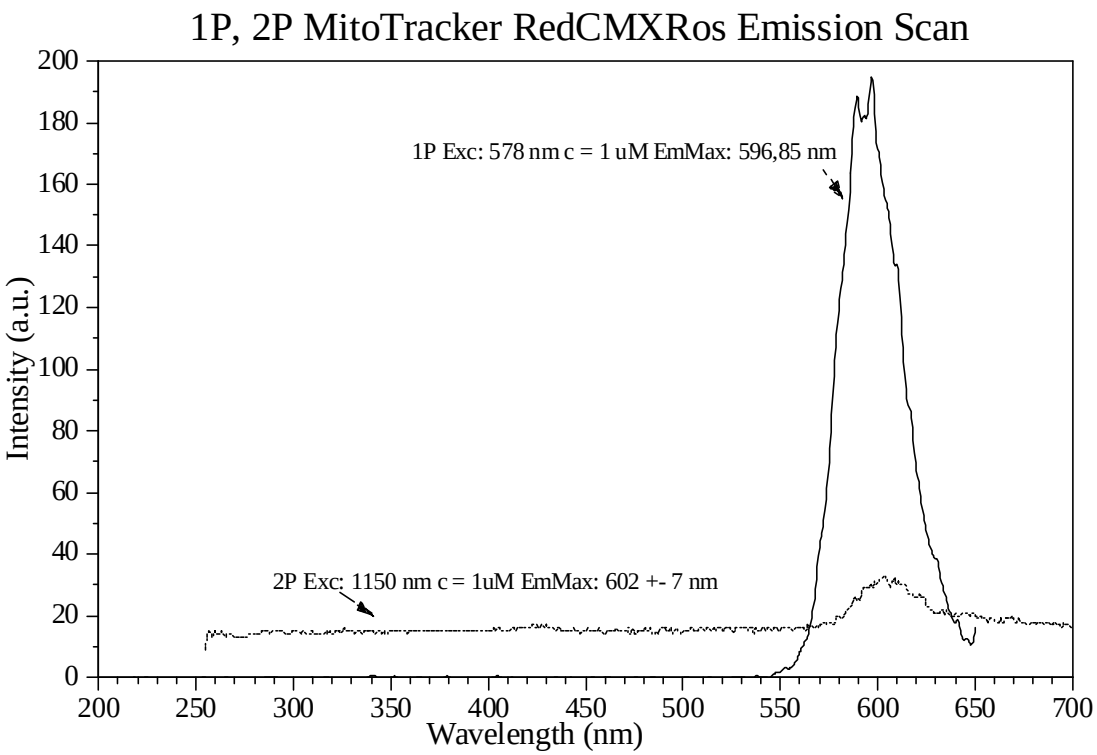

FIG 8_11: One and TPE Emission wavelength scan of MitoTrackerCMxRos, excited at the absorption maximums: 578nm for 1P, concentration c = 1 µM, the highest available wavelength was 1150 nm for 2P, c = 1 µM

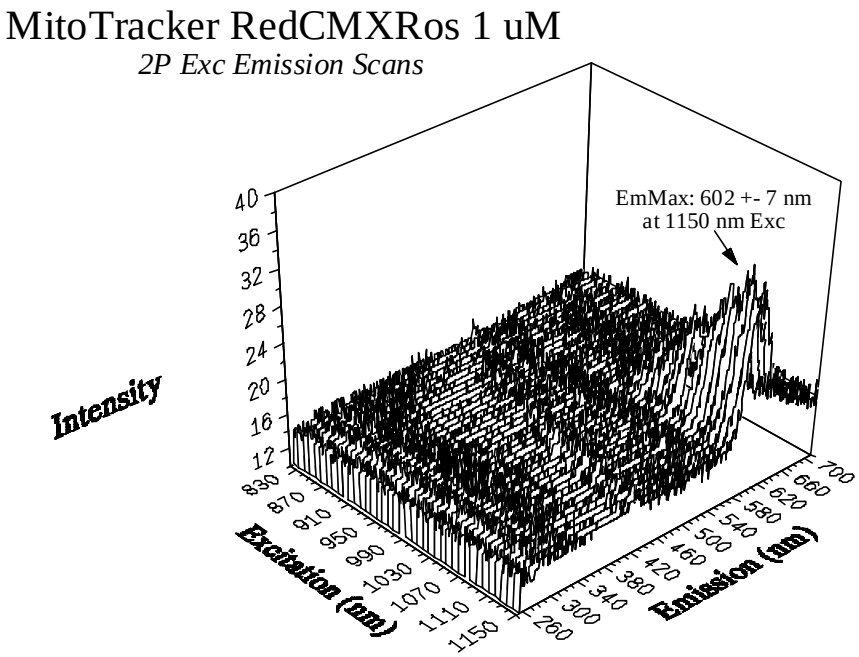

FIG 8_12: TPE Emission scans of MitoTracker RecCMXRos 1 µM in PBS, from 820 to 1150 nm Excitation every 6 -7 nm an emission wavelength scan was performed over a range of 254 to 800 nm.

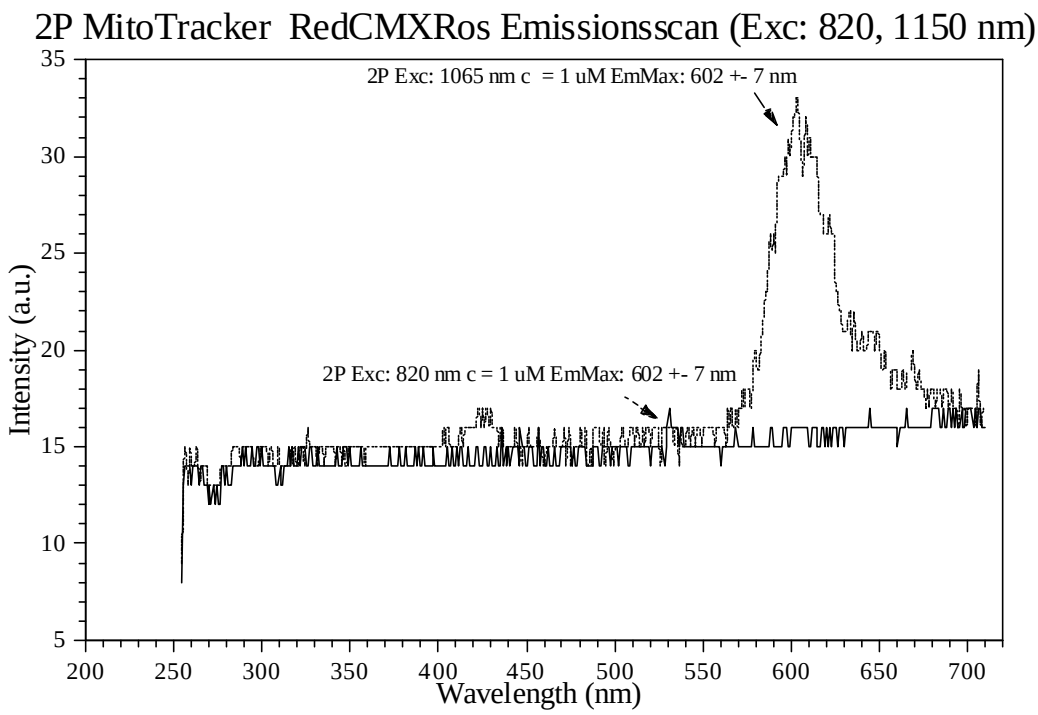

FIG 8_13:Two TPE emission scans of MitoTrackerRed CMXRos c = 1 µM in PBS. One at the excitation maximum of 1065 nm, the other near the used excitation wavelength of 798 nm for TPE LSM

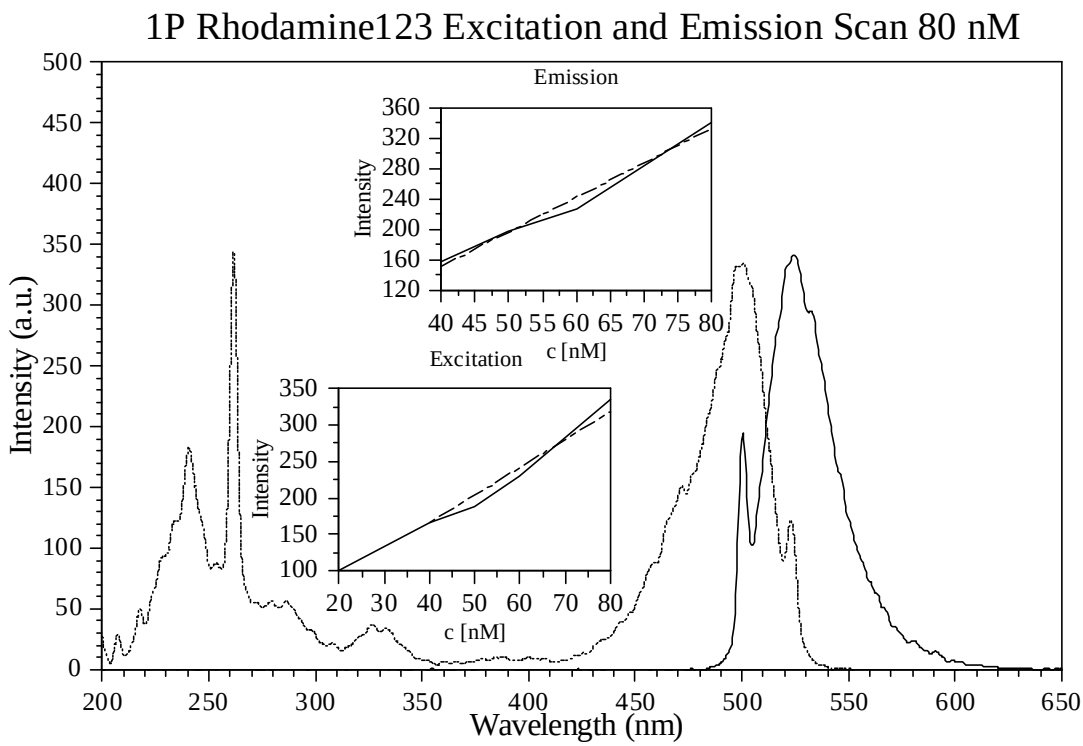

FIG 8_14: One Photon Fluorescence Spectroscopy of Rhodamine 123, c = 80 nM ····Excitation, — Emission. The small boxes illustrate the linear dependency of fluorescence intensity on the concentration for the measured range for Excitation Max: 502 ± 5 nm and Emission Max: 523.5 ± 2.5 nm --- Regression line

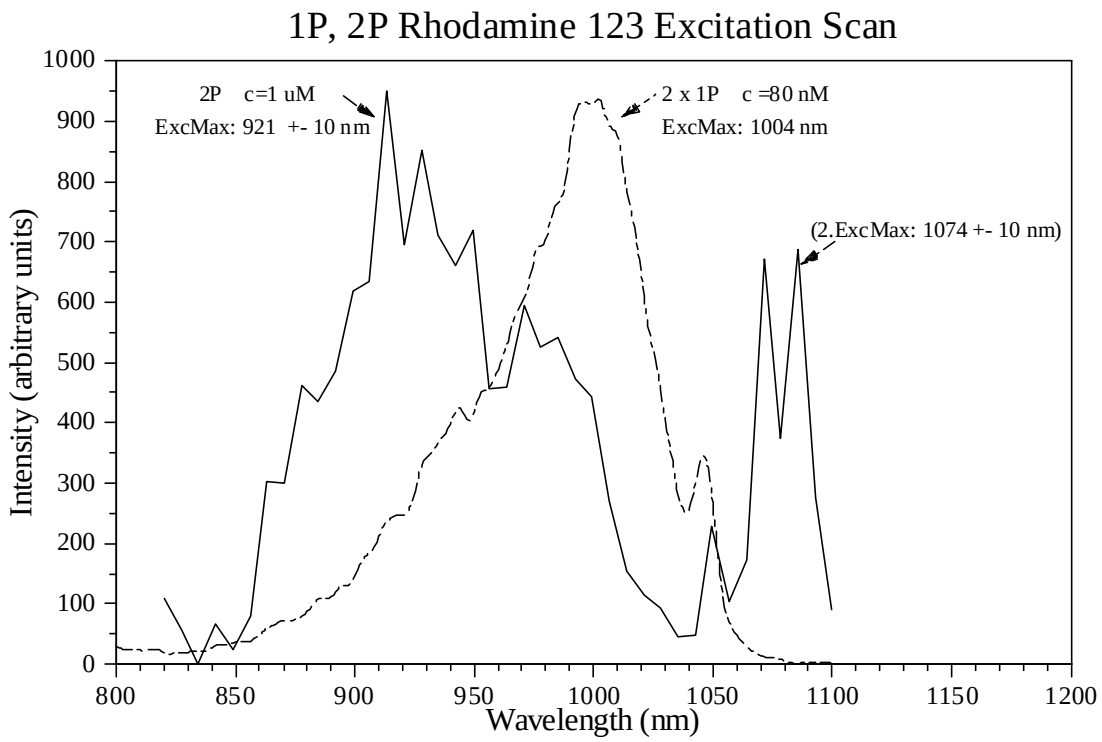

FIG 8_15: _._. Theoretical doubled one photon excitation scan (c = 80 nM) , ExcMax: 1004 nm and ___TPE excitation wavelength scan (c = 1 µM), ExcMax: < 820, 921± 10 nm of Rhodamine 123

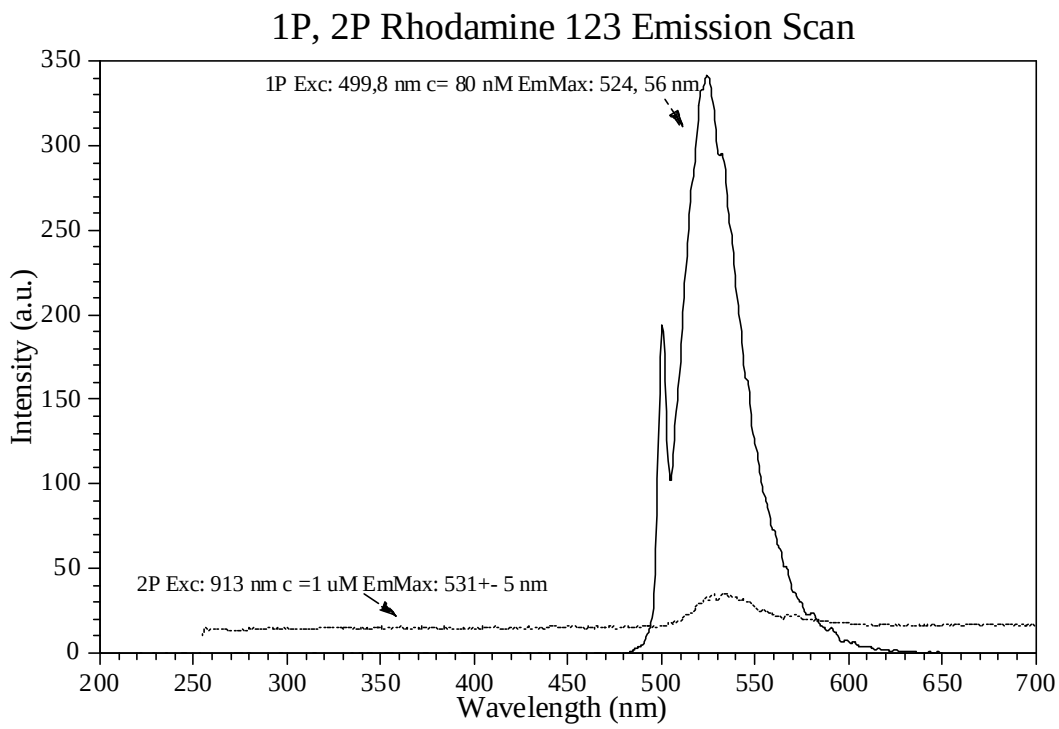

FIG 8_16: One and TPE Emission wavelength scan of Rhodamine 123, excited at the absorption maximums: 499.8 nm for 1P, concentration c = 80 nM, 913 nm for 2P, c = 1 µM

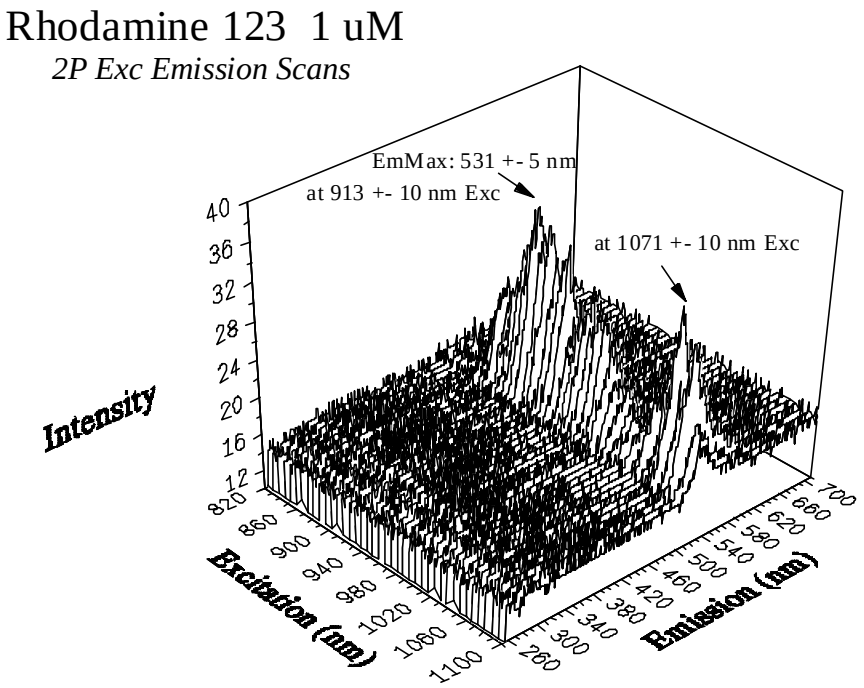

FIG 8_17: TPE Emission scans of Rhodamine123 c = 1 µM in PBS, from 820 to 1150 nm excitation every 6 -7 nm an emission wavelength scan was performed over a range of 254 to 800 nm.

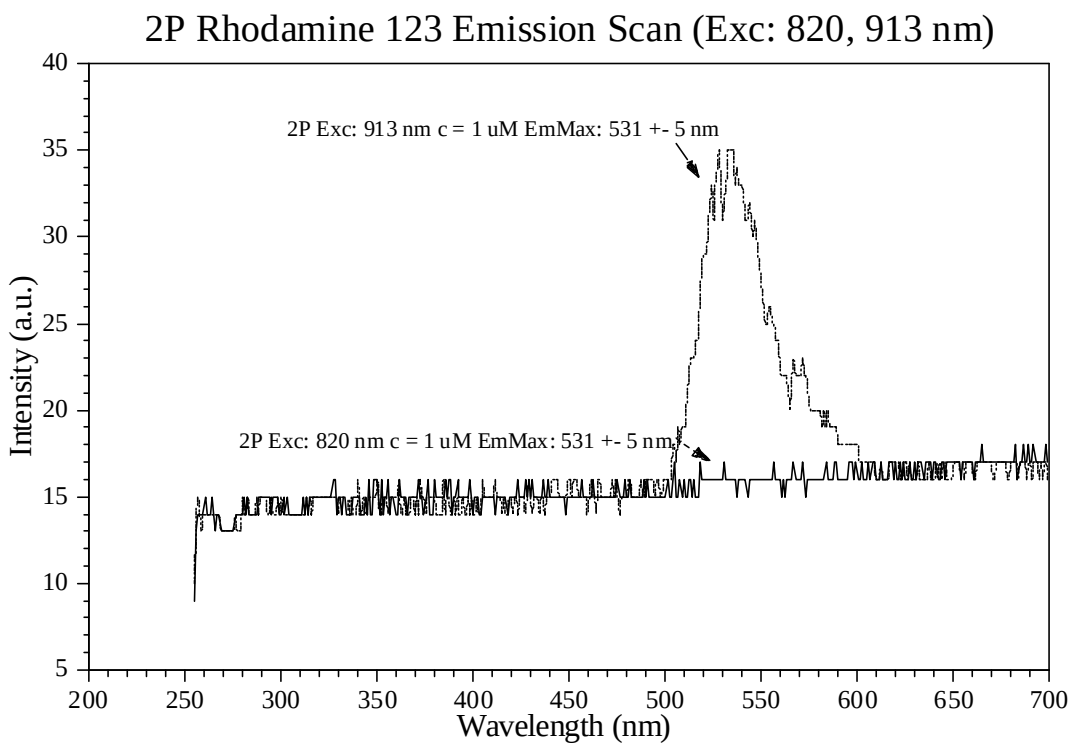

FIG 8_18 :Two TPE emission scans of Rhodamine c = 1 µM in PBS. One at the excitation maximum of 913 nm, the other near the used excitation wavelength of 798 nm for TPE LSM

As the spectroscopic measurements (OPE and TPE) were performed on different instruments, intensity levels cannot be compared directly. Therefore for extrapolation and comparison of OPE and TPE excitation maximums absolute intensity levels were abolished. (arbitrary units)

Fluorescent Dyes	Excitation Maximums in nm			Emission Maximums in nm	
	1 P (AbsMax)	2 x 1 P	2 P	1 P	2 P
DAPI	358 (n.d.)	716	690 ± 10	461 (n.d.)	455 ± 5
2´,7´-DCF	501 ± 1 (503)	1002	1065, > 1150	522.5 ± 1.5	530 ± 3
MTRed	575 ± 2 (578)	1150	> 1150	594.5 ± 3.5	602 ± 7
Rho 123	502 ± 5 (500)	1004	921 ± 10, 1074 ± 10	523.5 ± 2.5	531 ± 5

Table 8 _4 Absorption (AbsMax), Excitation and Emission Maximums of the applied dyes in one and two photon spectroscopy and microscopy. (2x1P , doubled one photon excitation spectra, are theoretical values) (n.d.: not determined by own experiments, www.probes.com, solvent: H_20)

Table _4 summarises excitation and emission maximums of the fluorescent dyes applied in the experiments. Compared with one photon excitation fluorescence spectroscopy DAPI and Rhodamine have a blue shifted excitation maximum whereas, MitoTrackerRed and 2’7’-DCF have a red shifted one in two photon excitation spectroscopy. The emission of DCF, MT Red and Rho 123 are slightly red-shifted in TPE. The OPE and TPE curves have different shapes.

8.3 Optical Barrier Filter Transmission Range

Dyes and optical barrier filters had to be optimised. Therefore the optical filter were chosen appropriate to the emission maximums. With one exception of the 1P Barrier 488 ± 5 nm which is an excitation filter, the represented filters are emission filters. The transmission range is demonstrated in Figures 8_19 a and b. The measured transmission range was corresponding to the specifications given by AF analysentechnik. All filter are bandpass filter, the 2P emission filter have additionally shortpass properties, they cut off the light above the transmitted wavelength range, whereas the 1P filter transmit light above around 700 nm (488 ± 5 nm, 515 ± 15 nm), respecively 800 nm (590 ± 30 nm).

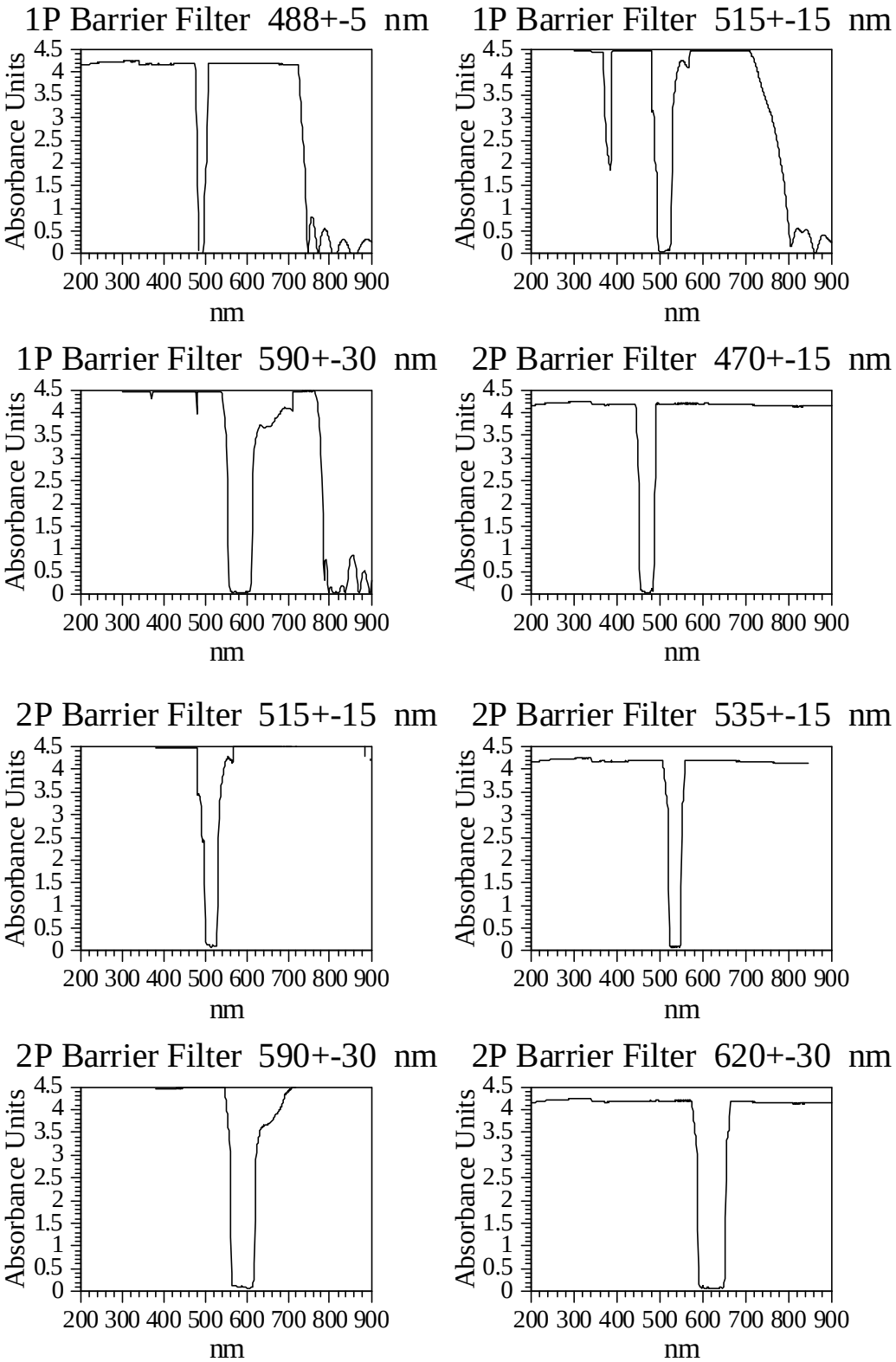

FIG 8_19: The transmission range of used Emission Optical Barrier Filter.. Light is cut off when Absorbance Units are high. Only the 1Photon (1P) filter of 488 ± 5 nm is an excitation filter, all the others are emission filter.

9. Determination of the theoretical and experimental Point Spread Function of the Laser Scan Microscope System

9.1 Theoretical Point Spread Function

9.1.1 Optical slices through theoretical PSFs and three dimensional visualisation

The theoretical determination of the point spread function requires specifications about the sampling density in lateral and axial direction, the used mode of microscopy, the aperture of the objective, the refraction indices of mounting and lens media, the excitation and emission wavelength respectively the middle wavelength of the used barrier filter and the number of excitation photons. For each experimental determined point spread function the theoretical one was computed and illustrated three-dimensionally: for one photon excitation CLSM in Figure 9_6 for orange fluorescent microspheres in PBS and the appropriate emission filter, for green fluorescent microspheres in Vectashield in Figure 9_7 and Figure 9_9, and in PBS in the latter figure, for orange fluorescent microspheres in Mowiol in the same Figure 9_9. For TPE CLSM the theoretical point spread functions of green, orange and red fluorescent microspheres in PBS and each with the appropriate emission filter are illustrated in Figure 9_12, for Mowiol and Vectashield as Mounting Media, there is practically hardly any difference. Thereby the bead model is used as basis for calculation. For 2P LSM PSF of green microspheres embedded in PBS additionally optical slices of the middle of all extensions x, y, z (centre of mass) were performed, for the theoretical one, shown in Figure 9_1 b-d. The represented slices have a distance of -0.45 µm, 0 µm, 0.45 µm for the xy-slices, –1.6 µm, 0 µm, and 1.6 µm for the xz and yz-slices from the centre of mass. For the corresponding experimental PSF optical slices are demonstrated in Figure 9_4 a-d. The xy- slices are at a distance of the centre of ± 1.8 µm, ± 0.9 µm and 0 µm, the xz- and yz-slices at a distance of ± 0.642 µm, ± 0.321 µm, 0 µm.

The intensity scale for Huygens 2 is shown in Figure 9_1a, h, s. The projection mode *linear mode* and the false colour representation was chosen, to show the intensity distribution with red the highest, over orange, green, blue, violet to the lowest intensity. The slices were saved as TIF files.

The parameters of this point spread function are:

Geometry (nm)	
x, y sample size:	48.828 nm
z sample size:	150.00 nm
Optical parameters	
Microscope type:	Wide field
Numerical aperture:	1.2
Pinhole radius (backprojected):	-
Refractive indexes:	
Lens (Water):	1.334
Medium:	1.334
Parameter for channel:	
Excitation wavelength:	798 nm
Emission wavelength:	515 nm
Excitation photons:	2

An overview about the parameters of the different measured point spread functions are given in Materials and Methods, section 7.4.5 in Tables 7_5 and 7_6, pages 62 and 63.

FIG 9_1 a Intensity scale

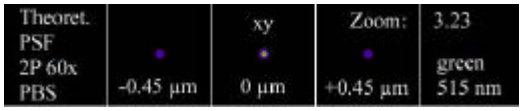

FIG 9_1 b Theoretical PSF: xy - slices

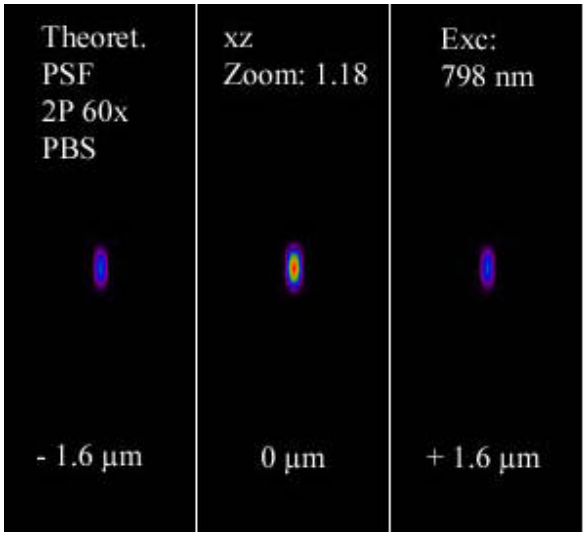

FIG 9_1 c Theoretical PSF: xz- slices

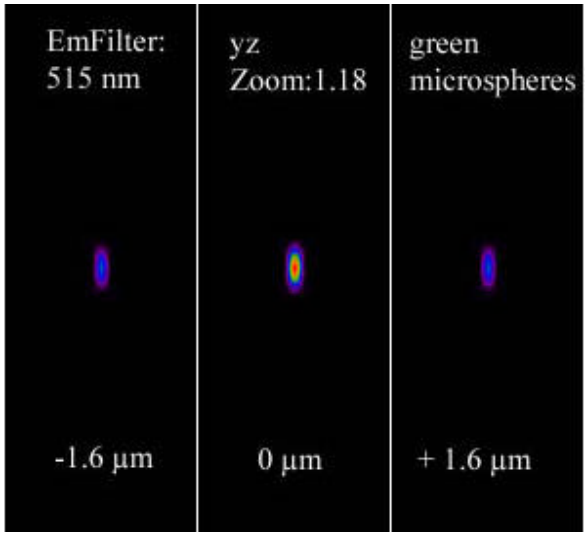

FIG 9_1 d Theoretical PSF: yz – slices

9.2 Theoretical and Experimental Full Width of Half Maximum (FWHM) of Intensity Distribution:

Determination of the resolution limits of the 2P PSF in PBS at an emission wavelength of 515 nm

The theoretical and the experimental full width of half maximum of the 2P LSM PSF of green microspheres embedded in PBS were determined by saving the middle slice of the xz optical cut as TIF file, converting it from 24 bit to a 8 bit grey scale image, drawing a line with Laser Sharp Processing (Image-> Scale -> Select Line Intensity) through the centre of the PSF in order to get an intensity distribution along this line, which was visualised with the software package TechPlot.

The theoretical FWHM of this PSF is graphed in Figure 9_2, the experimental FWHM in Figure 9_3. Each time the lateral (a) and the axial (b) resolution limit was determined at an emission wavelength of 515 nm, and an two photon excitation wavelength of 798 nm.

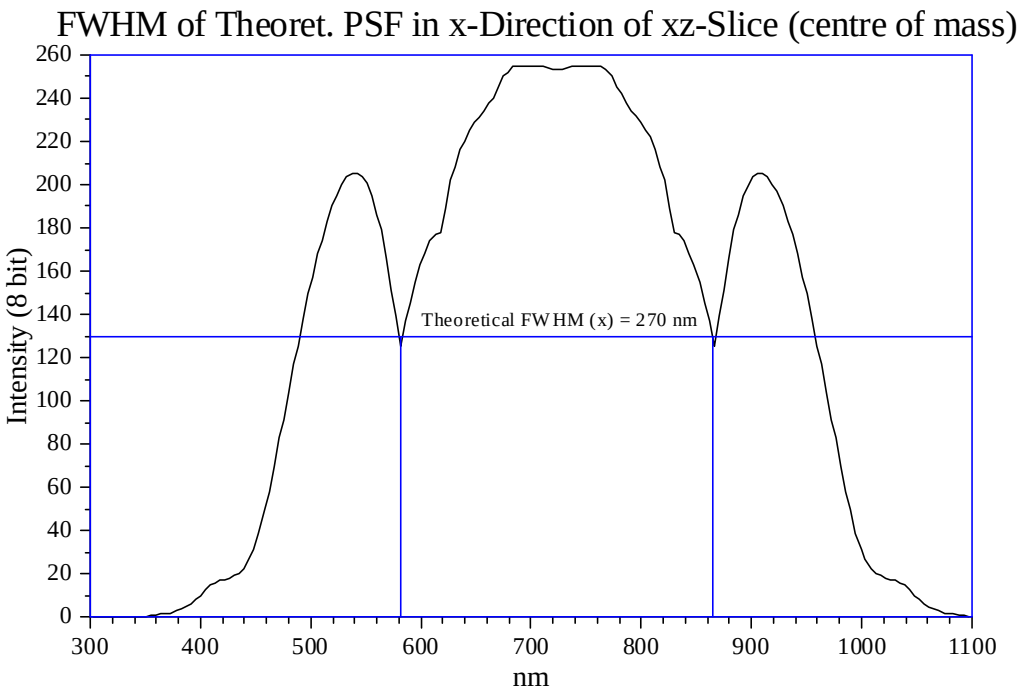

FIG 9_2 a Theoretical Full Width of Half Maximum in x-direction: 270 nm is the theoretical lateral resolution limit at 515 nm emission wavelength

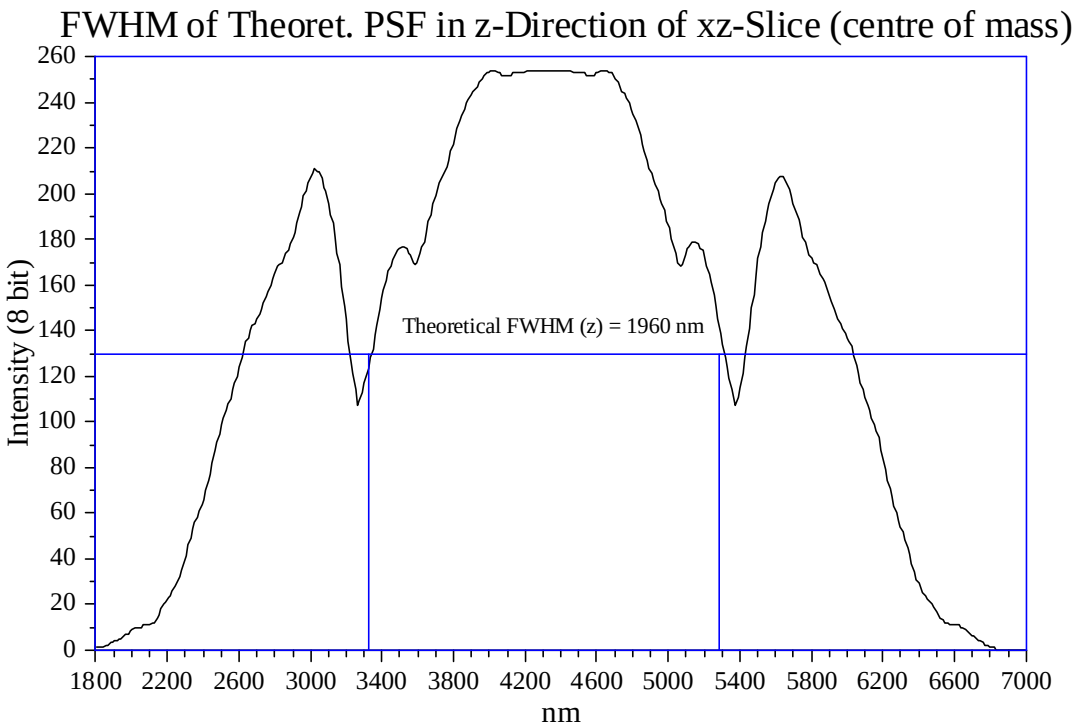

FIG 9_2b Theoretical Full Width of Half Maximum in z-direction: 1960 nm is the theoretical axial resolution limit at 515 nm emission wavelength (8 bit grey scale)

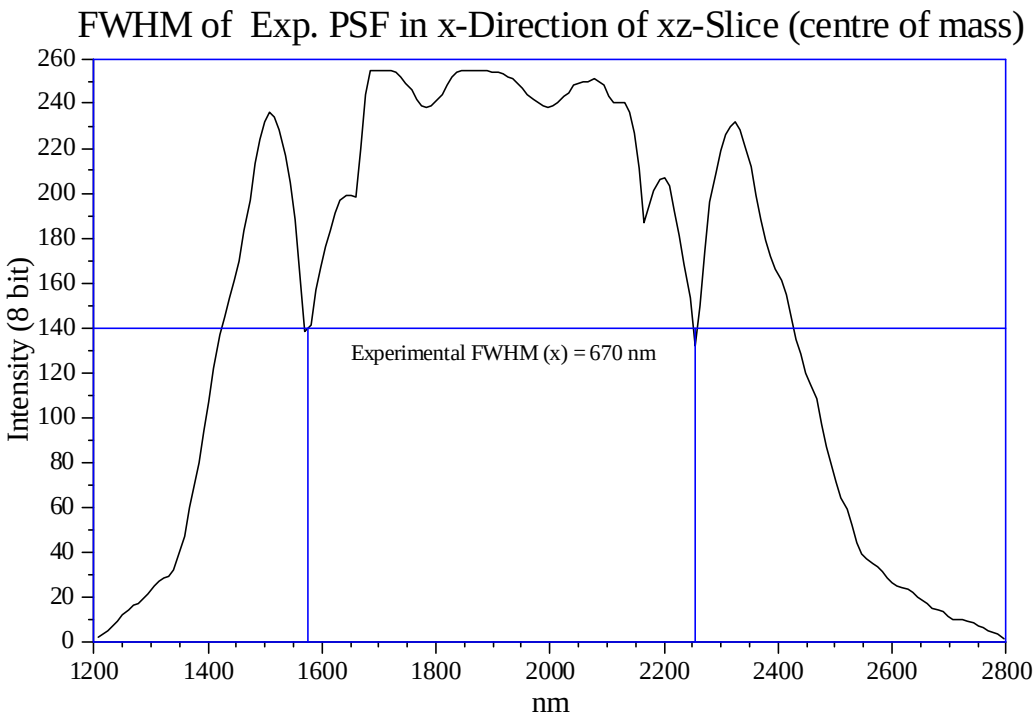

FIG 9_3 a Experimental Full Width of Half Maximum in x-direction: 670 nm is the experimental lateral resolution limit at 515 nm emission wavelength

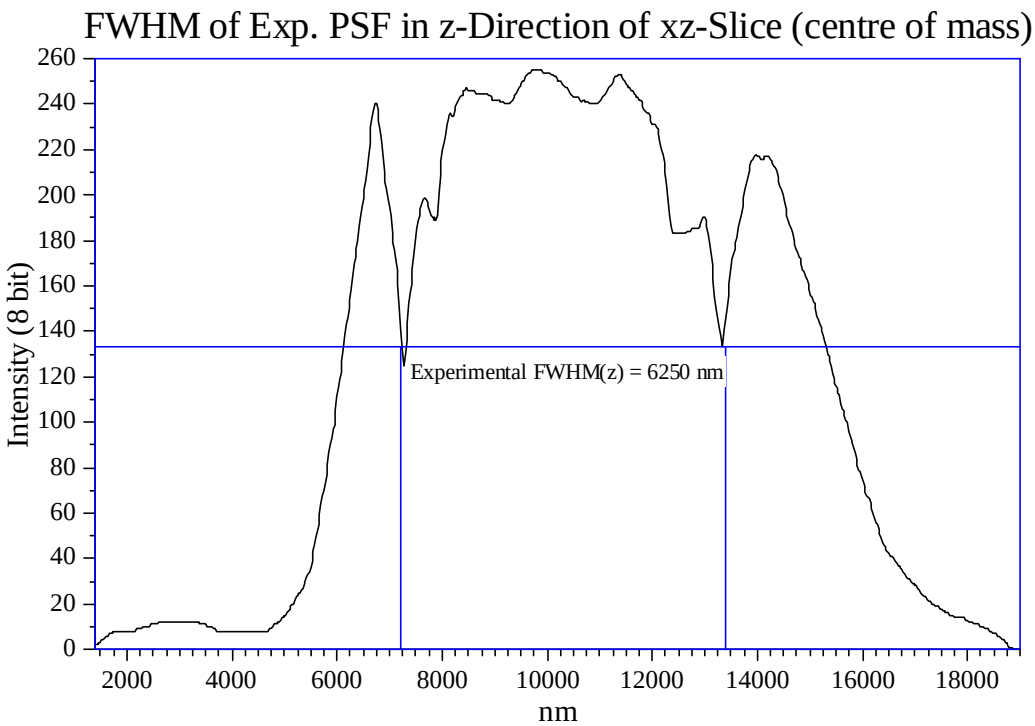

*FIG 9_3*b Experimental Full Width of Half Maximum in z-direction: 6250 nm is the experimental axial resolution limit at 515 nm emission wavelength

9.3 Measured Experimental Point Spread Functions

9.3.1 Determination of Averaged Beads and Signal to Noise Ratio of the PSFs

Excitat. Photons	Excitation (nm)	Objective (x)	r (Pinhole) (µm)	Medium	EmFilter (nm)	n (Beads)	Signal / Noise
1	488	40	10	Vectash.	515 ± 15	12	11.347
1	543.5	40	10	Mowiol	590 ± 30	14	12.798
1	488	60	10	Vectash.	515 ± 15	12	24.398
1	543.5	60	10	Mowiol	590 ± 30	19	34.693
1	488	60	10	PBS	515 ± 15	36	16.360
1	543.5	60	10	PBS	590 ± 30	52	25.253
1	543.5	60	25	PBS	590 ± 30	28	10.755
1	543.5	60	WF	PBS	590 ± 30	8	2713.607
2	798	60	WF	Vectash.	515 ± 15	5	15.980
2	798	60	WF	Mowiol	590 ± 30	6	25.938
2	798	60	WF	PBS	515 ± 15	31	22.256
2	798	60	WF	PBS	590 ± 30	22	24.206
2	798	60	WF	PBS	620 ± 30	23	23.195

Table 9_1 Number of averaged beads (n) and signal (S) to noise (N) ratio of measured point spread functions after final baseline adjustment WF: Wide field mode, Vectash.: Vectashield

Table 9_1 shows the number of beads which were needed to become the indicated signal to noise ratio. The signal (S) to noise (N) ratio was determined by:

$$S / N = \sqrt{\max voxelvalue / background}$$

9.3.2 Optical slices through experimental PSFs

Optical slices of the corresponding experimental PSF for TPE LSM of green microspheres embedded in PBS are shown in Figures 8_23b-d. These are TIF-files of the PSF, cut in xy, xz, yz-direction within the centre of mass. For the other experimental determined point spread function x, z and y, z slices on the level of the centre of mass are presented in Figures 8_23 d to p. The projection mode *linear mode* and the false colour representation was chosen, to show the intensity distribution with red the highest, over green, blue, violet to the lowest intensity. The slices were saved as TIF files.

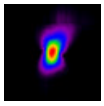

FIG 9_4a: MIP-projection

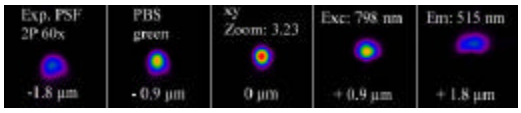

b: xy – slice

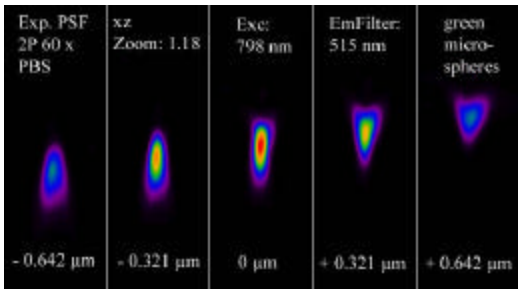

c

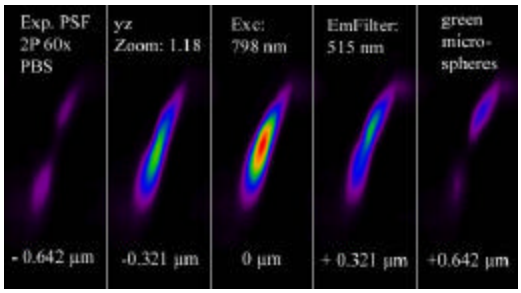

d

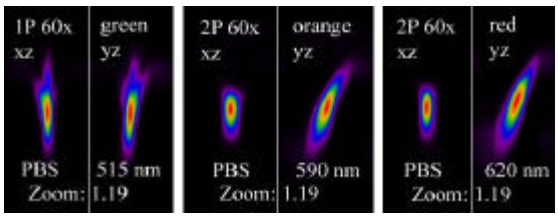

e *f* *g* *h*: Intensity scale

FIG 9_4 a Maximum Intensity Projection (MIP): For each vertical column of voxels a ray is traced and corresponds to a pixel in a in the 2D Projection Image: The largest value is selected and assigned to the screen image of the experimental 2P PSF, green microspheres in PBS, Exc: 798 nm, Em: 515 nm

FIG 9_4 b -d xy, xz, yz – slices of the exp. 2P PSF, green, PBS, Zoom factor: 3.23 for *b*, 1.18 for *c, d* 0 µm is the middle of its extension

FIG 9_4 c – g xz and yz slices through experimental PSF in the middle of their extension, if not specified; Zoom between 1.18 and 1.21 *h* Intensity scale of Huygens 2

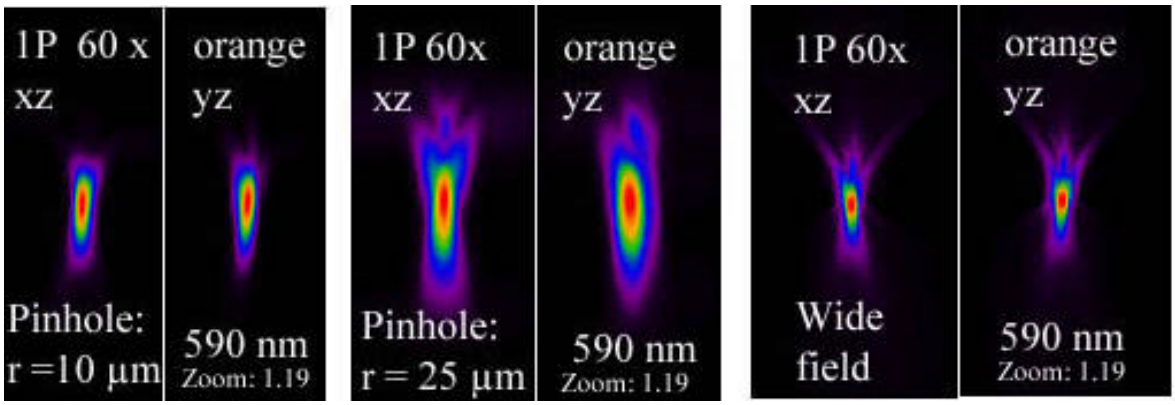

i *j* *k*

FIG 9_4 i-k xz and yz slices through experimental PSF in the middle of their extension, if not specified; Zoom: 1.19, 1P PBS orange 60x, small, big pinhole and without pinhole

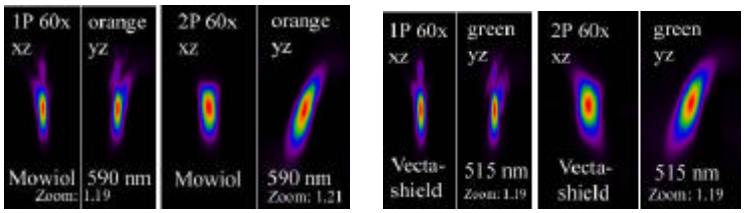

Remark: The wide field (OPE) had the double sampling distance

l *m* *n* *o*

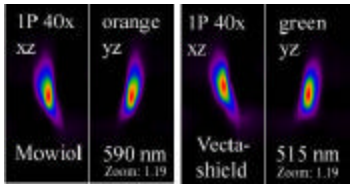

p *r* *s*: intensity scale

FIG 9_4 l –r xz and yz slices through experimental PSF in the middle of their extension, if not specified; Zoom between 1.18 and 1.21

FIG 9_4 s Intensity scale of Huygens2, Maximal Intensities are shown in red, lower over yellow, green in violet, the background is shown in dark

Remark: The wide field (w/o pinhole) had around the double sampling distance as the other PSF, therefore the cut should be demonstrated in a bigger field, which was not possible due technical restriction in the Huygens2 system as the PSFs were always depicted in the same-sized window

Figure 9_4 demonstrates asymmetries along the z-axis, especially for the y-z slices. This is illustrated in more detail for the PSF 2P in PBS green in Figure 9_4b (xy), c (xz), d (yz) . The point spread function PBS orange with big pinhole in Figure 9_4j demonstrates a much more extended volume than for the one measured with the small pinhole in Figure 9_4i. The shape of Figure 9_4j is much more complex than that of the small pinhole and

resembles to the shape of the wide field PSF in Figure 9_4k . In general the x, y extensions of the 1P PSFs 60x (Figures 9_4 e, i, l, n) are less than that of the corresponding 2P PSF (Figures 9_4 c, f, m, o). Compared to the 40 fold magnification oil immersion 1P PSFs (Figure 9_4 p, r) the x, y extensions of a 1P PSFs 60 x with the water objective in Mowiol and Vectashield (Figure 9_4 l, n) are smaller.

Because of too weak fluorescence signals the PSFs in PBS either of green or orange fluorescent microspheres could not be determined for the oil immersion objective 40x. The PSF in Vectashield could only be measured for the green fluorescent microspheres, the PSF in Mowiol only for the orange fluorescent microspheres at least for one photon excitation CLSM. For TPE LSM the corresponding PSFs were measured. Additionally, the PSF in PBS of the red fluorescent microspheres was possible to determine.

9.3.3 Three-Dimensionally Visualised Point Spread Functions

Point Spread Functions were measured for one photon excitation CLSM and are visualised in Figures 9_5 to 9_9, for TPE LSM PSFs are illustrated in Figures 9_10 to 9_12.

In Figure 9_5, 9_6, 9_8, 9_9 three-dimensional theoretical and experimental point spread functions in different mounting media visualised by AVS/Express are shown for one photon excitation CLSM with the water objective 60 fold magnification.

In Figure 9_7 the oil immersion objective 40 fold magnification was used.

In Figure 9_10 and 9_11 experimental point spread functions, in Figure 9_12 theoretical point spread functions are shown for two photon excitation laser scanning microscopy.

The PSF for wide field fluorescence microscopy (Fig 9_5 red) is more extended than that for confocal fluorescence microscopy both with big (Fig 9_5 yellow, which appears orange because of overlapping effects) and small pinhole (Fig 9_5 blue). The PSF imaged through the appropriate small pinhole with a radius of 10 µm which should be used for 60 fold as well as for 40 fold magnification exhibits the smallest dimensions.

In different mounting media different distortions in different directions emerge.

The longer the emission wavelength the more extended is the point spread function, however the experimental 2P PSF in PBS of green and orange fluorescent microspheres overlap nearly totally. They were measured the same day with the same settings of the laser scanning microscope.

One Photon Excitation Confocal Laser Scanning Microscopy
Visualised by Advanced Visual Systems (AVS), Surface Rendering:
Point spread functions (PSFs) in PBS - Magnification: 60x Water Objective

Object: orange fluor(escent) microspheres
Mounting Medium: PBS Em(mission) Filter: 590 ± 30 nm

Blue: With Small Pinhole,Ø = 20 µm (optimal), backprojected pinhole radius: 167 nm
Yellow: With Great Pinhole, Ø = 50 µm, backprojected pinhole radius: 417 nm
Red: Without Pinhole (like Conventional Wide Field Fluorescence Microscopy

FIG 9_5 Experimental (Exp) PSF orange in PBS under different conditions

The small pinhole (20 µm diameter) appropriate for a 60 fold magnification was applied for cellular measurements.

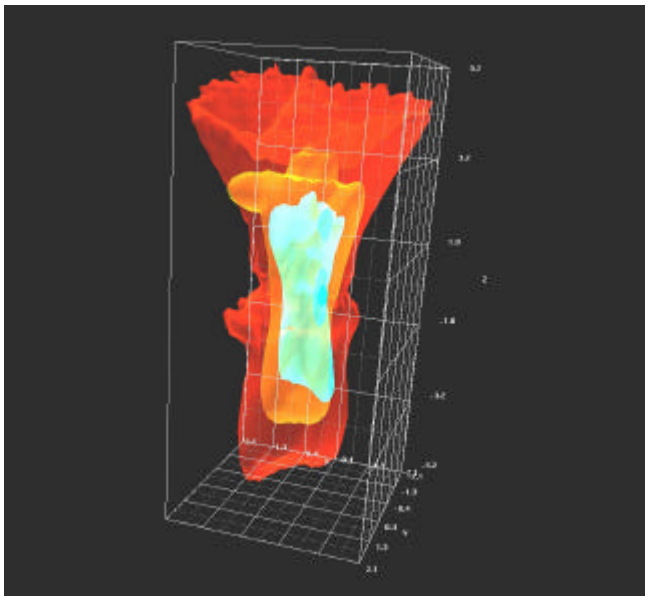

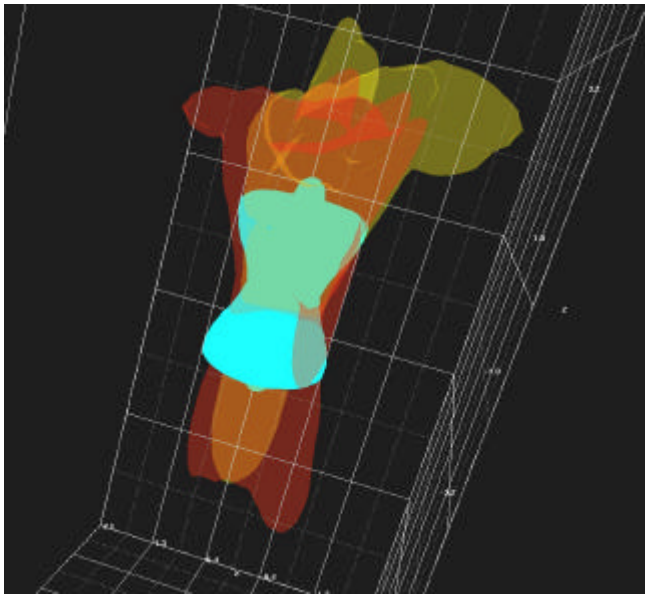

FIG 9_6 Theoretical (Theo) and Exp. PSF in PBS

Small Pinhole,Ø = 20 µm, backprojected pinhole radius: 167 nm
Mount(ing) Med(ium): Phosphate Buffered Saline (PBS)

Blue: Theo. PSF orange (fluor. Microspheres) Em Filter: 590 ± 30 nm
Yellow: Exp. PSF green (fluor. Microspheres) Em Filter: 515 ± 15 nm
Red: Exp. PSF orange(fluor. Microspheres) Em Filter: 590 ± 30 nm

One Photon Excitation Confocal Laser Scanning Microscopy Visualised by Advanced Visual Systems (AVS/Express), Surface Rendering: Point Spread Function - Magnification: 40x Oil Immersion Objective Mounting Media: Mowiol and Vectashield (Antifade Reagent)

Small Pinhole: Ø = 20 µm, backprojected pinhole radius: 250 nm

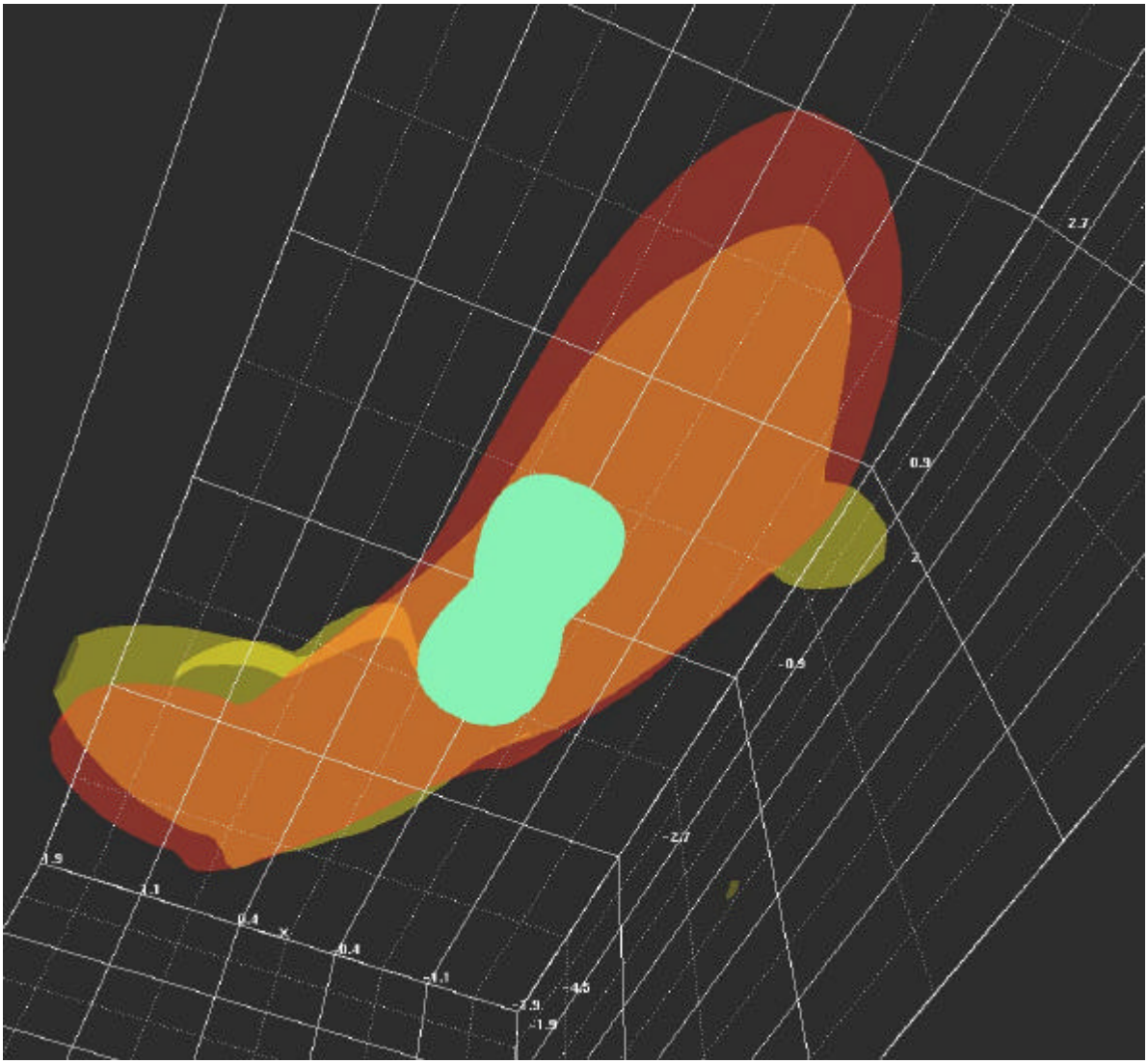

FIG 9_7 Theo. and Exp. PSF in Vectashield and Mowiol

Blue:	Theoret. PSF green	Mount. Med: Vectashield	Em.Filter: 515 nm ± 15 nm
Yellow:	Exper. PSF green	Mount. Med.: Vectashield	Em.Filter: 515 nm ± 15 nm
Red:	Exper. PSF orange	Mount. Med.: Mowiol	Em.Filter: 590 nm ± 30 nm

One Photon Excitation Confocal Laser Scanning Microscopy
Visualised by Advanced Visual Systems (AVS/Express), Surface Rendering :
Point Spread Function - Magnification: 60x Water Objective
Theoretical (Theo) and Experimental (Exp) Point Spread Function (PSF)
Different Mounting Media

Small Pinhole: Ø = 20 µm, backprojected pinhole radius: 167 nm

Blue:	Mounting Medium: PBS	Exp. PSF green	Em Filter: 515 ± 15 nm
Yellow:	Mounting Med: Vectashield	Exp. PSF green	Em Filter: 515 ± 15 nm
Red:	Mount. Medium: Mowiol	Exp. PSF orange	Em Filter: 590 ± 30 nm

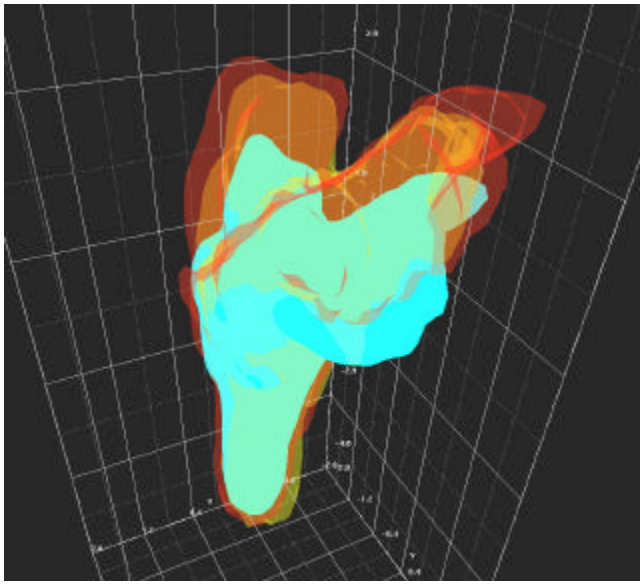

FIG 9_8 Exp PSF in various Mounting Media

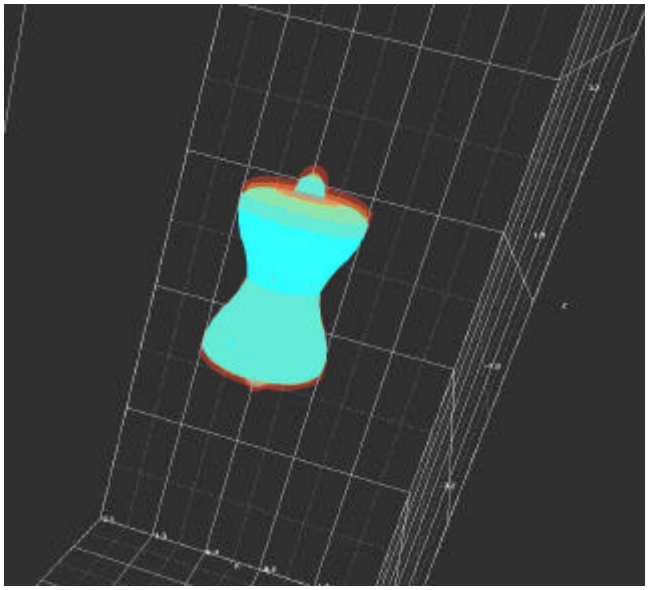

FIG 9_9 Theo PSF in various Mounting Media

Blue:	Mounting Medium: PBS	Theo. PSF green	Em Filter: 515 ± 15 nm
Yellow:	Mount. Med: Vectashield	Theo. PSF green	Em Filter: 515 ± 15 nm
Red:	Mount. Medium: Mowiol	Theo. PSF orange	Em Filter: 590 ± 30 nm

One Photon Excitation Confocal Laser Scanning Microscopy
Visualised by Advanced Visual Systems (AVS), Surface Rendering:
Point spread functions (PSFs) in PBS - Magnification: 60x Water Objective

Object: orange fluor(escent) microspheres
Mounting Medium: PBS Em(mission) Filter: 590 ± 30 nm

Blue: With Small Pinhole,Ø = 20 µm (optimal), backprojected pinhole radius: 167 nm
Yellow: With Great Pinhole, Ø = 50 µm, backprojected pinhole radius: 417 nm
Red: Without Pinhole (like Conventional Wide Field Fluorescence Microscopy)

FIG 9_5 Experimental (Exp) PSF orange in PBS under different conditions

The small pinhole (20 µm diameter) appropriate for a 60 fold magnification was applied for cellular measurements.

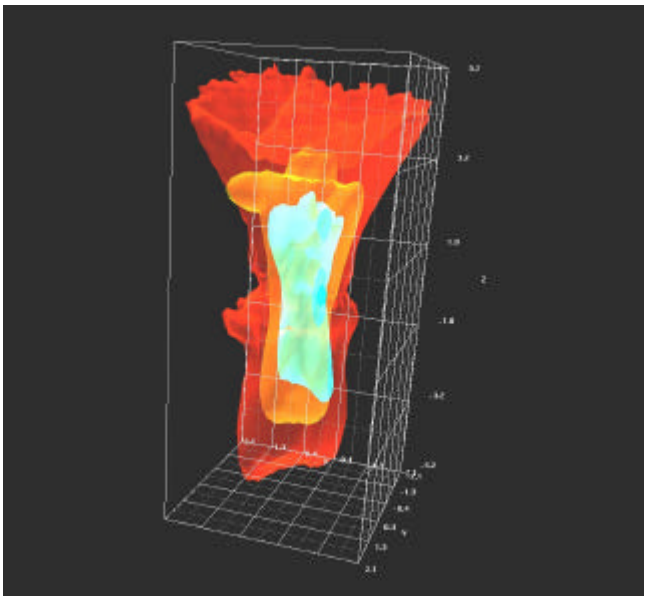

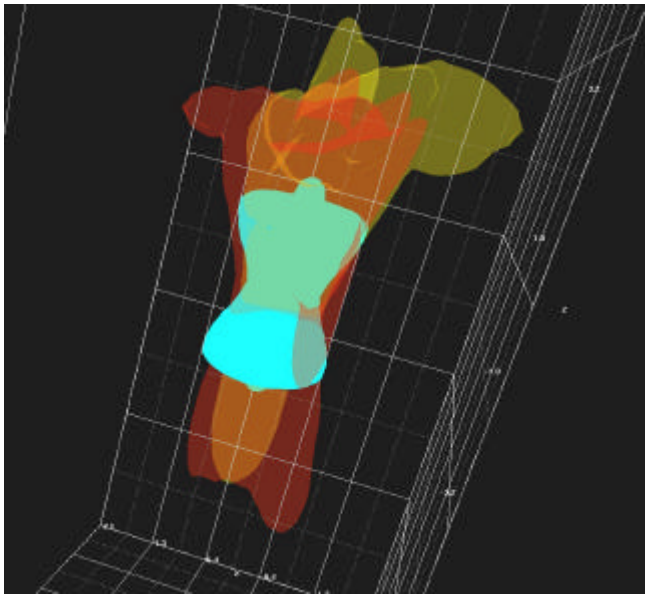

FIG 9_6 Theoretical (Theo) and Exp. PSF in PBS

Small Pinhole,Ø = 20 µm, backprojected pinhole radius: 167 nm
Mount(ing) Med(ium): Phosphate Buffered Saline (PBS)

Blue: Theo. PSF orange (fluor. Microspheres) Em Filter: 590 ± 30 nm
Yellow: Exp. PSF green (fluor. Microspheres) Em Filter: 515 ± 15 nm
Red: Exp. PSF orange(fluor. Microspheres) Em Filter: 590 ± 30 nm

10. Localisation of Reactive Oxygen Species in HepG2 Cells

The localisation of ROS were performed by one photon excitation CLSM pictured as 3D visualisation in the Figures 10_1, 10_2, 10_3 and by TPE LSM illustrated three dimensionally in the Figures 10_4, 10_5, 10_6, 10_7, 10_8, and 10_9. One single or two Hep G2 cells (Fig 10_7) are shown in these figures. Perinuclear mitochondrial mass, stained with MitoTracker Red, is depicted in pink. DCF and Rhodamine fluorescence in green, the hot spots in blue, the highest intensities in white or yellow.

Figure 10_1 represents one single HepG2 cell with perinuclear mitochondrial mass as well as Rhodamine 123 (RHO) fluorescence. Yellow probably indicates the hypothesized hot spots located inside and outside of mitochondrial compartments surrounding the cell nucleus. RHO can never be found in the cell nucleus in contrast to DCF after long term use shown in Figure 10_3. Figure 10_2 and 10_3 both demonstrate the perinuclear compartment filled up with mitochondrial mass and DCF fluorescence. DCF is first found perinuclear in the cytoplasm inside and outside of mitochondria in Figure 10_2. This image was recorded about 20 min after staining HepG2 cells. About 30 min after staining DCF can be imaged with different fluorescence intensities also inside the cell nucleus illustrated in Figure 10_3. The cells were imaged immediately one after the other in the same specimen.

Visualised by two photon excitation laser scan microscopy Figure 10_4 represents one single HepG2 cell with clear separation of perinuclear non mitochondrial and mitochondrial compartments containing hot spots of RHO generation. Shortly after staining DCF can be imaged in the perinuclear space as shown in Figure 10_5 and about 30 min after staining within the cell nucleus illustrated in Figure 10_6.

In Figure 10_7 nuclear space marked by DAPI fluorescence of two HepG2 cells (depicted in red) is surrounded by mitochondrial compartments (pink) and non mitochondrial compartments containing the hypothesised hot spots of RHO generation (white or blue and green). Triple labelled cells with DCF fluorescence are pictured in Figure 10_8 and Figure 10_9. DAPI fluorescence (red) overlaps with DCF fluorescence (green, hot spot in white) in the cell nucleus surrounded by mitochondrial mass (pink).

The Signal to Noise ratio, the number of performed iterations and the Quality factor of the estimated non deconvoluted images are shown in Table 10_1.

Figure	Staining	Maximal Voxel Value	Estimated background	Signal to Noise ratio	Number of Iterations	Quality factor
10_1	1P DHR MT	255 255	12.120469 10.090449	4.587 5.027	67 27	2.49364 1.77756
10_2	1P DCF MT	111 183	11.294317 11.419381	3.135 4.003	44 32	4.0826 6.9862
10_3	1P DCF MT	145 255	10.388564 11.508786	3.736 4.707	51 34	4.4393 3.9655
10_4	2P DHR MT	255 255	6.789117 8.111981	6.129 5.607	89 38	1.8771 1.9447
10_5	2P DCF MT	255 255	9.328216 9.999952	5.228 5.050	28 28	1.5317 1.8533
10_6	2P DCF MT	228 222	9.206805 8.563297	4.977 5.092	58 56	2.1903 2.94767
10_7	2P DAPI DHR MT	255 255 255	9.508552 9.854968 10.244842	5.1786 5.0868 4.989	30 34 30	2.8595 3.0364 2.6838
10_8	2P DAPI DCF MT	255 255 255	9.999222 10.812318 10.513561	5.050 4.856 4.925	29 24 23	4.55994 3.00361 3.88723
10_9	2P DAPI DCF MT	255 255 255	10.216226 12.855393 11.575617	4.996 4.454 4.694	27 22 20	3.98164 2.13333 1.8893

Table 10_1 Specifications about the Signal to Noise ratio of the non-deconvoluted image, the number of iterations to obtain the convoluted image and the quality factor (I-divergence measure) of the performed deconvolution process.
1P = 1Photon Excitation, 2P = 2Photon Excitation, DCF = 2',7'-Dichlorofluorescein, DHR = Dihydrorhodamine 123, MT = MitoTrackerCMXRos, DAPI = 4',6-diamidino-2-phenylindole, dihydrochloride
Confocal images of different dyes which contribute to one figure had to be deconvoluted seperately.

A signal to noise (S /N) ratio below 5 actually lowered the lateral resolution using the MLE estimation (A S / N below 3 reduces the axial resolution).

One Photon Excitation Confocal Laser Scanning Microscopy of Human Hepatoma Cells (HepG2) visualised by AVS/Express, Surface Rendering, Magnification: 60 x Water Objective Mounting Medium: PBS

FIG 10_1 One HepG2 cell stained with:

MitoTracker Red CMXRos (MT)
shown in violet, Iso level: 300
EmFilter: 620 ± 30 nm

Dihydrorhodamine123 (DHR) converted in (»)
Rhodamine 123 (RHO)
shown in green, Iso level:300
EmFilter: 515 ± 15 nm
The hot spots of ROS generation
are shown in blue, Iso level: 3400; and
yellow, Iso level: 5450.
Maximal value of Isosurface RHO: 6810.5

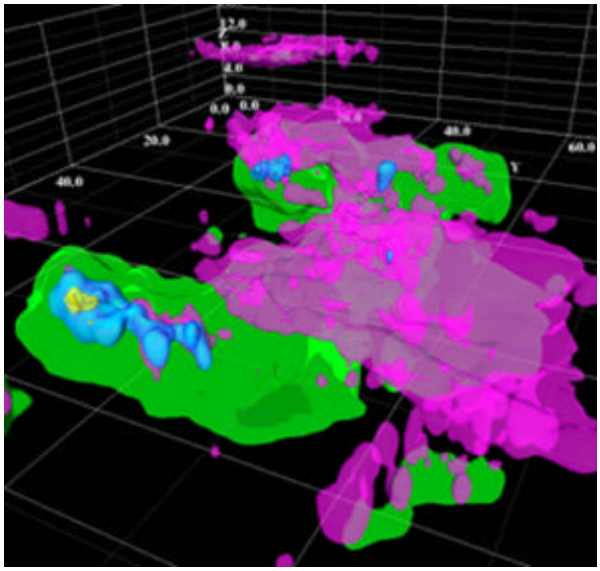

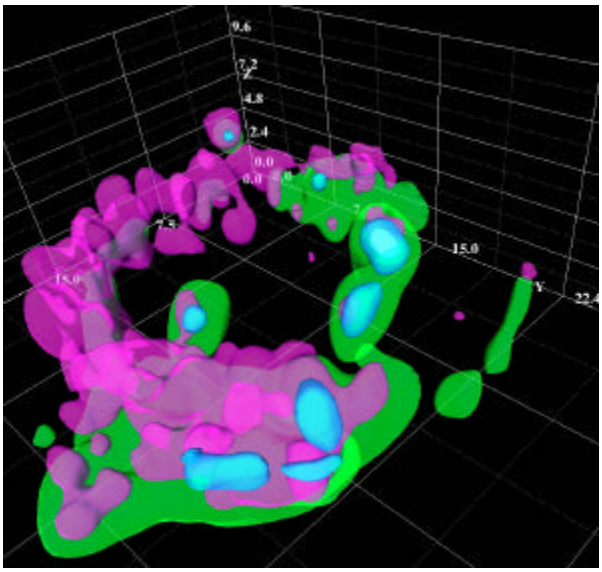

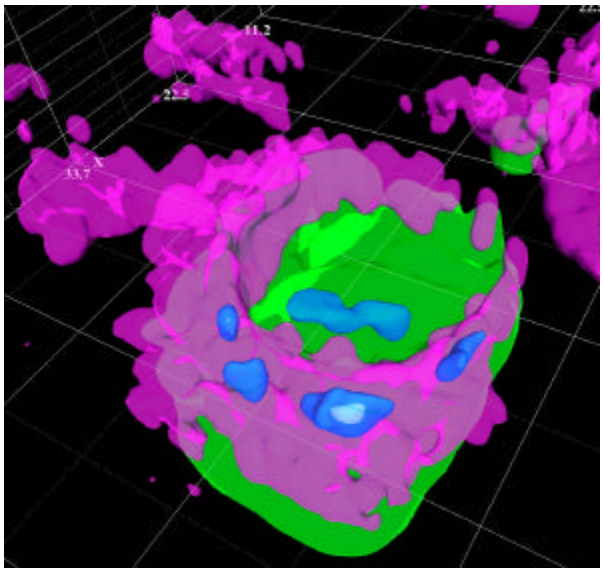

FIG 10_2 One HepG2 cell 20 min after staining, stained with:

2‘,7‘ Dichlorodihydrofluorescein diacetate
(H_2DCFDA) » 2‘,7‘ Dichlorofluorescein (DCF)
green, Iso level: 80
hot spot in blue, Iso level: 250
highest intensities in white, Iso level: 400
Maximal value of Isosurface DCF: 491.3
EmFilter: 515 ± 15 nm
MT shown in violet, Iso level: 80
EmFilter: 590 ± 30 nm

FIG 10_3 One HepG2 cell 30 min after staining, stained with:

H_2DCFDA » DCF

green, Iso level: 80
hot spot in blue, Iso level: 300
highest intensities in white, Iso level: 400
Maximal value of Isosurface DCF: 1150.1
EmFilter: 515 ± 15 nm
MT shown in violet, Iso level: 130
EmFilter: 620 ± 30 nm

Two Photon Excitation Laser Scanning Microscopy
of Human Hepatoma Cells (HepG2)
Visualised by Advanced Visual Systems (AVS/Express), Surface Rendering:
Magnification: 60 x Water Objective
Mounting medium: PBS

FIG 10_4 One HepG2 cell stained with:

MT
shown in violet, Iso level: 300
EmFilter: 620 ± 30 nm

DHR » RHO
shown in green, Iso level: 300
EmFilter: 515 ± 15 nm

The hot spots of ROS generation
are shown in blue, Iso level: 1000; and
white, Iso level: 3500.
Maximal value of Isosurface RHO: 4379.2

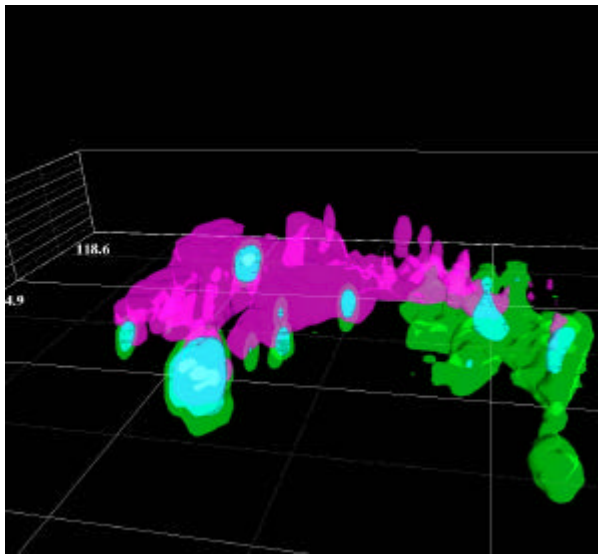

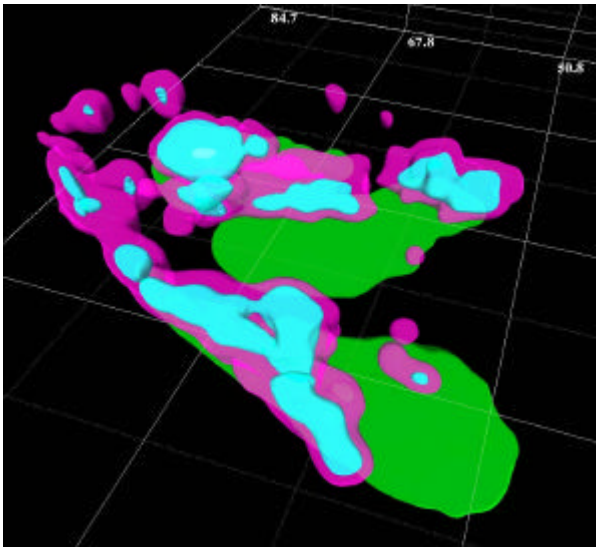

FIG 10_5 One HepG2 cell shortly after staining

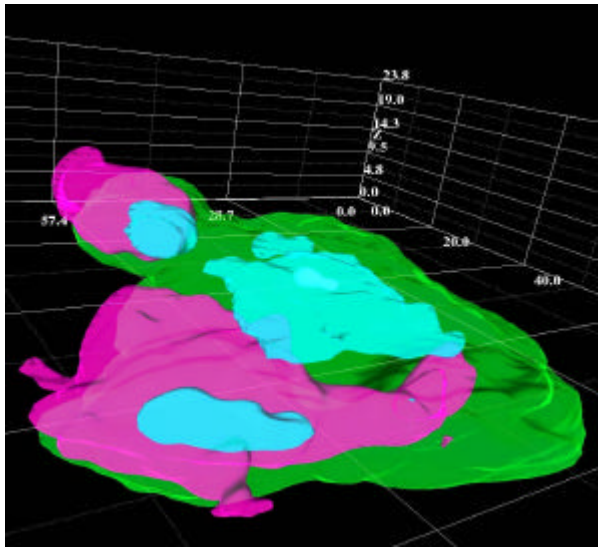

FIG 10_6 One HepG2 cell 30 min after staining

Both are stained with:

H_2DCFDA » DCF EmFilter: 515 ± 15 nm
green, Iso level: 300
hot spots: blue, white; Iso level:1000, 4250
Maximal value of Isosurface DCF: 5314.5

MT EmFilter: 620 ± 30 nm
violet, Iso level: 300

green, Iso level: 300
hot spots: blue, white; Iso level: 1000, 2340
Maximal value of Isosurface DCF: 2932.9

MT Em Filter: 590 ± 30 nm
violet, Iso level: 300

Two Photon Excitation Laser Scanning Microscopy
of Human Hepatoma Cells (HepG2)
Visualised by Advanced Visual Systems (AVS / Express), Surface Rendering
Magnification: 60 x Water Objective
Mounting Medium: PBS

FIG 10_7 Two HepG2 cells stained with:

Dye		Emmission Filter	Iso level
DAPI	red	470 ± 15 nm	300
MT	violet	620 ± 30 nm	300
DHR » RHO	green	515 ± 15 nm	300
Hot spots of RHO fluorescence	blue		600
Maximal value of Isosurface RHO			2356.5

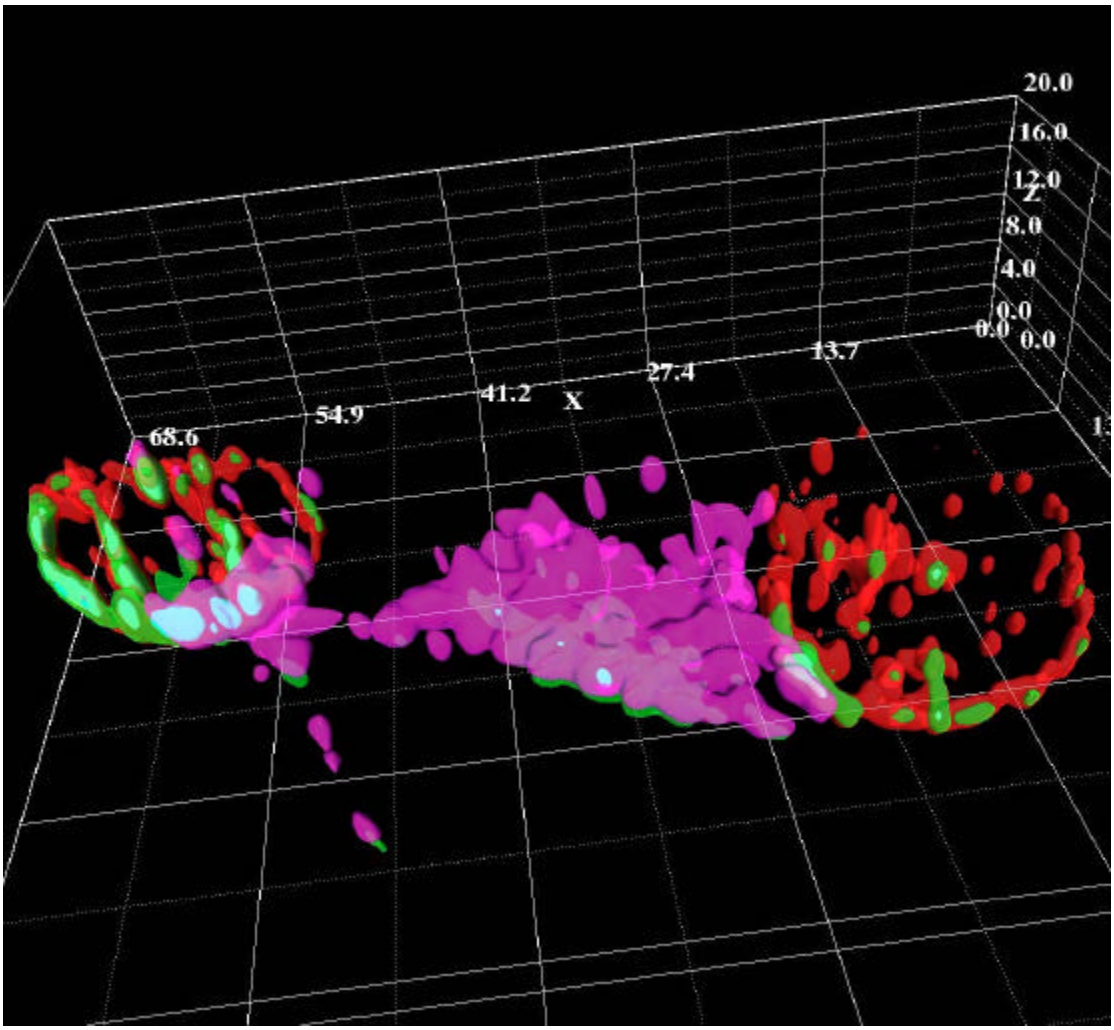

The hot spots of RHO fluorescence are shown in light blue, they are localised perinuclear.

Two Photon Excitation Laser Scanning Microscopy
of Human Hepatoma Cells (HepG2)
Visualised by Advanced Visual Systems (AVS / Express), Surface Rendering:
Magnification: 60 x Water Objective
Mounting medium: PBS

Hep G2 cells stained with:

Dye		Emission Filter
DAPI	red	470 ± 15 nm
H_2DCFDA » DCF	green	535 ± 15 nm
hot spots of DCF	light blue / white	
MT	violet	620 ± 30 nm

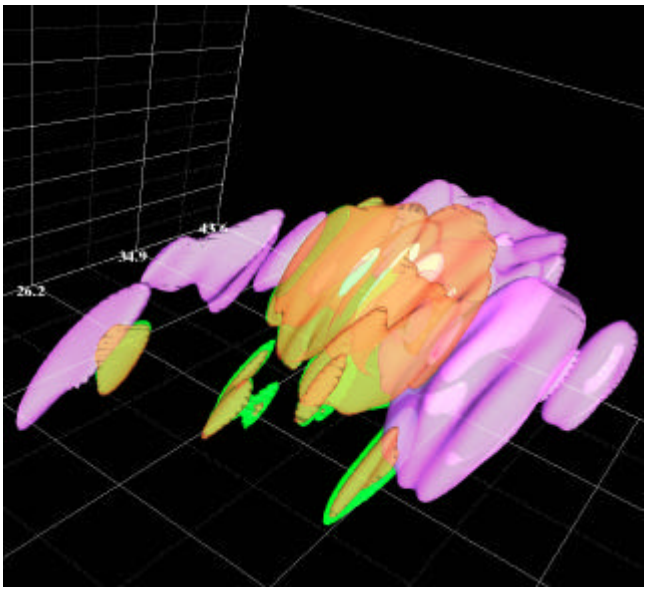

FIG 10_8 One HepG2 cell with fluorescence of

	Iso level
DAPI	150
MT	200
DCF	200
Iso level of hot spot of DCF:	700
Max. value - DCF Isosurface:	1043

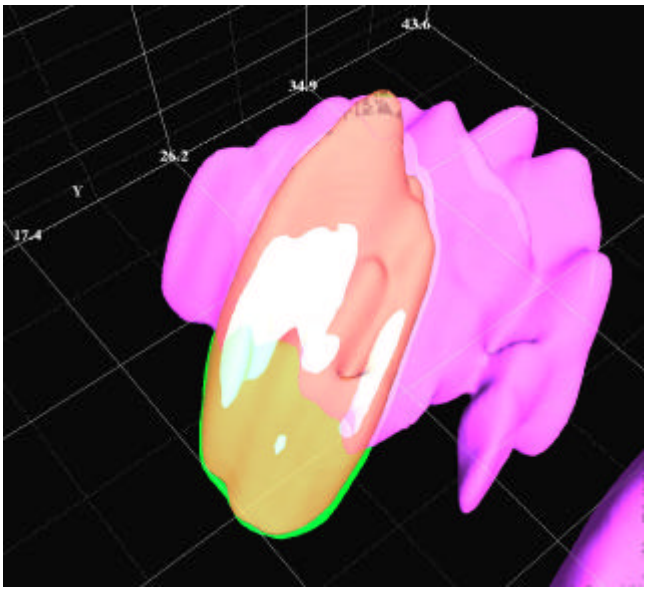

FIG 10_9 One HepG2 cell with fluorescence of

	Iso level
DAPI	200
MT	200
DCF	200
Iso level of hot spot of DCF:	800
Max. value - DCF Isosurface:	1066

The hot spots of DCF are shown in light blue, they are localized in the nucleus.

10.1 Signal to noise ratio of OPE CLSM versus TPE LSM for visualised HepG2 cells before deconvolution

To investigate the improvement by the new implemented method, a comparison of Signal to Noise ratio of the non-deconvoluted cell data of OPE CLSM and TPE LSM was performed. Table 10_2 shows the represented Figures 10_1 to 10_6, the PMT gain, the signal to noise ratio of deconvoluted data, the lowest Iso level which was used as a threshold between background and fluorescence intensities, and the Maximal value of Isosurface.

Figure	Staining	PMT gain (DHR/DCF)	back-ground	Signal to Noise ratio	lowest Iso level	Maximal value of Isosurface
10_1	1P DHR MT	2.9	12.120	4.587	300	6810.5
10_2	1P DCF MT	3.2	11.294	3.135	80	491.3
10_3	1P DCF MT	2.7	10.388	3.736	80	1150.1
10_4	2P DHR MT	3.8	6.789	6.129	300	4379.2
10_5	2P DCF MT	2.8	9.328	5.228	300	5314.5
10_6	2P DCF MT	3.4	9.206	4.977	300	2932.9

Table 10_2 Comparison signal to noise ratio OPE CLSM vs. TPE CLSM

During data acquisition usually the maximal voxel value of the images usual was 255. Only for OPE CLSM images for cells stained with DCF and MT, this could not be achieved as the background fluorescence was increasing so quick, that more PMT gain would have lead to no more visible structures or hot spots.(for Figure 10_2: 111, for Figure 10_3: 145). This appears also in the low value of the Iso threshold, which had to be set on 80, as mostly for OPE CLSM, for not loosing any information.

As a tendency it can be seen that the background fluorescence is less for 2P CLSM, therefore the Signal to Noise ratio is improved, although this is not directly correlated to the maximal value of isosurface. However if the maximal voxel value could not be achieved and the signal to noise ratio was low, either the maximal value for the Iso level.

For the two different staining methods and the two different acquisition methods, the averaged signal to noise ratios and their standard deviations were as it is represented in Table 10_3.

Imaging Staining	1P DHR MT	1P DCF MT	2P 590 DHR MT	2P 620 DHR MT	2P 590 DCF MT	2P 620 DCF MT
∅ S/N	4.373	4.075	5.000	5.9285	4.879	5.105
Std deviation	0.479	0.781	0.4285	0.1618	0.4845	0.2526
No of images	7	4	15	6	11	13

Table 10_3 Signal to noise ratio and standard (std) deviation of convoluted data for Rhodamine 123 respectively DCF.

The signal to noise ratio is better for TPE LSM in comparison to 1P CLSM, and better for Rhodamine 123 than for DCF.

IV DISCUSSION

11.The fluorophores DCF and DHR, MT and DAPI are they suitable for Two Photon Excitation Laser Scan Microscopy?

As summarised in Table 8_4 the fluorescent dyes DAPI and Rhodamine have blue shifted excitation maximums, MitoTrackerRed and 2'7'-DCF have red shifted ones compared to extrapolated doubled OPE excitation maximums. This demonstrates indeed that that TPE excitation maximums cannot be derived from extrapolated doubled OPE excitation maximums. Furthermore the compared spectra have different shapes, this may be due to different transitions that may occur during OPE respectively TPE because of different selection rules and the effects of vibronic coupling as it explained in paragraph 3.1. The emission maximums should not change, as emission should always take place from the same, the lowest vibrational level of the singulett S_1 level, but they show a shift of 10 –15 nm. This could be due on the one hand because fluorescence spectroscopy is an absolute measure, already variations of ± 5 nm are allowed for the same sample measured with the same instrument. As the measurements were undertaken on different instruments mayor variations of mayor differences may occur. Or is this due to effects of vibronic coupling?

Although the excitation maximums of the discussed dyes are more or less in the tunable range of MIRA from 710 to 1000 nm: DAPI at 690 ± 10 nm, Rhodamine 123 at 921 ± 10 nm, 2',7'-DCF at 1065 nm and at > 1150 nm, only MT has its maximum somewhere > than 1150. Maximal excitation, which can be derived from the low intensity level of emission, was not at all reached by the laser output fixed for the experiments at 798 nm (as tuning demands a lot of adjustments). The low levels of emission at this wavelength are represented in Figures 8_3 for DAPI, 8_8 for DCF, 8_11 for MT, and 8_18 for Rhodamine. But as the spectroscopic measurements (OPE and TPE) were performed on different instruments intensity levels cannot be directly compared. The induced excitation still

was sufficient as TPE LSM could successfully exerted, perhaps pointing out that this kind of microscopy is very sensitive.

11.1 Appropriate dye – filter combinations

Appropriate dye-emission filter combination were as it is represented in the following table. All filters were Bandpass Filters, as they transmit light only within a defined spectral band of either 10 nm, 30 nm or 60 nm.
The 2P Filter additionally were Shortpass Filters as they transmit only below 700 nm.

Dye	DAPI	RHO	DCF	MT
Filter 1P	-	515	515	590 (or 620)
Filter 2P	470	515 or 535	515 or 535	590 or 620

Table 11_1 Appropriate Dye - Filter combinations

The 2P optical barrier filter could either be used for 1P excitation, but not vice versa, because of the excitation wavelength of 798 nm the shortpass properties of the 2P filters were needed for TPE LSM.

12. Considerations about the measured and calculated PSFs

12.1 Point Spread Function of a Conventional versus a Confocal LSM (OPE)

The comparison of the PSF of a conventional wide field fluorescence microscope with one of a CLSM, illustrated in Figure 9_5 may make clear where the optical sectioning capacity of a CLSM comes from. In both cases looking close to the focal point as it is illustrated in

Figures 9_4 i and k they have a shape reminding at the ideal point spread function as it was described in chapter 4 and they show a diffraction pattern which is due to the lens. If the point source of light is perfect we will get a high symmetrically pattern like it can also be seen in the theoretical point-spread function in Figure 9_1of which the central part in the transverse plane (perpendicular to the symmetry axis of the lens) is an 'Airy Disc'. This disk has its maximal light intensity in the central point, represented in Figure 12_1. The radius of the inner dark ring is an resolution element (or resel) as it is the measure of the resolving power of the microscope and nearly the same as the diameter of the disc at 50 % intensity (FWHM), which we took to measure the resolution power of the TPE LSM. The measured FWHM corresponds to the dark ring surrounding the blue ring in the illustrations.

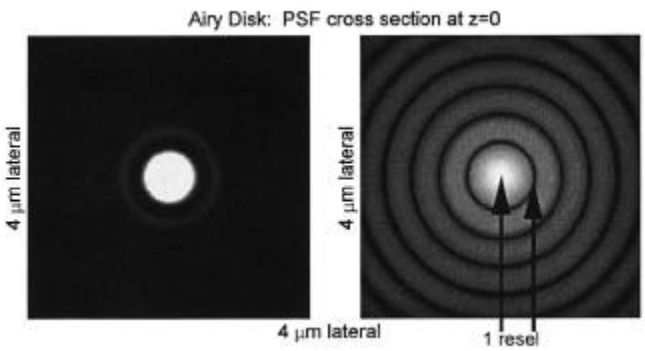

FIG 12_1 The point-spread function in the focal plane *Left*: Linear grey scale *Right*: Logarithmic grey scale (Webb 1999)

12.1.1 Principle of calculation of a PSF for a standard fluorescence microscope

When the lens is illuminated by a perfect point source, the amplitude PSF $h(x,y)$ of a lens is defined as the transverse spatial variation of the amplitude of the image received at the detector plane. But due to diffraction coupled with aberrations like it is seen in Figure 9_4 in the lens and on the optical pathway the image of a perfect point source will be smeared out into the blur spot occupying a finite area of the image plane. Because of reciprocity, the function $h(x,y)$ then denotes also the amplitude variation at the focal plane. The intensity PSF of an object, $I_h(x,y) = |h(x,y)|^2$, can be defined in the same way as the spatial variation

of the intensity of the image received at the detector plane when the lens is illuminated by a perfect point source.

The main difference between the imaging characteristics of a standard fluorescence microscope and the confocal one lies in the method of illumination and detection. The epifluorescence microscope illuminates the entire sample uniformly from an incoherent light source, comparable to the non-use of the pinhole, i.e. a spatially incoherent type of illumination is used and a large-area detector made up of many pixels, detects the image. Already the use of a wider detection pinhole which is seen in Figure 9_5 will reduce the confocal effect, because of the bigger size of the PSF. (see below). In the standard fluorescence microscope, a point on the sample is imaged as a diffraction-limited spot on the detector only by the objective lens. Therefore the amplitude of the image field at the detector of a point object is given by the Airy function $h(r)$. The intensity PSF of the microscope of an ideal instrument is subsequently since the source is incoherent equal to the square of the amplitude response of the objective lens lens $I_s(r) = |h(r)|^2$.

12.1.2 Principle of calculation of a PSF for a CLSM

As in the CLSM only one point on the sample is illuminated at a time through the objective, this point source illumination is spatially coherent. The amplitude of the illuminating field at the sample is then given by the PSF of the objective onto a point detector, thus the amplitude PSF of this microscope is given by $A_C(r) = |h^2(r)|^2$, where the subscript C denotes a confocal microscope. (Corle 1996)

In contrast to the used intensity PSF in the standard fluorescence microscope, for the CSLM the amplitude PSF must be used in imaging calculations.

Why the PSF of a confocal microscope is the square of a standard one?

Because the image in a confocal microscope is formed by recording light primarily from a small focal volume, largely ignoring points to the side or above or below. That volume, described as PSF, is the product of two similar functions that are generated by the objective lens. The integral is of ‘light that reached a sample point *and* got back through the pinhole.’ (Webb 1999) Although the PSF are similar, there are independent. One is the point-spread function for the illumination source PSF_S. (S for source) The other one is the point-spread function for the collection pinhole PSF_P. (P for pinhole)

If the sample is featureless, its “remittance” (that include reflection, scattering, refraction, diffraction, fluorescence – all things that the sample does to redirect light) is everywhere the same, as it would be in a fluorescent liquid. The detector is going to register light coming through the pinhole, from every part of the sample illuminated by PSF_S and sampled by PSF_P. Every point ‘feels’ the influence of both point-spread functions which are independent to each other, subsequently they should be multiplied. The product point-spread function is a point-spread function for the whole microscope, a confocal point-spread function.

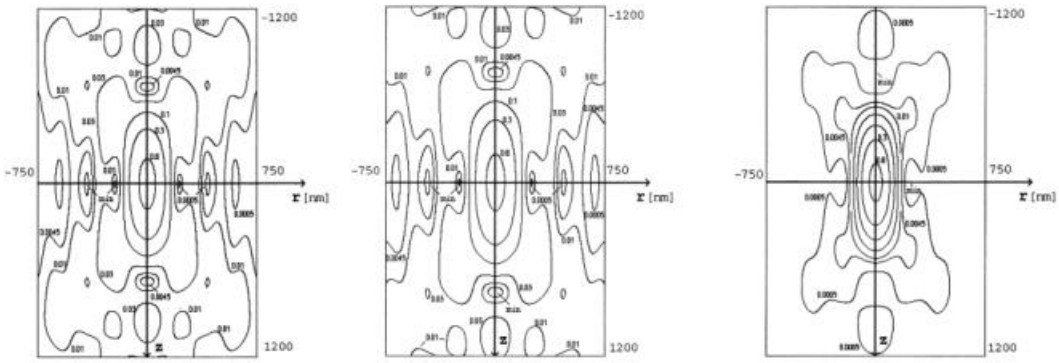

FIG 12_2a λ= 488 nm *b* λ=550 nm *c* λexc= 488 nm λem =550 nm

Figure 12_2 The calculated intensity PSF $|h(r)|^2$ for an ideal objective (NA=1,3)in (a) for λ = 488 nm, in (b) for 550 nm and in (c) for confocal microscope with these excitation and emission wavelengths. The PSF corresponds to the illumination intensity distribution in the focal region when a point like illumination is applied. The contours mark points of equal intensities (isophotes). The highest intensity is reached at the focal point (r=0, z=0) The function $|h(r)|^2$ is proportional to the probability that an excitation photon reaches an object point on the circle (r,z) for a, for b that a fluorescent photon is emerging from (r,z) is able to reach the point detector, for c the calculated function $H_{conf}(r,z)$ is proportional to the probability that an excitation photon reaches an object point (r,z) and and an emission photon is subsequently detected in the photodetector. The isophotos of $H_{conf}(r,z)$ which is equivalent to an increased stepness and an improvement of the point resolution along all directions. (Kriete 1992)

Expressed in terms of probability: The probability of detecting a photon is the probability that a photon goes through the pinhole to the sample and back from the sample through the pinhole. These are independent probabilities, such as the mutual probability is their product: $PSF_{CF} = PSF_S \times PSF_P$, the same is valid for the mutual intensity. Because of that multiplication, the recorded light is greater than even the integrated total of the light from all other points in a thick sample. Figure 12_2 shows how much sharper the confocal point-

spread function is than either the source or the pinhole point-spread function. Subsidiary peaks that were 0.01 times the main peak become now 0.0001. That reduction of the intensity away from the central peak is the source of the increased contrast and the optical sectioning capacity. The blurring in the wide-field microscope is therefore due to his PSF. The signal to noise ratio of the averaged bead was very high (>2000 in contrast to around 20), because light from all image planes contributed to the intensity. Figure 9_4k, which shows the optical cut through the wide field PSF seems to contradict the three-dimensional reconstruction in Figure 9_5 as the optical slice and the explained calculations. To resolve this contradiction, the different sampling densities and the size of the sampled area has to be taken into account, being for the wide field mode twice the sampling distance and subsequently the field of the corresponding confocal PSF. This bigger size is represented within the same size of area, because the used window in Huygens2 to save these cuts were the same as for the other PSFs whose sampling distances are very close to each other; you may do this scale up in thought. For the same settings in 1P and 2P the same sampling distances were taken, therefore the latter can be compared directly.

12.2 Detector Aperture Size

A small pinhole detector is needed for the optical sectioning capacity, but it cannot be as small as one would like because of signal to noise ratio problems. The image formation in a fluorescence microscope (either confocal or conventional) will only be linear at moderate values. At high excitation intensity the fluorescent dyes will be saturated. Furthermore, at the very high intensities which can be obtained with pulsed lasers, the realm of non-linear optics is entered, e.g. in two photon excitation. The occurring non-linear phenomena can be used as ‘contrast mechanism’ (i.e. as the quantity which is imaged).

A ‘point’ pinhole does not exist as a point is a mathematical fiction, so tiny that no light would come from it. However, a star is a pretty good real point source because the image of the star is smaller than the point-spread function of the lens we use to observe it. The same is true for a point pinhole. If the extent of the pinhole is less than the point-spread function of the lens, then the pinhole is the point source.

The resolution data given in section 4.1.1 are based on the assumption that an infinitely small detector is used. If the size of the detector pinhole aperture is increased, the imaging properties approaches those of a conventional microscope, the lateral resolution first suffers as shown in Figure 9_4. For TPE LSM as a second pinhole is not used and all the diffusing photons are collected and the excitation wavelength is doubled, the lateral resolution is also diminished which can be derived from the broader dark blue ring. The depth resolution is not so critically dependent on a small aperture size. Although a larger aperture size gives in general a higher signal level, as it is extremely shown for the widefield fluorescence microscopy, where the signal to noise ratio of the averaged beads is very high, opening the aperture beyond a certain limit will mainly add stray light from out-of-focus planes to the signal.

If the maximum permissible deterioration in the FWHM depth discrimination is set to 10 %, the maximum detector diameter for fluorescence microscopy, is $D = \frac{0.855\, lM}{NA}$

where l is the wavelength, M the objective magnification and the NA the numerical aperture of the objective.

For a 40 fold magnification , oil immersion objective with NA 1.3, λ of 515 nm the appropriate pinhole aperture is 13, 5 µm, for a 60 fold magnification, the same wavelength, water immersion objective with NA 1.2, the recommended diameter is 22 µm. In both cases we used a pinhole with 20 µm diameter. (Radius r = 10 µm) For the bigger pinhole of 50 µm diameter, the signal to noise ratio was lowered because of stray light and lateral and depth resolution was less, which is derivable from the bigger PSF three dimensionally depicted in Figure 9_5 than that for the smaller pinhole, which was used for the conditions under which the HepG2 cells were imaged.

12.3 Aberrations

Due to refractive mismatch as it is explained in chapter 4, the PSF in PBS could not be determined for the 40x oil objective.

All the measured point spread functions in Figure 9_4 show different aberrations depending on the settings which were used at that day and they will always differ after a longer manipulation period. Therefore there is the postulation that the PSF should be determined

before each manipulation, every day would be ideal, however this is difficult to perform. One step is to optimise the illumination such as the focal plane is illuminated more even. Aberrations appeared more in TPE LSM than in OPE CLSM using the water objective, in particular to demonstrated in the yz-plane of the 2P PSF LSM cuts in Figure 9_4 f, g, m, o. In OPE PSF images with the oil immersion objective 40 aberrations in Mowiol or Vectashield can be seen mostly in the xz-plane Figure in both OPE and TPE this will lead to deteriorate the resolution limits. The smallest lateral FWHM occur in OPE CLSM imaging with the water objective (60 x) illustrated in Figures 9_4 e, i or l (qualitatively estimated). The FWHM of the 2P 'green' PSF in PBS was quantitatively determined as well.

12.4 The resolution limits of TPE LSM for 515 nm emission wavelength

As demonstrated in FIG 9_2 270 nm is the theoretical lateral resolution limit at 515 nm emission wavelength, it should be a bit less as the PSF is reaching the maximal value of 255 (8 bit grey scale) too early, the corresponding theoretical Full Width of Half Maximum in z-direction is shown FIG 9_2b: 1960 nm is the theoretical axial resolution limit at 515 nm emission wavelength, it should be a bit less as the PSF has a plateau at the maximal value of 255 (8 bit grey scale)

Looking at Figure 9_2 a, illustrating the experimental Full Width of Half Maximum in x-direction, 670 nm seems to be the experimental lateral resolution limit at 515 nm emission wavelength, but perhaps of superposition effects of the averaged beads, the fluorescence intensity could not fall at its half value when the intensity diminishes the first time at 1175 nm and 2000 nm, i.e. 225 nm would be the FWHM which would correspond to expected value between 0.61λ / NA = 0.61 * 515 nm / 1.2 = 262 nm and

$0.46\ \lambda$/NA = 0.46 * 515 nm / 1.2 = 197 nm. But still all determined FWHM are above the expected values, because the histogram of the PSF showed an exaggerated intensity distribution with a expanded plateau at 255. Even the theoretical PSF exhibit a plateau as they are restored with the values of the experimental PSF except for aberrations. For the focal plane x, y a lateral resolution limit between 0.61 λ /NA for wide field one photon excitation fluorescence microscopy and 0.46 λ /NA for CLSM is expected with λ = 515 nm and NA = 1.2 , i.e. between 262 nm and 197 nm, but the value for theoretical x,y resolution

derived from the intensity distribution demonstrates already a bigger value of 270 nm. For axial resolution, in direction of the z-(optical) axis, Jens Eilers, Max-Planck-Institute for Brain Research in Frankfurt found for his TPE CLSM a value of 1,7 µm (private communications).The experimental value of the used CLSM seems to be very high with 6,25 µm. If the shape of the curve is compared with the theoretical one, it seems that superposition has happened, perhaps because several beads are averaged which do not have the same shape as they were imaged at different sites and the illumination was differing.

However, the FWHM describes the resolution, which is a theoretical value, that is nearly never achieved as there are certain fundamental differences between optical and physical sections. The latter will produce well-defined ones between the sections without 'spill over'. However, there is no sharp boundary between consecutive optical sections. There is a certain 'spill-over' of light from one section to the next. Regardless of the distance between the sections, light from extremely bright specimen parts will often be clearly visible over much larger vertical distances than the FWHM value. Additionally all specimen parts above the recorded layer may absorb and/or in influence the light travelling to and from the focus layer. Optional sectioning is therefore only useful for fairly light transparent objects.

The given lateral and depth discrimination data are based on the assumption of aberration-free optics. This is not true in our case, therefore the resolution is lower. Especially concerning the depth discrimination aberrations are problematic, since microscope objectives are designed to perform well in conventional rather than confocal microscopes. In particular chromatic aberrations may noticeably deteriorate the optical sectioning performance in confocal fluorescence LSM.

13. Localised ROS generation in HepG2 cells

Chandel et al (1998) has asked: 'Could ROS originate at nonmitochondrial sites?'

His answer was 'ROS can be generated by membrane NADPH oxidase or cytochrome P_{450}. However these sites would be expected to decrease ROS generation at low O_2 concentrations. Although such oxdidase systems exist in HepB3 cells, their role in the EPO-response has not been reported.'

The three dimensional visualisation of the HepG2 cells represented in Figures 10_1, 10_2, 10_4, 10_7 illustrate that the fluorescence of DCF and RHO was brightest in the vicinity of nuclei, i.e. the ROS generation was the highest perinuclear within mitochondria well distinguishable by MitoTrackerRedCMXRos staining, and outside of mitochondria. In fluorescence microscopy, used to detect the object by confocal laser scanning, mitochondria were seen as worm-like structures as long as the cell was living. (This appearance served also as indicator for the vitality of the cells, as mitochondria will become round when the cell is dying). As surface rendering was used for visualisation, i.e. the fluorescence above a certain level will be seen, the structures seems to be more broadened. It is known that the fluorogenic dyes for ROS detection do not directly detect superoxide, but rather react with hydrogen peroxide in the presence of peroxidase, cytochrome *c* or Fe^{2+}. Own experiments (not shown) confirmed this. H_2O_2 itself is an inert reaction partner hinting at the possible importance of the degradation products of H_2O_2 either mediated by the different scavenging systems like glutathione, thioredoxine and catalase, or the Fenton reaction. Fluorescence intensity hot spots could be found mitochondrial and non mitochondrial. Therefore we conclude that reactive oxygen species are generated mitochondrial as well as non mitochondrial. For the first time a clear distinction between both compartments can be seen, evidencing an involvement of non-mitochondrial sites of ROS generation.

13.1 Intracellular sites of ROS generation

Korsmeyer postulated 1995 that intracellular sites where free radicals of oxygen are generated include mitochondria, the endoplasmatic reticulum (ER) and, perhaps nuclear membranes. Further 3D reconstruction by surface and volume rendering of stably transfected HepG2 cell confocal data revealed indeed perinuclear ER as the dominant cellular compartment housing the Fenton reaction followed by mitochondria and Golgi apparatus. Cells were stabely transfected with gene constructs in which expression of red fluorescent protein was directed to signal peptides specifically to mitochondria, endoplasmatic reticulum and Golgi apparatus (Wotzlaw et al. 2001) Investigations with both dyes 2',7'-dichlorofluorescin and dihydrorhodamine in cultured endothelial cells (Royall and Ischiropoulos 1993) demonstrated that 2',7'-dichlorofluorescin diacetate which is cell membrane

permeable and undergoes conversion by intracellular esterases to 2',7'-dichlorofluorescin (dichlorodihydrofluorescein) and is proposed to be trapped intracellularly, is not trapped within endothelial cells, nor is 2'-7'-dichlorofluorescein. For that reason perhaps DCF can also easily pass the nuclear membran. Or if DCF diacetate is not completely converted by intracellular esterases, it is nuclear membran permeable (, then esterases should also be in the nucleus.)

Hempel et al. (1999) conclude from their experiments with different probes to detect ROS that both dyes are not detecting a specific species, such as H_2O_2, but rather function as detectors of a broad range of oxidizing reactions that may be increased during intracellular oxidant stress. Even intracellular catalase was able to oxidise the probes to fluorescence. However, they found that DHR123 is the probe most readily oxidised by H_2O_2. Also Royall and Ischiropoulos report that dichlorofluorescein was oxidized by H_2O_2 in the presence of iron, by H_2O_2 plus horseradish peroxidase and by horseradish peroxidase alone. This oxidation was most likely mediated by formation of ferryl ion, which has similar reactivity and is kinetically indistinguishable from hydroxyl radical.

Could it be that ROS are generated, perhaps not imperatively by a Fenton reaction in the nuclear membran and still cell membran permeable DCFDA arrives in the nucleus, being deacetylated, or DCF itself, which then reacts with intranuclear oxidants or is oxidised DCF passing the cell membrane either by diffusion or using special pores? Interestingly peroxisome proliferator-activated receptors (PPAR) agonists generate reactive oxygen (without involving mitochondria), inducing dimerization of PPAR with the retinoid X receptor-ß (RXRß). PPAR/RXRß dimers responsible as a the transcription factor for induction of acyl-CoA oxidase, an enzyme that transfers electrons directly to oxygen to produce H_20_2. (Dalton et al. 1999)

Rhodamine 123 obviously cannot pass the nuclear membrane and is therefore better suited for detecting cytoplasmatic hot spots, but it is accumulating in mitochondria and fluorescence will be seen in mitochondria dependent on the potential of the inner mitochondrial membrane. The fluorescence is first quenched by a high potential, but becomes visible with decreasing mitochondrial membrane potential thus at the end of the observation time it was mostly found in mitochondria. Perhaps it gives a hint to the vitality of the stained cells, which perhaps diminishes with decreasing mitochondrial potential andincreasing RHO fluorescence.

13.1.1 Mitochondrial formation of ROS

As explained in the introduction ROS can be generated either by cytochrome c oxidase or together with the proton-motive Q-cycle. Reduced coenzyme Q prefers to scavenge reactive oxygen, whereas a high rate of oxygen utilization, coupled with a more-oxidised coenzyme Q state, will promote higher rates of mitochondrial superoxide formation, like does energy uncoupling of mitochondria by Ca^{2+} (if the cytosolic level of Ca^{2+} is high) and the opening of the mitochondrial permeability transition pore(MPTP) which is affected by the redox state of thiols and pyridine nucleotides. MPTP is a cyclosporin A-sensitive, Ca^{2+} -dependent, voltage-gated channel which allows passage of molecules of a molecular mass not greater than 1300-1500. Ca^{2+} -loaded mitochondria produce H_20_2 and lipid peroxides, a process inhibited by cyclosporin A, which blocks the pore. One site of the two voltage-sensing regions of MPTP - gated by a critical dithiol - regulates opening of the pore, when GSH is oxidised to GSSG. Opening the pore results in energy uncoupling by a Ca^{2+} -dependent decrease of mitochondrial inner-membrane potential. The second voltage-sensitive site in the MPTP is in redox equilibrium with the pyridine nucleotide pool. This site regulates opening of the pore by an increase in the (NAD+NADP) : (NADH+NADPH) ratio, even when GSH remains fully reduced. In general this pore is opened when the redox state of the cell tends to become more oxidised, then the calcium influx will decrease mitochondrial inner-membrane potential. (Dalton et al.1999) A decreased activity of mitochondrial respiratory enzymes could favour an increased availability of NAD(P)H. High concentrations of NADH will maintain the iron-sulfur clusters of mitochondrial redox enzymes such as complex I in a more reduced steady state. This situation will favour auto-oxidation of the iron-sulfur clusters with molecular oxygen, thereby producing ROS at sites distant from the ubiquinone substrate site of mitochondrial dehydrogenases. (Esposti et al. 1999) This could be a reason for dequenched fluorescence of RHO when the mitochondrial potential is decreased.

The leakage in mitochondria of ROS is probably most likely due to cytochrome c which serves as carrier between b-c1-complex and cytochrome-oxidase complex, situated on the side of the inner mitochondrial membrane in direction to the intermembran space, i.e. the cytosol. (Kwast 1999)

13.1.2 Non-mitochondrial, perinuclear formation of ROS

In the cytosol ROS may also be formed by enzymes with peroxidase activity, such as cytochromes *P*-450, which sequentially transfer two electrons from NADPH to bound molecular oxygen or by dioxygenases, such as cyclooxygenases and lipooxygenases. In the course of electron transfer, some of the activated oxygen is released as superoxide and/or H_20_2. (Dalton et al.1999) Furthermore Görlach et al. (1993) mentioned that inducing cytochrome *P*-450, a member of the cytochrome *b* family, by phenobarbital application enhanced EPO production in HepG2 cells, which is at first view a contradictory result, whereas addition of exogenous H_2O_2 inhibited hypoxia-induced EPO production in HepG2 cells like it does added menadione or the catalase-inhibitor, aminotriazole by dose-depending elevation of endogenous H_2O_2 levels, hence lowering EPO formation. By co-incubation with catalase this effect could be overcome. Low GSH levels facilitate H_2O_2-induced inhibition in HepG2 cells, perhaps by affecting thiol groups in regulatory proteins. Dependent on pericellular O_2 – tension H_2O_2 is generated endogenously in HepG2 cells.
These findings are supporting the hypothesis that oxygen radicals and H_2O_2 in particular are playing a crucial role in oxygen sensing and that ROS may be produced by a variety of cytochrome *b*-(haem protein and FAD/FADH) containing eukaryotic membranes e.g. interacting with cytosolic NADPH oxidising and NADP reducing enzymes.

13.2 The specificity of ROS detection

Ehleben et al. suggested (1997) because of the perinuclear dihydrorhodamine reaction 123 product, rhodamine 123 that the Fenton reaction occurs at distinct Fe-S cluster in HepG2 cells close to the cell nucleus, which might be linked to transcription factors as described for the aconitase regulating the half life of ferritin and transferrin receptor m-RNA as an iron-responsive binding protein.
Electron microscopy on freeze-dried cryosections of primary hepatocytes and HepG2 revealed cells mass dense particles located in the cytoplasm cells in the close vicinity of the nucleus containing undoubtedly iron. The ionic state of the iron or whether the iron is

bound to proteins could not be determined. However, it was possible to colocalise iron and dihydrorhodamine 123 conversion of H_2O_2 in an iron mediated Fenton reaction in the very near of the cell nucleus to yield $^{\bullet}OH$ which is the reactive molecule. (Kietzmann et al. 1998, Porwol et al (1998) Further, di- and tetra-methylthiourea, two scavengers of $^{\bullet}OH$, which are cell-permeable and have been found to reduce the effects of hydroxyl in several other cell systems, were able to antagonise the H_2O_2-dependent inhibition on hypoxia-induced EPO production in HepG2 cells.(Fandrey et al.1997)

Although the incubation with cobalt or with desferrioxamine led to a decrease of the intra-cellular H_2O_2 level revealed by dihydrorhodamine 123 technique in HepG2 cells, the expression and secretion of VEGF in human leukemia cell line HL 60 was not induced by hypoxia, but by iron chelators, indicating that the induction of VEGF secretion by iron chelators use different pathways. (Cremer et al. 2001) This shows the necessity to further investigate, if different cells use different pathways and if metal ions really mimick hypoxia or have other effects on the oxygen sensing pathway. However for the HepG2 cell line results were consistent with the hypothesis of a involved Fenton reaction.

13.2.1 The chemical lineage of ROS

Because of the chemical lineage illustrated in Figure 13_1, detection of other ROS beside hydroxyl radicals could be possible. However, DHR123 is the probe most readily oxidised by H_2O_2, and the dyes are preferably oxidised by hydroxyl radicals as it was explained in section 7.5.6. The following presentation of the activated species beside the already reported findings will show that most probably a Fenton reaction is involved.

Molecular oxygen can be activated in two ways: to singlet oxygen or to superoxide anion (radical). To be able to react with singlet, diamagnetic, 'ordinary' molecules with paired electrons, $^3O_2$ has –to overcome the rules of spin conservation by flipping the spin of one of the two unpaired electrons to become singlet oxygen $^1O_2$ with paired electrons. (reaction *1*) This conversion requires 22.7 kcal mol-1, corresponding to a near infrared photon (1270 nm), emitted when $^1O_2$ is losing its excitiation energy, or to three times the energy released in the hydrolysis of ATP to ADP. This energy can come from a variety of chemical or photochemical reactions (in vivo and in vitro). The most common is the energy transfer to oxygen from another molecule (a sensitizer), itself previously excited by light. As we used

in 2P LSM a longer wavelength than for 1P CLSM photochemical reactions were reduced. $^1O_2$ has an exceptionally long lifetime ~ 2 µsec in *water*, (usually only 10^{-6} sec) having a reach of 1-2 µm.(Speit and Dennog 2000) An isolated $^1O_2$ molecule protected against de-activating collisions lasts 45 min, because the transition to the triplet ground state is spin-forbidden. In contrast to $^3O_2$, singlet oxygen reacts fast and selectively with high electron density sites in many unsaturated organic compounds via spin-allowed processes resulting in various labile peroxides (hydroperoxides and endoperoxides). These can react further, often yielding free radicals. These radicals, e.g. hydroxyl radicals are producing then oxidative damage rather than $^1O_2$ itself. $^{\bullet}OH$ abstracts hydrogen atoms from many substrates and initiates autooxidation chains.

Other sources of $^1O_2$ are the reaction of peroxynitrite anion, $ONOO^-$, with H_2O_2 (reaction *10*) as well as, quantitatively, in the acidification of alkaline solutions of peroxynitrite (reaction *11*), both shown by spectroscopic results . $ONOO^-$ is formed at diffusion-limited rate in the reaction of superoxide with nitric oxide (reaction *8*). Peroxynitrite might be the (cyto)toxic responsible for some effects that neither NO nor O_2^- alone can produce. Activated macrophages, for example, generate high concentrations of both NO and O_2^-, $ONOO^-$ is fairly stable under physiological conditions, has a long lifetime and diffusion radius, is a strong oxidant of lipids. Its very weak O-O bond (only half as strong as the already weak O-O bond in hydrogen peroxide breaks up easily (reaction *9*) to give $^{\bullet}NO_2$ and an intermediate with $^{\bullet}OH$ reactivity.

Furthermore the bacteriocidal system of neutrophils forms $^1O_2$ (reaction *13)* via the hypochlorite ion, OCl^-, which is generated e.g. by the enzyme myeloperoxidase from Cl^- and the cosubstrate H_2O_2. OCl^- is a strong oxidant that directly peroxidises and/or chlorinates many biological molecules. Even simple acidification of OCl^-generates singlet oxygen (reaction *14*)

The first reduction product of stepwise addition of an electron indicated in the scheme of chapter 1 (reaction *2*) is O_2^-. It is a base in equilibrium with its conjugate acid $HO_2^{\bullet}$. When $^3O_2$, the ultimate electron acceptor in enzymatic systems, acquires an extra electron in an exothermic process, for example from semiquinones (intermediates in the reduction of ubiquinone), or from flavins or in xanthine/xanthine oxidase system, the resulting superoxide anion, O_2^-, is a free radical and thus also a paramagnetic species. The reaction has a low mid point potential, thus the electron donor to the oxygen molecule must also have a low-oxidation-reduction potential, if superoxide is to be formed with good kinetics.

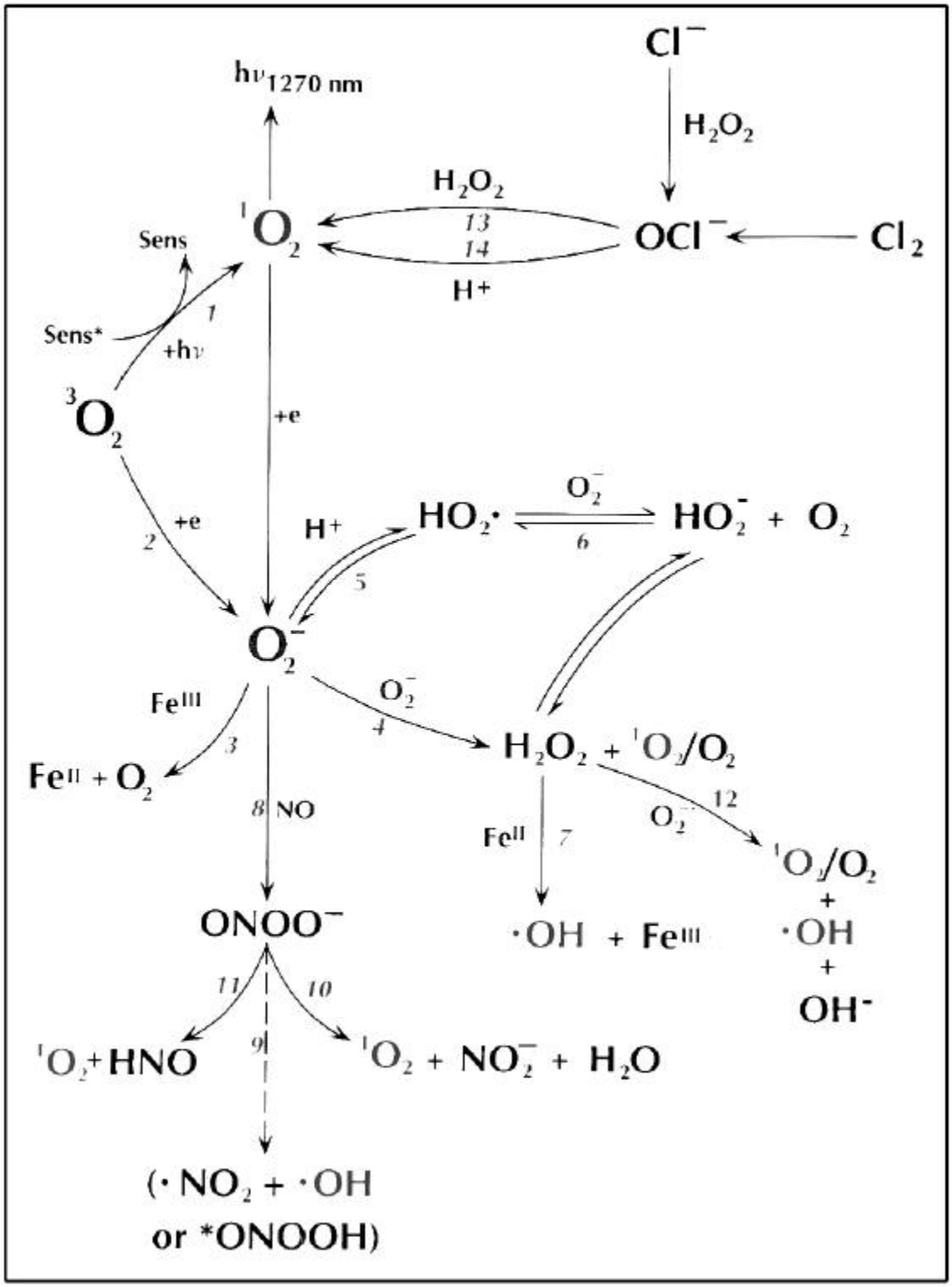

FIG 13_1 The main reactions creating , consuming and interconverting ROSs. The numbered processes are further described in the text. Sens*, sensitizer (Khan and Wilson 1995)

Superoxide is not an oxidant at neutral pH , its pK is near 4.9, thus it is largely charged at pH 7.0 and unreactive towards most organic molecules. Two O_2^- molecules undergo dis-

mutation (reaction *4*) in water to produce two species: one is either $^3O_2$ or $^1O_2$, the other a double reduced species, hydrogen peroxide H_2O_2 either spontaneously or catalysed by intracellular enzyme superoxide dismutase (SOD). Spontaneous the rate of dismutation is maximal at pH 4.8(k = 8 x 10^7 $M^{-1}s^{-1}$) and it is still fast, although two orders of magnitude slower, at physiological pH; catalysed in the wide range of pH 5.3 – 9.5, the rate is k = 1.6 x 10^9 $M^{-1}s^{-1}$. This keeps the concentration of superoxide extremely low. Superoxide is highly solvated in water and not expected to be transported through membranes or to penetrate into hydrophobic regions of cells and peroxidize lipids. However, it is a moderately efficient one-electron reductant, for example of transition-metal complexes, used in analytical methods to identify superoxide, such as the cytochrome c method, reducing Fe^{III} to Fe^{II}. (reaction *3*) This formation of Fe^{II} used to be regarded as the critical step in pathways responsible for the toxicity of O_2 as Fe^{II} is necessary in the Fenton reaction (reaction *7*), when H_2O_2 is iron-dependent non-enzymatically converted in hydroxyl radicals $OH^{\bullet}$ and hydroyxl ions OH^-, (see chapter 1) but reductants such as glutathione are more likely to reduce Fe^{III} within the cell.

O_2^- is a weak base, and owing to its unreactivity also of superoxide anion radical $O_2^{\bullet-}$, it should be able to diffuse a long way from its site of production. In biological milieu superoxide has an estimated half-life of 400-10^{-6} ns and a diffusion pathway of 55 nm -3 µm. (Burdon 1995) But at low pH (pk_a=4.8), it becomes reactive by its protonation that gives the hydroperoxy radical ($HO_2^{\bullet}$), which becomes the dominant species. (reaction *5*) $HO_2^{\bullet}$ is still not a very reactive radical, although being a better oxidant than superoxide. Both together disproportionate to give the basic form of hydrogen peroxide $HO_2^-$and molecular oxygen. (reaction *6*) At neutral or acidic pH, hydrogen peroxide exists almost entirely in the fully protonated form, H_2O_2 (pK around 11.0) In contrast to O_2^- and $HO_2^{\bullet}$, hydrogen peroxide is a good oxidant (although not directly), a well established germicide, cytotoxic via a variety of mechanisms. It is a the substrate of heme and glutathione peroxidases generating a host of free radicals and excited state molecules, and of catalases most abundant in peroxisomes reducing it extremely quickly to H_2O and O_2. In peroxisomes there are a variety of oxidases which catalyse the two-electron reduction of oxygen generating H_2O_2. The decomposition of H_2O_2 takes place in the cytosol and mitochondria, it can also be non-enzymatically converted in the presence of Fe^{2+} in a Fenton reaction, a one-electron process.

Activated neutrophils and macrophages produce significant amounts of singlet oxygen and several other reactions of superoxide, such as the one of the steps of the Haber-Weiss cycle, (reaction *12*) i.e. the reduction of H_2O_2 by superoxide radicals and Fe(II) or Cu(I) to singlet oxygen or oxygen, $^{\bullet}OH$, and OH^-, proven by spectroscopy to be sources of $^1O_2$. Speit and Dennog pretend that the Haber-Weiss reaction does not take place in biological systems because of higher reaction speed of the dismutation reaction by Superoxide Dismutase (see above). Khan and Wilson are of the opinion that it is hard to evaluate how significant this process is in physiological conditions, especially since both water and superoxide are excellent quenchers of $^1O_2$ and the reaction is slow. But, the chemical effects of singlet oxygen and of hydroxyl radicals will be amplified downstream by secondary free radical reactions. (see above)Thus, even if only a small amount of $^1O_2$ survives quenching, it may still have a significant effect.

Fridovich calls the process in which the superoxide anion radical, $^{\bullet}O_2^-$, increases “free” iron by oxidizing the [4Fe-4S] center of dehydrases such as dihydroxy acid dehydrase, 6-phosphogluconate dehydrase, 6-phosphogluconate dehydrase, fumarases A and B, and aconitase the *in vivo* Haber-Weiss reaction. The released iron is kept reduced by cellular reductants, and the Fe(II) reacts with H_2O_2, as in the Fenton reaction, to yield Fe(III) + $^{\bullet}OH$ or its formal equivalent, Fe(II)0 (see above). (Fridovich 1997)

Beside the Haber-Weiss reaction which probably proceeds poorly at physiological pH, the Fenton reaction is the only reaction which needs iron. The detection that iron is indispensable for the generation of hydroxyl radicals should be enough to assume that a Fenton reaction is involved. Colocalisation with another fluorescent indicator which detect the presence of Fe^{2+} / Fe^{3+} would be a smart solution. The fluorescence intensity should become brighter in the presence of a specific iron ion state, as the deconvolution process seeks for maximal fluorescence dye concentration. The fluorescence of available iron detectors like Phen Green is, however, quenched in the presence of iron ions.

13.3 Advantages of TPE CLSM for ROS detection

Both methods illustrate in principle the same results, but TPE showed several advantages in comparison to one photon excitation. The cell nucleus stained with DAPI could only be visualised by TPE as we only use 488 nm and 543 nm laser light in one photon excitation.
Applying TPE CLSM the time frame for observation was longer, because the used laser light of 798 nm is less energetic, and is not inducing reactive oxygen species generation via photoreduction of flavins and/or flavin-containing oxidases within peroxisomes and mitochondria (and probably cytoplasmatic sites as well) as does violett-blue light of 400 nm to 490 nm. This photoreduction results in H_2O_2 production as the cell organelle endeavours to keep a homeostasis between reduced and oxidised flavins and/or flavin-containing oxidases, subsequently the reduced flavin will be reoxidised by reducing O_2 to H_2O_2. (Hockberger et al. 1999) Further endogenous peroxidase and oxidase enzymes convert H_2O_2 to water coupled with oxidation of 2',7'-Dichlorodihydrofluorescein or Dihydrorhodamine 123. Catalase competitively inhibits oxidation of DCF or DHR by directly metabolising H_2O_2 to $H_2O$and O_2.When production of H_2O_2 exceeds its catabolism within the organelles, it diffuses into cytoplasm, where it stimulates additional dye reduction by cytoplasmatic enzymes or non-enzymatically.
The increase of fluorescence was high when observing the cells by one photon excitation in comparison to TPE, where light-induced H_2O_2 production and therefore a quick increase of fluorescence was prevented. The dye-loaded cells both with H_2DCF or DHR responded when irradiated with blue light with an uniform increase in fluorescence that obscured subcellular structures.
At the same time the fluorescence invariably declines, although the conversion of either H_2DCF or DHR is not thought to be a reversible process, and the signal remains declined even when irradiation is halted. This phenomenon is therefore due to photobleaching of the fluorophore rather than decreased production of H_2O_2, and will not be noticed using TPE microscopy.
As well as phototoxic effects which are known specifically for violet (400-450 nm) and blue (450-490 nm) light, that cause mutations and even death of cultured mammalian cells at irradiation doses of 2 J/cm², which is equivalent to 5-10 min of direct sunlight, (Hockberger et al. 1999), do not appear under TPE microscopy, because the total excitation vol-

ume when using TPE is relatively small and fixed.(about 1 µm³). Thus differences in fluorescence signals because of differences in cell thickness are minimised.

Because of these intrinsic confocal properties and because background levels of fluorescence (perhaps also due to autooxidation of the dye in blue light) are less, the signal to noise ratio is highly improved for TPE. This can be seen as a tendency in Table 10_2 and 10_3. The background level in TPE was lower than for OPE for the imaged cells, which were recorded acquisited under the same surrounding conditions.

Summarised TPE LSM has following advantages in comparison to one photon excitation CLSM:

- The inherent potential for 3-D-imaging, i.e. the rejection of out-of-focus signals without spatial filtering (because of quadratic dependence on the excitation intensity for two-photon absorption excitation occurs highly localised)
- High contrast and improved signal to noise ratio, because of suppression of 'out-of-focus' fluorescence, no background fluorescence due to excitation of medium, immersion oil, contamination or optics
- No bulk fluorescence
- All fluorescence from focus point is collected by the detector
- Reduced photobleaching and photodamage / photostress as a confinement of excitation to the focus only
- Reduced biological damage, therefore more favourable conditions for the observation of live biological specimen for extended periods of time
- Reduced Scattering of excitation light due to red and NIR (near infrared) wavelengths, because of the spectral window of biological specimen, the signal to noise ratio is better
- Higher penetration depth of NIR radiation due to the inverse fourth power dependence on wavelength of the probability for elastic scattering and because more laser light is arriving at the focal region as it is not absorbed beforehand, therefore deeper optical sectioning of biological specimen is possible up to ~ 300 µm instead of ~100 µm
- Improved axial resolution because of nonlinear processes involved. In two-photon processes, the excitation cross section is proportional to the square of the laser intensity. The cross section for two-photon fluorescence is inversely proportional to the *fourth power* of the distance from the focal point of the laser beam. In one-photon, the intensity of the (Gaussian) beam decreases only (roughly) as the square of the distance from

the peak. Use of three-photon excitation can enhance the z-axis resolution even more because of smaller cross section and greater non linearity of 3-photon transition.

- Because of different selection rules the technique may also probe additional sensitivities of the fluorescent probe to its environment, providing new contrast parameters and additional information about the microenvironment of the fluorescent probe (Brakenhoff, Müller, Ghauharali 1996)
- Excitation of UV-Dyes without need of UV-optics therefore simplified optics can be used for UV transitions (Jenei et al. 1999, König et al. 1996)
- Excitation of UV- autofluorescence (thyrosine, serotonin, NADH)
- In opposite to high frequent light the less energetic long wave electromagnetic radiation in the NIR region scarcely has negative influence on the cell activity
- Inherent potential for lifetime imaging due to short excitation pulses and high repetition rates
- Even multiple scattered fluorescence photons contribute, equally to the image formation because of used widefield detection, in contrast with confocal microscopy, where unscattered photons form the confocal image

13.3.1 Drawbacks of TPE LSM

The possible drawbacks of MPE are:

- Surface resolution (x-y) with TPLSM will be slightly worse than with OPE LSCM using the same fluorophore, because the excitation wavelength is (roughly) twice as long and no pinhole is used, which broadens the point spread functions. (The latter could be circumvented with the use of a pinhole, but was not possible due to low signal to noise ratio, when applied)
- Thermal heating due to high peak power
- The fluorescence generation is less efficient for TPE than for OPE, because of different selection rules. The total exposure required for equivalent fluorescence generation by single-photon absorption (SPA) is at least an order of magnitude lower than by two-

photon absorption (TPA), therefore biological damage can even worse (Brakenhoff, Müller, Ghauharali 1996)

- Danger of dielectric breakthrough only at very high peak powers as, for instance, in 3-photon excitation
- Demanding technology: In case of tunable Ti:S lasers a laser engineer or physicist is recommended
- Higher precautions for laser safety due to high peak power and invisible NIR.
- And it is very expensive(150 –250 kDM)

13.4 Factors which may lead to misinterpretation of results

The interpretation of measurements may be contaminated because of nuclear accumulation of DCF by long term use and because both dyes function as ROS scavenger, mimicking hypoxia inducible gene expression of erythropoetin gene and perhaps of the multi-drug resistent *mdr1b* gene, upregulated accumulating RH under hypoxia. We are drawing this conclusion as the multi-drug restistence transporter (MDR)/transporter associated with antigen processing (TAP) transporter subfamily, member of the ATP-binding cassette(ABC) protein superfamily, has several members including the mdr-proteins (also termed P-glycoproteins, P-gp) and the bile salt-export-pump, bsep, which are situated in the hepatocyte apical canicular membrane and hence can also be found in human hepatoma cells. Numerous lipophilic, often cationic, xenobiotics and endobiotics are transported by the human MDR1 and the rodent mdr1a/mdr1b isoform into the bile in vivo. It is assumed that they have a protective role in eliminating potential toxic xeno- and endobiotics. mdr1-type P-glycoproteins are also expressed an the apical luminal surface of secretory cells in the small intestine, the colon, and the proximal tubules of the kidney supporting this suggestion of protection. In quiescent cell areas of large multicellular prostate tumour spheroids increased levels of the 170 kDa P-glycoprotein were observed in parallel to central hypoxia, lowered endogenous generation of ROS and an increased expression of the transcription factor HIF1α. The highest overexpression of P-gp occurred under $CoCl_2$ and desferrioxamine treatment which are known for mimicking hypoxia. (Wartenberg 2001)

V CONCLUSION

14. Conclusions and future directions

We could demonstrate that ROS are obvious produced in other compartments beside mitochondria in human hepatoma HepG2 cells. Future experiments have to focus on the significance of the generated ROS for the oxygen sensing pathway.

Both dyes, Dihydrorhodamine 123/ Rhodamine 123 and 2',7'-Dichlorodihydrofluorescein/ 2',7'-Dichlorofluorescein, behave in a significant different manner, and lead to irreversible reactions, therefore perhaps new dyes have to be invented such as kinetic studies under hypoxia could be performed in a superfusion chamber.

VI REFERENCES

15. References

Abo, A., Webb, M.R., Grogan, A., Segal, A.W. (1994) *Activation of NADPH oxidase involves the dissociation of p21ras from its inhibitory GDP/GTP exchange protein (rhoGDI) followed by its translocation to the plasma membrane* Biochem.J. 298: 585-591

Acker, H. (1994) *Mechanism and meaning of cellular oxygen sensing in the organism* Respiration Physiology 95: 1-10

Acker H., Xue D. (1995) *Mechanisms of oxygen sensing in the carotid body in comparison to other oxygen sensing cells* NIPS 10: 211-217

Acker H. (1996) *PO_2 affinities, heme protein, and reactive oxygen intermediates involved in intracellular signal cascades for sensing oxygen* Adv Exp Med Biol 410: 59-64, 1996

Acker, H. (1998) *Reactive oxygen intermediates as mediators for regulating ion channel activity and gene expression in the process of cellular oxygen sensing* in: López-Barneo, J., Weir, E.K. *Oxygen regulation of ion channels and gene expression*. Armonk, N.Y.: Futura Publishing Company, Inc.

Albota, M.A., Xu, C., Webb, W.W. (1998) *Two-photon fluorescence excitation cross sections of biomolecular probes from 690 to 960 nm* Applied Optics 37: 7352-7356

Amos, W.B. (2000) *Optimum Optical Design Characteristics for Confocal and Multi-Photon Imaging Systems* Biorad Technical Note 09

Allen, R.G., Tresini, M. (2000) *Oxidative Stress and Gene Regulation* Review Article. Free Radical Biology & Medicine 28: 463-499

Ashaf, I. (1989) *Quantum Theory of two-photon micromaser and laser* Department of Physics Quaid-i-Azam University, Islamabas, Pakistan

Arsac, J. (1961) *Transformation de Fourier et Théorie des Distributions* Dunod, Paris

Barrow, G.M. (1982) *Physikalische Chemie: Lehrbuch für Chemiker* Bohmann-Verlag Wien

Bastian, N.R., Hibbs, J.B. (1994) *Assembly and regulation of NADPH oxidase and nitric oxide synthase* Current Opinion in Immunology 6: 131-139

Benna, J.E., Faust LR P., Babior, B.M. (1994) *The Phosphorylation of the Respiratory Burst Component p47 ^{phox} during Neutrophil Activation*. Phosphorylation of Sites Recognized by Protein Kinase C and by Proline-directed Kinases. The Journal of Biological Chemistry 269: 23431-23436

Bio-Rad Molecular Bio-Science Group Microscopy Division *Multi-Photon Fluorescence Microscopy from Bio-Rad* Technical Note 03, Bio-Rad Microscopy Division, Hemel Hempstead, UK

Boguski, M.S., McCormick, F. (1993) *Proteins regulating Ras and its relatives* Nature 366: 643-654

Bokoch, G.M., Bohl, B.P., Chuang, T.H. (1994) *Guanine Nucleotide Exchange Regulates Membrane Translocation of Rac/Rho GTP-binding Proteins* The Journal of Biological Chemistry 269: 31674-31679

Böss, F. (1997) *Reactive Oxygen Species and Tumor Necrosis Factor in Drug-induced Hepatotoxicity* A Dissertation submitted to the Swiss Federal Institute of Technology Zürich

Brakenhoff, G.J., Müller, M., Ghauharali R.I. (1996) *Analysis of efficiency of two-photon versus single-photon absorption for fluorescence generation in biological objects.* Journal of Microscopy, Vol.183

Brand, V., Porwol, T., Acker, H. (2001) *1 and 2 photon laser microscopy of dihydrorhodamine and dichlorodihydrofluorescein for localising reactive oxygen species in HepG2 cells* P47-6 in: European Journal of Physiology Supplement to Volume 441, No. 6

Birge, R.R. (1986) *Two-Photon Spectroscopy of Protein-Bound Chromophores* Acc. Chem. Res. 19: 138-146

Brown, S.B. (1980) *An Introduction to Spectroscopy for Biochemists.* Academic Press, London, New York, Toronto, Sydney, San Francisco

Bunn, H.F., Poyton, R.O. (1996) *Oxygen Sensing and Molecular Adaption to Hypoxia* Physiological Reviews 76: 839-885

Burdon, R.H. (1995) *Superoxide and Hydrogen Peroxide in relation to mammalian cell proliferation* Free Radical Biology & Medicine 18: 775-794

Carlsson, K. (1990) *The influence of specimen refractive index, non-uniform scanning speed, and detector signal integration on the image quality in confocal microscopy* Paper presented at MICRO 1990, London 2-6-July 1990: 219-222 (chapter 8) IOP Publishing Ltd

Castano, P., Rumio, C., Donetti, E. (1998) *Using the light microscope – Course of Light Microscopy for Bio-Medical Sciences* Nikon, University of Milan (Italy)

Chandel, N.S., Maltepe E., Goldwasser, E., Mathieu, C.E., Simon, M.C., Schumacker P.T. (1998) *Mitochondrial reactive oxygen species trigger hypoxia-induced transcription* Proc. Natl. Acad. Sci. 95: 11715-11720

Chandel et al. (2000) *Reactive oxygen species generated at mitochondrial complex III stabilize hypoxia-inducible factor-1α during hypoxia* A mechanism of O_2 sensing. The Journal of Biological Chemistry 275: 25130-25138

Chandel, N.S., Schumacker, P.T. (2000) *Cellular oxygen sensing by mitochondria: old questions, new insight* Invited review. J. Appl. Physiol. 88: 1880-1889

Chang-Giu Wang (1996) *Confocal Laser Scanning Microscope: A Pre- defocus Imaging Mode, Sample Aberration and Application*, Acta Polytechnica Scandinavia, Applied Physics Series No. 207, Academic Dissertation Helsinki

Chen, S.Y., van der Meer, B.W. (1993) *Theory of two-photon induced fluorescence anisotropy decay in membranes* Journal of Biophys. 64: 1567-1575

Coherent Laser Group (1997) *Operator´s Manual The Coherent Mira Model 900-F Laser* Coherent, Inc. Santa Clara CA (USA)

Coherent Laser Group (1998) *Operator´s Manual VerdiTM V-2/V-5 Diode Pumped Laser* Coherent Inc. Santa Clara, CA (USA)

Coherent Laser Group (1999) *GDC Fiber Delivery System Operator´s Manual* Coherent, Inc. Santa Clara CA (USA)

Coherent Laser Group (2000) *Multiphoton Excitation Microscopy MPE Tutorial* Coherent, Inc. Santa Clara CA (USA)

Conn, M. (1999) *Confocal Microscopy,* Methods in Enzymology, Volume 307, Academic Press, San Diego

Cool, R.H., Merten, E., Theiss, C., Acker, H. (1998) *Rac1, and not Rac2, is involved in the regulation of the intracellular hydrogen peroxide level in HepG2 cells* Research Communication. Biochem. J.332:5-8

Corle, T.R.; Kino, G.S. (1996) *Confocal Optical Microscopy and Related Imaging Systems*. Academic Press, San Diego, London

Cremer, M., Frede, S., Fandrey, J. (2001) *Expression and secretion of VEGF in human leukemia cell lines is not induced by hypoxia but by iron chelators* P34-11 in: European Journal of Physiology Supplement to Volume 441, No. 6

Cross, A.R., Henderson, L., Jones, O.T.G Delpiano, M.A., Hentschel, J.(1990) *Involvement of an NAD(P)H oxidase as an PO2 sensor protein in the rat carotid body* Biochem.J. 272: 743-747

Daagsgaard, C., Taylor, L.E., Brient, K., Poyton, R.O. (2001) *Effects of Anoxia and the Mitochondrion on Expression of Aerobic Nuclear COX Genes in Yeast* The Journal of Biological Chemistry 10: 7593-7601

Dalton, T.P., Shertzer, H.G., Puga, A(1999) *Regulation of gene expression by reactive oxygen* Annu. Rev. Pharmacol. Toxicol. 39: 67-101

DeLeo, F.R., Quinn, M.T. (1996) *Assembly of the phagocyte NADPH oxidase: molecular interaction of oxidase proteins* Journal of Leukocyte Biology 60: 677-691

Delysse, S., Raimond, P., Nunzi, J.M. *Two-photon absorption in non-centrosymmetric dyes* Chemical Physics 219: 341-351

Denk, W., Piston, D., Webb, W.W. (1995) *Two-photon molecular excitation in laser scanning microscopy* in: Handbook of Confocal Microscopy (Pawley, J.B., ed.): 445-457, Plenum, New York

Denk, W., Strickler, J.H., Webb, W.W. (1990) *Two-Photon Laser Scanning Fluorescence Microscopy* Science Reports 248: 73-76

Diaspro, A., Robello, M.(1999) *Multi-Photon Excitation Microscopy to Study Biosystems* European Microscopy and Analysis. March: 5-7

Diaspro, A., Corosu, M., Ramino, P., Robello, M. (1999) *Adapting a Compact Confocal Microscope System to a Two-Photon Excitation Fluorescence Imaging Architecture* Microscopy Research and Technique 47: 196-205

Dick, B (1981) *Zweiphotonenspektroskopie Dipol-verbotener Übergänge* Inauguraldissertation, Universität zu Köln

Dixon, A. *The Advantages of Femtosecond Pulsed Lasers in Multi-Photon Microscopy* Technical Note 07 Bio-Rad Microscopy Division, Hemel Hempstead, UK

Drake, A.F. (1994) *Optical Spectroscopy* Principles and Instrumentation. in: Microscopy, Optical spectroscopy, and macroscopic techniques - Methods in molecular biology. Humana Press. Totowa, New Jersey

Dreher, D., Junod, A.F. (1996) *Role of Oxygen Free Radicals in Cancer Development* European Journal of Cancer 32A: 30-38

Doussiére, J., Vignais P.V. (1992) *Diphenylene iodonium as an inhibitor of theNADPH oxidase complex of bovine neutrophils* Eur. J. Biochem 208: 61-71

Ehleben, W., Porwol, T., Fandrey,J., Kummer, W., Acker,H. (1997) *Cobalt and desferrioxamine reveal crucial members of the oxgen sensing pathway in HepG2 cells* Kidney International 51: 483-491

Ehleben, W., Bölling, B., Merten, E., Porwol, T., Strohmaier, A.R., Acker, H. (1998) *Cytochromes and oxygen radicals as putative members of the oxygen sensing pathway* Respiration Physiology 114: 25-36

Ehricke, H.H. (1997) *Medical Imaging* Digitale Bildanalyse und -kommunikation in der Medizin. Vieweg; Braunschweig, Wiesbaden.

Eggeling, E., Widdengren J., Rigler R., Seidel CAM (1998) *Photobleaching of fluorecent dyes under conditions used for single-molecule detection: Evidence of Two-Step Photolysis* Analytical Chemistry 70: 2651-2659

Espoti, M.D., Hatzinisirou, I., McLennan, H., Ralph, S. (1999) *Bcl-2 and Mitochondrial Oxygen Radicals* New Approaches with Reactive Oxygen Species-Sensitve Probes. The Journal of Biological Chemistry 274: 29831-29837

Falbe, J., Regitz, M. (Hrsg.) (1989/1992) *Römpp Chemielexikon* 9. Aufl. Thieme-Verlag. Stuttgart, New York

Fandrey, J. (1995) *Hypoxia-inducible gene expression* Respiration Physiology 101: 1-10

Fandrey, J., Frede, S., Jelkmann, W. (1994) *Role of hydrogen peroxide in hypoxia-induced erythropoeitin production* Bioch.J. 303: 507-510

Fandrey, J., Frede, S., Ehleben, W., Porwol, T., Acker, H., Jelkmann, W. (1997) *Cobalt chloride and desferrioxamine antagonize the inhibition of erythropoetin production by reactive oxygen species* Kidney Int 51: 492-496

Fischer, W.G., Wachter, E.A., Lytle F.E., Armas, M., Seaton, C. (1998) *Source-Corrected Two-Photon Exited Fluorescence Measurements between 700 and 880 nm*
Applied Spectroscopy 52: 536-545

Fischer, W.G., Wachter, E.A., Armas, M., Seaton, C. (1997) *Titanium: Sapphire Laser as an Excitation Source in Two-Photon Spectroscopy* Applied Spectroscopy 51: 218-226

Fridovich, I. (1997) *Superoxide Anion Radical,($^{\cdot}O_2^{-}$), Superoxide Dismutases, and Related Matters*. Minireview. The Journal of Biological Chemistry 272: 18515-18517

Fukai, M.U., Zafari, A.M., Fukui, T., Ishizaka, N., Griendling, K.K. (1996) *$p22_{phox}$ Is a Critical Component of the Superoxide-generating NADH/NADPH Oxidase Systhem and Regulates Angiotensin II- induced Hypertrophy in Vascular Smooth Muscle Cells* The Journal of Biological Chemistry 271: 23317-23321

Galbraith, W., et al. (1991) *Imaging Cytometry by Multiparameter Fluoresscence*
Cytrometry 12: 579-596

Galla, H-J. Unter Mitarbeit von Müller, H.-J. (1988) *Spektroskopische Methoden in der Biochemie*. Georg Thieme Verlag, Stuttgart, New York

Gamaley, I.A., Klyubin, I.V. (1999) *Roles of Reactive Oxygen Species: Signaling and Regulation of Cellular Functions* International Review of Cytology 188: 203 - 255

Gauderon,R., Lubkins, P.B., Sheppard, C.J.R. (1999) *Effect of a Confocal Pinhole in Two-Photon Microscopy*. Microscopy Research Technique

Gauthier, D. (1995) *Compact, High Power Two-Photon Lasers* Duke University, Durham

Gleadle, J.M., Ebert, B.L., Ratcliffe, P.J. (1995) *Diphenylene iodonium inhibits the induction of erythropoietin and other mammalian genes by hypoxia* Eur. J. Biochem. 234: 92-99

Göppert-Mayer, M. (1931) *Über Elementarakte mit zwei Quantensprüngen* Ann. Phys. 9: 273-295

Görlach, A. et al. (1993) *Photometric characteristics of haem proteins in erythropoetin-producing hepatoma cells (HepG2)* Biochem. J. 290: 771-775

Görlach, A., Fandrey, J., Holtermann, G., Acker, A. (1994) *Effects of cobalt on haem proteins of erythropoietin-producing HepG2 cells in multicellular spheroid culture* FEBS Letters 348: 216-218

Goldberg, M.A., Schneider, T.J. (1994) *Similarities between the Oxygen-sensing Mechanisms Regulating the Expression of Vascula Endothelial Growth Factor and Erythropoetin* The Journal of Biological Chemistry 269: 4355-4359

Goldschmidt-Clermont, P.J., Moldovan, Leni (1999) *Stress, Superoxide, and Signal Transduction* Gene Expression 7: 255-260

Gong, W., Hao, B., Mansy, S.S., Gonzalez, G., Gilles-Gonzalez, M.A., Chan, M.K. (1998) *Structure of a biological oxygen sensor: A new mechanism for heme-driven signal transduction* Proc. Natl. Acad. Sci. USA 95:15177-15182

Gottwald, W.; Herbert, K. H. (1998) *UV/VIS – Spektroskopie für Anwender*. Wiley-VCH, Weinheim

Grauw, C.J., Vroom, J.M., van der Voort H.T., Gettitsen, H.C. (1999) *Imaging properties in two-photon excitation microscopy and effects of refractive-index mismatch in thick specimens* Applied Optics 38: 5995-6003

Haugland, R.P (1996) *Handbook of Fluorescent Probes and Research Chemicals* Molecular Probes, Inc. Eugene, ORHempel, S.L., Buettner, G.R., Malley, Y.Q., Wessels, D.A., Flaherty, D.M. (1999) *Dihydrofluorescein Diacetate is superior for detecting intracellular oxidans: comparison with 2',7'-Dichlorodihydrofluorescein diacetate, 5(and 6)-Carboxy-2',7'-dichlorodihydrofluorescein diacetate, and Dihydrorhodamine 123* Free Radical Biology & Medicine 27: 146-159

Hempel, S., Buettner, G.R., Malley, Y. Q., Wessels, D.A., Flaherty, D.M. (1999) *Dihydro-fluorescein diacetate is superior for detecting intracellular oxidants: comparison with 2',7'-Dichlorodihydrofluorescein diacetate, 5 (and 6)-Carboxy-2',7'-dichlorodihydrofluoresein diacetate, and dihydrorhodamine 123* Free Radical Biology & Medicine 27: 146-159

Heyworth, P.G., Knaus, U.G., Settleman, J. Curnutte, J.T., Bokoch, G.M. (1993) *Regulation of NADPH Oxidase Activity by Rac GTPase Activating Protein(s)*
Molecular Biology of the Cell 4: 1217-1223

Hirsch-Ernst, K., Kietzmann, T., Ziemann, C., Jungermann, K., Kahl, G.F. (2000) *Physiological oxygen tensions modulate expression of the mdr1b multidrug-resistance gene in primary rat hepatocyte cultures* Biochem. J. 350: 443-451

Huang, L.E., Arany,Z., Livingston, D.M., Bunn, H.F. (1996) *Activation of Hypoxia-inducible Transcription Factor Depends Primarily upon Redox-sensitive Stabilization of Its α-Subunit* The Journal of Biological Chemistry 271: 32253-32259

Hockberger, P.E. et al. (1999) *Activation of flavin-containing oxidases underlies light-induced production of H_20_2 in mammalian cells* PNAS 96: 6255-6260

Irani, K., Goldschmidt-Clermont (1998) *Ras, Superoxide and Signal Transduction*
Bioch. Pharmacology 55: 1339-1346

Jähne, B. (1989) *Digitale Bildverarbeitung*. Springer-Verlag. Berlin, Heidelberg

Jenei, A., Kirsch, A. K., Subramaniam, V., Arndt-Jovin, D.J., Jovin, T.M. (1999) *Picosecond Multiphoton Scanning Near-Field Optical Microscopy* Biophysical Journal 76: 1092-1100

Jelkmann, W. (1992) *Erythropoetin: Structure, Control of Production, and Function* Physiological Reviews 72: 449-481

Khan, A.U., Wilson, T. (1995) *Reactive oxygen species as cellular messengers* Review. Chemistry and Biology 2: 437-445

Kietzmann, T., Porwol, T., Zierold, K., Jungermann, K., Acker, H. (1998) *Involvement of a local Fenton reaction in the reciprocal modulation by O2 of the glucagon-dependent activation of the phosphoenolpyruvate carboxykinase gene and the insulin-dependent activation of the glucokinase gene in rat hepatocytes* Biochem.J 335: 425-432

Kietzmann, T., Fandrey, J., Acker H. (Aug 2000) *Oxygen Radicals as Messengers in Oxygen-Dependant Gene Expression*. News in Physiological Sciences, Vol.15

Knaus, U.G., Heyworth, P.G., Evans, T., Curnutte, J.T., Bokoch, G.M. (1991) *Regulation of Phagocyte Oxygen Radical Production by the GTP-Binding Protein Rac2* Science 254: 1512-1515

König, K., Simon, U., Halbhuber, K.-J. (1996) *3D Resolved Two-Photon Fluorescence Microscopy of Living Cells Using a Modified Confocal Laser Scanning Microscope* Cellular and Molecular Biology 42: 1181 – 1194

Knecht, T. (2000) *Theorie des Lichts* www.tu-chemnitz.de/~njo/olang/wirk06/

Kner, P.A. (1991) *A Two-photon Fluorescence Autocorrelator for a Nd:YLF Modelocked Laser* Massachusetts Institute of Technology

Korsmeyer, S. J. (1995) *Regulators of cell death* Review. TIG (Trends in Genetics) 11

Kriete, A. (1992) *Visualization in Biomedical Microscopies – 3D Imaging and Computer Applications*. VCH, Weinheim.

Kuo, S.S., Saad, A.H., Koong, A.C., Hahn, G.M., Giaccia, A.J. (1993) *Protassium-channel activation in response to low doses of g-irradiation involves reactive oxygen intermediates in nonexcitatory cells* Proc. Natl. Acad. Sci. USA 90:908-912

Kwast, K., Burke,P., Staahl, B.T., Poyton, R.O. (1999) *Oxygen sensing in yeast: Evidence for the involvement of the respiratory chain in regulating the transcription of a subset of hypoxic genes* PNAS 96:5446-5451

Kwong, C.H., Adams, A.G., Leto, T.L. (1995) *Characterization of the Effector-specifying Domain of Rac Involved in NADPH Oxidase Activation*
The Journal of Biological Chemistry 270: 19868-19872

Lahiri, S (2000) *Historical perspectives of cellular oxygen sensing and responses to hypoxia* J Appl Physiol 88: 1467-1473

Lakowicz, J. R., (1999) *Principles of fluorescence spectroscopy*, 2nd edition. Kluwer Academic/ Plenum Publishers, New York, Boston, Dordrecht, London , Moscow

Lakowitz, J., Terpetschnig, E., Szmacinski, H., Malak, H. (1995) *Metal-ligand complexes as a new class of long-lived fluorophores for protein hydrodynamics and fluorescence polarization immunoassay* in: Advances in fluorescence sensing technology 2388: 32-41

Lander, H.M. (1997) *An essential role for free radicals and derived species in signal transduction* FASEB J. 11: 118-124

Lenz, R., Seger, O. (1990) *A review of operator methods in Fourier optics* Paper presented at MICRO 1990, London 2-6-July 1990: 243-245 (chapter 8) IOP Publishing Ltd

López-López, J.R., González, C., (1992) *Time course of K+ current inhibition by low oxygen in chemoreceptor cells of adult rabbit carotid body*
Fed. of Eur. Biochemical Societeis 299: 251-254

Madeo, F., Fröhlich, E., Ligr, M., Grey, M., Sigrist, S.J., Wolf, D.H. (1999) *Oxygen Stress: A Regulator of Apoptosis in Yeast* The Journal of Cell Biology 145: 757-767

Mainen, Z.F., Maletic-Savatic, M., Shi, S.H., Hayashi, Y., Malinow, R., Svoboda, K. (1999) *Two-PhotonImaging in Living Brain Slices* Methods18: 231-239

Mäntele, W. (1999) *Fluoreszenzverfahren in der Molekularbiologie* Biospektrum 3: 210- 220

Masthay, M.B. (1988) *Molecular orbital and two-photon spectroscopic studies of conjugated p- systems*. Submitted in Partial Fulfillment of the Requirements for the Degree of Doctor of Philosophy in Chemistry, Department of Chemistry Carnegie-Mellon University (P3,7,11)

Maxwell, P.H., Pugh, C.W., Ratcliffe P.J. (1993) *Inducible operation of the erythropoietin 3´enhancer in multiple cell lines: Evidence for a widespread oxygen-sensing mechanism*
Proc. Natl. Acad. Sci. 90: 2423-2427

Mazure, N. M., Chen, E.Y., Yeh, P., Laderoute, K.R., Giacca, A.J. (1996) *Oncogenic Transformation and Hypoxia Synergistically Act to Modulate Vascular Endothelial Growth Factor Expression*. Advances in Brief. Cancer Research 56, 3436-3440

McNally, J.G., Karpova, T., Cooper, J., Conchello, J.A. (1999) *Three-Dimensional Imaging by Deconvolution Microscopy* Methods 19: 373-385

Minsky, M. (1988) *Memoir on Inventing the Confocal Scanning Microscope*
Naumer, C. , Spectra-Physics GmbH, Darmstadt (1999) *Diodengepumpte Festkörperlaser für wissenschaftliche und industrielle Anwendungen* Lasertechnik Photonik 1: 6-10

Niswender, K.D., Blackman, S.M., Rohde, L., Magnuson, M.A., Piston, D.W. (1995) *Quantitative imaging of green fluorescent protein in cultured cells: comparison of microscopic techniques, use in fusion proteins and detection limits*
Journal of Microscopy 180: 109-116

Packer, L, Cadenas, E (1994) *Biological oxidants and antioxidants* (New Strategies in prevention and therapy). Hippokrates Verlag, Stuttgart

Paddock, S.W. (1999) *Confocal Microscopy – Methods and Protocols*. Humana Press, Towota, New Jersey

Pahl, H., Baeuerle (1994) *Oxygen and the Control of Gene Expression*
Bio Essays 16: 497-502

Pawley, J. B. (ed.) (1995) *Handbook of Biological Confocal Microscopy*. Plenum Press, New York

Pellequer, J.-L.; Brudler, R., Getzoff, E.D. (1999) *Biological sensors: More than one way to sense oxygen* Current Biology 9: R416- R418

Piston D. W. (1999) *Imaging living cells and tissues by two-photon excitation microscopy* Review, trends in Cell Biology 9: 66-69

Porwol, T., Merten, E., Opitz, N., Acker, H. (1996) *Three-dimensional imaging of Rhodamine 123 fluorescence distribution in human melanoma cells by means of confocal laser scanning microscopy* Acta Anatomica 157: 116-125

Porwol, T., Ehleben, W., Zierold, K., Fandrey, J., Acker, H. (1998) *The influence of nickel and cobalt on putative members of the oxygen-sensing pathway of erythropoetin-producing HepG2 cells* Eur. J. Biochem. (FEBS) 256: 16-23

Porwol, T. , Strohmaier A.-R. , Spiess E. (1999) *Cytomography* in: Conn, M. *Confocal Microscopy*, Methods in Enzymology, Volume 307, Academic Press, San Diego

Porwol, T., Ehleben, W., Brand,V., Acker, H. (in press 2001) *Oxygen sensor function of cyctochrome c oxidase species and NADPH oxidase in tissue* Respiration Physiology

Potter, S.M., Wang, C.M., Garrity, P.A., Fraser, S.E. (1996) *Intravital imaging of green fluorescent protein using two-photon laser-scanning microscopy* Gene 173:25-31

Powis, G., Briehl, M., Oblong, J. (1995) *Redox signalling and the control of cell growth and death* Pharmac. Ther. 68: 149-173

Rao, C.N.R. (1975) *Ultra-Violet and Visible Spectroscopy*, Chemical Applications. Third Edition, Butterworth & Co. (Publishers) Ltd., London

Ratcliffe, P.J., Maxwell, P.H., Pugh, C.W.(1997) *Beyond erythropoetin: the oxygen sensor* Molecular Basis of Renal Disease. Nephrol. Dial. Transplant 12: 1842-1848

Robenek, H.(Hrsg.) (1995) *Mikroskopie in Forschung und Praxis* GIT-Verlag, Darmstadt

Royall, J.A., Ischiropoulos, H. (1992) *Evaluation of 2', 7'-Dichlorofluorescin and Dihydrorhodamine 123 as Fluorescent Probes for Intracellular H_2O_2 in Cultered Endothelial Cells* Archives of Biochemistry and Biophysics 302: 348-355

Rost, F.W.D. (1991) *Quantitative fluorescence microscopy.* Cambridge University Press, Cambridge, New York, Port Chester, Melbourne, Sydney

Sanders, R (1995) *Fluorescence Lifetime as Contrast Mechanism in Confocal Imaging* Proefschrift Universiteit Utrecht, NL

Schaffer, J., Volkmer, A., Eggling, Subramian, C., Striker, G., Seidel, C.A.M. (1999) *Identication of Single Molecules in Aqueous Solution by Time-Resolved Fluorescence* The Journal of Physical Chemistry A 103: 331-334

Schmidt, Werner (2000) *Optische Spektroskopie* Eine Einführung 2.Auflage, Wiley-VCH, Weinheim

Schmidt, R., Thews, G. (1995) *Physiologie des Menschen* 26., vollstängig überarbeitete Aufl., Springer-Verlag Berlin-Heidelberg

Schmidt, Werner (2000) *Optische Spektroskopie* Eine Einführung 2.Auflage, Wiley-VCH, Weinheim

Schreck, R., Rieber, P., Baeuerle, P.A. (1991) *Reactive oxygen intermediates as apparently widely used messengers in the activation of the NF-κB transcription factor and HIV-1*
The EMBO Journal 10: 2247-2258

Schweiki, D., Itin, A., Soffer, D., Keshet, E. (1992) *Vascular endothelial growth factor induced by hypoxia may mediate hypoxia-initiated angiogenesis* Nature 359: 843-845

Semenza, G.L. (1999) *Perspective on Oxygen Sensing* Minireview. Cell 98: 281-284

Semenza, G.L., Nejfelt, M.K., Chi, S.M., Antonarakis, S.E. (1991) *Hypoxia-inducible nuclear factors bind to an enhancer element located 3´to the human erythropoietin gene*
Proc. Natl. Acad. Sci. USA 88: 5680-5684

Shaw, P.J., Rawlins, D.J. (1990) *Measurement of the point spread function and its use in deconvolution of confocal microscope images* Paper presented at MICRO 1990, London 2-6-July 1990: 227-230 (chapter 8) IOP Publishing Ltd

Sheppard, C.J.R., Cogswell, C.J. (1990) *Optimization of the confocal microscope system* Paper presented at MICRO 1990, London 2-6-July 1990: 231-234 (chapter 8) IOP Publishing Ltd

Sheppard, C.J.R. (1988) *Aberration in high aperture conventional and confocal imaging systems* J. Microscopy, 154: 243-256

Sheppard, C.J.R.; Shotton, D.M. (1997) *Confocal Laser Scanning Microscopy*. Royal Microscopical Society Microscopy Handbooks 38. BIOS Scientific Publishers, Oxford, UK.

Speit, G., Dennog, C. (2000) *Untersuchungen zur genotoxischen Wirkung von oxidativem Streß* Forschungsbericht FZKA-BWPLUS, Förderkennzeichen: PUG U 97 002, Baden-Württemberg

Stevens, J.K.; Linda, R.M.; Trogadis, J.E. (1994) *Three-Dimensional Confocal Microscopy: Volume Investigations of Biological Systems*. Academic Press, Inc., San Diego, London

Strohmaier, A.R., Porwol, T., Acker, H., Spiess, E. (1999) *Three-Dimensional Organization of Microtubules in Tumor Cells Studied by Confocal Laser Scanning Microscopy and Computer-Assisted Deconvolution and Image Reconstruction*
Cells Tissues Organs 167: 1-8

Stuer, D.J., et al. (1991) *Inhibition of macrophage and endothelial cell nitric oxide synthase by diphenyleneiodonium and its analogs* Cornell University Medical College, New York,
New York 10021, USA

Suzuki, Y.J., Forman H.J., Sevanian, A. (1997) *Oxidants as stimulators of signal transduction* Free Radical Biology & Medicine 22: 269-285

Tradowsky, K. (1979) *Laser* kurz und bündig Grundlagen, Technik, Anwendung. Vogel-Verlag, Würzburg

Uszczapowski, G. (1985) *Fourier-Transformation, Fourier-Integral* Demmig-Verlag Nauheim

van der Voort (1999) *The Huygens System User´s Guide* Scientific Volume Imaging b.v., Hilversum, the Netherlands

Varley, P.G. (1994) *Fluorescence Spectroscopy* in: Microscopy, Optical spectroscopy, and macroscopic techniques - Methods in molecular biology. Humana Press. Totowa, New Jersey

Vassella E., Straesser, K., Boshart, M. (1997) *A mitochondrion-specific dye for multicolour fluorescent imaging of Trypanosoma brucei* Short communication. Molecular and Biochemical Parasitology 90: 381-385

Visser, T.D., Groen, F.C.A., Brakenhoff, G.J. (1991) *Absorption and Scattering Correction in Confocal Microscopy*, J.Microscopy, 163, pp.189-200

Visser, T.D. (1992) *Diffraction of Electromagnetic Waves and Image Formation in Confocal Microscopy* Academisch Proefschrift, Universiteit van Amsterdam (and References in it)

Visser, T.D., Groen, F.C.A., Brakenhoff, G.J. (1991) *Absorption and Scattering Correction in Confocal Microscopy*, J.Microscopy, 163, pp.189-200

Volkmer, A., Hatrick, D.A., Birch, D.J.S.(1997) *Time-resolved nonlinear fluorescence sprctroscopy using femtosecond multiphoton excitation and single-photon timing detection* Meas. Sci. Technol. 8: 1339-1349

Vroom, J.M. (1998) *Two-photon excitation fluorescence lifetime imaging: development and biological applications* Proefschrift. Universiteit Utrecht

Walling, Ch. (1975) *Fenton´s Reagent Revisited* Accounts Chem Res 8: 125 - 131

Wang, G.L., Semenza, G.L. (1996) *Oxygen sensing and response to hypoxia by mammalian cells* Review Article. Redox Report 2: 89-96

Wang, G.L., Semenza, G.L. (1993) *General involvement of hypoxia-inducible factor 1 in transcriptional response to hypoxia* Proc. Natl. Acad. Sci. USA 90: 4304-4308

Wang, G.L., Jiang, B.H., Rue, E.A., Semenza, G.L. (1995) *Hypoxia-inducible factor 1 is a basic-helix-loop-helix-PAS heterodimer regulated by cellular O_2 Tension* Proc. Natl. Acad. Sci. USA 92: 5510-5514

Wang, C.-H. (1996) *Confocal Laser Scanning Microscope: A Pre-defocus imaging Mode, Sample Aberration and Applications* Acta Polytechnica Scandinavia, Applied Physics Series 207

Wartenberg, M., Ling, F.C., Acker, H., Gassmann, M., Hescheler, J., Sauer, H. (2001) *Regulation of multidrug resistance in tumor spheroids by hypoxia, reducing agents and radical scavengers* P21-1 in: European Journal of Physiology Supplement to Volume 441, No. 6

Wartenberg, M., Acker,H. (1996) *Induction of Cell Death by Doxorubicin in Multicellular Spheroids as Studied by Confocal Laser Scanning Microscopy* Anticancer Research 16: 573-580

Webb R.H. (1999) *Theoretical Basis of confocal microscopy* in: Conn, M. (1999) *Confocal Microscopy,* Methods in Enzymology, Volume 307, Academic Press, San Diego

Weber, G (1997) *Fluorescence in Biophysics: Accomplishments and Deficiencies* in: Fluorescence Spectroscopy. Methods in Enzymology 278: 1-15

White, J. (with Dixon, A.) *Applications of Multi-Photon Fluorescence Microscopy in Cell and Developmental Biology using a mode-locked, all-solid state Nd:YLF laser* University of Wisconsin, USA

Williams,D.H.; Fleming, I. *Spektroskopische Methoden in der Organischen Chemie*. Übersetzt von Bernd Zeeh (1971), 2.deutsche Auflage. Georg Thieme Verlag, Stuttgart, New York

Wilson, T. (1990) *Confocal Microscopy*. Academic Press Inc., San Diego

Wilson, T.& Carlini, A.R. (1989) *The effect of aberrations on the axial response of confocal imaging systems* J. Microscopy, 154: 243-256

Wilson, D.F., Mokashi, A., Chugh, D., Vinogradov, S., Osanai, S., Lahiri, S. (1994) *The primary oxygen sensor of the cat carotid body is cytochrome* a_3 *of the mitochondrial respiratory chain* FEBS Letters 351: 370-374

Wotzlaw, C. (2001) *Hochauflösende nichtlineare Fluoreszensmikroskopie der subzellulären Lokalisation von Tumorzellaktivitäten* Diplomarbeit, Fachhochschule Gießen-Friedberg, University of Applied Sciences

Wotzlaw, C., Berchner-Pfannschmidt, U., Kietzmann, T., Acker, H. (2001) *3D imaging of reactive oxygen species generating intracellular compartments by 2 photon microscopy* P47-1 in: European Journal of Physiology Supplement to Volume 441, No. 6

Xiao, G. (1990) *Confocal Optical Imaging Systems and their Application in Microscopy and Range Sensing*. Stanford University

Xu, C., Webb, W.W. *Measurement of two-photon excitation cross sections of molecular fluorophores with data from 690 to 1050 nm* Optical Society of America 13: 481-491

Xu, C., Zipfel, W., Shear, J.B., Williams, R.M., Webb, W.W. (1996) *Multiphoton flurescence exitation: New spectral windows for biological nonlinear microscopy*
Natl. Acad. Sci. USA 93: 10763-10768

Yagisawa, M. et al. (1996) *Superoxide Release and NADPH Oxidase Components in Mature Human Phagocytes: Correlation between Functional Capacity and Amount of Functional Proteins* Biochemical and Biophysical Research Communications 228: 510-516

Yang, S, Madyastha, P., Bingel, S., Ries, W., Key, L. (2001) *A New Superoxide-generating Oxidase in Murine Osteoclasts* The Journal of Biological Chemistry 276: 5452-5458

Youngson, C., Nurse, C., Yeger, H., Cutz, E. (1993) Oxy*gen sensing in airway chemoreceptors* Nature 365: 153-155

Zhu, H., Bunn, H.F. (1999) *Oxygen sensing and signaling: impact on the regulation of physiologically important genes* Respiration Physiology 115: 239-247

16. Links in the Internet

http://msa.microscopy.com

http://www.bioimage.org

http://www.bocklabs.wisc.edu/imr/home2.htm

http://confocal.med.unc.edu/wwwleica/Operation/Operating.htm (2001) *Principles of Confocal Scanning* Cell & Molecular Physiology Department, UNC.

http://www.chroma.com

http://www.cshl.org

http://www.image1.com

http://www.jacksonimmuno.com

http://www.lasertec.co.jp

http://www.leica.com

http://www.lsr.co.uk

http://www.mbl.edu

http://www.microscopy.bio-rad.com

http://www.mdyn.com

http://www.nikon.com

http://www.noran.com

http://www.olympus.co.jp

http://www.omegafilters.com/prod/photonics.html

http://optics.jct.ac.il/~aryeh/Confocal/hints.confocal.html

http://www.optiscan.com.au

http://www.ou.edu/research/electron/mirror/web-org.html

http://www.physikinstrumente.com

http://www-phys.rrz.uni-hamburg.de/serv.../fachinfo_Kurzfassungen/dok-tkel.html

http://www.probes.com

http://www.cshl.org

http://www.svi.nl/galleryRestLowLight.html

http://www.technical.com

http://www.videomicroscopy.com

http://www.zeiss.com

http://www2.uchc.edu/htterasaki